

**A MEASUREMENT OF THE ULTRA-HIGH
ENERGY COSMIC RAY FLUX WITH THE HIRES
FADC DETECTOR**

BY ANDREAS ZECH

**A dissertation submitted to the
Graduate School—New Brunswick
Rutgers, The State University of New Jersey
in partial fulfillment of the requirements
for the degree of
Doctor of Philosophy
Graduate Program in Physics and Astronomy**

Written under the direction of

Prof. Gordon Thomson

and approved by

New Brunswick, New Jersey

October, 2004

© 2004

Andreas Zech

ALL RIGHTS RESERVED

ABSTRACT OF THE DISSERTATION

A Measurement of the Ultra-High Energy Cosmic Ray Flux with the HiRes FADC Detector

by Andreas Zech

Dissertation Director: Prof. Gordon Thomson

We have measured the ultra-high energy cosmic ray flux with the newer one of the two detectors of the *High Resolution Fly's Eye* experiment (*HiRes*) in monocular mode. An outline of the *HiRes* experiment is given here, followed by a description of the trigger and Flash ADC electronics of the *HiRes-2* detector. The computer simulation of the experiment, which is needed for resolution studies and the calculation of the detector acceptance, is presented in detail. Different characteristics of the simulated events are compared to real data to test the performance of the Monte Carlo simulation. The calculation of the energy spectrum is described, together with studies of systematic uncertainties due to the cosmic ray composition and aerosol content of the atmosphere that are assumed in the simulation. Data collected with the *HiRes-2* detector between December 1999 and September 2001 are included in the energy spectrum presented here. We compare our result with previous measurements by other experiments.

Preface

The question about the origin of ultra-high energy cosmic rays, with energies up to around $10^{20}eV$, is among the greatest puzzles physicists are trying to solve today. The detection of cosmic rays with energies exceeding a theoretical limit derived from elementary particle physics, the so-called “GZK cut-off”, has led to an increased interest in this topic in the recent years. With a multitude of sometimes contradictory theories in existence, new experimental results are necessary to provide new insights into the questions of acceleration mechanism, sources and composition of cosmic ray particles with energies many orders of magnitude larger than can be achieved in man-made accelerators. The answers to those questions will have implications for both astrophysics and particle physics, and thus add to our understanding of nature on the smallest and largest scale.

The *Hires* experiment consists of two air fluorescence detectors that observe particle cascades caused by cosmic ray showers in the earth’s atmosphere. This work describes the measurement of the cosmic ray flux at energies above $10^{17}eV$ with the newer *HiRes-2* detector. The calculation of the flux from the measured cosmic ray showers is a problem of unfolding the distribution of reconstructed cosmic ray energies from the distortions of the detector. Detailed computer simulations are necessary for this process and played a prominent role in the analysis.

This work is organized in the following way:

Chapter 1 provides a brief introduction into cosmic ray physics, with some theoretical background on extensive air showers and particle acceleration. A survey of experimental data is presented, with focus on the flux measurements in the ultra-high energy regime.

In the next two chapters, the *HiRes* experiment is described in some detail. An outline of the history of the *HiRes* experiment, including a short description of *Fly's Eye* and *Hires/MIA*, is presented in **Chapter 2**, together with an overview of the two *HiRes* sites and the detector calibration. The Flash ADC electronics and trigger system of the *HiRes-2* detector, which was used for the measurement presented here, are explained in **Chapter 3**.

The development of the *HiRes-2* detector simulation is presented in **Chapter 4**. Details on the shower library, trigger database, background noise and other improvements to the Monte Carlo programs are given here. I have also included a description of the atmospheric analysis, whose results were implemented in the simulation programs in the form of a database with hourly entries.

The data analysis is presented in the following chapters. The reconstruction of the event geometry and energy, including a correction for “missing energy” and for a difference in the calibration of the two detectors, is described in **Chapter 5**. A summary of quality cuts that were applied in the data selection process is given in **Chapter 6**. Estimates of the energy resolution and resolution of the event geometry from Monte Carlo simulations were the basis for selecting suitable cuts. They are presented in the same chapter. A set of comparison plots for different characteristics of data and simulated events can be found in **Chapter 7**. These comparisons serve as direct tests for the quality of the simulation programs.

The simulated acceptance of the detector is shown in **Chapter 8**, followed by calculations of its aperture and exposure. The measured energy spectrum is presented here, together with studies of systematic uncertainties due to the assumptions about the cosmic ray composition and the atmosphere in the simulation programs. Since the regular analysis presented here uses average values to describe the atmosphere, a comparison with a second analysis, which uses the atmospheric database, is presented.

In **Chapter 9**, fits are applied to the spectrum to measure the spectral index of the cosmic ray flux. Our result is compared to previous measurements.

Acknowledgements

My thanks go out to:

Gordon, first and foremost. I could not have had a better advisor.

My family for their continuing support and encouragement. Vielen Dank euch allen !

Flo for her support and for being there for me.

Doug for lots of help with my work.

John B. and Eric for answering all my questions about the *HiRes-2* detector.

John M. and Stan for their help with calibration work and data taking in Utah.

The whole *HiRes* group for their support and for providing the data that went into this dissertation. It was fun working with you!

Ruadhan and Ben for good times and some deeper insights.

Kathy, Helen and Nancy for strong support in the daily struggle with the Rutgers bureaucracy ... and for cookies.

The staff of the Center for International Faculty and Student Services for their support in the daily struggle with the U.S. bureaucracy.

John D., Pieter and Bob for their support with all computer problems.

My thesis committee for advise during my research.

The National Science Foundation (NSF) for their financial support of this work.

The U.S. Army Dugway Proving Ground for hosting the *HiRes* detector sites.

Dedication

To Flo.

There is a theory which states that if ever anybody discovers exactly what the Universe is for and why it is here, it will instantly disappear and be replaced by something even more bizarre and inexplicable.

There is another theory which states that this has already happened.

(Douglas Adams)

Table of Contents

Abstract	ii
Preface	iii
Acknowledgements	v
Dedication	vi
List of Tables	xi
List of Figures	xii
1. An Introduction to Cosmic Ray Physics	1
1.1. Cosmic Rays and Extensive Air Showers	1
1.2. Measurements of the Ultra-High Energy Cosmic Ray Flux	5
1.2.1. Features of the Energy Spectrum	5
1.2.2. Ground Arrays	7
1.2.3. Air Fluorescence Detectors	9
1.2.4. Other Detection Techniques	13
1.3. Acceleration Mechanism and Candidate Sources	14
1.4. UHE Cosmic Rays and the GZK effect	20
1.5. Composition Measurements	26
1.6. Anisotropy Measurements	28
1.7. Future Experiments	31
2. The High Resolution Fly’s Eye Experiment	34
2.1. History of the HiRes Experiment	34

2.1.1.	The Fly’s Eye Experiment	34
2.1.2.	The HiRes Prototype Experiment and HiRes/MIA	35
2.2.	The High Resolution Fly’s Eye Experiment	38
2.3.	Detector Calibration	43
2.4.	Atmospheric Monitoring	46
2.5.	HiRes Measurements	48
2.5.1.	Energy Spectrum	48
2.5.2.	Composition	51
2.5.3.	Anisotropy	53
3.	The HiRes FADC Detector	55
3.1.	Layout	55
3.2.	Signal Processing and Trigger	57
3.3.	Data Processing	60
4.	Monte Carlo Simulation of the HiRes FADC Detector	65
4.1.	Unfolding the Cosmic Ray Spectrum	65
4.2.	Outline of the HiRes-2 Simulation Programs	70
4.3.	Air Shower Generator and Shower Library	73
4.3.1.	Air Shower Generation with CORSIKA	73
4.3.2.	The Shower Library	75
4.4.	Detector Response Monte Carlo	81
4.4.1.	Input and Output of the Detector Response MC	81
4.4.2.	Overview of the Detector Response Simulation	82
	Defining the Shower Geometry and Profile.	84
	Light Generation, Propagation and Ray Tracing.	86
	Simulation of Electronics and Trigger.	87
4.4.3.	Trigger Database	88

4.4.4.	Simulation of Noise & Noise Assisted Triggering	91
4.4.5.	Atmospheric Analysis	102
	Molecular and Aerosol Scattering	102
	Measurement of Vertical Aerosol Optical Depth	104
	Measurement of Aerosol Attenuation Length and Phase Function. 108	
	Atmospheric Database	111
5.	Event Reconstruction & Analysis	118
5.1.	Reconstruction of the Shower Geometry	118
5.2.	Reconstruction of Shower Profile and Energy	123
5.3.	Calibration Correction	127
5.4.	Analysis Programs	129
6.	Data Cuts & Resolution	131
6.1.	Cuts & Data Statistics	131
6.2.	Monte Carlo Resolution Studies	134
7.	Comparisons between data and Monte Carlo	140
7.1.	Comparisons of Geometric Parameters	140
7.2.	Comparisons of Shower Characteristics	143
7.3.	Comparisons of Trigger Characteristics	146
7.4.	Comparisons of fit χ^2	149
7.5.	Conclusion	149
8.	HiRes-2 Energy Spectrum & Systematics	151
8.1.	HiRes-2 Aperture	151
8.2.	Energy Spectrum	155
8.3.	Systematic Uncertainties	158
8.3.1.	Uncertainties in the Input Composition	158

8.3.2. Atmospheric Uncertainties	162
9. Conclusions	167
Appendix A. List of Acronyms	178
References	179
Vita	184

List of Tables

3.1.	Main entries in the <i>frawl</i> bank.	61
3.2.	Main entries in the <i>ftgl</i> bank.	62
4.1.	Slopes of Gaisser-Hillas fit parameters vs. log(energy).	80
4.2.	Main entries in the <i>fmcl</i> bank.	83
5.1.	Main entries in the <i>rufpln</i> bank.	121
5.2.	Main entries in the <i>rufift</i> bank.	122
5.3.	Main entries in the <i>ruspgf</i> bank.	126
6.1.	Data cuts.	133
8.1.	Cosmic ray flux measured by <i>HiRes-2</i>	157

List of Figures

1.1. Particle components of extensive air showers.	3
1.2. Heitler’s toy model for electromagnetic cascades.	4
1.3. Cosmic ray energy spectra from the “knee” to the “second knee”.	6
1.4. UHECR energy spectrum measured by <i>Haverah Park</i>	8
1.5. UHECR energy spectrum measured by <i>Yakutsk</i>	10
1.6. Nitrogen fluorescence yield spectrum used in this analysis.	11
1.7. UHECR energy spectrum measured by <i>Fly’s Eye</i> in stereo mode	12
1.8. Fermi acceleration at a shock wave front.	15
1.9. Hillas Diagram of possible UHECR sources.	19
1.10. Highest energy points seen by <i>Yakutsk</i> , <i>Haverah Park</i> and <i>SUGAR</i>	23
1.11. UHECR energy spectrum measured by <i>AGASA</i>	24
1.12. The GZK feature for different over-densities of sources.	25
1.13. X_{max} distributions seen by different experiments	27
1.14. Clustering of UHECR arrival directions seen by <i>AGASA</i>	29
1.15. Effective detection areas of cosmic ray experiments.	33
2.1. Geometrical arrangement of <i>Fly’s Eye</i> PMT pixels in the sky.	35
2.2. Configuration of the <i>HiRes-1</i> prototype mirrors.	36
2.3. Detector housings of the <i>HiRes</i> experiment.	38
2.4. <i>HiRes-2</i> mirror configuration.	39
2.5. UV filter transmission and PMT quantum efficiency.	40
2.6. Detector units used in the <i>HiRes</i> experiment.	42
2.7. <i>HiRes</i> mirror with phototube cluster.	43

2.8. UHECR energy spectrum measured by <i>HiRes</i> in stereo mode (PRE-LIMINARY).	49
2.9. UHECR energy spectrum measured by <i>HiRes-1</i>	51
2.10. UHECR composition measured by <i>HiRes/MIA</i> and <i>HiRes</i> stereo.	52
3.1. Overview of the <i>HiRes-2</i> site on Camel’s Back Ridge.	55
3.2. <i>HiRes-2</i> communications diagram.	56
3.3. Air shower seen in the <i>HiRes-2</i> event display.	63
3.4. High-gain and trigger channel response to an air shower.	64
4.1. Data-MC Comparison: energy distribution for E^{-3} input spectrum in MC.	67
4.2. Data-MC Comparison: energy distribution for <i>Fly’s Eye</i> input spectrum in MC.	68
4.3. Ratio of simulated acceptances for different input spectra.	69
4.4. Schematic layout of the <i>HiRes-2</i> Monte Carlo Programs.	72
4.5. Gaisser-Hillas fit to a simulated air shower.	76
4.6. Variation of Gaisser-Hillas parameters with zenith angle.	77
4.7. Variation of G.-H. parameters with energy (proton primaries).	78
4.8. Variation of G.-H. parameters with energy (iron primaries).	79
4.9. Energy- R_p Cut applied in the MC.	85
4.10. Data-MC Comparison: noise channels in DS2 with only ambient noise in MC.	92
4.11. Data-MC Comparison: noise channels in DS2 with realistic noise in MC.	94
4.12. Data-MC Comparison: track angles in DS2 with only ambient noise in the MC.	95
4.13. Data-MC Comparison: track angles in DS2 with realistic noise in the MC.	96
4.14. Noise channel distributions in DS2 and DS3.	97

4.15. Data-MC Comparison: noise channels in DS3 before correction. . . .	98
4.16. Data-MC Comparison: track angles in DS3 before noise correction. . .	99
4.17. Data-MC Comparison: noise channels in DS3 after correction.	99
4.18. Data-MC Comparison: track angles in DS3 after noise correction. . .	100
4.19. FADC distribution from a DS3 snapshot.	100
4.20. Data-MC Comparison: track angles in DS3 after cut.	101
4.21. Aerosol phase function used in the MC and reconstruction code. . . .	103
4.22. Sine fits to north over south ratios of horizontal laser shots.	105
4.23. Scattered light from vertical lasers in the different epochs.	107
4.24. Scattered light distribution from dust aerosols with fit.	110
4.25. Horizontal laser profile in a night with small aerosol concentration. . .	113
4.26. Horizontal laser profile in a night with large aerosol concentration. . .	114
4.27. Correlation between aerosol attenuation length and recorded number of photons.	115
4.28. VAOD and inverse HAL for DS1 nights.	115
4.29. VAOD and inverse HAL for DS2 nights.	116
4.30. VAOD and inverse HAL for DS3 nights.	116
4.31. VAOD and inverse HAL for all three datasets.	117
4.32. VAOD and inverse HAL for all nights included in the atmospheric database.	117
5.1. Geometry of the shower-detector plane.	119
5.2. Fit to the track of an event.	120
5.3. Time versus angle fit of an event.	122
5.4. Reconstructed photoelectron distribution of an event.	123
5.5. Profile fit of an event.	125
5.6. Illustration of detection in stereoscopic mode.	127
5.7. Ratio of <i>HiRes-1</i> and <i>HiRes-2</i> energies.	128

5.8.	Correction for “missing energy”.	129
6.1.	Energy resolution at third cut level.	135
6.2.	Energy resolution at second cut level.	136
6.3.	Energy resolution at first cut level.	136
6.4.	Energy resolution for different energy ranges.	137
6.5.	Resolution in X_{max} .	138
6.6.	Resolution in R_p .	138
6.7.	Resolution in the ψ -angle.	139
7.1.	Data-MC Comparison: R_p .	141
7.2.	Data-MC Comparison: ψ .	141
7.3.	Data-MC Comparison: zenith angle.	142
7.4.	Data-MC Comparison: pseudo-distance.	142
7.5.	Data-MC Comparison: p.e. per degree of track.	143
7.6.	Data-MC Comparison: average Čerenkov contribution.	144
7.7.	Data-MC Comparison: X_{max} .	144
7.8.	Data-MC Comparison: energy distribution.	145
7.9.	Data-MC Comparison: “good” tubes.	147
7.10.	Data-MC Comparison: track length.	147
7.11.	Data-MC Comparison: mirrors per event.	148
7.12.	Data-MC Comparison: tracks per mirror.	148
7.13.	Data-MC Comparison: χ^2 /d.o.f. of linear time fit.	149
7.14.	Data-MC Comparison: χ^2 /d.o.f. of time tangent fit.	150
8.1.	Acceptances of DS1, DS2 and DS3.	152
8.2.	Instant aperture.	153
8.3.	Exposure.	154
8.4.	Smoothed exposure.	154
8.5.	UHECR energy spectrum measured by <i>HiRes-2</i> .	156

8.6.	Exposures for pure iron and pure proton MC sets.	159
8.7.	Systematic uncertainties due to input composition.	161
8.8.	Energy distribution with atmospheric database.	163
8.9.	Difference in reconstructed energies due to atmospheric variations. . .	164
8.10.	Energy resolution with atmospheric database.	165
8.11.	Ratio of energy spectra analyzed with and without atmospheric database.	166
9.1.	Fit to the <i>HiRes-2</i> spectrum below the “ankle”.	168
9.2.	Fit to the <i>HiRes-2</i> spectrum above the “ankle”.	169
9.3.	UHECR energy spectrum measured by <i>HiRes</i> in monocular mode. . .	170
9.4.	<i>HiRes</i> monocular and stereo measurements of the UHECR spectrum. .	171
9.5.	<i>HiRes</i> monocular and <i>Fly’s Eye</i> stereo measurements of the UHECR spectrum.	172
9.6.	<i>HiRes</i> monocular and <i>HiRes/MIA</i> measurements of the UHECR spec- trum.	173
9.7.	<i>HiRes</i> monocular and <i>Yakutsk</i> measurements of the UHECR spectrum.	174
9.8.	<i>HiRes</i> monocular and <i>Haverah Park</i> measurements of the UHECR spectrum.	175
9.9.	<i>HiRes</i> monocular and <i>AGASA</i> measurements of the UHECR spectrum.	176

Chapter 1

An Introduction to Cosmic Ray Physics

1.1 Cosmic Rays and Extensive Air Showers

The birth of cosmic ray physics dates back to 1912, when Victor Hess discovered an until then unknown “penetrating radiation” from space. He made the first measurement of cosmic rays equipped with a gold leaf electroscope in a balloon at an altitude of about 5000 meters. It took two more decades until it was established that cosmic rays are in fact particles and that their name was therefore poorly chosen. Hess’s discovery, for which he got awarded the Nobel Prize in 1936, laid the foundation for a new field of physics, which today combines questions, experimental techniques and analysis methods from the fields of particle physics and astrophysics.

Elementary particle physics itself came into existence as a consequence of discoveries made by observations of cosmic rays crossing through cloud chambers. The positron and muon were the first two elementary particles discovered in this way in the 1930s, followed by other subatomic particles. In the 1950s, particle physicists turned their focus to accelerators and colliders and away from experiments with cosmic rays. Today, the particle physics community shows a revived interest in cosmic ray physics, since we can now observe naturally occurring particles with energies orders of magnitude higher (up to around 10^{20} eV) than what can be achieved in man-made accelerators.

A very important step for the field of cosmic ray physics was Pierre Auger’s discovery of “extensive air showers” (EAS) in 1938. From time coincident signals in two particle detectors, which were placed a few meters apart in a location high up in the

Alps, he concluded the existence of cascades of secondary particles, initiated by the interaction of a single cosmic ray particle with the atmosphere. With this indirect method of cosmic ray detection, Auger already observed showers with energies of 10^{15} eV.

The interaction of the cosmic ray nucleon or nucleus with an air nucleus high up in the atmosphere starts a nucleonic cascade of high energy hadrons. This hadronic core of the shower feeds the muonic component through the decay of charged pions and kaons. The electromagnetic component is generated primarily by photons from the decay of neutral pions and η particles. Each of these highly energetic photons starts an electromagnetic sub-shower fueled by alternate pair production and bremsstrahlung processes. The electromagnetic shower component keeps growing up to a maximum, when electrons and positrons reach the critical energy of about 80 MeV, below which continuous energy loss due to ionization becomes the dominating process and the electromagnetic particles quickly lose their remaining energy. A scheme of the different shower components is shown in Figure 1.1.

Each generation of the nucleonic cascade converts about 30% of its energy into the electromagnetic component [1]. The rapidly growing numbers of electrons and positrons become the most numerous shower particles and eventually lose about 90% of the total shower energy to ionization. This includes energy deposited into the atmosphere by muons, which lose their energy more slowly, mostly by ionization. The remaining 10% of the total shower energy, the so-called “missing energy”, is deposited into the ground in the form of muons and neutrinos or is lost in nuclear excitations.

A simple toy model (Figure 1.2) introduced by Heitler [2] for electromagnetic cascades illustrates some basic features of the development of air showers in general. Each line can be interpreted as a shower particle, which transfers half of its energy to a new particle (a new branch in the model) after one collision length λ . When the cascade has passed through an atmospheric slant depth (i.e. atmospheric depth along its axis) X , the number of particles is given as $N(X) = 2^{X/\lambda}$, and the energy of each particle is $E(X) = E_0/N(X)$, where E_0 is the energy of the primary particle. The splitting

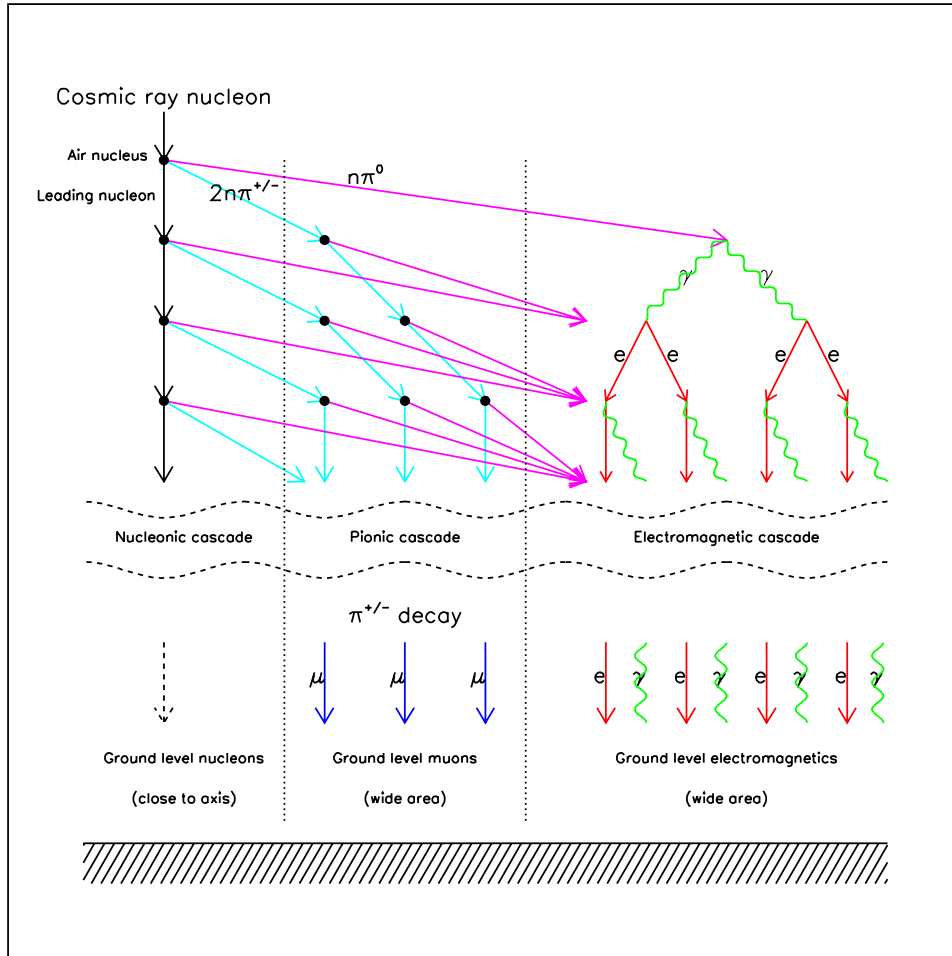


Figure 1.1: Particle components of extensive air showers. [1]

process continues until the particles reach a critical energy E_c , as in the case of electrons and positrons when ionization losses dominate. The shower reaches its maximum particle number at this energy. The corresponding atmospheric slant depth is called the “shower maximum” or X_{max} . The number of particles at X_{max} is called N_{max} and is given by

$$N_{max} = N(X_{max}) = E_0/E_c$$

Thus follows

$$X_{max} \propto \lambda \cdot \log(E_0/E_c) \quad (1.1)$$

This gives us the basic relations for high energy electromagnetic cascades:

$$\begin{aligned} N_{max} &\propto E_0 \\ X_{max} &\propto \log(E_0) \end{aligned} \quad (1.2)$$

These relations between the energy of the primary particle and the shower profile appear to be valid even for hadronic air showers, as will be shown with Monte Carlo simulations in Chapter 4.

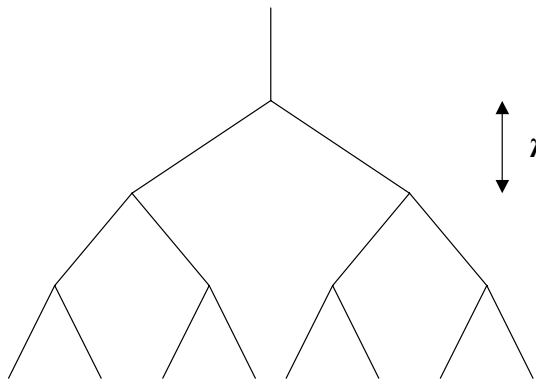


Figure 1.2: Heitler's toy model for electromagnetic cascades. [2]

Not only the energy of the primary cosmic ray particle, but also its chemical composition influences the profile of the resulting air shower. The “superposition” model provides a simplified description of the differences between air showers initiated by protons or light nuclei, as opposed to heavy nuclei. This model assumes that a nucleus with mass number A and energy E_0 can be approximated by A independent nucleons, each of energy E_0/A . The A nucleons are then assumed to interact independently with the atmosphere, which results in a superposition of A nucleon induced sub-showers. This leads to the same relation for the N_{max} of the total shower as above. However, since the energy of each sub-shower is only a fraction of the total energy, the shower maximum is now given by

$$X_{max} \propto \lambda \cdot \log [E_0 / (A \cdot E_c)] \quad (1.3)$$

This means that heavier nuclei initiate showers that develop higher up in the atmosphere compared to showers from light nuclei or nucleons. This feature can be used to distinguish between a light and heavy composition of cosmic rays. The logarithmic dependence on the mass number and statistical fluctuations in X_{max} make a more specific measurement of the composition very difficult, though. This model also explains why fluctuations in the longitudinal shower development are smaller in the case of heavy nuclei, where fluctuations of many nucleons are superimposed. A more realistic description is achieved with sophisticated simulation programs of hadronic interaction processes, which will be discussed briefly in Chapter 4.

1.2 Measurements of the Ultra-High Energy Cosmic Ray Flux

1.2.1 Features of the Energy Spectrum

The cosmic ray flux follows roughly an E^{-3} power law. Two widely acknowledged features of the energy spectrum can be seen in Figure 1.3. Shown here is the differential cosmic ray flux (i.e. the flux divided by the width of the energy bins, usually referred to as the energy spectrum) measured by various experiments. The differential flux has been multiplied by the cube of the energy of each bin, in order to make features in the spectrum become more apparent. A kink in the spectrum is observed at around $10^{15.5}$ eV. This is the so-called “knee” region. Several theories try to describe the change in the spectral index: In one model, galactic cosmic rays reach an energy at which they cannot be confined any longer by the galactic magnetic field and start leaving the galaxy, thus leading to a flux reduction. Another possible cause for the observed feature could be a turn-off of the accelerating source at the “knee” energy. In both cases, the change in the spectrum should coincide with a shift in the composition from light to heavier elements, due to the smaller Larmor radius of heavier nuclei. This shift has actually been observed, as will be described below.

At higher energies, the flux remains remarkably flat on the JE^3 plot up to an energy

of about $10^{17.5}$ eV, where another reduction causes the “second knee”. This feature is probably caused by e^+e^- pair production of photons of the cosmic microwave background radiation (CMBR) in the rest frame of the cosmic ray particle [3]. A third feature that is seen in several experiments (see the figures on the following pages) is the “ankle”, a steepening of the flux at about $10^{18.5}$ eV. It is being assumed that the “ankle” reflects a transition from a mainly galactic to a mainly extragalactic cosmic ray flux. A fourth feature, the flux suppression above an energy of about $10^{19.8}$ eV, often called the “GZK cut-off”, will be discussed below and in the next chapter.

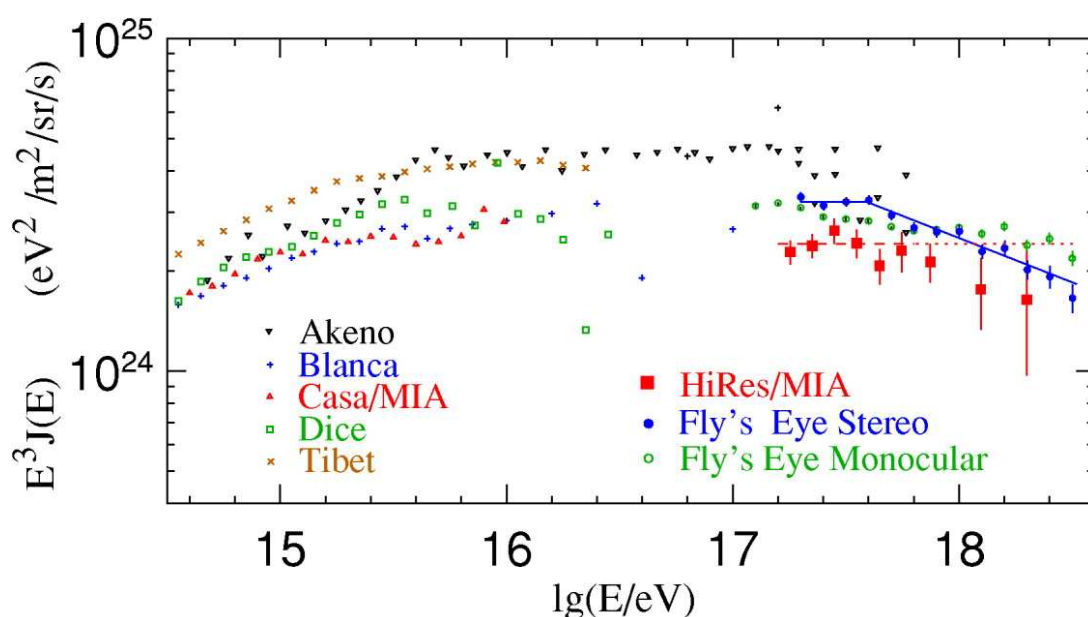


Figure 1.3: Cosmic ray energy spectra from the “knee” to the “second knee”, observed by different experiments. [4] The solid line is a fit to the *Fly’s Eye* stereo spectrum, the dashed and dotted line is a fit to the six lowest energy points of the *HiRes/MIA* spectrum. The “knee” and the “second knee” can be seen at energies of $10^{15.5}$ eV and $10^{17.5}$ eV, respectively.

Figure 1.3 points out a problem that appears in comparisons of energy spectra from different experiments: The absolute normalization of the flux depends strongly on the calibration of the experiment. Differences in the absolute energy scale lead to offsets in the plots of data points from different experiments and make it difficult to directly compare their measurements. However, the shapes of the shown spectra agree quite

well, even if the energies at which the features occur vary slightly.

The steep decrease of the cosmic ray flux with energy causes flux measurements to become more and more difficult with increasing energy. Above about 0.1 EeV the flux is lower than $10^{-10} \text{ m}^{-2}\text{s}^{-1}\text{sr}^{-1}$ and does not allow direct detection any longer. Indirect measurements of the cosmic ray flux through EAS provide the tool to detect cosmic rays at the highest energies, including ultra-high energy cosmic rays (UHECR). The ultra-high energy regime is usually defined to begin around 10^{17} eV. The two main techniques for observation of EAS up to the highest energies are surface detectors, usually arranged in large arrays, and fluorescence detectors.

1.2.2 Ground Arrays

The ground array technique was developed in the late 1940s by a group from the Massachusetts Institute of Technology (MIT) [5]. Ground arrays employ scintillation counters or water Čerenkov detectors to sample the lateral density profile of charged particles from EAS on the ground. The pattern of observed densities is used to determine the location of the shower core. The geometry of the shower axis is derived from differences in the arrival times of shower particles among the various detectors. The lateral distribution function of the observed showers is compared to model calculations, which provides an estimate of the energy of the primary cosmic ray.

Among the ground arrays that observed EAS at ultra-high energies are *Volcano Ranch* in New Mexico (1959), and later *Haverah Park* in England (1962), the *Yakutsk* array in Siberia, the *Sydney University Giant Air-Shower Recorder (SUGAR)* in Australia and the *Akeno* array in Japan. The *Volcano Ranch* array [6] covered an area of almost 10 km^2 with plastic scintillation counters of about 3 m^2 , spaced about 1 km apart. It was the first experiment to detect a cosmic ray whose energy was estimated to be 10^{20} eV.

The *Haverah Park* array [7] consisted of water Čerenkov detectors deployed over an area of about 12 km^2 . The spectrum measured by this experiment between 3×10^{17}

and 1×10^{19} eV is shown in Figure 1.4. The two curves represent the measurement of the differential spectrum analyzed for two assumptions of primary composition (pure iron and pure proton). A recent bi-modal composition measurement by the *Haverah Park* group [8] gave an estimate of 66% iron and 34% proton in the energy range shown in Figure 1.4. The old *Haverah Park* result, obtained before re-analysis with modern simulation programs, is also shown in the plot. The new spectra show the “ankle” at about 4×10^{18} eV.

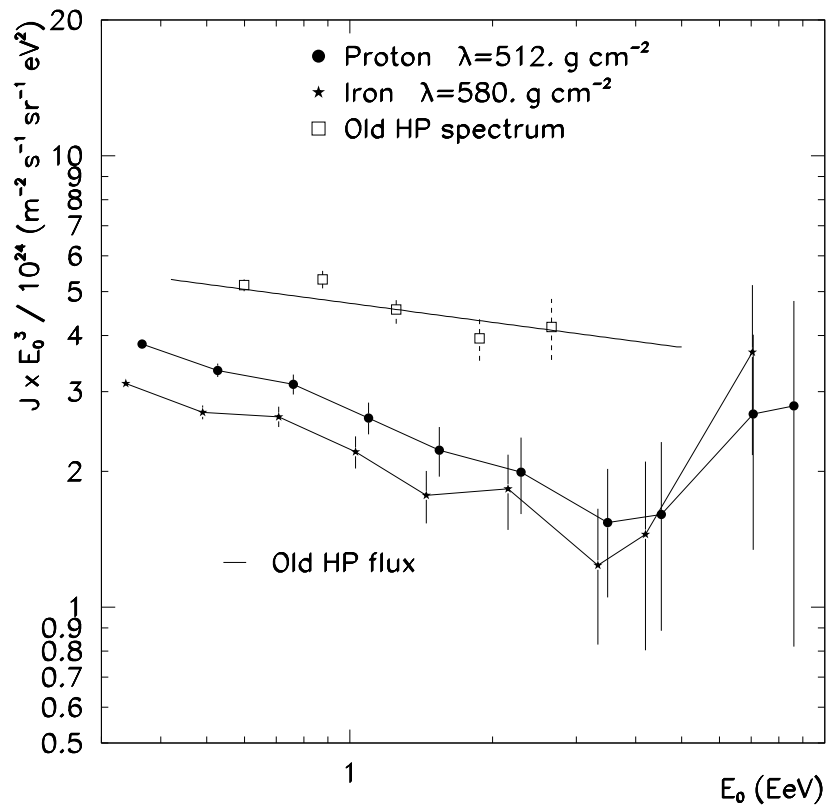


Figure 1.4: UHECR energy spectrum measured by *Haverah Park* [7]. Shown is the differential spectrum analyzed for two assumptions of primary composition (circles: pure proton, stars: pure iron). The quoted values for λ are the assumed attenuation lengths that describe the zenith angle dependence of the measured particle density. The old *Haverah Park* flux measurement is included as well (squares).

The *SUGAR* array measured only the muon component of EAS with 6 m^2 scintillation counters buried under ground. Its counters covered an area of over 60 km^2 , but the large 1.6 km spacing between stations and after-pulsing in the photo-multipliers caused

problems throughout the lifetime of the experiment. A reanalysis of *SUGAR* data can be found in [9]. The reported differential flux JE^3 between $10^{19.85}$ eV and $10^{20.05}$ eV is about $10^{24.5}$ eV²m⁻²s⁻¹sr⁻¹.

The *Yakutsk* array made use of three different types of detectors: scintillation detectors and muon counters measured the lateral profile of charged particles and muons; an array of photo-multiplier tubes (PMTs) observed the lateral distribution of Čerenkov photons from the EAS. The Čerenkov light measurement was used to calibrate experimentally the energy scale of the experiment, instead of using model calculations. The array covered 18 km² in 1974 and was re-arranged to 10 km² in 1995. The spectrum measured by *Yakutsk* is shown in Figure 1.5. *Yakutsk* measured the “knee” at about 3×10^{15} eV and the “ankle” at around 10^{19} eV [10]. A recent re-analysis of the highest energy part of the *Yakutsk* data, including data from the “trigger-1000” sub-array, which are not shown here, can be seen in Figure 1.10 and will be discussed below.

The *Akeno* array [11] consisted of scintillation counters, 1 m² to 4 m² in area, and about 200 m² of muon counters. The array covered about 20 km². The *Akeno* measurement of the spectrum is included in Figure 1.3. The *Akeno Giant Air Shower Array (AGASA)* later extended the area covered by *Akeno* to 100 km². The results of this experiment will be discussed below.

Several ground arrays have measured the cosmic ray spectrum at energies around the “knee” region. Included in Figure 1.3 are the *Casa-MIA* [12] array of scintillators and muon counters and the *Tibet* array [13] of plastic scintillators. *Dice* [14] consisted of two imaging Čerenkov telescopes, and *Blanca* [15] was an array of Čerenkov counters; these techniques will be described below.

1.2.3 Air Fluorescence Detectors

Air fluorescence detectors observe the longitudinal development of the air shower in the atmosphere. UV fluorescence light from excited nitrogen molecules in the shower

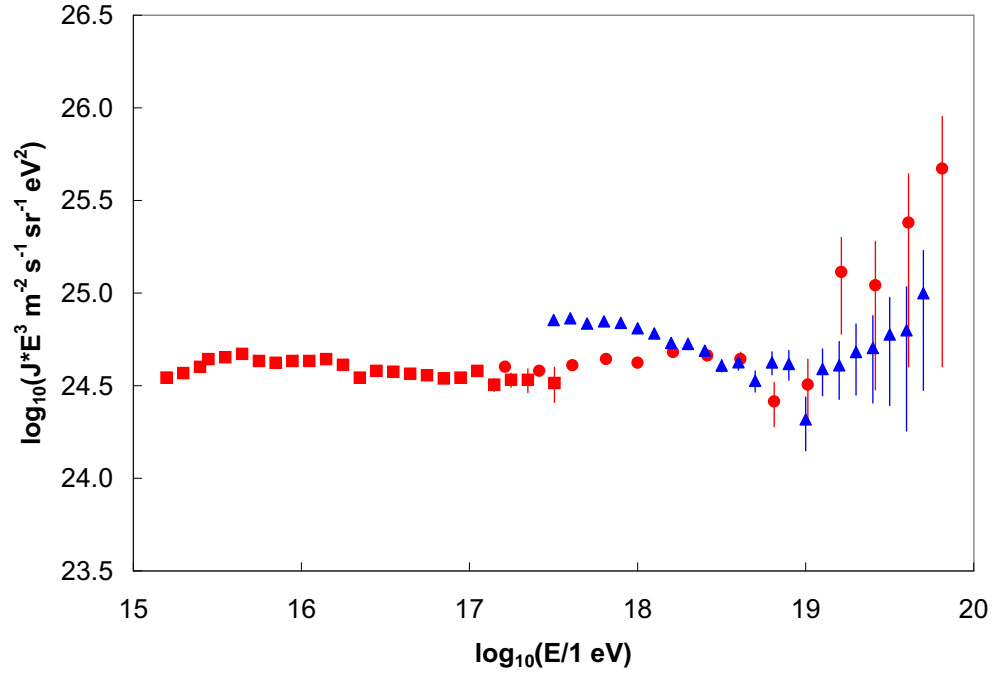


Figure 1.5: UHECR energy spectrum measured by *Yakutsk* [10]. (Circles: medium sub-array of Čerenkov detectors, squares: autonomous array of Čerenkov detectors, triangles: charged particle detectors “trigger-500”).

path is collected in mirrors on the ground and projected onto clusters of PMTs. Surface detectors collect information on the lateral shower profile at a certain point in the shower development, whereas fluorescence detectors observe the whole development of the shower in the air. The atmosphere is used as a calorimeter, in which about 90% of the cosmic ray energy is deposited. The measured flux of fluorescence photons is directly proportional to this energy deposit. Observing the longitudinal shower profile also has the advantage that one can determine X_{max} of the shower directly and infer the cosmic ray composition.

Air fluorescence at UV wavelengths between 310 nm and 400 nm is due to electronic excitations in nitrogen molecules. It has been shown ([16], [17]) that the observed fluorescence light is due to transitions from the second positive (2P) band of

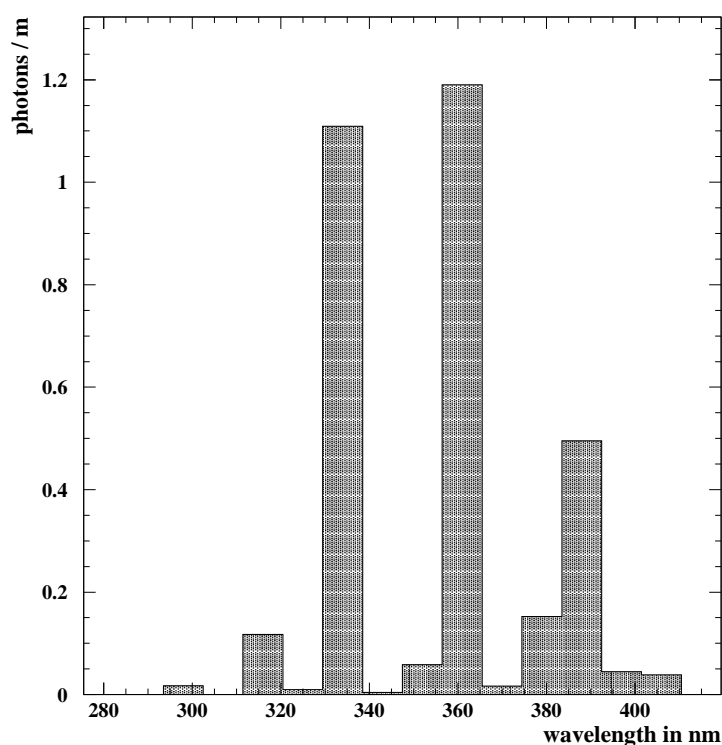


Figure 1.6: The nitrogen fluorescence spectrum used in this analysis. Shown is the spectral distribution of the fluorescence yield in air for 1.4 MeV electrons at 14° C and 1 atmospheric pressure.

nitrogen molecules and the first negative (1N) band of nitrogen ions. A variety of spectral lines is generated by many different vibrational states. The nitrogen fluorescence spectrum, which is used in this analysis, can be seen in Figure 1.6. This spectrum was compiled by H.Y.Dai using the absolute yield measurement by Kakimoto et al. [18] and the three main spectral lines from that analysis (at 337 nm, 357 nm and 391 nm). The remaining spectral lines were determined from the relative yields measured by Bunner [16]. A more detailed description can be found in [19]. The total fluorescence yield as a function of the electron energy follows the energy deposit dE/dx . The yield is roughly five photons per electron per meter of path length for electrons at the critical energy [18] and is only mildly dependent on altitude and temperature.

The *Cornell* experiment [20] was the first to use the new technique in 1964 on Mt.

Pleasant near Ithaca. However, this first attempt to measure fluorescence light from EAS was unsuccessful. First detection was achieved in 1968 in an experiment at Mt. Dodaira near Tokyo [21] and could be verified in 1976 with optical detectors in coincidence with the Volcano Ranch array [22]. The first experiment to successfully employ the air fluorescence technique to measure the cosmic ray flux was the *Fly's Eye* experiment [23], the predecessor of *HiRes*. *Fly's Eye* started taking data in 1982. Like *HiRes*, this experiment already consisted of two fluorescence detectors that allowed stereoscopic observation of EAS. The layout of the *Fly's Eye* experiment will be described in the next chapter. Part of the *Fly's Eye* data points in monocular mode (i.e. data from only one detector) and stereoscopic mode are included in Figure 1.3. The full *Fly's Eye* stereo spectrum is shown in Figure 1.7. The “second knee” can be seen at about 4×10^{17} eV, the “ankle” at about 3×10^{18} eV.

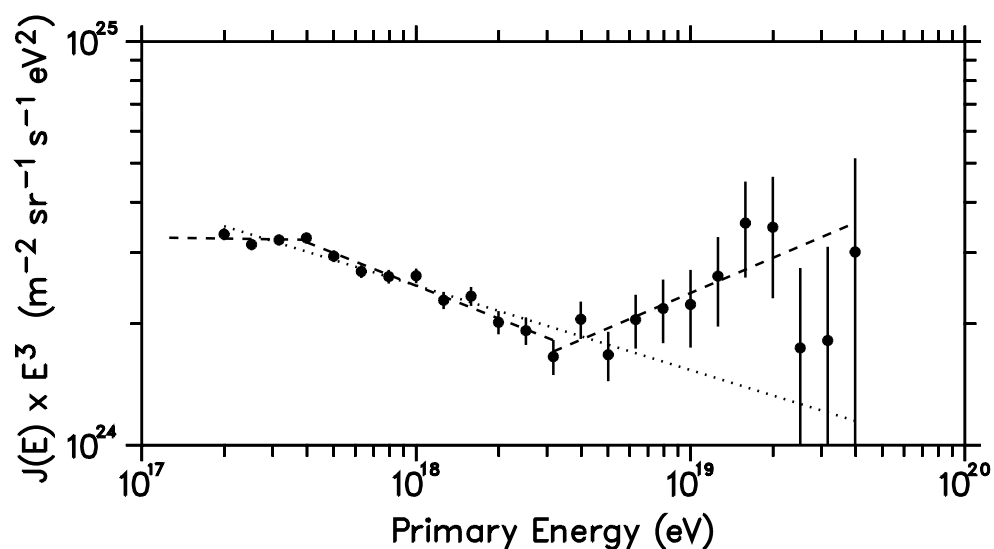


Figure 1.7: UHECR energy spectrum measured by *Fly's Eye* in stereo mode [24]. Dotted line: best fit up to $10^{18.5}$ eV, dashed lines: best fit in each energy region.

1.2.4 Other Detection Techniques

In air fluorescence experiments, Čerenkov light from the air shower is part of the background light one has to subtract in order to get a clean fluorescence light signal. However, Čerenkov light itself can be used for the detection of air showers, mostly at lower energies. Čerenkov photons are generated by electrons in the EAS whose velocities exceed the speed of light in air, i.e. $v > c/n(h)$ with c the speed of light in vacuum. The threshold energy for this effect depends on the refraction index $n(h)$ of the atmosphere, and thus on the height h . The maximum emission angle of Čerenkov light with respect to the particle direction is given by $\theta_{max} = \cos^{-1}(1/n)$, which leads to an intense Čerenkov beam within about six degrees of the shower core. Scattering of the Čerenkov photons by the atmosphere, however, allow light detection at much larger angles. The total Čerenkov light flux at the surface is proportional to the track length of shower electrons above threshold energy and can thus be used to estimate the total shower energy. Čerenkov light detectors in the form of arrays of phototubes have been used in coincidence with the *Yakutsk* and *Haverah Park* arrays, and in the *Blanca* experiment. Čerenkov telescopes like *H.E.S.S.* [25], *HEGRA* [26], *VERITAS* [27] and *MAGIC* [28] are used to observe air showers generated by gamma rays in the TeV range.

Radio emission from EAS was predicted already in the 1960s and tested by several experiments. The favored theory behind this phenomenon is coherent synchrotron emission from highly relativistic electron positron pairs, which are part of the air shower and gyrate in the earth's magnetic field. The radio signal can be picked up with arrays of antennae. This should in principle allow the detection of air showers of energies starting at about 1 PeV. Real interest in the application of this technique to detect cosmic rays is emerging only now. Some of the first few experiments that investigate this detection method are radio stations as part of the *KASCADE* ground array [29], the demonstrative *CODALEMA* experiment [30] and *LOPES* [31], the prototype for the planned *LOFAR* array.

The combination of different techniques in a single experiment allows for tests of new techniques, but also for complementary measurements of EAS characteristics, such as shower geometry, profile and energy. Simultaneous observation of cosmic ray events with ground arrays and Čerenkov detectors, radio antennae or fluorescence detectors provide a more complete description than each method on its own. The *HiRes/MIA* hybrid detector is an example for the successful combination of the two major techniques in UHECR physics, surface and air fluorescence detectors. Its measurement of the energy spectrum is included in Figure 1.3. This experiment will be discussed in more detail in Chapter 2.

1.3 Acceleration Mechanism and Candidate Sources

One of the major open questions in cosmic ray physics concerns the origin of the highly energetic particles, or more precisely the question about their sources and acceleration mechanisms.

Acceleration of the bulk of cosmic rays occurs most likely at the shock waves of supernova explosions. The mechanism in this case is known as “Fermi acceleration”. A similar form of acceleration is assumed in many models, even for some candidate sources of cosmic rays at the highest energies. This mechanism will therefore be discussed here in some detail. The discussion follows mainly the one given in Gaisser’s book [32].

Energy from a shock wave can be transferred to a single charged cosmic ray particle in repeated encounters, where one encounter is defined as the crossing of the charged particle from the unshocked gas region upstream of the shock front to the shocked gas region downstream, and back again into the upstream region (see Figure 1.8). If we assume that the particle’s energy increases in each encounter by an amount proportional to its energy, its final energy after n encounters will be:

$$E_n = E_0(1 + \zeta)^n \quad (1.4)$$

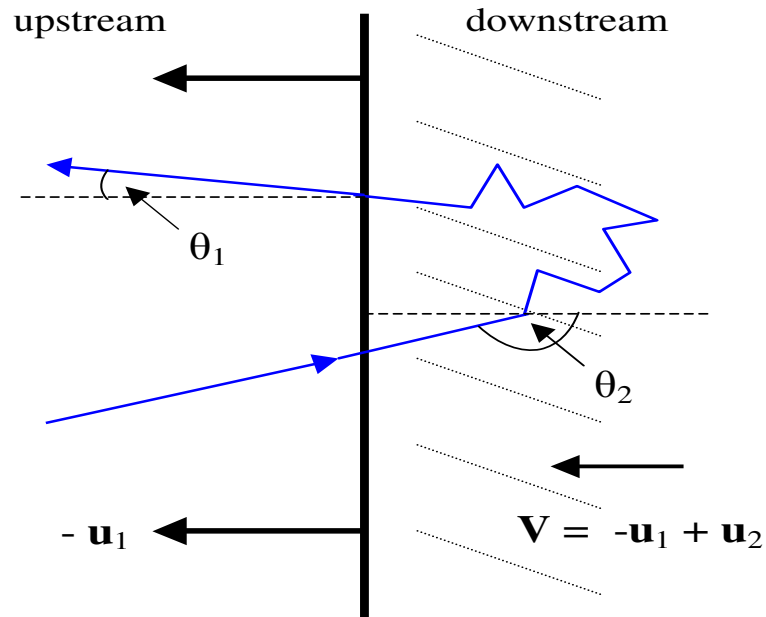


Figure 1.8: Fermi acceleration at a shock wave front. The thick vertical line represents the shock wave front, the thin line describes the path of a particle. More explanations are given in the text.

with E_0 its initial energy and the energy increase per encounter $\Delta E = \zeta E$. From this follows that the number of encounters needed to reach a certain energy E is given by:

$$n = \ln\left(\frac{E}{E_0}\right) / \ln(1 + \zeta) \quad (1.5)$$

If the accelerator has a limited lifetime, this sets an upper limit on the energy the particle can reach.

If P is the probability that the particle will escape from the accelerating region, the proportion of particles accelerated to energies greater than E is given by:

$$N(\geq E) \propto \sum_{m=n}^{\infty} (1 - P)^m = \frac{(1 - P)^n}{P} \quad (1.6)$$

Substituting n in this expression yields:

$$N(\geq E) \propto P^{-1} \cdot (E/E_0)^{-\gamma}$$

where $\gamma = \ln\left(\frac{1}{1-P}\right) / \ln(1+\zeta)$ (1.7)

As can be seen from Equation 1.7, the Fermi acceleration mechanism leads to a power law spectrum of particle energies, which is needed to describe the cosmic ray flux. Here γ only depends on the fractional energy gain ζ and on the escape probability P , which can be expressed as the ratio of the characteristic time for the acceleration cycle over the characteristic escape time.

In order to estimate the average fractional energy gain, one has to look more closely into the acceleration mechanism. In the case of an infinite plane shock front, which moves with velocity $-\vec{u}_1$, the shocked gas has a velocity $\vec{v} = -\vec{u}_1 + \vec{u}_2$ relative to the unshocked gas (upstream), with $|\vec{u}_2| < |\vec{u}_1|$. An encounter begins when a charged cosmic ray particle crosses the shock front from the upstream region under angle θ_2 against the direction of the front. The particle scatters on the irregularities in the turbulent magnetic field, which is carried along with the moving plasma in the downstream region. The interaction between particle and shock front is only defined as an encounter when the particle crosses the front again, this time from the downstream to the upstream region. With this definition, every encounter results in an energy gain, which can be calculated as follows: If the initial energy of the particle is $E_1 \simeq pc$, i.e. the particle is sufficiently relativistic, a Lorentz transformation gives its energy in the rest frame of the moving plasma in the following form:

$$E_2 = \gamma E_1 (1 - \beta \cos \theta_2) \tag{1.8}$$

Here, $\beta = v/c$ and $\gamma^2 = \frac{1}{1-\beta^2}$. Energy is transferred to the particle when it collides with the fast moving magnetic field that is carried with the plasma. In the rest frame of the moving plasma, the scatterings are not due to actual collisions, but are caused only by the motion in the magnetic field and are therefore elastic. Thus the energy of

the particle in the moving frame stays the same until it leaves the downstream region. Then its energy in the laboratory frame is:

$$E_3 = \gamma E_2(1 + \beta \cos \theta_1) \quad (1.9)$$

The fractional energy gain from a single encounter can then be calculated as:

$$\frac{\Delta E}{E_1} = \frac{E_3 - E_1}{E_1} = \frac{1 - \beta \cos \theta_2 + \beta \cos \theta_1 - \beta^2 \cos \theta_2 \cos \theta_1}{1 - \beta^2} - 1 \quad (1.10)$$

Assuming an isotropic flux, $\langle \cos \theta_2 \rangle = -2/3$ and $\langle \cos \theta_1 \rangle = 2/3$, which leads to an average fractional energy gain:

$$\frac{\langle \Delta E \rangle}{E_1} = \frac{1 + \frac{4}{3}\beta + \frac{4}{9}\beta^2}{1 - \beta^2} - 1 \quad (1.11)$$

As long as the shock velocities are non-relativistic, this can be approximated as

$$\frac{\langle \Delta E \rangle}{E_1} \simeq \frac{4}{3}\beta \quad (1.12)$$

The average fractional energy gain thus depends only on the velocity of the shocked gas relative to the unshocked gas. Due to the linear velocity dependence, acceleration on at shock wave fronts is referred to as “first order” Fermi acceleration. “Second order” processes occur in interactions with gas clouds. For a given escape probability, the fractional energy gain derived from Equation 1.12 defines a minimum value of γ , the index of the injection power spectrum, according to Equation 1.7. A more realistic calculation of the acceleration process in a supernova blast wave is rather complicated. Gaisser estimates the upper energy limit in this process to about 100 TeV.

Fermi acceleration at supernova shock fronts could lead to cosmic ray energies a few orders of magnitude higher than this estimate, if the shock front is driven into supernova remnants or if the magnetic field configuration in the shocked plasma has a component parallel to the shock front. Maybe the observation of the “knee” in the cosmic ray spectrum is a signature of the upper limit of energies that can be reached with this acceleration mechanism? It is speculated that acceleration to higher energies

using Fermi acceleration could occur in the termination shock of a stellar wind or a galactic wind [32] [33].

An alternative to the gradual energy gain in diffuse sources would be a very fast acceleration in compact acceleration regions with very high magnetic fields. Neutron stars could drive the acceleration either with rotational energy or through the release of potential gravitational energy of mass falling onto the star. Binary star systems that include neutron stars or black holes offer several possible acceleration mechanisms that all include accretion of matter from the companion star [34].

There are only a few possible sites for acceleration of cosmic rays up to the very end of the observable spectrum. Figure 1.9 shows an updated version of the often quoted “Hillas diagram” [35]: It presents possible astrophysical sources of UHECR particles as a function of the extent of the source and its magnetic field. For the ultra-high energy range considered here, the maximum energy the cosmic ray particle can reach often depends on how long the particle can be confined in the acceleration region (as was seen from Equation 1.5). A particle can only be confined as long as its gyroradius

$$r_G \simeq \frac{1}{Z} \frac{E/10^{18} eV}{B/10^{-6} G} kpc \quad (1.13)$$

is smaller than the size of the acceleration region. This puts a constraint on the combination of source extent and magnetic field for a certain maximum energy. Possible sources for cosmic rays of a certain energy lie above diagonal lines in the $\log(B)$ vs. $\log(L)$ diagram, i.e. they follow the condition $r_G < \beta L$. For the proton and iron lines plotted in the diagram, an acceleration parameter $\beta = 1$ is assumed, e.g. describing Fermi acceleration at an ultra-relativistic shock front. For smaller β the resulting lines would lie higher. For a discussion of a more general definition of the acceleration parameter (e.g. in the case of gamma ray bursts) see [34]. Apart from the constraint on size and magnetic field, other limiting factors for the maximum energy are the lifetime of the source, as mentioned above, and energy loss mechanisms during the acceleration process, e.g. synchrotron radiation or inelastic scattering.

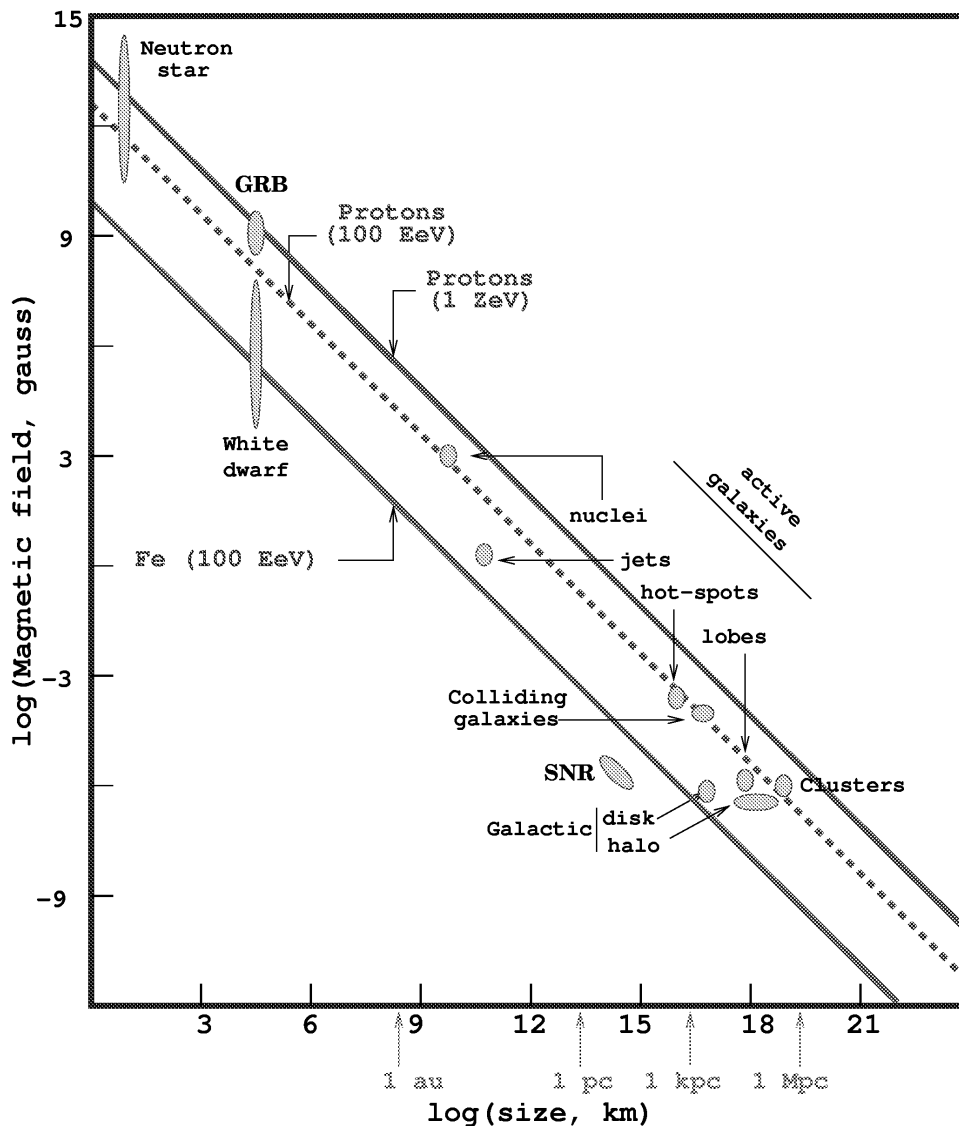


Figure 1.9: The Hillas Diagram of possible UHECR sources. Adapted from [34]. Explanations are given in the text.

Among the suggested sources for UHECR, which are currently in discussion, are rapidly rotating magnetized neutron stars, gamma ray bursts (GRB) and hot spots of radio galaxies. Iron nuclei could be accelerated to the highest energies in the magnetosphere of rapidly rotating neutron stars, but this would not be consistent with the observation of a light cosmic ray composition at the highest energies, which will be discussed below. Maximum cosmic ray energies from acceleration in ultra-relativistic

shock waves in GRB are today believed to lie only around 10^{18} eV. Thus their position in the Hillas diagram presented here is somewhat controversial. Acceleration in relativistic shocks in hot spots of FRII radio galaxies seems to be the main candidate source. A further candidate is the galactic wind model: similar to the solar wind, the galactic wind is thought of as an outflow of gas, leading to a shock wave on a galactic scale [33].

Apart from these “bottom-up” models, which explain the acceleration of cosmic ray particles to extremely high energies starting from average energies, there have also been suggestions of various “top-down” models, in which UHECR are the decay product of even more energetic, exotic source particles. Topological defects, such as cosmic strings, domain walls and magnetic monopoles, are suggested to have formed during phase transitions in the early universe. Their decay could lead to super-massive particles, which in their turn could decay and generate a flux of UHECR. Magnetic monopoles have also been suggested as possible UHECR particles themselves.

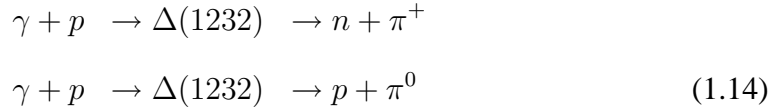
The distinction between the different proposed source models and acceleration mechanisms is only possible with precise measurements of the cosmic ray energy spectrum, composition and anisotropies of arrival directions.

1.4 UHE Cosmic Rays and the GZK effect

The cosmic ray flux we observe on earth depends not only on the source spectrum, but also on propagation effects, which have an impact on the energy distributions of cosmic rays on their way from the source to the observer.

The propagation effect most discussed today was proposed in 1966 by Greisen [36], and independently by Zatsepin and Kuz'min [37]. The so-called GZK effect predicts that an extragalactic proton cosmic ray with an energy around 6×10^{19} eV will interact with the cosmic microwave background radiation (CMBR) and experience energy loss due to pion photo-production (the onset of the effect occurs at 3×10^{19} eV according

to [38]). In the rest frame of the proton, photons from the CMBR, which has an average temperature of 2.7 K, have energies exceeding the threshold for inelastic pion photo-production. The proton and photon excite a Δ resonance [39], which decays into a proton and π^0 or a neutron and π^+ .



This process can be seen in laboratory experiments at the equivalent center of mass energy. It implies that one would expect a significant suppression of the cosmic ray flux at an energy around 6×10^{19} eV for protons that arrive at the earth from farther than 50 Mpc away. For nuclei, photo-spallation leads to an additional energy reduction.

Another propagation effect, which has been mentioned already as a possible explanation for the “second knee” in the cosmic ray energy spectrum, is the e^+e^- pair production of CMBR photons, which has a threshold of $10^{17.8}$ eV. Continuous energy losses due to the expansion of the universe (red-shifting) also play an important role for cosmic ray propagation from far away sources. Deflection of charged particles in the intergalactic magnetic field, which is assumed to have a field strength of the order of nG, and more so in the galactic magnetic field, which is of the order of μ G, are important for anisotropy studies.

Where the other propagation effects cause more or less prominent features in the cosmic ray spectrum, the GZK effect sets in fact an upper limit to energies of extragalactic cosmic rays. Its presence or absence in the cosmic ray spectrum is therefore an important indicator of the validity of the standard model of particle physics at the highest observable energies.

Several experiments had claimed detection of cosmic rays with energies exceeding 10^{20} eV. Some of the highest energy events that had been reported were later estimated to have lower energies, when more modern analysis methods, especially Monte Carlo simulations, became available. After re-analysis of their data, the *SUGAR* group sees a

few events above $10^{19.7}$ eV [9]. The most energetic event reported in a re-analysis of the *Haverah Park* data [7] has an energy of 8.3×10^{19} eV. In a very recent re-analysis of *Yakutsk* data [40], one shower above 10^{20} eV (at 1.3×10^{20} eV) was found. Figure 1.10 shows the upper end of the spectrum measured by *Yakutsk* and the highest data points seen by *SUGAR* and *Haverah Park*. The *Yakutsk* spectrum shown here contains a set of triggers that was not included in their earlier publication, shown in Figure 1.5. The *Yakutsk* UHECR spectrum is about a factor of 2.5 higher than the *Fly's Eye* spectrum, which is likely due to a difference in energy estimation. The spectral shape clearly shows the “ankle” and is consistent with a flux suppression indicative of the GZK effect. The highest energy cosmic ray event was observed in 1991 by the *Fly's Eye* experiment [41]. The energy of this event was reconstructed at 3×10^{20} eV.

Apart from *HiRes*, whose results will be discussed in the next chapter, *AGASA* is at this time the only other experiment with a large enough aperture to measure the GZK suppression in the cosmic ray spectrum. *AGASA* has been taking data since 1990. It consists of 111 plastic scintillators, each with an area of about 2.2 m^2 , which measure the lateral charged particle profile of EAS. The muon distribution is measured by 27 additional detectors under absorbers. The surface detectors are spread over an area of about 100 km^2 . Against the theoretical predictions, the *AGASA* data are consistent with an unchanged continuation of the cosmic ray spectrum and show no sign of the GZK effect, as can be seen from Figure 1.11. The comparison of the *AGASA* spectrum with a simulated spectrum assuming a uniform source distribution shows a significant discrepancy above the GZK energy threshold.

Berezinsky describes in [38] how the sharpness of the GZK feature depends on the assumption of the distribution of sources. Figure 1.12 shows three different models in comparison with data points from *Akeno* and *AGASA* (a previous result of the *AGASA* spectrum is included here): The lowest curve (1) is generated by a model with uniform source distribution, whereas the other two models assume a local over-density

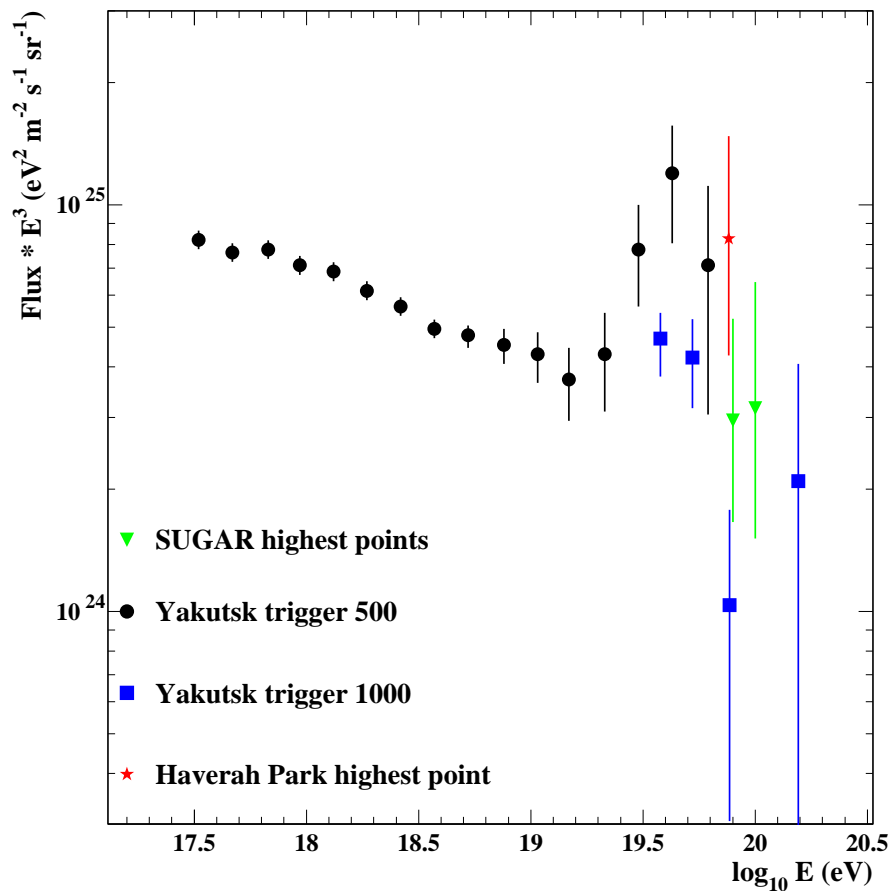


Figure 1.10: The most recent re-analysis of *Yakutsk* data, including “trigger 1000” data are shown [40], together with flux measurements for the highest energy events of *Haverah Park* [7] and *SUGAR* [9].

of sources (within 30 Mpc). The curve in the middle (2) is generated assuming a local over-density similar to what is being observed within the Local Supercluster from distributions of galaxies. This corresponds to about a factor of 2 compared to the average extragalactic density of galaxies. If one assumes an over-density of 10, the “GZK cutoff” becomes much softer, as can be seen from the top curve (3). However, this last assumption is very unlikely. All galaxy-like objects, including the astrophysical candidate sources for UHECR, would follow the observed over-density of 2, which is still inconsistent with the *AGASA* data.

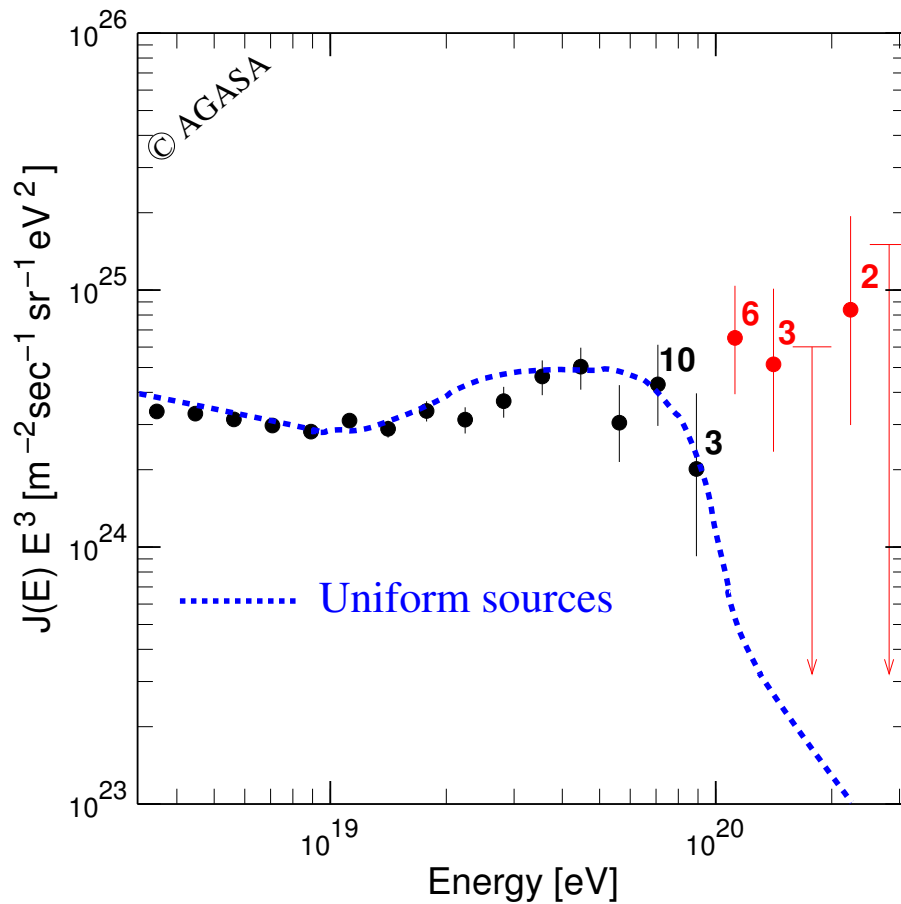


Figure 1.11: UHECR energy spectrum measured by *AGASA* [42]. Numbers attached to points show the number of events in each energy bin. The dashed curve represents a theoretical prediction of the spectrum assuming uniformly distributed extragalactic sources and a GZK flux suppression.

The detection of cosmic rays so far above the energy limit set by the GZK effect and the total absence of the effect suggested by the *AGASA* data has led to a multitude of theories on new physics at the highest observable energies: Exotic primaries, such as supersymmetric baryons or magnetic monopoles, have been suggested, since cosmic ray particles heavier than protons would raise the GZK threshold energy. Neutrinos, interacting with a relic neutrino background in so-called “Z-bursts”, could generate a flux of cosmic ray particles within distances smaller than the GZK interaction length.

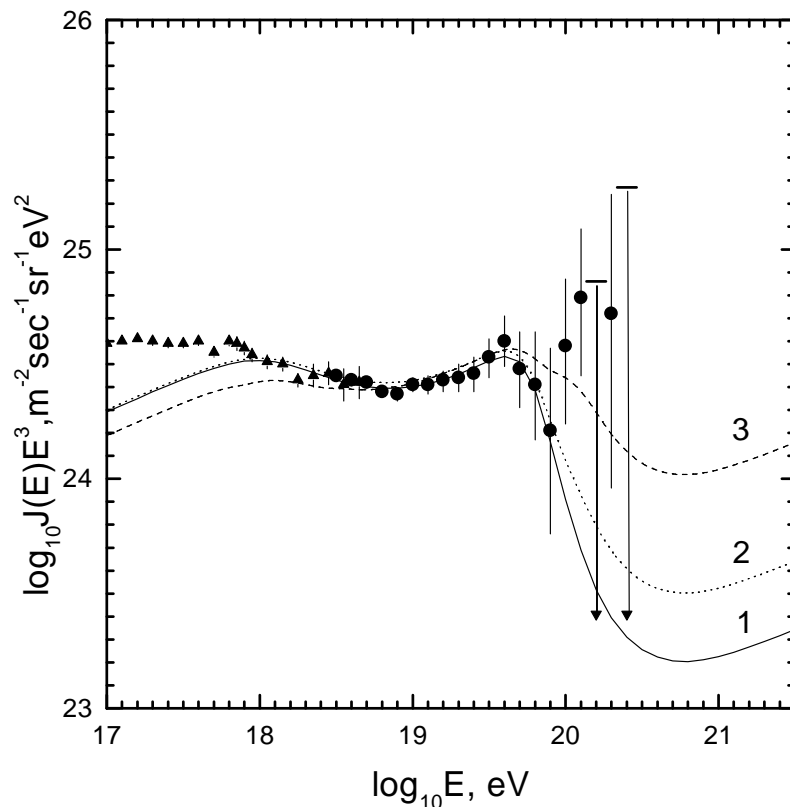


Figure 1.12: The GZK feature for different over-densities of sources [38].

New physics laws, such as the breakdown of Lorentz invariance at ultra-high energies, are another scenario, in which pion photo-production could be avoided. A wide range of exotic nearby accelerators, such as decaying super-massive particles, topological defects and primordial black holes, have been suggested. The existence of such sources within our galactic halo could explain the absence of the GZK feature in the flux measured by *AGASA*. All of the suggested models should be distinguishable in an experiment with high enough statistics at the highest energies by their specific signatures, such as anisotropies on a certain scale, spectral index of the cosmic ray flux and accompanying neutrino and gamma ray fluxes.

In the absence of new physics, one would have to find sources that are able to accelerate particles to the measured energies and can be found in the close neighborhood

of our galaxy. Nearby point sources would cause strong anisotropies in the detected UHECR arrival directions, though, which have not been observed. The assumption of a purely galactic origin of the detected UHECR would also lead to strong anisotropies, correlated with the Galactic Disc, which exceed the observed values. Furthermore, galactic UHECR would have to be heavy nuclei, since protons cannot be confined in the galactic magnetic field at these energies. This again contradicts most observations. So far, suitable nearby sources have not been found.

1.5 Composition Measurements

Measurements of the composition of the cosmic ray flux at different energies have important implications for candidate sources and acceleration mechanisms. They also probe the validity of propagation models.

The bulk of the cosmic ray matter has a relative abundance that is very similar to the average composition of stellar material in the solar system. An overabundance of lighter elements in the cosmic rays is due to spallation of heavier elements in propagation effects. Another difference, which is not well understood, is that elements with $Z > 1$ are more abundant compared to protons than in the solar system material.

At TeV to PeV energies, i.e. in the energy range below the “knee”, the cosmic ray composition is about 50% protons, 25% α particles, 13% iron nuclei, and the rest nuclei of intermediate mass numbers [33].

At energies where a direct detection of the cosmic ray composition becomes impossible, the depth of the shower maximum X_{max} is being used to distinguish between light and heavy primary particles. Two different techniques are employed to measure X_{max} : The imaging technique uses telescopes (air fluorescence or Čerenkov) to obtain a direct image of the shower longitudinal profile, whereas the non-imaging technique derives X_{max} by comparing lateral Čerenkov light or particle distributions, measured by ground arrays, with model calculations. The measured X_{max} in a certain energy

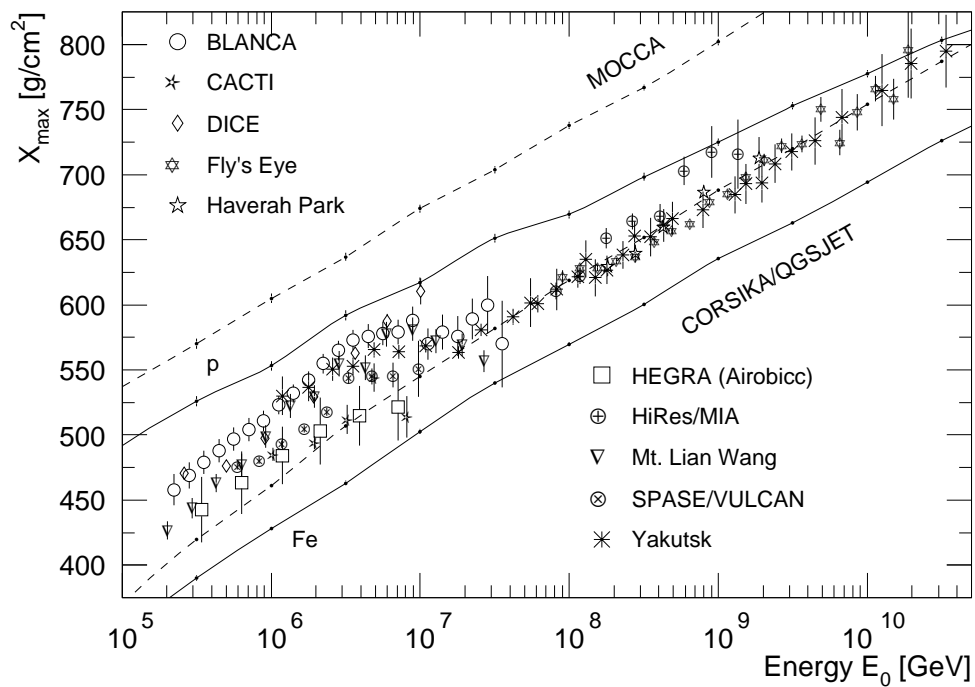


Figure 1.13: X_{max} distributions seen by different experiments [43]. The lines marked with “p” and “Fe” show the X_{max} simulation for pure proton and pure iron showers, respectively, using the *CORSIKA/QGSJET* programs. The dashed lines show simulations from an outdated program.

bin is compared to simulated average X_{max} values for light and heavy, i.e. proton and iron, showers. Fluctuations in the depth of the shower maximum between showers of the same energy are large. Therefore, only estimates of the average composition at a certain energy can be made. A differentiation of the measured composition in more than two components is very difficult at the highest energies.

A plot of the elongation rate (X_{max} versus energy) is shown for several experiments in Figure 1.13. A shift of the composition from light to heavy can be seen in the “knee” region, as mentioned above. At the highest energies, *Yakutsk*, *Fly’s Eye* and *HiRes/MIA* measure a shift from heavy nuclei back to lighter elements. This shift at the high energy end might come from a transition of galactic to extragalactic sources, since heavy nuclei from extragalactic sources would break up due to spallation processes before reaching earth. It should be mentioned, though, that measurements by the *Haverah*

Park group between 2×10^{17} eV and 3×10^{18} eV, using a different method [8], yield a composition of two thirds iron, which contradicts the other experiments.

1.6 Anisotropy Measurements

The search for anisotropies in the arrival directions of UHECR at different scales is the most direct investigation of possible sources. However, this search is complicated not only by the limited data statistics at the high energy end of the spectrum, but also by our incomplete knowledge of the propagation in galactic and extra-galactic magnetic fields.

At energies below 10^{18} eV, no significant anisotropies have been found in the cosmic ray arrival directions. This is consistent with the expectation that diffusion of the particles in the chaotic and regular galactic magnetic field, which has a field strength of the order of μG , would render all arrival directions isotropic.

At higher energies, however, anisotropies are expected to remain observable in spite of some diffusion in the magnetic field, especially in the case of light nuclei or protons, which have a larger Larmor radius than heavy nuclei. An anisotropy toward the Galactic Disc would be an indication of galactic sources at these energies. In 1999, the *AGASA* group reported a 4.5σ excess near the Galactic Center for a combination of data from the *Akeno* and *AGASA* ground arrays at energies around 10^{18} eV [44] [45]. The *Fly's Eye* experiment found a Galactic Plane enhancement in their data at comparable energies [46], and a recent analysis of *SUGAR* data confirmed an excess of cosmic rays from the Galactic Center region [47]. The observed anisotropy is thought to be due to either protons or neutrons of galactic origin. Anisotropy towards the Cygnus X-3 region has also been observed by the *Fly's Eye* and *AGASA* groups at 4σ and 3.9σ , respectively [48] [49], but could not be confirmed by *Haverah Park* [50]. Cygnus X-3 is a powerful X-ray source and part of a binary system, at a distance of about 10 kpc from earth, and thus an interesting candidate source for cosmic rays.

A Galactic Plane enhancement with a peak at about 2×10^{19} eV was found in a study of data from *Akeno*, *Haverah Park*, *Yakutsk* and *SUGAR* [51]. This peak was not found in the more recent *Fly's Eye* [46] and *AGASA* [52] data, though. A correlation with the Supergalactic Plane for cosmic rays with energies greater than 4×10^{19} eV has been claimed by Stanev et al. [53] based on *Haverah Park* data. This could not be confirmed by data from other experiments.

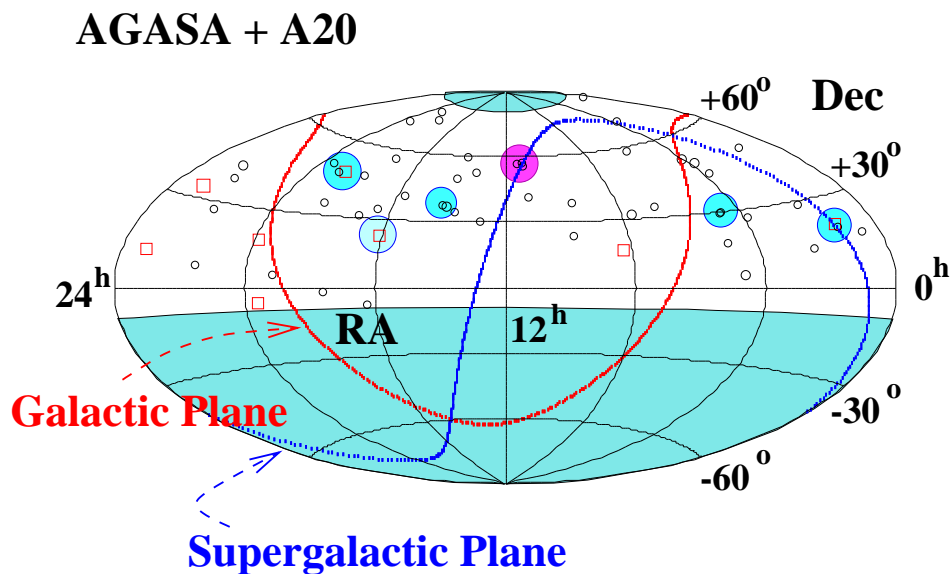


Figure 1.14: Clustering of UHECR arrival directions seen by *AGASA* [54]. Shown are arrival directions of cosmic rays with energies between 4 and 10×10^{19} eV (small circles) and $\geq 10^{20}$ eV (squares) in equatorial coordinates. Large circles indicate event clusters within 2.5° . Data from *Akeno* (“A20”) have been included as well.

Small-scale anisotropies in arrival directions have been claimed by the *AGASA* experiment [52] [54]. Clusters of events with arrival directions within 2.5° have been observed at energies above about 4×10^{19} eV. Five doublets and one triplet of events have been published so far, with one doublet and the triplet at locations close to the Supergalactic Plane (see Figure 1.14). Clustering of cosmic ray arrival directions would imply that there exist compact sources and that observed cosmic ray events can be

traced back to those sources. It has been claimed that the *AGASA* clusters show a significant correlation with a set of selected BL Lacertae objects [55], a certain kind of active galactic nuclei (AGN). Results from *HiRes* have been left out here and will be discussed briefly in the next chapter. More definite answers from anisotropy studies at the highest energies will have to wait for better statistics in the available data.

1.7 Future Experiments

The search for sources of the highest energy cosmic rays and for a solution to the puzzle around the observed super-GZK events has led to plans for new UHECR detectors with vastly larger apertures than the existing ones.

The first of the next generation UHECR experiments is already taking data in a prototype configuration. The *Pierre Auger Observatory (Auger)* [56] is operated by a large international collaboration. *Auger* is laid out as two giant ground arrays, located in the Northern and Southern hemisphere, in order to allow almost full sky coverage. The surface detectors, cylindrical water tanks with a diameter of 3.6 m and a height of 1.2 m, will be spaced apart by 1.5 km, which permits a full detection efficiency above 10^{19} eV. The water Čerenkov detectors of the ground arrays will be complemented with air fluorescence detectors. Thus, a fraction of events can be detected in hybrid mode. This will be an important advantage over previous ground arrays, since the absolute energy calibration of the experiment can be verified with the help of the calorimetric energy measurement provided by the fluorescence detectors. The ground array has the advantage of allowing observation 24 hours a day. Fluorescence detectors can only operate on clear, moonless nights, which leads to a duty cycle of only 10%. Currently, first data from prototype detectors of southern *Auger* — situated in the state of Mendoza, Argentina — are being analyzed, while new detectors are still being installed to increase the aperture to its final size. At the time of writing, funding of two thirds of the southern *Auger* site is secured. Once the southern site is completed, four fluorescence detectors will overlook an array of 1,600 surface detectors, covering an area of 3,000 km². An equally sized northern site is currently at the stage of proposal.

Another experiment has received funding and will begin construction in Millard County, Utah, in 2004. The *Telescope Array (TA)*, operated by a collaboration between Japan and the USA, will consist of a ground array of 576 plastic scintillator counters. The individual units have a total effective detection area of 3 m² each and will be

separated by 1.2 km to cover a total area of over 800 km². Three fluorescence detectors will overlook the ground array to allow hybrid detection. The aperture of the main ground array of *TA* will be about 1,400 km² sr above 10¹⁹ eV. A proposal has been made by the *HiRes* group to extend the energy range that *TA* will be able to observe down to energies below the “second knee”. The *Telescope Array Low Energy Extension (TALE)* would use a fluorescence detector in a tower configuration to overlook a part of the *TA* array that would be filled in with additional surface detectors to achieve a smaller spacing between stations. This configuration, which is somewhat similar to the *HiRes/MIA* experiment, would provide *TA/TALE* with the ability to measure the “second knee”, the “ankle” and possibly the GZK flux suppression in hybrid mode in a single experiment.

With *Auger* the upper limit of aperture for ground based cosmic ray detectors will most likely be reached. Two space-based experiments have been proposed in order to reach the next level of aperture at the highest energy end of the spectrum. The *Extreme Universe Space Observatory (EUSO)* [57] is a mission of the European Space Agency (ESA), which is currently under study. The experiment would consist of an air fluorescence detector on board of the International Space Station (ISS). Air showers in the earth’s atmosphere caused by UHECR and neutrinos of energies greater than 5×10^{19} eV could be observed from about 400 km above the earth. Monitoring of the atmosphere and of cloud coverage would require a lidar system accompanying the detector.

At the top of the detection area comparison plot in Figure 1.15 is the *Orbiting Wide-angle Light-collector (OWL)* [58]. This NASA project envisages two satellites in a near equatorial orbit, about 1,000 km above the earth, carrying two air fluorescence detectors. Like *EUSO*, *OWL* would observe EAS in the earth’s atmosphere, but it would detect events in stereo, thus reaching a better energy resolution. The aperture of *OWL* would reach about 10⁶ km²sr.

The realization of northern *Auger*, *EUSO* and *OWL* is likely to depend on the question whether *Auger* sees a continuation of the UHECR flux above the *GZK* threshold, as suggested by *AGASA*.

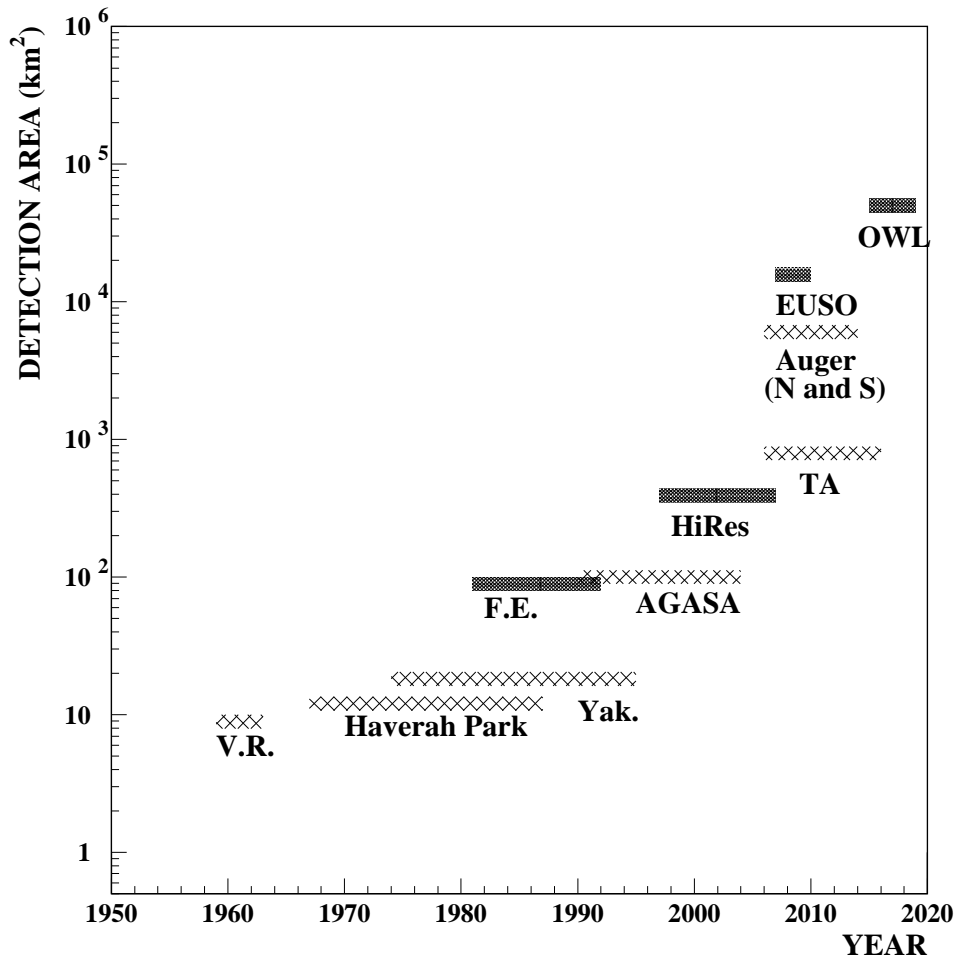


Figure 1.15: Effective detection areas of cosmic ray experiments. The detection area has been divided by 10 for pure air fluorescence detectors (filled rectangles), in order to take the 10% duty cycle into account. The construction of the northern *Auger* site and the *EUSO* and *OWL* projects are still subject to funding; dates are speculative. Based on [59].

Chapter 2

The High Resolution Fly's Eye Experiment

2.1 History of the HiRes Experiment

2.1.1 The Fly's Eye Experiment

The cosmic ray group from the University of Utah, which had successfully measured a fluorescence signal from air showers at *Volcano Ranch*, built the first cosmic ray telescope based on the new detection technique. The *Fly's Eye* experiment was given its name due to the hexagonal pattern of its PMTs, whose projection onto the sky resembles the pattern in a fly's compound eye. The geometrical arrangement of PMT pixels in the sky can be seen in Figure 2.1.

The experiment consisted of two air fluorescence detectors, located in the U.S. Army Dugway Proving Ground, about 160 km south-west from Salt Lake City, Utah. *Fly's Eye I (FE I)* was set up on top of Little Granite Mountain (also called "Five Mile Hill") and started operation in 1981; *Fly's Eye II (FE II)* was located at a distance of about 3.3 km, in the middle of the *CASA-MIA* [12] array, and was not completed until 1986. The detector was taking data — first in monocular mode with *FE I* and later in stereoscopic mode using both detectors — until July 1992. *FE I* consisted of 67 spherical mirrors, each with a diameter of about 1.5 m. Groups of 12 or 14 hexagonal PMTs, together with Winston light collectors, were mounted in the focal plane of the mirrors. The mirror units were housed in motorized steel drums, which could be rotated to the ground during the day to protect mirror and PMTs from rain and sunlight. During the night, the mirror units pointed to fixed positions in the sky to allow full coverage

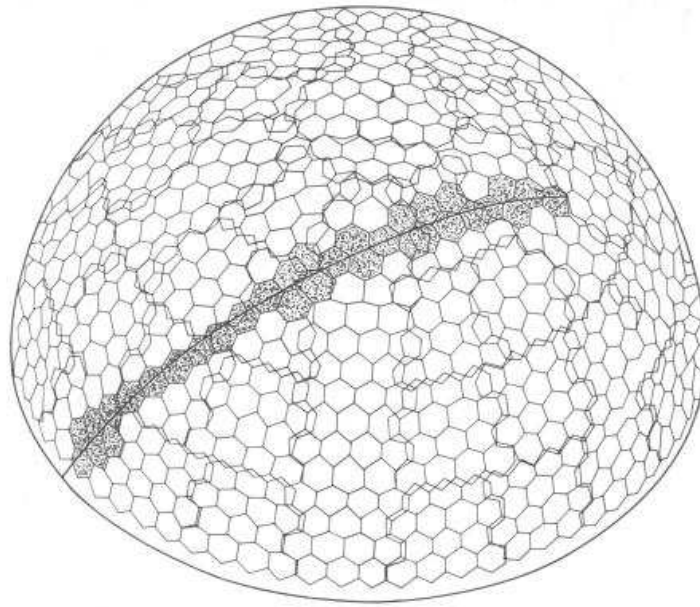


Figure 2.1: Geometrical arrangement of *Fly's Eye* PMT pixels in the sky. [33]

of the celestial hemisphere (as shown in Figure 2.1), with each pixel covering about $5^\circ \times 5^\circ$. *FE II* was a smaller site, containing only 8 mirror units. The *FE II* detector units covered about 90° in azimuth and 2° to 38° in elevation. Stereoscopic observation of EAS, using information from both sites simultaneously, was first introduced in this experiment. During its lifetime, *Fly's Eye* reached a monocular exposure of roughly $930 \text{ km}^2 \text{ sr years}$ and a stereo exposure of about $150 \text{ km}^2 \text{ sr years}$ at an energy of $5 \times 10^{19} \text{ eV}$. The *Fly's Eye* measurement of the UHECR energy spectrum and composition has been included in Figures 1.3 and 1.13, respectively. More detailed information on this experiment can be found in [23].

2.1.2 The HiRes Prototype Experiment and HiRes/MIA

After the successful operation of the *Fly's Eye* experiment and the detection of “super-GZK” events, the *High Resolution Fly's Eye* experiment was designed with the goals of increasing the data rate above 10^{19} eV by an order of magnitude and improving

the X_{max} resolution for composition studies and the angular resolution for anisotropy studies. These goals should be reached by decreasing the field of view of each PMT and increasing the mirror size. Before the new experiment was installed completely, a prototype version was set up to test the new design. Apart from stereo measurements with the two sites of the *HiRes* prototype, the *HiRes* group also undertook the first hybrid measurement of the UHECR spectrum and composition by combining the *HiRes* prototype and the *Michigan Muon Array (MIA)*.

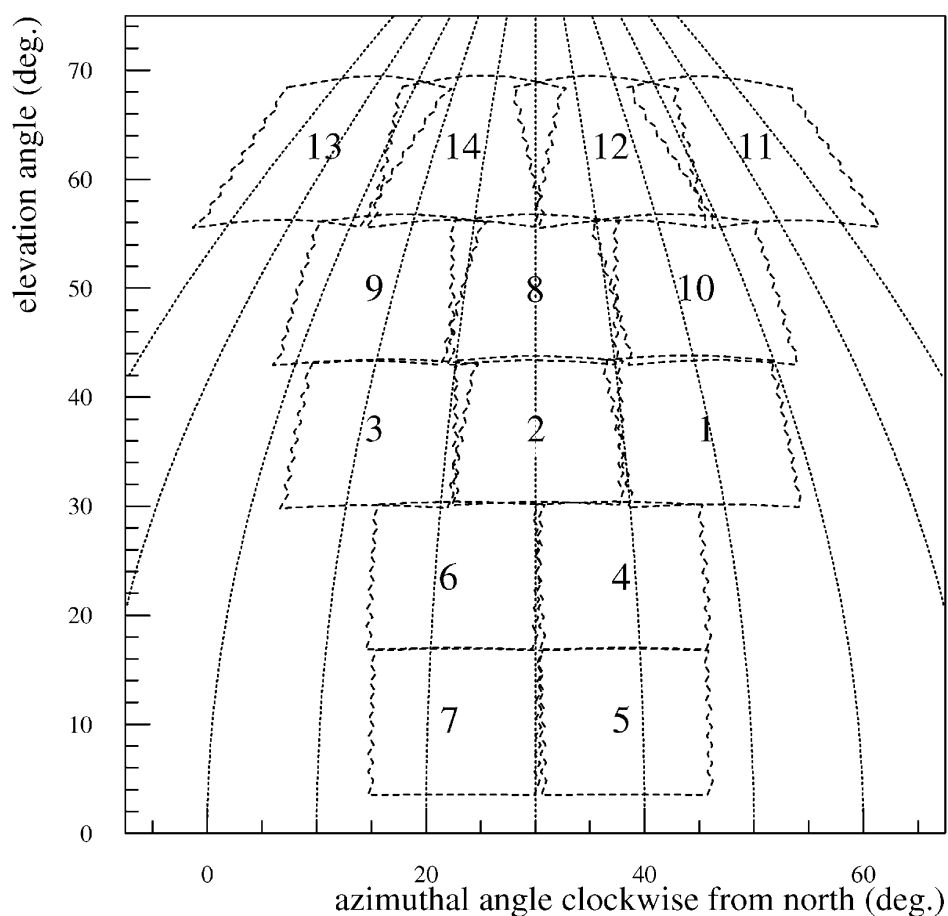


Figure 2.2: Configuration of the *HiRes-1* prototype mirrors. [60]

The *HiRes-1* prototype detector was situated on the original *Fly's Eye I* site on “Five Mile Hill”. It consisted of 14 mirrors, which were arranged in a “tower of power” configuration, as depicted in Figure 2.2, covering an elevation angle range from 3° to

70°. The large elevation coverage allowed the *HiRes-1* prototype detector to observe air showers that were nearby and developed high up in the atmosphere, and thus to detect events at energies lower than we can see today with the 1-ring and 2-ring configurations of the *HiRes* experiment (described below). The *HiRes-1* prototype overlooked the site of the *Chicago Air Shower Array (CASA)* and *MIA* [12]. The *HiRes-2* prototype consisted of only four mirrors, arranged in two elevation rings (from 3° to 30°). It had the *HiRes-1* prototype and the *CASA/MIA* array in its field of view. More details on the *HiRes* prototype setup can be found in [60].

The *HiRes/MIA* hybrid experiment measured air showers that were seen by the *HiRes-1* prototype detector and the *MIA* muon counters simultaneously. *MIA* consisted of 16 patches of 64 scintillation counters each, which were buried about 3 m underground. It had an active area of over 2,500 m². When the *HiRes* prototype detector was triggered by an EAS, it sent a xenon light flash to *MIA*. An event triggering *MIA* was only selected if the light flash was received by *MIA* within 50 μ s or if the charged particles of the EAS triggered the *CASA* surface scintillation detectors simultaneously and in coincidence with the *HiRes* trigger within ± 3 ms, according to the GPS clocks of each site. The timing information from the muon arrival times measured by *MIA* was used to constrain the geometry of the air shower, whose profile was recorded with the *HiRes-1* prototype detector. This led to a significant improvement in the shower geometry determination. The air fluorescence measurement of the longitudinal profile along the well defined shower axis was then used to determine the energy of the event. The *HiRes/MIA* experiment was taking data from 1993 until 1996. 4,034 hybrid events were recorded during this time period. The measurement of the energy spectrum and composition of UHECR between 10¹⁷ eV and 10^{18.3} eV have been included in Figures 1.3 and 1.13, respectively. A more detailed description can be found in [4] and [61].

The *HiRes* prototype detector was shut down in November 1996, when its mirrors and electronics were reorganized to merge into the final *HiRes* configuration.

2.2 The High Resolution Fly’s Eye Experiment

The *HiRes-1* detector is located on “Five Mile Hill” ($112^{\circ}50'9''$ W longitude, $40^{\circ}11'43''$ N latitude), 1,597 m above mean sea level, which corresponds to a mean atmospheric depth of 860 g/cm^2 . The *HiRes-1* site started operation in June of 1997. It consists of 21 mirror units housed in prefabricated garages as shown in Figure 2.3. The *HiRes-1* mirrors are arranged in a circle and view a band of the night sky covering 3° to 17° in elevation and almost 360° in azimuth.



Figure 2.3: Detector housings of the *HiRes* experiment. Two detector units (mirror and PMT cluster) can fit in one building.

HiRes-2 sits on top of “Camel’s Back Ridge” ($112^{\circ}57'32''$ W longitude, $40^{\circ}7'55''$ N latitude), at an altitude of 1,553 m above mean sea level. The *HiRes-2* site is located 12.6 km south-west of *HiRes-1*. It started full operation two years after *HiRes-1*, in fall of 1999. *HiRes-2* has 42 mirror units, which are arranged in two rings to cover elevation angles from 3° to 31° . Figure 2.4 shows the configuration of the *HiRes-2* mirrors.

The detector units at both sites are very similar. The spherical mirrors, with an area

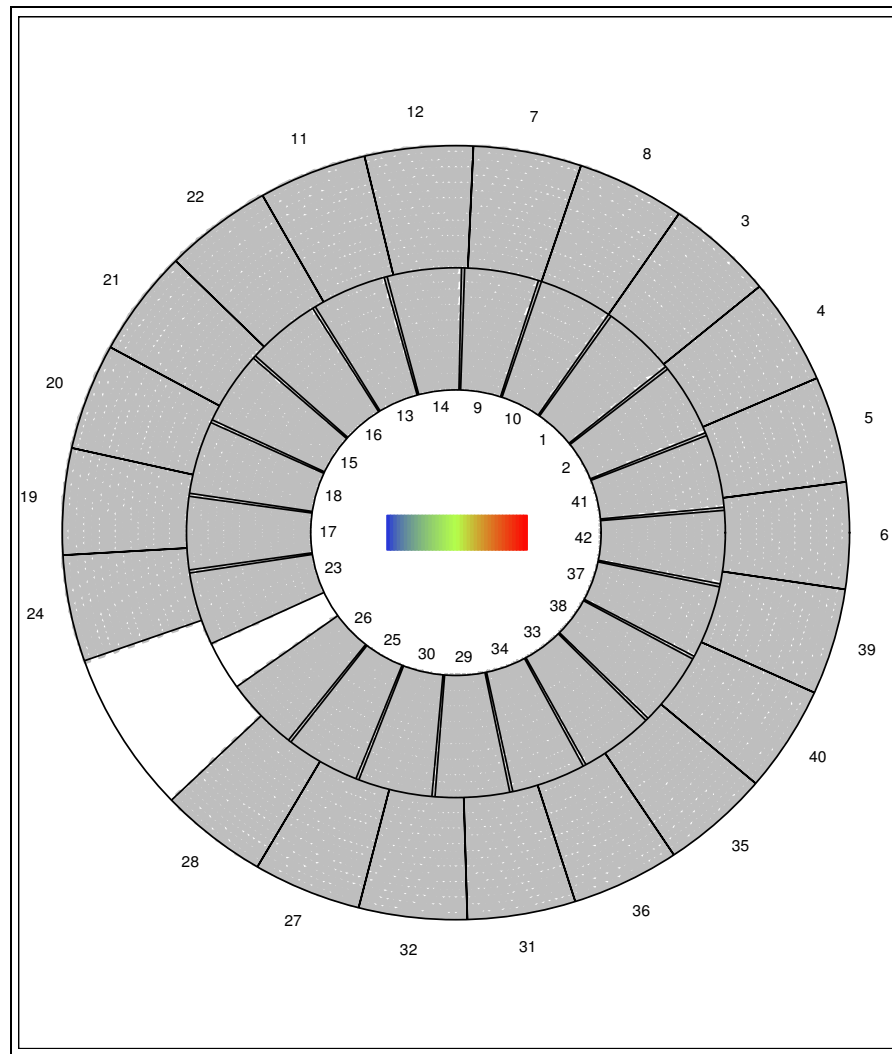


Figure 2.4: This *HiRes-2* event display shows the mirror configuration [62]. The outer ring covers 3° to 17° in elevation, the inner ring 17° to 31° . The gap in the south-western quadrant is a real gap in azimuthal coverage. *HiRes-1* has only an outer ring of mirrors. The gap in the *HiRes-1* configuration is smaller (due to an additional mirror) and in the south-eastern quadrant.

of 5.1 m^2 , collect fluorescence light from the air shower and project it onto a cluster of PMTs, which is mounted in the focal plane (see Figures 2.6 and 2.7). Each cluster consists of 256 hexagonally shaped phototube pixels, which are densely packed in 16 rows and 16 columns. The PMTs cover each a 1° cone of the sky. The smaller pixel size and larger mirror area compared to the *Fly's Eye* detector result in a sevenfold increase

in the signal-to-noise ratio. A UV bandpass filter (300 nm to 400 nm) is placed in front of the PMT to further improve the signal-to-noise ratio. The filter transmission and PMT quantum efficiency are shown as functions of wavelength in Figure 2.5. The original mirror reflectivity was measured to be 85% at 355 nm. This is somewhat reduced by dust settling on the mirror surface. A value of 81%, which represents the actual reflectivity in the field over the recorded wavelength range, has been assumed for this analysis. The long term variability of the mirror reflectivity due to dust is currently under study.

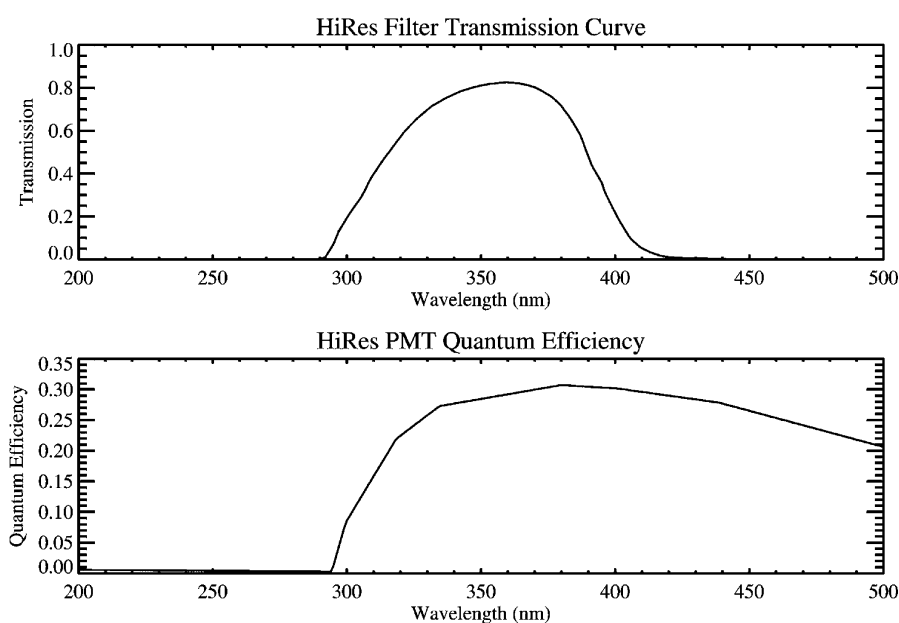


Figure 2.5: The wavelength dependence of transmission through the UV filters used in the *HiRes* experiment (upper panel) and of the PMT quantum efficiency (lower panel).

The mirror electronics, including the data acquisition system, a programmable pulse generator, as well as a power supply for the PMT pre-amplifiers and a PMT high-voltage supply, are housed in a VME crate within the mirror building. The mirror CPUs are connected with a central computer over an ethernet line at *HiRes-1* and over optical fiber links at *HiRes-2*, for data exchange. They are also linked to a central GPS (Global Positioning System) clock, which synchronizes the units to absolute UTC. The

uncertainty in the relative timing between the two *HiRes* sites is of the order of 50 ns.

The main difference between the two detectors, apart from the number of mirrors, lies in the data acquisition system. The *HiRes-1* detector uses a sample-and-hold system to measure the total integrated pulse within a time-window of $5.6 \mu\text{s}$, which is long enough to contain signals from all reconstructible cosmic ray events. The pulse of the signal is recorded together with the PMT triggering time. *HiRes-2* is equipped with a Flash ADC (FADC) system, operating at 10 MHz. The digitized pulse and timing information are recorded in 100 time slices of 100 ns duration for each triggered PMT. A description of the *HiRes-1* electronics can be found in [60]. *HiRes-2* will be described in more detail in the following chapter.

The detectors are operated on clear, moonless nights, which yields a duty cycle of about 10%. The garage doors are kept closed, except for the duration of the actual data taking process, to protect the detector units from bad weather, daylight and rodents. Nightly checks and calibration of the system are performed before and after data taking. During the night shifts, the operators at each site control the data acquisition process, do maintenance work (e.g. replacing defective PMTs, fixing problems of the electronics and door controls) and record weather changes.

After the events of September 11 in 2001, the U.S. Army closed Dugway Proving Ground for most civilians, including the members of the *HiRes* collaboration. In order to continue the data taking process, scientists from Los Alamos National Laboratory were hired by the *HiRes* group to operate the *HiRes-2* detector and do maintenance work at the *HiRes-1* site, beginning in spring 2002. The *HiRes-1* detector was operated remotely from the University of Utah with a virtual network connection (VNC) over the Internet. A backup modem connection to “Five Mile Hill” could be used to control the detector over a phone line, in the case of network problems. I have installed a similar remote system at Rutgers University (New Jersey, USA) in spring of 2003, with the help of an undergraduate student, Liam macLynne. This allowed *HiRes*

collaborators from Rutgers and Columbia University to resume data taking. Beginning in fall of 2003, U.S. citizens from the *HiRes* collaboration were allowed access to Dugway again. Since then, detector maintenance and *HiRes-2* operation are mainly the responsibility of the U.S. citizens of the *HiRes* group, whereas *HiRes-1* is operated remotely from the University of Utah, Rutgers University and very recently from Columbia University by the other members of the Collaboration.

The *HiRes* collaboration consists today of members from eight different institutions: University of Adelaide (Australia), Columbia University (USA), Los Alamos National Laboratory (USA), University of Montana (USA), University of New Mexico (USA), Rutgers University (USA), University of Tokyo (Japan) and University of Utah (USA). The *HiRes* detectors have, at the time of writing, the largest aperture of all cosmic ray experiments. It is planned that data taking will continue for at least three more years.

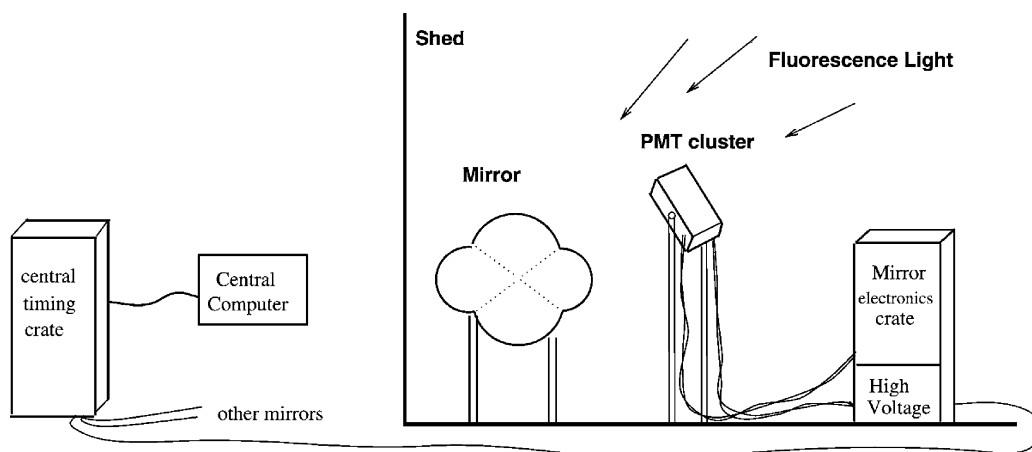


Figure 2.6: Scheme of a single detector unit used in the *HiRes* experiment. [60]



Figure 2.7: *HiRes* mirror unit. The UV filter has been removed, so that the hexagonal pattern of the phototubes can be seen as a reflection in the mirror.

2.3 Detector Calibration

The conversion of the recorded signals into useful information on the observed EAS requires a very good understanding of the different detector components. The calibration of the electronics and the PMTs plays therefore a crucial role in the data taking process.

At the start and end of each night, the electronics response of the pre-amplifiers of each PMT is measured with a square pulse from a **programmable pulse generator (PPG)**, which is located in each mirror crate. The pulse is compared to the signals from charge digital converters (QDCs) at *HiRes-1* and FADCs at *HiRes-2*. Electronics response of the time digital converters (TDCs) at *HiRes-1* is measured as well.

The TDCs are calibrated using snapshots, during which the PMTs of all mirror

units are made to trigger repeatedly for one minute. The snapshots start the TDCs and the hold-off counter. The counter stops TDC integration when it reaches a specified value. Hold-off times used range from 500 ns to 18,000 ns in 500 ns steps. A fit to the TDC values is used to relate them to the physical times. A detailed description of the TDC calibration can be found in [63].

The response of the PMTs, i.e. quantum efficiency, gain as a function of voltage and the uniformity across the PMT face, were measured before installation at a testing facility at the University of Utah.

The absolute calibration of the PMTs is done several times a year at the detector sites using the so-called **Roving Xenon Flasher (RXF)**, a portable xenon flashlight that is mounted in the center of each mirror and illuminates uniformly the face of the phototube cluster. The response of the PMTs to the calibrated light source is used to measure the conversion factor of photons into QDC or FADC counts.

The number of photoelectrons generated by the light flux in the PMT is given by

$$pe = qe \cdot ce \cdot A \cdot \gamma \quad (2.1)$$

with qe the quantum efficiency of the PMT, A its area, ce the collection efficiency of the first dynode, and γ the photon flux in photons/area. The product of quantum efficiency and collection efficiency of the PMTs was determined from comparisons with NIST (National Institute of Standards and Technology) calibrated phototubes. The QDC or FADC signal caused by the photoelectrons (p.e.) is given by

$$\begin{aligned} \mu &= G \cdot pe \\ \sigma &= G \cdot \sqrt{\alpha \cdot pe} \end{aligned} \quad (2.2)$$

Here μ is the mean of the recorded signal, σ its width, and G the gain of PMT and pre-amplifier. The α factor depends on gain variations in the first dynode of the PMTs. It was determined to be 1.50 for the PMTs at *HiRes-1* by measurements of the response of PMTs to a laser signal of known energy. At *HiRes-2* α was measured from a single

photoelectron peak for a sample PMT to be 1.29 and later corrected to be 1.35 for better consistency with *HiRes-1*.

The *HiRes-2* calibration, carried out by John Boyer and Eric Mannel, uses the RXF as a standard candle. The software-controlled gains of all the PMTs are adjusted individually to yield one FADC count per p.e. Unfortunately, the RXF calibration procedure at the *HiRes-2* site encountered problems during the period of data taking presented in this work, due to security related closures of Dugway Proving Ground. In this analysis, the absolute PMT calibration measured for *HiRes-1* is therefore used to determine the absolute energy scale of the experiment. A comparison of the *HiRes-1* and *HiRes-2* energy scales, which will be described in Chapter 5, yielded correction factors of up to 21% for the *HiRes-2* energies. These corrections were applied in the analysis presented here.

The *HiRes-1* calibration, carried out by John Matthews and Stan Thomas, uses a different method: The gain of the PMTs is determined from the response to the RXF as $G = \sigma^2/(\alpha\mu)$, which follows from Equations 2.2. The measured gain can then be used to convert QDC or FADC signals into p.e., with $pe = \mu/G$.

The RXF is being calibrated at the University of Utah against a hybrid photo-diode (HPD), before and after its use for the on-site calibration of the PMTs. The absolute efficiency of the HPD was determined with respect to a NIST calibrated silicon sensor, using a Mercury arc lamp with a grating monochromator as a light source. The HPD is used to calibrate the RXF with an accuracy close to 7%. We have started using the HPD to calibrate the photon flux of the RXF only recently. The calibration of the RXF with the HPD allows now a very accurate and stable direct comparison of the incident photon flux with the QDC or FADC signal of the detector. Before use of the HPD, the photon flux of the RXF was measured using NIST calibrated detectors. The absolute calibration of the *HiRes* detectors is described in more detail in [64].

A nightly relative calibration of the PMTs uses a **YAG laser**, which is located in the central trailer at each detector site and whose light is distributed to each PMT

cluster over optical fibers. Two bundles of fiber optic cables deliver the light to each mirror. One bundle ends in the center of the mirror, illuminating the phototube cluster directly. The end of the other bundle is attached to the cluster and illuminates the PMTs indirectly, after the light has been reflected back from the mirror. The light from the fiber bundles is diffused by teflon sheets for uniform illumination. Two sets of calibration data, each consisting of 50 laser pulses, are taken each night — one before and one after data taking. More details on this system can be found in [65].

Snapshots are taken frequently during the run to allow measurement of electronic and sky noise. Since no trigger requirements have to be met during snapshots, all the mirror units record background signals for a preset time interval. The mean value of the QDC or FADC readout during a snapshot yields the electronic pedestal for the channel, which does not change with the background light level due to the AC coupling of the PMT signal. The RMS variation provides a measurement of the electronic and sky noise. Snapshots are taken with closed doors and open doors, providing measurements of only electronic noise and electronic plus sky noise, respectively.

Calibrations of the mirror pointing directions have been performed by observations of the positions of stars. Two different methods were used: observation with a CCD camera [66] and with the *HiRes* detector itself [67].

2.4 Atmospheric Monitoring

Additionally to the detector calibration, a detailed understanding of the atmospheric conditions during the data taking process is very important for the *HiRes* experiment. The atmosphere is used as a calorimeter, in which the EAS deposits its energy, but it is also the medium through which the light signal propagates to the *HiRes* detectors. A close monitoring of the atmosphere is therefore necessary. Weather conditions and variations in the aerosol content of the atmosphere are both monitored with several systems.

The *HiRes* detectors do not take data on nights with precipitation or severe weather conditions (strong winds, high humidity, etc.). During the nightly shifts, the operators check the weather conditions frequently. A weather code, containing information on low lying clouds, overhead cloud coverage and haze, is entered into the nightly log once an hour. Clouds can reduce the aperture of the detectors or block out parts of an air shower from the detector's field of view, thus changing the structure of the received light profile. In order to obtain more specific information on cloud coverage, two **cloud monitoring systems** have been installed at the *HiRes-1* site [68]. Infra-red sensors are used to detect temperature differences between the clear night sky in the background and clouds, which are at thermal equilibrium with the air at a particular height and emit blackbody radiation. Eleven "horizon monitors", mounted in mirror buildings, view up to 30° in elevation and 330° in azimuth. Additionally, a "scanning cloud monitor" with a 3° field of view scans the entire sky once every 12 minutes. The "horizon monitors" were fully installed in August 1999, the "scanning cloud monitor" in March 2001. Weather stations, which provide information on humidity, wind speed and temperature, are located at both detector sites.

The predominant atmospheric attenuation processes in the wavelength range of interest for *HiRes* (300 to 400 nm) are molecular (Rayleigh) scattering and aerosol (Mie) scattering. Rayleigh scattering is very well understood and depends only on the density profile of the atmosphere. Variations with seasonal temperature changes are taken into account in our analysis. Mie scattering depends on the aerosol content of the atmosphere, which can change considerably over time. At Dugway Proving Ground, the aerosol content is observed to be relatively stable over the course of a night. Two different systems have been installed to monitor atmospheric changes caused by aerosol: xenon flashers and steerable lasers.

Ten radio-controlled **vertical flashers** [69] have been set up between the two detector sites, close to the line of sight that connects both sites. The flashers consist of xenon flash bulbs, mounted in cylinders at the focal points of spherical mirrors. The

different flashers fire in a pattern that is periodically repeated during the night. The signal from the flashers that is seen in each detector can then be used to estimate the horizontal extinction length at a certain time. An inclined flasher, called the “inter-site flasher” is located at the center of the old *CASA* array. Its signal can be seen in both detectors over a range of mirrors and was originally used to obtain a rough estimate of the scattering phase function.

A more modern system, which is in use since 1999, consists of two **steerable lasers**, located at the two detector sites. The circularly polarized YAG lasers fire a pattern of 1,000 to 1,300 shots per hour, synchronized by a GPS clock. The shots are 7 ns pulses at a wavelength of 355 nm. The maximum beam energy is 7 mJ, lower energies can be selected with an automated filter wheel. The lasers are firing at a set of different azimuth and elevation angles. Scattered light from the laser situated at one detector site is recorded by the detector at the opposite site. Vertical laser shots can be used to measure the vertical aerosol optical depth. Nearly horizontal shots, whose scattered light can be seen in several mirrors under different scattering angles, provide information on the aerosol phase function and horizontal extinction length. The analysis of laser shots is described in more detail in Chapter 4. A third, vertical laser has been installed in 2002 at a location closer to the boundary of the *HiRes* aperture (at Terra, Utah) to provide the possibility of an additional measurement with both detectors. Details on the atmospheric monitoring systems of the *HiRes* experiment can be found in [70], [71] and [72].

2.5 HiRes Measurements

2.5.1 Energy Spectrum

The *HiRes* Experiment was planned and built as a **stereoscopic** detector of EAS. The detection of EAS with both eyes yields improved resolution of the shower geometry, and thus an improvement in energy resolution. The shower track seen by each eye

defines the plane that contains the shower axis and the origin of the eye. In stereoscopic mode, the exact geometry of the shower axis within this shower-detector plane can be determined as the intersection of the two planes. (A more detailed description of the geometric reconstruction will be given in Chapter 5.) The main objective of the *HiRes* experiment is thus the measurement of the energy spectrum in stereo mode. The stereoscopic analysis is currently under way. A preliminary spectrum can be seen in Figure 2.8.

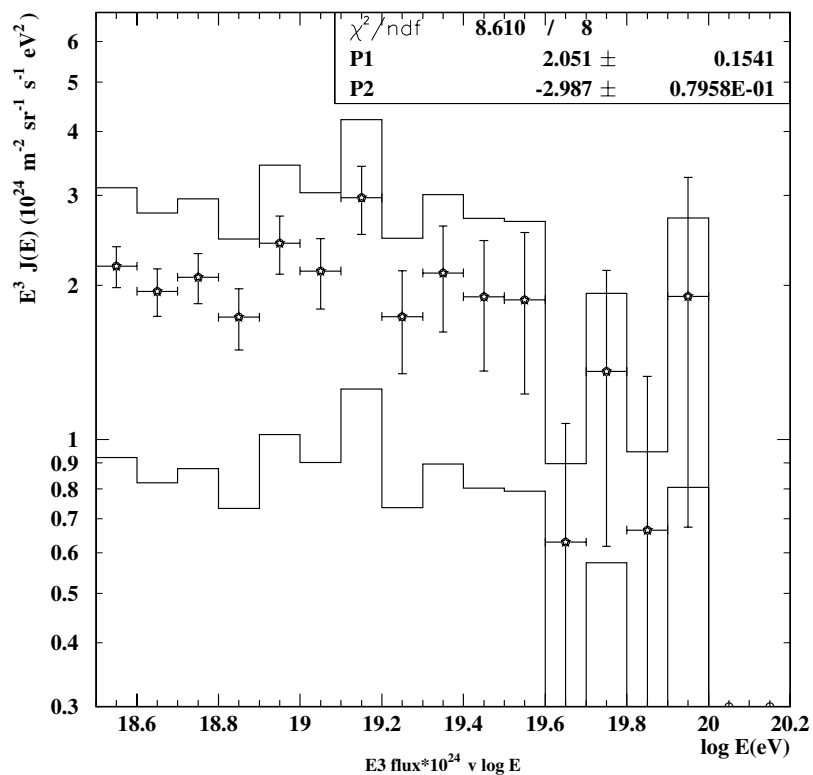


Figure 2.8: **Preliminary** UHECR energy spectrum measured by *HiRes* in stereoscopic mode. Error bars are statistical uncertainties; systematic uncertainties are indicated by the error band. A fit yields a spectral index of $-2.987 \pm 0.079(\text{stat.})$ for energies between $10^{18.5}$ eV and $10^{19.4}$ eV.

Despite the lower resolution, a spectrum measurement with *HiRes* in **monocular** mode, i.e. using either data from the *HiRes-1* or the *HiRes-2* detector, does have certain advantages. Since *HiRes-1* started operation two years before *HiRes-2*, the *HiRes-1*

event sample is larger than the stereo sample. Events with energies less than $10^{18.5}$ eV cannot be reconstructed reliably with the time resolution provided by this detector's sample-and-hold electronics, but at the high energy end of the spectrum, reconstruction of *HiRes-1* events is very good with an energy resolution of 17%. The uncertainty in the measured flux is $\pm 31\%$. Figure 2.9 shows the *HiRes-1* monocular spectrum: The GZK feature is clearly visible, at an energy around $10^{19.8}$ eV. This result has been published in [3] (see also [73]). Against the expectation of a continuation of the UHECR spectrum above the GZK threshold energy, as supported by the *AGASA* measurement, the UHECR energy spectrum measured by *HiRes* in monocular mode is consistent with the prediction of a flux suppression due to pion photo-production with the CMBR. In a comparison of data from *Fly's Eye*, *HiRes* and *Yakutsk*, John Bahcall and Eli Waxman found strong evidence for the detection of the GZK feature [74]. The discrepancy between the only two experiments that have a large enough aperture to measure the upper end of the UHECR spectrum (at the time of writing) has led to a considerable amount of controversy (see for example [75] [76]).

A monocular measurement using only data from the *HiRes-2* detector is being presented in this thesis. The *HiRes-2* event sample cannot provide the statistical power of the *HiRes-1* data at the high energy end. However, the *HiRes-2* monocular event sample has a different advantage over both *HiRes-1* mono and stereo data: It contains very well reconstructed events at energies lower than *HiRes-1* mono and stereo events. Due to the greater elevation coverage that leads to longer tracks and due to the much better time resolution, *HiRes-2* events can be reliably reconstructed down to energies of about 10^{17} eV. This is also about a decade lower in energy than the lower limit for stereo events. The lower energy limit of the latter is constrained by the separation between the two detectors: events with the lowest observable energy lie half-way between the two detectors and have thus a distance of about 6 km from each detector, which sets a lower limit to their observable energies. Additionally, events that are close to the line of sight connecting the two detectors are problematic to reconstruct, since the intersection

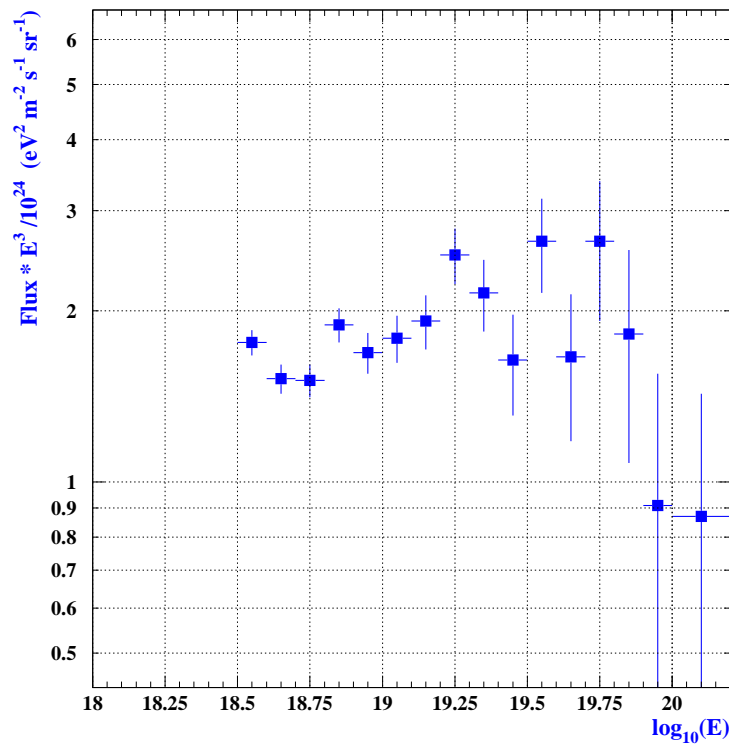


Figure 2.9: UHECR energy spectrum measured by the *HiRes-1* detector.

of the two shower-detector planes yields angles close to 180° . The *HiRes-2* measurement of the UHECR spectrum is intended to complement the *HiRes-1* measurement at lower energies, where the features of the “second knee” and the “ankle” provide a recognizable signature of the cosmic ray flux, which can be used to compare the *HiRes* measurements to previous experiments.

2.5.2 Composition

As mentioned before, air fluorescence detectors like *HiRes* are particularly suited for composition measurements, since they observe the maximum shower depth X_{max} directly.

Figure 2.10 shows two measurements of the UHECR composition: The *HiRes/MIA* hybrid detector determined the elongation rate of cosmic rays with energies between

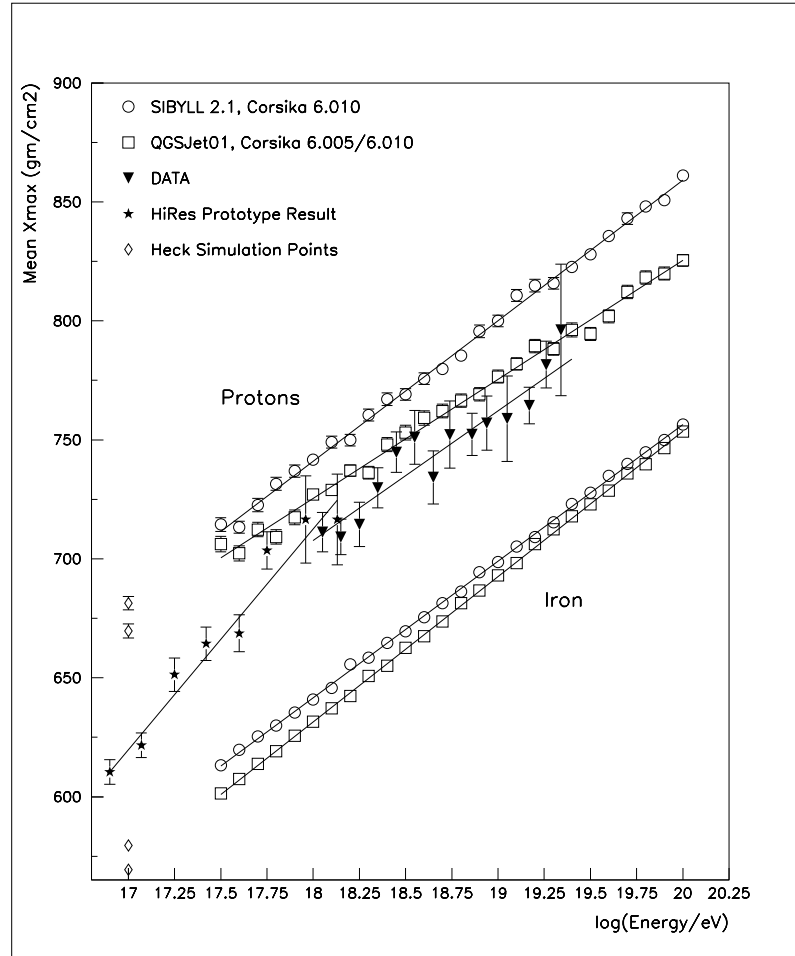


Figure 2.10: UHECR composition measured by *HiRes/MIA* and by *HiRes* in stereoscopic mode [77]. The stars are *HiRes/MIA* measurements, triangles are *HiRes* stereo measurements. Squares, circles and diamonds are Monte Carlo simulations of pure proton and pure iron showers for comparison. Simulations with two different hadronic interaction models, *QGSJet* and *SIBYLL*, are shown.

10^{17} eV and 3×10^{18} eV to be 93.0 g/cm^2 per decade in energy [4]. This is consistent with the shift from a heavy to a lighter component, which had been observed previously by *Fly's Eye* and *Yakutsk*. A recent analysis of *HiRes* data collected between November 1999 and September 2001 in stereoscopic mode shows a change in the elongation rate at higher energies [77]. The X_{max} distribution measured between 10^{18} eV and $10^{19.4}$ eV is consistent with an only slowly changing and predominantly light composition. The elongation rate at these energies was measured as 55.2 g/cm^2 per decade in energy.

A preliminary composition measurement using *HiRes-2* mono data [78] is consistent with a light composition of UHECR in the same energy range.

2.5.3 Anisotropy

Recently, several papers have been published with the first results of anisotropy measurements using *HiRes* mono and stereo data. A brief overview of the latest results is given here. More publications are in preparation.

Theoretical source models suggesting the galaxy M87, Centaurus A or the Galactic Center as sources of UHECR predict a potential **dipole enhancement** in the distribution of cosmic ray arrival directions, oriented towards those sources. The distribution of *HiRes-1* data above $10^{18.5}$ eV has been compared to simulated isotropic datasets, taking into account the non-uniform exposure of the *HiRes* experiment. The analysis of the dipole function of the dataset and an independent check using a fractal dimensionality analysis do not confirm the anisotropy towards the Galactic Center seen by *Fly's Eye*, *AGASA* and in the *SUGAR* re-analysis, reported in Chapter 1. The results from this analysis are consistent with an isotropic source model [79].

The existence of nearby, compact sources should be visible in **small-scale clustering** of arrival directions at the highest energies, where the Larmor radius is large enough to allow UHECR to point back to their sources. A search for small-scale anisotropies has been performed using *HiRes* stereo data [80]. The autocorrelation study of *HiRes* data found no significant evidence for clustering on any angular scale up to 5° and at any energy threshold above 10^{19} eV, when compared to detailed Monte Carlo simulations. This lack of clustering would be consistent with the assumption that UHECR sources are distributed at large distances from our galaxy. A similar autocorrelation study using *HiRes-1* data above $10^{19.5}$ eV is also consistent with the absence of clustering in UHECR arrival directions [81].

In a re-analysis of the *AGASA* dataset that led to the claim of clustering at the highest energies, it could be shown that the signal is weaker than has been claimed [82].

Simultaneous autocorrelation scans over threshold energies and threshold angles were performed on the *AGASA* data in comparison with simulated events and an independent set of data. From these scans, a statistical penalty factor could be calculated for the *a posteriori* choice of an optimal threshold energy and angle, which would maximize the clustering signal, in the *AGASA* analysis. The new analysis finds that the *AGASA* data are consistent at the 8% level with the assumption of isotropically distributed arrival directions.

Chapter 3

The HiRes FADC Detector

3.1 Layout

The 21 buildings that house the 42 mirror units of the *HiRes-2* detector in pairs are arranged in a circle around a central facility, as can be seen from the photograph in Figure 3.1.



Figure 3.1: Overview of the *HiRes-2* site on Camel's Back Ridge. The 21 mirror buildings are arranged in a circle around a central facility.

The central computer, a PC running Linux, is located in a trailer, in which an office has been set up for the nightly on-site data taking. Optical fibers connect all the crates in the mirror buildings directly to the central facility and allow the central clock signal

to be distributed to each crate at a frequency of 10 MHz. Additionally, two independent optical fiber rings run around the circumference of the circle of mirror buildings and are connected to the central facility. These rings provide trigger and data communications between the mirror crates and the central computer.

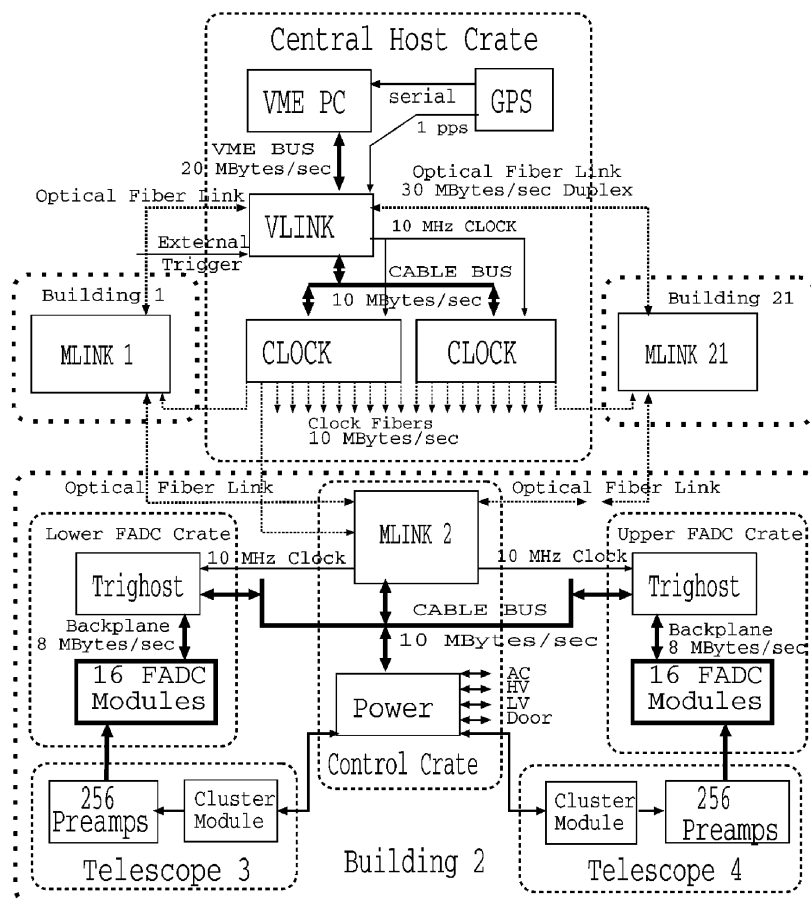


Figure 3.2: Diagram of the *HiRes-2* communications system [83].

The diagram in Figure 3.2 shows the details of the communications system between the central facility (central host crate) and the mirror buildings. The GPS connected to the central PC sets the time for the 10 MHz clock signal, which is sent out to each mirror building over optical fibers of equal length. The two telescopes, i.e. two mirrors with PMT clusters, in each mirror building are connected to a single electronics rack, which holds the control crate and two FADC crates.

The **control crate** has a module (MLink) for communications links with the central host crate and the FADC crates. A power module in the same crate controls all the power supplies, the PPG, heaters in the cluster box, heat exchangers in the crate, and the doors. It also monitors temperatures, voltages, light levels and the door status.

The **FADC crates** contain 16 FADC cards and a module that processes triggers and provides communication with the control crate. The signals from the PMTs are superimposed on the ~ 1 kV high voltage of the anode (the cathode is at ground potential) and are AC coupled to the pre-amplifier with a $500 \mu\text{s}$ time constant. Shielded twisted-pair cables are used for transmission of the signals to the FADC crates. All PMTs in a cluster are gain balanced by use of a digital to analog converter amplifier (DAC). Each FADC card digitizes the signals from 16 PMTs of the same vertical column. Signals are digitized every 100 ns and stored in a ring buffer as 8 bit numbers. The gain of the 16×16 high-gain (HG) channels is set to 1 photoelectron per FADC count. Additionally, each FADC card also processes two analog sums (one column and one row of the PMT cluster). These sums are digitized with a low gain (8 photoelectrons per FADC count) to provide an extension of the dynamical range by adding 2×16 low-gain (LG) channels. The sums are also digitized with a longer filter time (nearly tenfold) to provide the 2×16 trigger channels that are compared against a threshold to form a first level trigger.

The PMT **cluster box** holds the 16×16 photo-multiplier tubes and the filter glass. It also contains the PPG and the electronics to monitor voltage and light level and to control the temperature with a heating strip.

3.2 Signal Processing and Trigger

When the shower front of an EAS crosses the night sky at nearly the speed of light, the image of the shower sweeps across one or more PMT clusters. Figure 3.3 is a snapshot of the *HiRes-2* event display. An event can be seen towards north-east, i.e. in the

direction of *HiRes-1*, in mirror 8 and 10. Each pixel in the display represents one PMT. The different colors correspond to different pulse heights in the recorded signals. In this case, the initial part of the shower trajectory (in mirror 10) is partially obscured by clouds, so that the shower becomes clearly visible only on its way down (in mirror 8). This event, recorded on the 18th of February of 2001, was reconstructed with an energy of more than 10^{20} eV at a distance of 27 km from the *HiRes-2* detector. However, the weather during that night was dominated by clouds and a rapidly changing atmosphere, so its reconstruction cannot be trusted and it has not been included in this analysis.

The pixels that are not part of the shower track are PMTs with noise above the readout threshold. The average ambient sky noise (mostly scattered light from man-made sources) was about 6 photoelectrons per FADC time bin for the data presented in this thesis. This results in an RMS deviation from the mean of about 2.4 FADC counts. The electronic noise at *HiRes-2* is much smaller, about 0.1 FADC counts (RMS). Main sources for electronic noise at *HiRes-2* are the gain amplifiers and high voltage. A more detailed discussion of sky noise analysis will follow in Chapter 4.

In order to pick air shower signals out of the background noise during the data taking process, an efficient trigger system is needed to control the readout. Signals from all 320 channels (HG, LG and trigger channels) are continuously stored in a ring buffer and delayed by 820 μ s. A first level trigger uses programmable logic devices (PLDs) to detect coincidences in space and time in the trigger channels. Instead of scanning all 256 HG channels for patterns, the primary trigger scans only the horizontal and vertical projections of the shower track in the 32 trigger sums. The signals from the trigger channels are compared to a threshold that is set to 12 counts above pedestal (which is at 20 counts). The pulse widths above threshold are doubled by incrementing a 7-bit counter when the signal is above threshold and decrementing otherwise but not allowing the counter to become negative. A twofold coincidence is found by requiring a counter and its immediately higher neighbor to be non-zero. The process is then repeated with another level of 7-bit counters, in order to find threefold space-time

coincidences. Roughly speaking, a threefold coincidence corresponds to three neighbor or next-to-neighbor row or column trigger channels above threshold, which are found within a certain time window. If two or more threefold coincidences are found, followed by $5 \mu\text{s}$ without coincidences or $102.4 \mu\text{s}$ elapsed trigger time, a **primary trigger** is formed. A digital signal processor (DSP) reads out the times of the first and last coincidences and the coincidence pattern. This information is stored locally and transmitted to neighboring mirrors. The trigger DSP also determines a time window. The information from all 320 channels from within this time window (a snapshot of $\sim 50 \mu\text{s}$) is sent to an event buffer in the Trighost module, which can store up to 3.2 ms. The combination of a ring buffer, fast primary trigger and large event buffer allows deadtimeless signal processing at *HiRes-2*.

The temporal development of the signal from an air shower in different HG and trigger channels can be seen in Figure 3.4. The event is the same as in Figure 3.3. Only the two mirrors that see the shower track are shown here (c). The waveforms of 5 HG channels that lie on the shower track in the upper mirror (mirror 10) and of 15 HG channels on the track in the lower mirror (mirror 8) are shown in (b). The duration of the event is $35 \mu\text{s}$. The HG pulses of this event are unusually large; the peaks are very well pronounced. 11 of the row sum trigger channels of mirror 8 are shown in (a). Dark bands under the waveforms in (a) indicate time above threshold. Mirror 8 easily fulfills the primary trigger criterion, whereas the signal in mirror 10 is too weak to trigger. HG channels of this mirror are only read out due to the adjacent mirror trigger, which will be discussed below.

16-bit DSPs scan all the HG channels that have been transferred to the event buffer in a single storage window. The signals are compared to a fixed threshold in this **confirming scan**. A pattern recognition algorithm, programmed in a PLD, is applied to those HG channels that are above threshold in order to search for signal clustering in space and time. If the pattern recognition confirms the primary trigger, a **secondary trigger** is formed. All channels in the storage window are then scanned a second time

and compared against a lower threshold in the **readout scan**. Only channels above readout scan thresholds are kept for later analysis. A pre-scaled subset of unconfirmed triggers is scanned and read out as well, to allow an analysis of the trigger efficiency.

The Mlink modules in each mirror building can broadcast triggers site-wide over optical fibers. If a secondary trigger is formed in a mirror unit, it can thus send a signal to all neighboring mirrors to cause a readout scan to be performed even without a primary or secondary trigger in these mirrors. This **adjacent mirror trigger** was activated when the event shown in 3.3 and 3.4 was recorded and led to the readout of all five adjacent mirrors, allowing the recording of the light weak part of the shower in mirror 10.

For stereo observation, an **inter-site trigger** has been installed at the *HiRes-1* site. Triggers in the *HiRes-1* detector can be broadcast over microwave to the *HiRes-2* site and force readout of events in the same time window.

A more detailed description of the *HiRes-2* electronics and data acquisition system is provided in [83] and [84].

3.3 Data Processing

The data generated during the nightly data taking process are in raw network format. All night's data are transferred over the network to the University of Utah and to Nevis Laboratories each morning. Several data streams are generated at *HiRes 2*: cosmic ray data, pedestal files, electronics diagnostics, YAG calibration data from the mirror and cluster fibers, and RXF calibration data between runs.

The first step in the processing of *HiRes-2* data is done at Nevis Laboratories: In “pass0”, the raw data are converted into a DST (“data storage tape”) file format (file extension “fpkt1.dst”). In the DST files, pre-defined variables in a set of data banks are filled with the information of each single event. In a second step, “pass1” decodes the raw data packets and fills the information into several banks (*fraw1*, *ftrg1*, etc.). It also

writes snapshots into separate files and corrects event times.

The standard repository for all software in use by the *HiRes* collaboration is called “dst2k” and resides in copies on the computer system of each collaborating institution.

Data analysis at Rutgers begins with the “pass1” files, which we copy from Nevis Laboratories over the network. The data files are processed with two programs that group mirror readouts of the same event together (“fma”) and remove inter-site triggers from the data (“m62filt”), since they are not part of the monocular data sets. All initial information we use is stored in two different DST databanks, the *fraw1* and *frg1* banks. The main information that is stored in these banks is displayed in Tables 3.1 and 3.2.

header:
event number
event code (different for data, snapshots, etc.)
number of the data part
Julian date and time of the start of the data part
number of mirrors that were read out
for each mirror read out:
mirror storage start time
mirror index
number of read out channels
for each channel read out:
channel index
start time of channel readout
number of recorded digitizations (100 for data)
for each digitization:
raw 8-bit FADC data

Table 3.1: Main entries in the *fraw1* bank.

More banks are added to the original DST files during the event reconstruction process: The *rufpln* and *spgf* banks with information on reconstructed geometry and profile of the shower will be discussed in Chapter 5. The output from Monte Carlo simulations is stored in the same banks as the data, i.e. *fraw1* and *frg1*. An additional bank (*fmc1*), is added to store information on the Monte Carlo input parameters.

header:
number of mirrors with trigger info (matches the number in fraw1)
for each mirror read out:
mirror index start time of the primary trigger window end time of the primary trigger window trigger code (information on the number of threefold coincidences) pattern of coincidences in the trigger row channels pattern of coincidences in the trigger column channels number of hits in the readout scan
for each hit in the readout scan:
channel index start time of channel readout mean time of pulse since start time width of pulse integral counts above pedestal

Table 3.2: Main entries in the *ftrg1* bank.

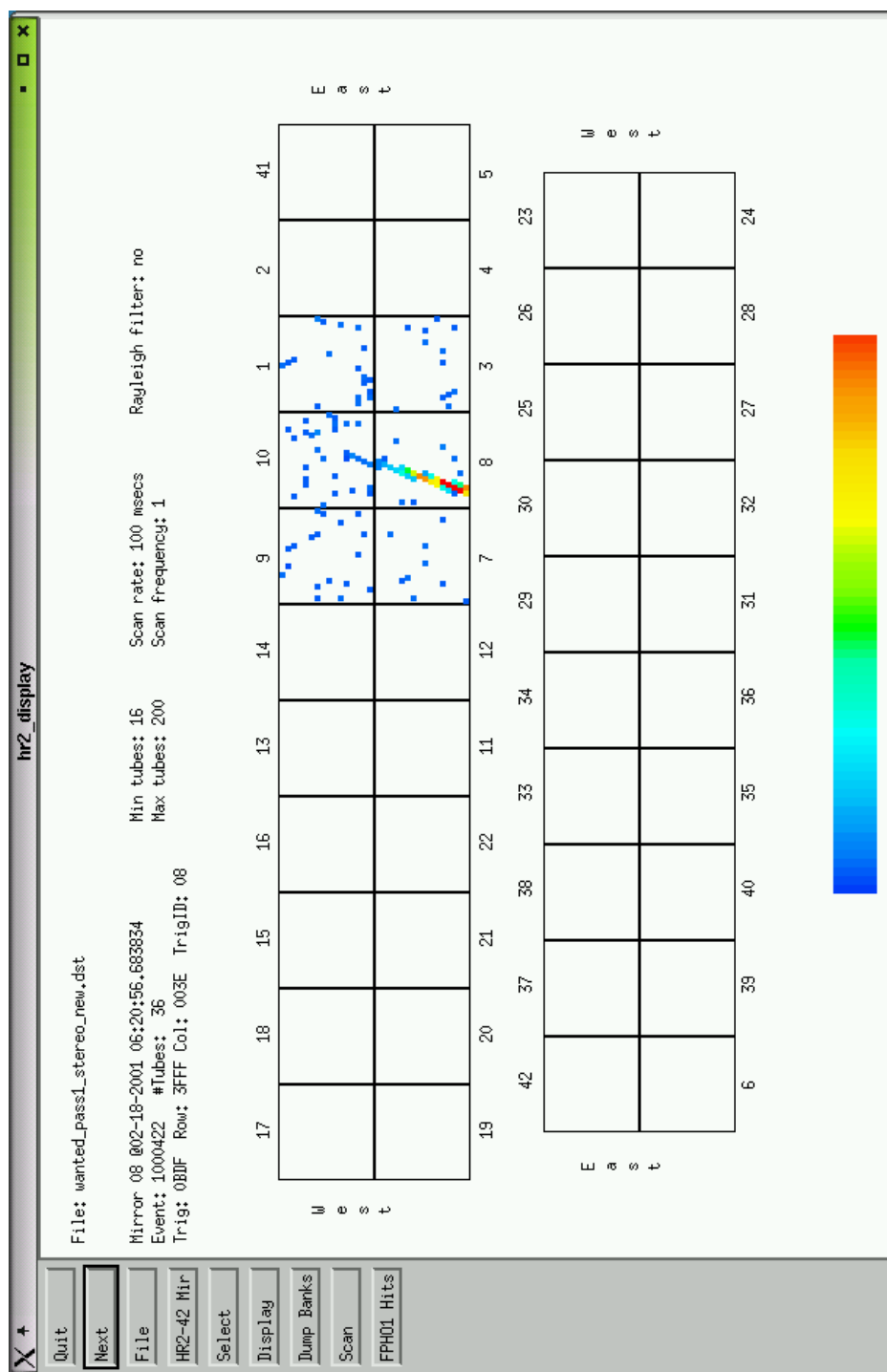


Figure 3.3: Air shower seen in the *HiRes-2* event display. (This figure was provided by Eric Mannel.)

Event @ 02-18-2001 06:20:56.683332

Mirror#	Event#	#Tubes	Row	Column
10	217	30	0000	0000
8	218	36	3FFF	003E

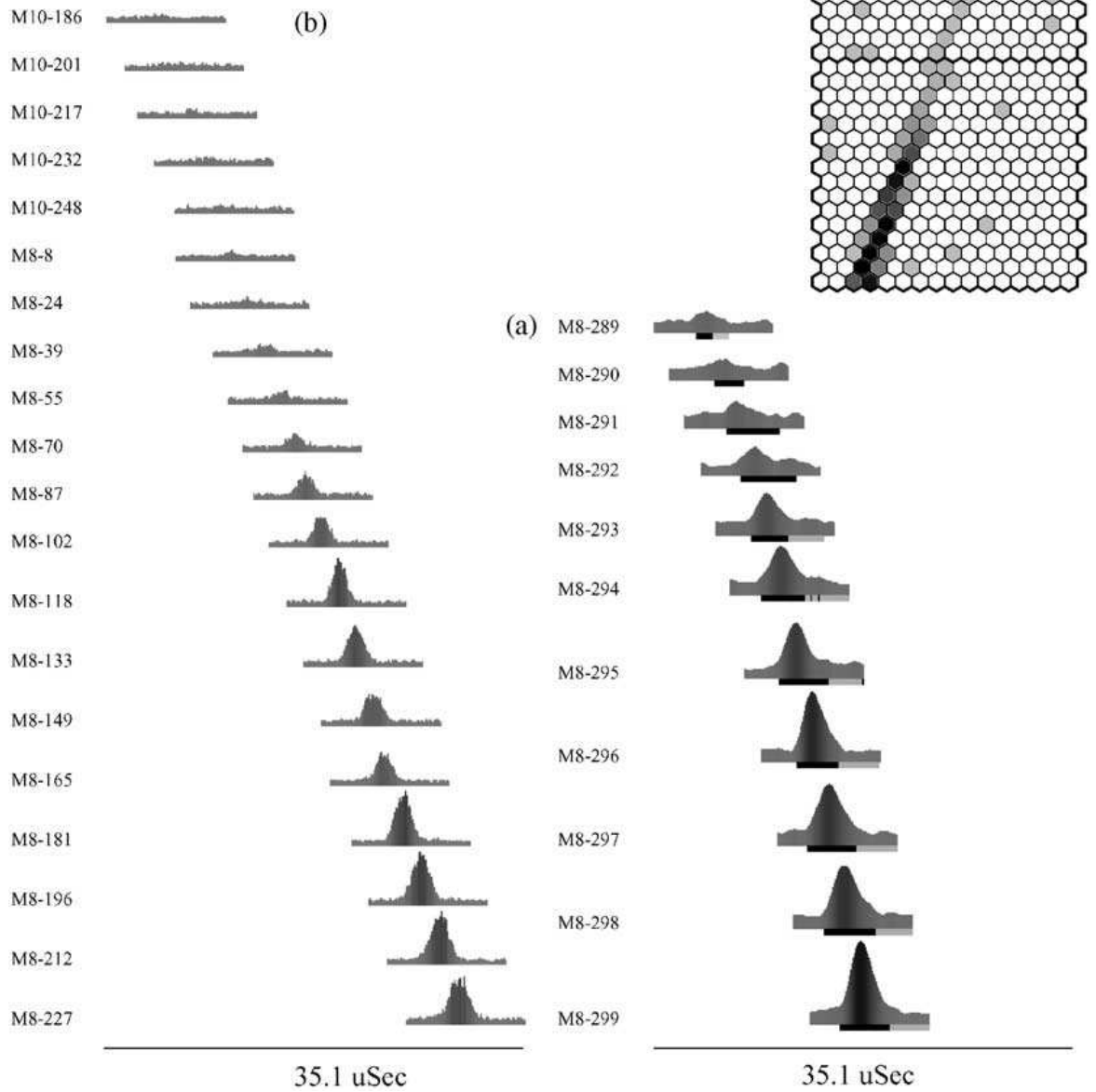


Figure 3.4: High-gain and trigger channel response to a high energy air shower [83]. Explanations in the text.

Chapter 4

Monte Carlo Simulation of the HiRes FADC Detector

4.1 Unfolding the Cosmic Ray Spectrum

The calculation of the cosmic ray energy spectrum from the measured energy distribution of events is a problem of unfolding the true spectrum of cosmic rays at their arrival in the earth's atmosphere from the distortions of the detector. The energy distribution provided by the detector is a convolution of the true spectrum with the detector response, i.e. the acceptance (or efficiency) of the detector and its limited resolution. Following Cowan [85], the problem of unfolding can be stated in the following way:

$$\nu_i = \sum_{j=1}^M R_{ij} \mu_j \quad (4.1)$$

Here, the true energy spectrum and the measured spectrum are divided into M energy bins. μ_j is the number of events in bin j of the true histogram, ν_i is the expectation value of the number of events in bin i of the measured histogram. R_{ij} is the response matrix, which describes the detector response in each energy bin. The off-diagonal elements in R_{ij} are due to the limited resolution of the detector, which distributes a fraction of events from a certain energy bin over adjacent bins.

The most straightforward way of determining the real event distribution μ_j from the measured values seems to be to calculate the response matrix and then apply its inversion on the measured distribution. Determining the response matrix requires knowledge of the resolution and detector acceptance, and a good estimate of the true spectrum. However, as Cowan shows, even with a complete knowledge of R_{ij} , this method

is in most cases not applicable, since it leads to huge variances in the unfolded histogram, if the resolution is not small enough compared to the bin width. These variances arise due to the Poisson distribution of the observed data around the expectation values ν_i .

In practice, the “method of correction factors” can be applied for deconvolution of the measured spectrum. This is the method used in this analysis. The estimator $\hat{\mu}_i$ for the true spectrum is written as:

$$\hat{\mu}_i = C_i \cdot n_i \quad (4.2)$$

where n_i are the observed data and C_i are multiplicative correction factors for each energy bin. These correction factors can be determined with Monte Carlo (MC) simulations of both the physical model under study and the complete measurement process. The correction factor is given by the ratio of generated over accepted events in the MC in each energy bin:

$$C_i = \frac{\mu_i^{MC}}{\nu_i^{MC}} \quad (4.3)$$

The simulation programs must describe the experiment in a realistic way in order to provide good estimates of the acceptance and resolution, which contribute to the correction factor.

Calculation of the expectation value for the estimator $\hat{\mu}_i$ provides an expression for the bias of the method of correction factors.

$$\begin{aligned} E[\hat{\mu}_i] &= C_i \cdot E[n_i] = C_i \cdot \nu_i = \frac{\mu_i^{MC}}{\nu_i^{MC}} \cdot \nu_i \\ &= \mu_i + \left(\frac{\mu_i^{MC}}{\nu_i^{MC}} - \frac{\mu_i}{\nu_i} \right) \nu_i \end{aligned} \quad (4.4)$$

The bias in the estimator $E[\hat{\mu}_i]$ is thus given by the expression in brackets times ν_i . The bias goes to zero as the simulated acceptance $\frac{\nu_i^{MC}}{\mu_i^{MC}}$ approaches the real acceptance of the experiment $\frac{\nu_i}{\mu_i}$. (The quantities referred to as ‘acceptances’ from here on have the detector resolution or its simulated resolution already folded in.) The more realistic the assumptions are that go into the MC simulation, the smaller the bias will be. One can estimate the bias by varying the model assumption used in the simulation.

I have calculated an estimate of the bias by varying the assumed true energy spectrum that is used as an input to the MC. It is useful to rewrite the equation for the bias in the following way:

$$b_i = \left(\frac{\mu_i^{MC}}{\nu_i^{MC}} - \frac{\mu_i}{\nu_i} \right) \nu_i = \left(\frac{\nu_i}{\mu_i} \left/ \frac{\nu_i^{MC}}{\mu_i^{MC}} - 1 \right. \right) \mu_i = (R - 1)\mu_i \quad (4.5)$$

The bias as a fraction of the real values μ_i is thus given by the ratio R of the true over the simulated acceptance, minus one. For my bias estimate, I assumed the true acceptance $\frac{\nu_i}{\mu_i}$ to be the result of a simulation using our best estimate of the input energy spectrum. The simulated acceptance $\frac{\nu_i^{MC}}{\mu_i^{MC}}$ was calculated using a simple E^{-3} power law for the input energy spectrum.

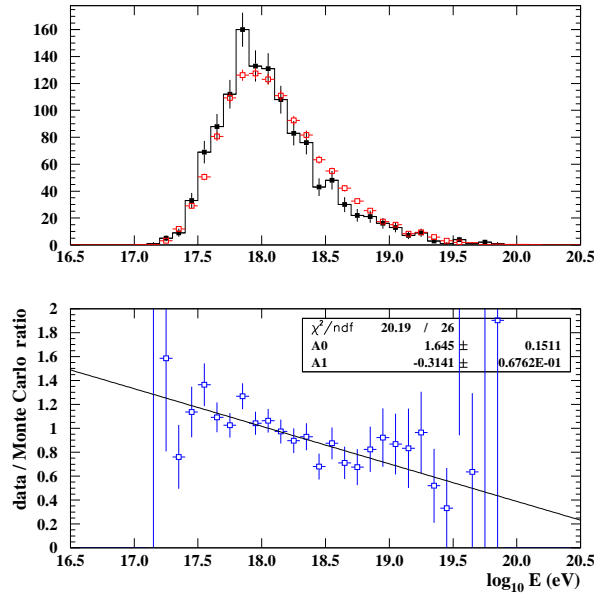


Figure 4.1: top: Distribution of events vs. $\log(\text{energy})$. Data (dataset 2, about one third of the data in this analysis) in filled squares, MC (assuming an E^{-3} input spectrum) in open squares.

Here, and in all following data-MC comparison plots, the distributions have been normalized to cover the same area. The y-scale is set by the data histogram.

bottom: Ratio of data over MC events with linear fit. Errors quoted are 1σ .

Figure 4.1 shows the measured distributions of events over energy bins for data (upper panel, filled squares) and for a MC simulation assuming an E^{-3} input spectrum

(open squares). The expectation values of these distributions correspond to ν_i and ν_i^{MC} , respectively. The input spectrum corresponds to μ_i^{MC} . As can be seen from this plot, and from a ratio plot of the two distributions (lower panel, data divided by MC), this choice of the input spectrum was not very good. The ratio is tilted because the assumed input spectrum does not have a break (“second knee”) and thus the fraction of events at the high energy end is too large.

The χ^2 values in the ratio plots of this and the following data-MC comparisons are not very meaningful since bins with small event numbers have been included in the fits. However, differences in data and MC become clearly visible in the linear fits.

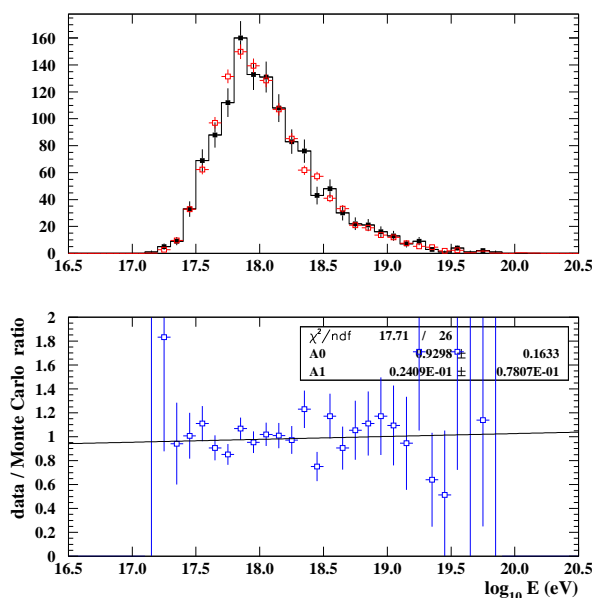


Figure 4.2: top: Distribution of events vs. $\log(\text{energy})$. Data (dataset 2) in filled squares, MC (assuming an input spectrum with a shape similar to the *Fly’s Eye* stereo spectrum) in open squares.

bottom: Ratio of data over MC events with linear fit.

This bias has been corrected in Figure 4.2: Instead of the E^{-3} spectrum, I now use a fit to the *Fly’s Eye* stereo spectrum to determine the shape of the input spectrum. Up to the “ankle”, the two fits shown in Figure 1.7 (dashed lines) have been adopted. Above the ankle, a linear fit to the *HiRes-1* spectrum (Figure 2.9) is used. The *HiRes-1*

spectrum above the “ankle” has a smaller slope (in the JE^3 plot) than the *Fly’s Eye* spectrum ($E^{-2.8}$ rather than $E^{-2.7}$). The GZK flux suppression has not been included when determining the input spectrum. The linear fit above the “ankle” is extended to the highest energies. The good agreement between data and MC proves that this choice of an input spectrum is much closer to the true spectrum μ_i , assuming the MC simulates all other aspects of the experiment correctly, which I will show in Chapter 7. This MC set is used to estimate the “real acceptance” $\frac{\nu_i}{\mu_i}$.

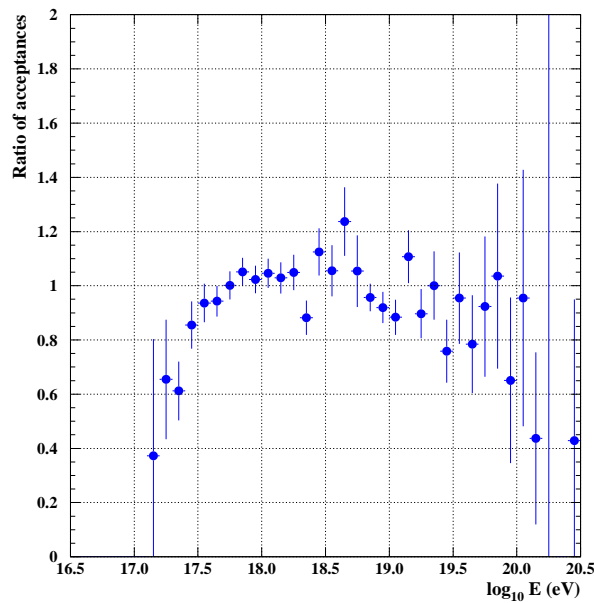


Figure 4.3: Ratio of two simulated acceptances: An input spectrum following the *Fly’s Eye* measurement was used for the acceptance in the numerator. An E^{-3} input spectrum was used for the acceptance in the denominator.

The bias I am avoiding by choosing a realistic estimate for the input spectrum can be seen in Figure 4.3. Shown is the ratio R of acceptances for the two MC simulations. Using a wrong (E^{-3}) input spectrum would cause a bias in the final energy spectrum of the order of $\pm 20\%$.

The flat ratio of the data and MC distributions in Figure 4.2 means that $\frac{\nu_i}{\nu_i^{MC}}$ is

approximately a constant if one chooses a realistic input spectrum. In this case, according to Equation 4.4, the energy dependence of the expectation value for the true spectrum $E[\hat{\mu}_i]$ is approximately given by the input spectrum μ_i^{MC} . Any differences in the unfolded spectrum can be fed back into the MC and will improve the agreement between the energy distributions in data and MC, thus reducing the bias in the spectrum calculation with the updated MC.

4.2 Outline of the HiRes-2 Simulation Programs

The purpose of the MC in the *HiRes* experiment becomes evident from the above outline of the unfolding process: the MC simulation is needed for an accurate description of the detector acceptance and resolution. A scheme of the *HiRes-2* MC simulation programs can be seen in Figure 4.4.

The simulation consists basically of two parts: an air shower generator and a detector response MC. In the first part of the simulation, large sets of EAS are generated at discrete energies and with different primary particles. Their profiles are saved in a library of air showers (shower library). From this library, the individual showers are read into the detector response MC and provided with different geometries. Energies in the detector response MC are chosen from a given continuous input spectrum. Shower profiles generated at a nearby, discrete energy are scaled to the chosen energy.

The detector response MC simulates the signal the *HiRes-2* detector would receive from a certain shower. This simulation includes: generation of fluorescence and Čerenkov light at the shower; propagation of light through the atmosphere; ray tracing of light through the detector's optical system; PMT response to the signal; simulation of noise; electronics and trigger simulation.

Two databases have been generated and are read by the detector response MC in order to allow event simulation under the exact data taking conditions. A trigger database

contains nightly information on the live-time of the detector and various trigger settings. An atmospheric database provides hourly measurements of the aerosol content of the atmosphere.

The recorded *HiRes-2* data have been broken up into datasets, each containing a few months of data. Major changes in the *HiRes-2* trigger determine the end of a dataset and the beginning of a new one.

The accepted MC events are written out in the same format as the data, which allows us to process them with the same reconstruction programs (described in Chapter 5) as the data. The reconstructed MC events can then be compared in detail with reconstructed data events (see Chapter 7), thus providing a direct check of all aspects of the simulation against the real experiment.

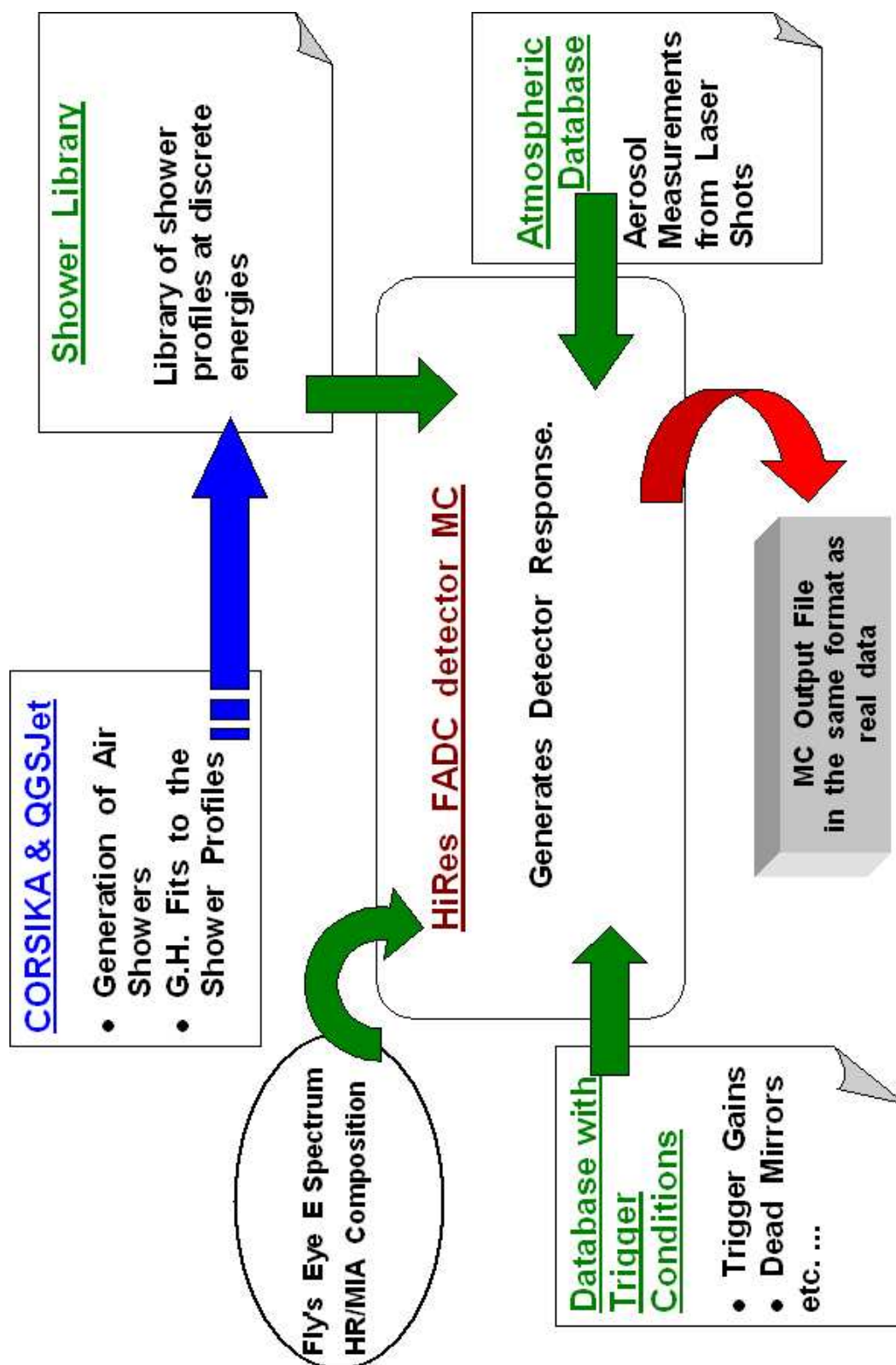


Figure 4.4: Schematic layout of the *HiRes-2* Monte Carlo Simulation. Explanations in the text.

4.3 Air Shower Generator and Shower Library

4.3.1 Air Shower Generation with CORSIKA

The air shower generator used in this analysis is called *CORSIKA* [86] (version 5.61). The *COsmic Ray Simulations for KAscade* program simulates in detail the evolution of EAS initiated in the atmosphere by photons, protons, nuclei and other particles. All known particle interactions, decays and interactions with the earth's magnetic field are taken into account. *CORSIKA* allows several choices of program modules that handle electromagnetic interactions and hadronic interactions. Since the CPU times scale roughly with the primary energy of the simulated shower, generating a large set of showers up to the highest energies, while simulating the evolution of each single shower particle, is in general not possible. *CORSIKA* is using a 'thin sampling' algorithm to achieve tolerable CPU times: If the energies of shower particles emerging from an interaction fall below a preset fraction of the primary energy (the thinning level), only one particle is followed in the simulation from there on with an appropriate statistical weight.

The thinning level that has been used for the generation of the shower library is 10^{-5} , i.e. thin sampling begins at particle energies of 10^{-5} times the primary energy. A geomagnetic field of $21.93 \mu\text{T}$ (horizontal component) and $48.26 \mu\text{T}$ (vertical component) has been calculated for the location of Dugway Proving Ground (see for example [87]). *CORSIKA* does not follow particles that fall below a preset energy threshold. The energy thresholds I chose were 0.3 GeV for hadrons, 0.7 GeV for muons and 0.1 MeV for electrons and photons. A correction for the energy that is lost due to this cut-off (about 10 %) has been applied to the detector response MC.

Electromagnetic interactions were simulated using the well established *EGS* [88] model within the *CORSIKA* program frame. *EGS* includes MC simulations of annihilation, Bhabha scattering, bremsstrahlung, Møller scattering and multiple scattering for electrons and positrons, as well as Compton scattering, e^+e^- -pair production and the

photoelectric reaction for photons. $\mu^+\mu^-$ -pair production and photonuclear reactions are also part of the *CORSIKA* version of *EGS*.

Interactions of hadronic particles with nuclei of the atmosphere were simulated by the *GHEISHA* [89] MC program at laboratory energies below 80 GeV. All cross-sections for these processes are derived from experimental data. The fundamental problem of any UHECR simulation program is the description of hadronic interactions at energies far above those reached in man-made particle accelerators. Cross-sections for these processes have to be extrapolated over many orders of magnitude. Interactions between hadrons and nuclei can be observed in the laboratory at center of mass energies up to 2,000 GeV. The step from these measurements to the UHECR energies of more than 10^{10} GeV seems gigantic. Two considerations make the task at hand seem less impossible: The highest energies of $p\bar{p}$ -interactions in colliders are equivalent to 2×10^6 GeV in the laboratory frame. Furthermore, at the low energy end of the *HiRes* spectrum measurement we expect mostly heavy nuclei, which — by invoking the superposition principle — very roughly correspond to protons two orders of magnitude lower in energy. Different phenomenological models based on the quark-gluon picture of hadronic interactions are available and are continuously being revised. All those models are made to agree with experimental data at the lower energies. Hard processes, i.e. processes with large momentum transfer, can be treated with perturbative QCD. This is not possible for soft processes because of the large coupling constant. The main difference between models is thus the description of soft and semihard processes, which are characterized by small transverse momentum.

The *Quark-Gluon-String model with Jets (QGSJet)* [90] has been used in this analysis. *QGSJet* is formulated entirely in terms of exchange of Pomerons, which are gluon ladders. It describes soft processes with the exchange of soft Pomerons. Minijet generation, which begins to dominate interactions at center of mass energies above \sim

40,000 GeV [91], emerges from the semihard Pomerons, soft Pomerons that incorporate a QCD parton ladder. Hadron-nucleus and nucleus-nucleus interactions are simulated using the Glauber approach [92], which yields a superposition of hadron-nucleon cross-sections in the limit where they are small, and the geometrical cross-section in the limit of large hadron-nucleon cross-sections. *GHEISHA* and *QGSJet* are both included in the *CORSIKA* program package. More information on hadronic interaction models can be found in [93].

4.3.2 The Shower Library

For each simulated air shower, the number of charged particles was saved in steps of 5 g/cm² vertical atmospheric depth. *CORSIKA* fitted a 4-parameter ‘‘Gaisser-Hillas’’ type function [94] to this shower profile:

$$N(X) = N_{max} \left(\frac{X - X_0}{X_{max} - X_0} \right)^{(X_{max} - X_0)/\lambda} e^{(X_{max} - X)/\lambda} \quad (4.6)$$

The total number of charged particles N at a certain atmospheric slant depth X is given by a parameterization of the maximum shower size N_{max} , depth of shower maximum X_{max} , and by two parameters X_0 and λ describing the onset and the exponential tail of the shower profile. X_0 has usually negative values in our fits and should not be misinterpreted as the depth of first interaction. λ has values of the order of the interaction length of the primary particle in the atmosphere. Figure 4.5 shows an example of a Gaisser-Hillas fit to a single air shower initiated by a proton cosmic ray with an energy of 10^{17} eV. The particle entered the atmosphere under a zenith angle of 36.9° (with respect to the vertical).

I have slightly modified the *CORSIKA* code to write out the four fit parameters into a shower library file for each generated air shower, together with the energy of the primary particle, the particle type, its zenith angle, the depth of first interaction in the atmosphere, and the χ^2 of the fit. Additionally, the actual charged particle distributions versus atmospheric depth were written out into a separate file to verify the quality of

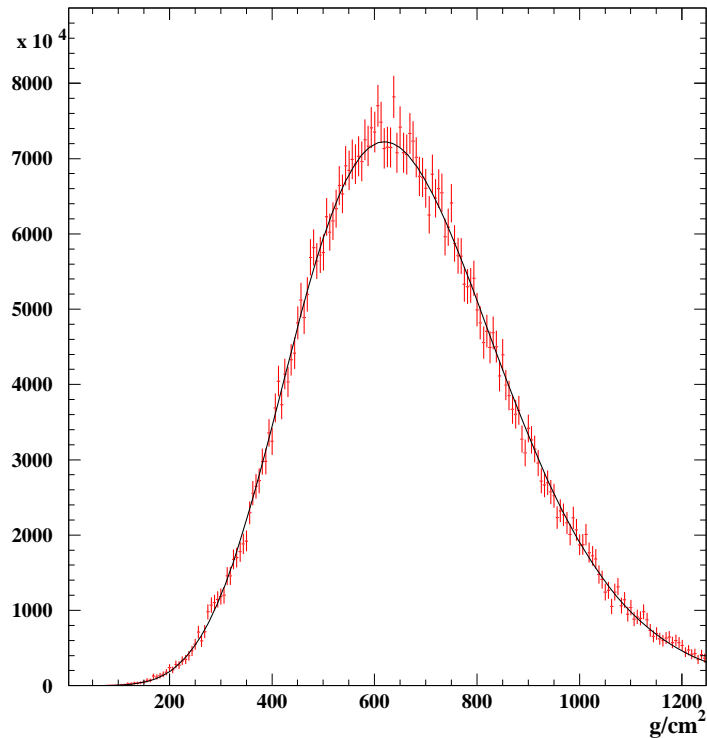


Figure 4.5: Gaisser-Hillas fit to an EAS simulated with *CORSIKA* and *QGSJet*. Primary particle was a proton with an energy of 10^{17} eV that entered the atmosphere under a zenith angle of 36.9° . The histogram shows the total number of simulated charged particles plotted against atmospheric slant depth.

the fits (as shown in Figure 4.5).

Shower library files were generated with proton and iron primaries at five discrete energies: 10^{16} eV, 10^{17} eV, 10^{18} eV, 10^{19} eV and 10^{20} eV. At each energy, 200 proton and 200 iron showers were simulated at each of three different zenith angles: 0° , 36.9° and 48.2° ($\sec(\theta) = 1, 1.25, 1.5$). Proton showers were also generated at an additional angle of 60° to test the effect of the horizontal atmosphere that is used in *CORSIKA*. This simplification leads to problems only at larger zenith angles ($> \sim 75^\circ$) and proves not to be significant for the angular range of the library showers. The parameters N_{max} and X_{max} (in slant depth) were found to be independent of the zenith angle of the shower. This can be seen from Figure 4.6. X_0 and λ show some variation with the

zenith angle.

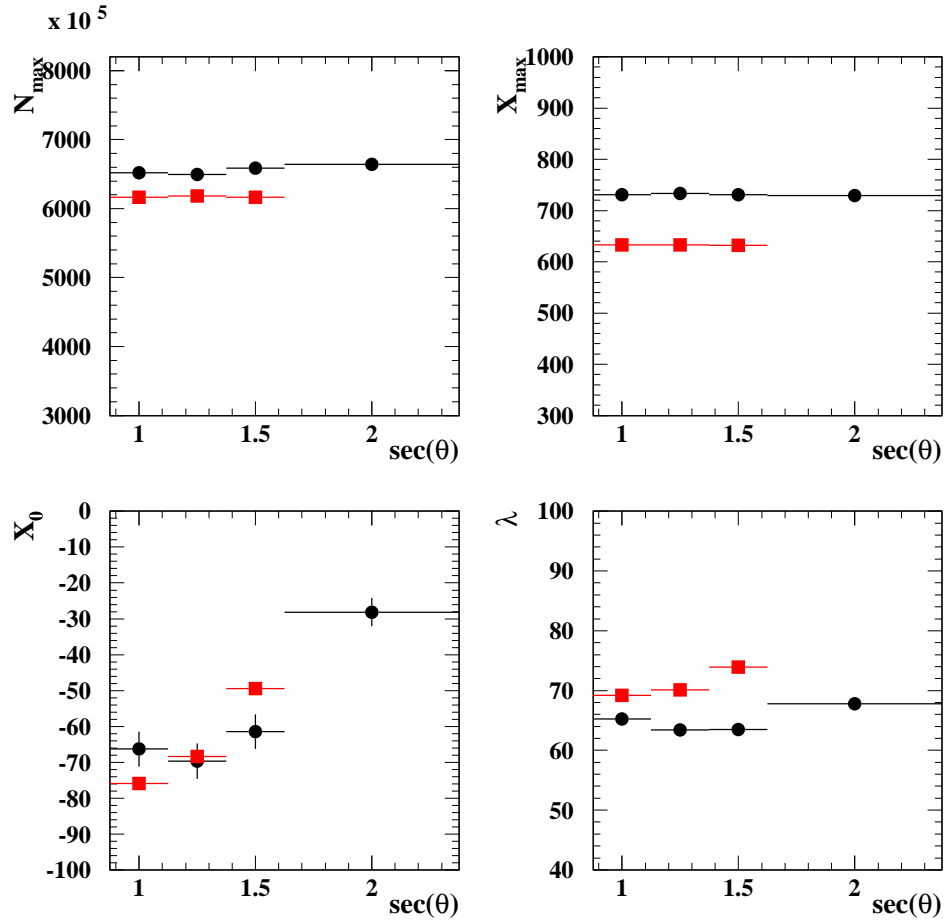


Figure 4.6: Variation of Gaisser-Hillas parameters with zenith angle. circles: proton showers , squares: iron showers , Each point is the average of 200 showers at 10^{18} eV. Error bars are RMS in the mean and are (except in the case of X_0) smaller than the markers.

The energy dependence of the Gaisser-Hillas parameters, which was derived from Heitler's toy model in Equation 1.2 can be studied in detail with the *CORSIKA* air showers. The linearity of the average parameters $\log(\langle N_{max} \rangle)$ and $\langle X_{max} \rangle$ with the logarithm of the cosmic ray energy can be seen in Figure 4.7 for proton and in Figure 4.8 for iron primaries with a zenith angle of 36.9° . The $\langle X_0 \rangle$ fit parameter is also roughly linear in $\log(E)$, whereas $\langle \lambda \rangle$ does not show a significant energy dependence. The parameters of fits to $\langle N_{max} \rangle$, $\langle X_{max} \rangle$ and $\langle X_0 \rangle$ are

summarized in Table 4.1.

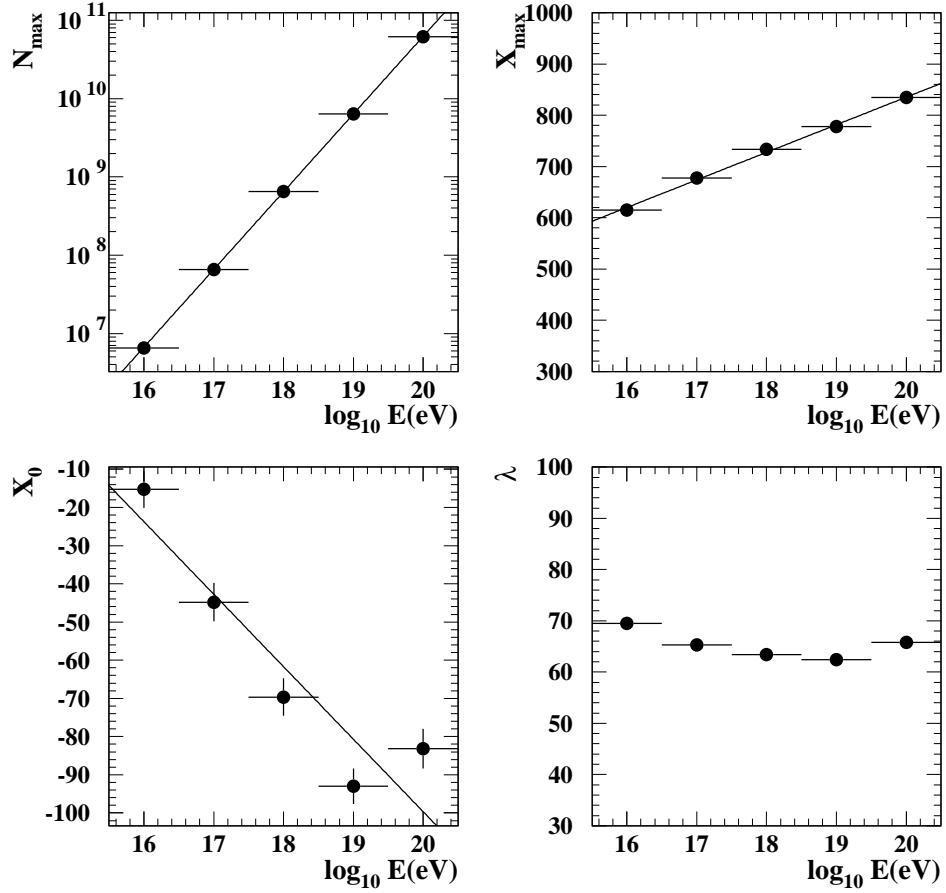


Figure 4.7: Variation of Gaisser-Hillas parameters with energy. Shown are the G.-H. parameters for proton showers at a zenith angle of 36.9° . Each point is the average of 200 showers. Error bars are RMS in the mean and are (except in the case of X_0) smaller than the markers. Linear fits in $\log(N_{max})$, X_{max} and X_0 versus the decadic logarithm of the energy are shown.

The direct correlation of $\langle N_{max} \rangle$ and $\langle X_{max} \rangle$ with the shower energy makes it possible to scale a chosen library shower profile to the energy that has been determined in the detector response MC for a given event. Scaling of the shower profile is achieved with the slopes of the linear fits in Figures 4.7 and 4.8:

$$\log [N_{max}(E_{MC})] = \log [N_{max}(E_{SL})] + A \cdot [\log (E_{SL}) - \log (E_{MC})] \quad (4.7)$$

Here, E_{MC} is the energy chosen in the MC from a continuous input energy spectrum,

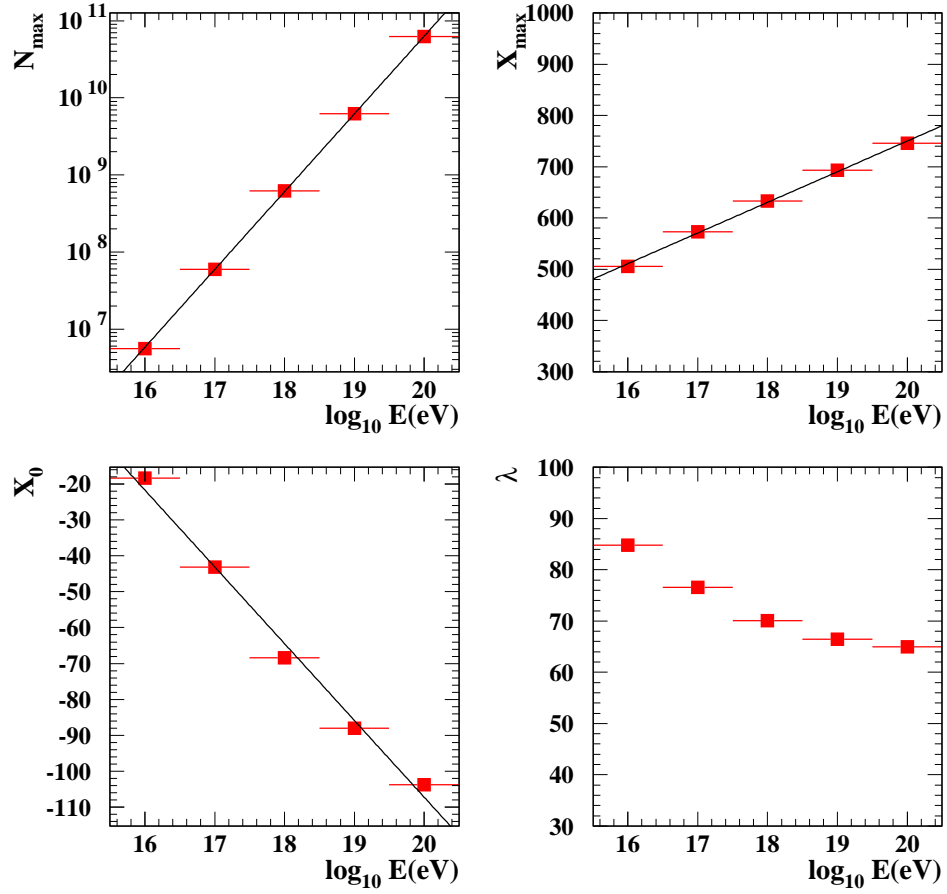


Figure 4.8: Variation of Gaisser-Hillas parameters with energy. Shown are the G.-H. parameters for iron showers at a zenith angle of 36.9° . Each point is the average of 200 showers. Error bars (RMS in the mean) are smaller than the markers. Linear fits in $\log(N_{\max})$, X_{\max} and X_0 versus the decadic logarithm of the energy are shown.

E_{SL} is the discrete energy of the nearest shower library file, and A is the slope of the fit of $\log(\langle N_{\max} \rangle)$ versus $\log(E)$. Similar equations can be written for $\langle X_{\max} \rangle$ and $\langle X_0 \rangle$ and the respective slopes. N_{\max} , X_{\max} and X_0 are scaled for each shower according to the energy dependence of the average $\langle N_{\max} \rangle$, $\langle X_{\max} \rangle$ and $\langle X_0 \rangle$, whereas λ and the depth of first interaction of each library shower are adopted without scaling in the detector response MC.

The zenith angle is taken from a solid angle distribution in the detector response MC. The shower profile used in the MC to simulate an event is also chosen to be from

the shower library file that is nearest in the secant of the zenith angle.

The use of a shower library in the detector response MC yields important advantages over previous simulation programs used in the *HiRes* data analysis. Air showers generated with *CORSIKA* and *QGSJet* display realistic fluctuations in their profiles, which are caused by fluctuations in the depth of first interaction. Instead of using a parameterization of an average shower profile, individual showers can be taken from the library, scaled to a chosen energy and viewed under a chosen geometry. The fluctuations between showers of the same energy are preserved. Re-using shower profiles under different geometries and energies allows the simulation of realistic showers in the detector response MC without the disadvantage of large CPU times, which is unavoidable in a detailed shower simulation code like *CORSIKA*. On the 440 MHz DEC ALPHA workstations I used to generate the library, it took of the order of 10 to 30 minutes to generate a shower with *CORSIKA* (depending on the shower energy), but only a few seconds to generate the detector response to a library shower.

sec (θ)	proton	$\log(N_{max})$	X_{max}	X_0	iron	$\log(N_{max})$	X_{max}	X_0
1.0		0.99	54.6	0.0		1.01	60.5	-14.4
1.25		0.99	53.8	-19.0		1.01	59.8	-21.4
1.5		0.99	53.4	-22.1		1.01	60.1	-27.6

Table 4.1: Slopes of Gaisser-Hillas fit parameters vs. $\log(\text{energy})$ at different zenith angles θ .

4.4 Detector Response Monte Carlo

4.4.1 Input and Output of the Detector Response MC

The detector response simulation program reads a single **input file** to set all parameters for a desired MC job. The input file is supplied by the user and contains the paths to all database files, histogram and DST files. Lower and upper limits are set on the range of zenith and azimuth angles of the shower axis, the angle of the impact point, the distance between shower and detector, and the energy of the primary particle. The spectral index of the input energy spectrum and the type of primary particle (proton or iron) can be selected. The user determines the number of events to be generated and the random number seed for each MC job. A correction factor for the PMT calibration can be chosen. Default values for the trigger settings and for the aerosol attenuation length and scale height are set in the input file, but can be overwritten by the use of databases. All other parameters are hard-coded in the MC program.

I have added an option to use a fit to the *Fly's Eye* stereo spectrum (see Figure 1.7) below the “ankle” and to the *HiRes-1* spectrum (see Figure 2.9) above the “ankle” as the shape for the **input energy spectrum**. If this option is chosen, the lower energy limit is fixed at $10^{16.5}$ eV and there is no upper limit. Another option allows the use of a mixed **composition** in the shower generation. The ratio of proton to iron showers has been taken from the fits to the composition measurement by *HiRes/MIA* at energies below $10^{17.85}$ eV and by *HiRes stereo* above, with respect to the *QGSJet* values for pure proton and iron showers (see Figure 2.10).

The path to the directory that contains the **shower library** files is specified in the input file. The same directory also contains two files with the parameters used for scaling the Gaisser-Hillas profiles of proton and iron showers. A switch in the input file allows the use of a single dataset of parameterized showers, which has to be supplied by the user, instead of the library. This option is mainly used for debugging. The *HiRes-2* detector simulation can also be used to read geometries and profiles from

events detected by *HiRes-1* and to simulate the *HiRes-2* response to those events. This allows the combination of the *HiRes-1* and the *HiRes-2* MCs in a “tandem” stereo analysis. The regular *HiRes* stereo analysis uses a new MC program, which simulates both detectors in one set of routines.

When simulating the operation of the detector for a certain time period (i.e. for a *HiRes-2* dataset), some parameters may vary during the chosen period. Their variation has to be taken into account in the MC programs to guarantee a realistic simulation. I have generated a **trigger database** containing variable trigger settings and lists of dead mirrors for each night included in the analysis. Background light has been included as an average for each dataset. Seasonal variations in the atmospheric density are accounted for in the MC. Strict cuts have been imposed to avoid variations in the weather during the selected nights (see Chapter 6): Only clear nights were included in this analysis. Measurements of variations in the aerosol content of the atmosphere were recorded in an **atmospheric database**.

Two streams of **output** are being generated. Detailed information on all triggered events is stored in a DST file. The actual FADC data are contained in the *fraw1* bank, details about the trigger response can be found in the *frg1* bank. An additional bank (*fmc1*) is written out into the DST file with information on the event geometry and energy that were used as inputs to the MC. The main entries of this bank are listed in Table 4.2 below.

Information on all events that were generated, including events that were not seen by the detector at all or were rejected at some trigger level, is written out in the form of histograms. The histogram file contains the energy distribution μ_i^{MC} of generated events, which is needed for calculation of the detector acceptance.

4.4.2 Overview of the Detector Response Simulation

The *HiRes-2* detector response simulation program, called “mcru”, has been developed based on an older version of the *HiRes* stereo simulation written mainly by John Boyer.

header:
zenith angle of shower vector azimuthal angle of shower vector distance of impact point azimuthal angle of impact point energy of primary particle type of primary particle (proton/iron) Gaisser-Hillas parameters depth of first interaction distance between shower and detector angle of shower axis in shower-detector plane unit vector of shower axis normal vector on shower-detector plane normal vector on shower axis in s.-d. plane number of mirrors with signal
for each mirror with signal:
mirror index number of channels with signal number of photoelectrons
for each channel with signal:
channel index average pulse time number of photoelectrons

Table 4.2: Main entries in the *fmc1* bank.

The basic layout of the MC and most of its routines (including the light generation and propagation, simulation of the detector electronics, and the formation of the primary trigger) have been taken over unchanged. Several members of the *HiRes* collaboration have contributed to the MC simulation programs. To name only a few: many routines, such as the lateral shower profile using the NKG function and PMT acceptance profile, have been added by Zhen Cao; Stan Thomas contributed the ray tracing program; Stefan Westerhoff wrote the routine for the latest secondary trigger algorithm. My own main additions are the atmospheric and trigger database, shower library, input spectrum and composition, energy correction for particles below the *CORSIKA* cut-off, background noise, lateral distribution of Čerenkov light and the combination of different trigger versions and DSP scans to a realistic trigger simulation. An overview of the

whole “mcru” program is given in the following.

Defining the Shower Geometry and Profile.

The simulation of each single event begins with the choice of its geometry, energy and particle type. The zenith angle was chosen from a solid angle distribution between 0° and 70° for this analysis; azimuthal and impact angle were chosen randomly from 0° to 360° . The distance between shower and detector (R_p) followed an R_p^2 distribution between 0.05 km and 35.0 km. The cosmic ray energy and composition were chosen according to previously measured distributions, as described above. A cut has been applied to skip the simulation of events whose ratio of energy over R_p falls below a certain threshold. It was verified in test simulations that the removed events were all much too far away to trigger the detector at the given energy. A histogram of energy versus R_p for simulated events can be seen in Figure 4.9 together with the cut threshold. The so-called “E- R_p ” cut is the only cut that is applied in the MC. It is necessary in order to achieve acceptable CPU times while using a continuous input spectrum and R_p distribution. The energy distribution of all generated events is written out into the histogram file before this cut.

Once a zenith angle, energy and primary particle are determined, a library shower profile is read into the MC and scaled to the energy as described above. A single entry is read from the trigger database to define the trigger settings for the following event simulation. Each entry describes the settings for a single night included in the analysis. If the atmospheric database is used, an entry whose date matches the date read from the trigger database is chosen to set the aerosol attenuation length and scale height. The fraction of events that are generated using a certain entry from the trigger database is determined from the recorded live-time fraction of the actual detector during that night. In this way, the simulated events are truly representative of the conditions during the time period under analysis.

A correction is applied to the absolute normalization of each shower profile, in

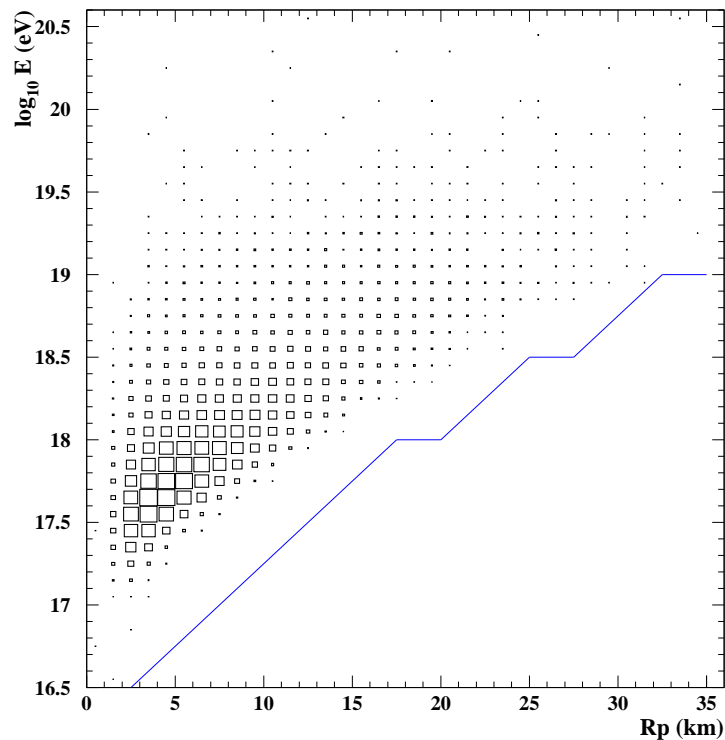


Figure 4.9: Energy- R_p Cut applied in the MC to reduce CPU time for events that are too far away and too low in energy. The input energy and input R_p of all reconstructed MC events used in this analysis (at the lowest cut level) is shown. The size of the boxes is proportional to the number of events in each bin. Events to the right from the line are being cut out.

order to account for the amount of calorimetric shower energy (E_{cut}) that is lost due to the energy thresholds in the *CORSIKA* program. With the thresholds used in this analysis, about 10% of the total shower energy is lost in the air shower simulation according to Song et al. [95]. I have verified this number for a sample of showers from the library. In order to determine the correction, first the “missing energy” for proton and iron showers as a fraction of the total shower energy (mfrac) was taken from *CORSIKA* simulations in the same paper. The total energy of the shower is the sum of ionization energy determined from the shower profile, “missing energy” and energy below the *CORSIKA* thresholds. The energy below threshold as a fraction of

the ionization energy (E_{ion}) is calculated in the following way:

$$\begin{aligned} E_{ion} &= E_{total} - E_{missing} - E_{cut} = E_{total} \cdot (1 - \text{mfrac} - 0.1) \\ E_{cut} &= 0.1 \cdot E_{total} = \frac{0.1}{1 - \text{mfrac} - 0.1} \cdot E_{ion} \end{aligned} \quad (4.8)$$

Thus, the N_{max} parameter of each shower profile is boosted by a factor of $1 + 0.1/(1 - \text{mfrac} - 0.1)$ in the detector response MC.

Light Generation, Propagation and Ray Tracing.

After calculation of a few geometrical quantities of the shower with respect to the detector, the part of the shower profile that is within the range of elevation coverage is determined and divided into segments of equal viewing angle (0.1°). For each shower segment, the amount of fluorescence light and Čerenkov light is calculated from the number of charged particles given by the shower profile. The fluorescence spectrum used in the simulation was shown in Figure 1.6. The Čerenkov beam that is generated along the shower axis has an opening angle of roughly 6° at standard pressure. I have compared the Čerenkov light profile along the shower axis that is calculated in “mcru” with *CORSIKA* simulations and found very good agreement. The detector response MC distinguishes four light components from each shower segment, which add up to the signal seen in the detector: fluorescence light scattered into the PMTs, “direct” Čerenkov light from the Čerenkov beam and two scattered Čerenkov light components, from molecular and aerosol scattering. The attenuation of all four components on their way to the detector is simulated, taking into account molecular, aerosol and ozone attenuation processes. Finally, the photons that contribute to the signal are converted into photoelectrons for each segment by using the quantum efficiency and filter transmission curves shown in Figure 2.5 and assuming a mirror reflectivity of 81%.

Before the ray tracing procedure, the photoelectrons (p.e.) from the different light components at each shower segment are spread out laterally around the shower axis.

The *Nishimura-Kamata-Greisen* (*NKG*) lateral distribution function [96] is used to determine the lateral spread of fluorescence p.e. and direct Čerenkov p.e. According to this parameterization, the particle density at a perpendicular distance r from the shower axis is proportional to:

$$\rho(r) \propto \left(\frac{r}{r_M}\right)^{s-2} \left(1 + \frac{r}{r_M}\right)^{s-4.5} \quad (4.9)$$

Here s is a measure of the shower age and r_M is the Molière multiple scattering unit, which depends on the atmospheric density and is 79 m at sea level [33]. I have added a parameterization of the lateral distribution of Čerenkov light based on fits to the Čerenkov light distribution of air showers generated with *CORSIKA*. This parameterization describes the lateral density profile with the superposition of three exponential functions in r . The model parameters depend only on the shower age and the zenith angle of the shower axis. The Čerenkov light simulation in *CORSIKA* has previously been tested against *HEGRA* data for r from 20 to 100 meters [97] and proven to be realistic.

A ray tracing routine loops over all p.e. in each shower segment and decides from the location of the p.e. whether a certain PMT was hit or not. The mirror optics, obscuration of the mirror by the PMT cluster, cracks between the PMTs in the cluster, and the actual acceptance profile, which has been measured for a sample of PMTs, are taken into account. The successful p.e. are stored in an array together with their arrival times and the mirror and PMT indices.

Simulation of Electronics and Trigger.

Next, raw data in digital FADC format are generated for all HG, LG and trigger channels of each viewing mirror from the recorded p.e. distributions. Ambient sky noise is added in the digitization process in all channels. Additional high amplitude sky noise is added from a measured distribution, as will be described below. Store windows are determined for each mirror, and the trigger sums are compared to the primary trigger

threshold. The confirming scan is applied on triggered mirrors, and patterns of hit PMTs are compared to the secondary trigger algorithm of the chosen data period. If the secondary trigger is successful, the readout scan is applied and all HG channels with pulses above the readout scan threshold are stored in an array. After all mirrors have been processed, mirrors that are triggered by the adjacent mirror trigger are read out in a second loop, where only the readout scan is applied. Finally, all channels with signals above the readout scan threshold are written into the DST file.

4.4.3 Trigger Database

The *HiRes-2* data included in this analysis have been divided into three **datasets**. Dataset 1 (DS1) contains data from the beginning of December 1999 until the end of May 2000. The *HiRes* experiment was shut down during the summer of 2000 due to problems with access to Dugway Proving Ground. With the beginning of September 2000, a change in the secondary trigger version was introduced, which led to a new dataset. DS2 contains data from the beginning of September 2000 until the 14th of March, 2001. After this date, servicing of the trigger DACs and of the pedestals of all channels, which will be explained below, was introduced. This defines the beginning of DS3, which contains data until the end of September 2001, when access to Dugway Proving Ground was again denied to the *HiRes* group.

One **trigger database** file has been generated for each dataset. The header of the file contains the number of nights and the total live-time of the detector for the dataset. It is followed by one entry for each selected night. Each entry consists of the date, nightly live-time of the detector, DSP scan thresholds, secondary trigger version, adjacent mirror trigger version, pre-scale factor and a list of dead mirrors.

The **live-time** of the detector in a specific night and during a specific data part has been taken from the “pass0” data. A script was provided by John Boyer to extract the total on-times and deadtimes from the data.

The **DSP scan thresholds** for the confirming and readout scan are written out and

stored in automated log files on the Nevis computers. From December 1999 to the 5th of January 2000, the thresholds were set to 36 and 24 for the confirming and readout scan, respectively. For later data (including most of DS1 and all of DS2 and DS3), the thresholds were lowered to 32 and 22, which allowed the extension to lower energies of recorded events.

The primary trigger requires a total of at least two threefold coincidences in the row and column sums, i.e. a mirror passes the primary trigger with either two threefolds in the row trigger channels, two threefolds in the column trigger channels, or one threefold in both. The primary trigger requirements do not change. The **adjacent mirror trigger** has been turned on with the beginning of DS2. Since it was not always active during the first months, I have histogrammed the number of recorded mirrors for each selected night of DS2 and DS3. Two nights in DS2 (10/03/2000 and 10/04/2000) showed an average of only two recorded mirrors instead of 6. The adjacent mirror trigger option was turned off in the database file for these nights. A change in the algorithm occurred with the transition from DS2 to DS3: In DS2 at least three threefold coincidences were required in a mirror with primary trigger to trigger adjacent mirrors. In DS3 the adjacent mirror trigger could also be activated by two threefold coincidences in either view in the primary trigger, with more than 10 recorded FADC time slices between the beginning and end of the read out trigger channels. This enabled even very light weak events to cause readout of adjacent mirrors. A change in the size of the store window coincided with the change in the adjacent mirror trigger version.

Three different versions of the **secondary trigger algorithm** were in use during the analyzed data period:

- In version 1 the secondary trigger simply required at least 6 hits above the confirming scan threshold in a mirror.
- With the change in the DSP scan thresholds, a new algorithm was introduced: Version 2 scanned through the 256 HG channels of a mirror, searching for a

cluster of at least 4 hits above confirming scan threshold within each possible 6x6 PMT sub-cluster. If a total of more than 15 hits was found within a mirror, the secondary trigger was satisfied without searching for clusters.

- In DS2 and DS3, a new algorithm was used. Version 3 of the secondary trigger sorted all confirming scan hits into clusters of adjacent hits. It then required at least one cluster with more than 3 hits. In order to avoid frequent triggering of the detector by blasts of direct Čerenkov light, a non-zero time spread between the hits was required for clusters with less than 10 hits.

The **pre-scales** used for trigger diagnostics have been added to the MC, although they do not have a significant effect on the final event selection. Pre-scale settings have been extracted from the trigger packets in the *fpkt1* banks of the data stream. The first pre-scale allows one out of eight mirrors with a single threefold in the trigger sums to pass the primary trigger. The second pre-scale allows a certain fraction of mirrors, which would normally be rejected by the secondary trigger, to be read out. The second pre-scale was not always active and the fraction changed between 1 out of 64 and 1 out of 128. This information has been added to the trigger database.

A list of **dead mirrors** has been compiled for each selected night. I have determined disabled mirror units by histogramming the number of read out tubes in each mirror for each selected night. Mirrors with zero or very few entries were added to the list of dead mirrors in the database file for this night. In most cases it was found that mirrors stayed disabled for several nights, before they could be repaired. Dead mirrors are taken out of the simulation before the secondary trigger.

In addition to the database file, I have generated a nightly list of average **trigger DAC** values that I extracted from the raw data (*fpkt1* bank). The list contains one entry for each mirror for each data part, together with the live-time and the number of the part. The trigger DACs set the gains of the trigger channels in the following way [98]:

$$gain = (DAC - 335)/510 \quad (4.10)$$

In DS1 one trigger DAC value was used per ring of mirrors. For most of the time, the DACs in ring 1 (lower elevation range) were set to 1,300, the DACs in ring 2 (higher elevation range) to 1,100. Variations from mirror to mirror were introduced in DS2 to improve the trigger rate of the detector. With the beginning of servoing of the trigger DACs in DS3, the DACs were set to a nominal value of 1,300 and allowed to drift in a preset range, if a trigger channel recorded high variances, e.g. due to starlight. The average DAC values per mirror were found to be mostly very close to the nominal value. The trigger gains influence directly the sensitivity of the detector by means of the primary trigger. (Raising the trigger gain, for example, is equivalent to lowering the trigger threshold.) Using the accurate trigger DACs in the detector simulation is therefore crucial for the calculation of the acceptance.

4.4.4 Simulation of Noise & Noise Assisted Triggering

Two components of background noise are distinguished in the MC simulation: Ambient noise, scattered light of low amplitude, mostly from man-made sources, is added to each FADC time slice in all channels. High amplitude skynoise, mostly light from bright stars, is added in the form of additional noise p.e. Electronic noise is included in the ambient noise measurement, but is much smaller than these backgrounds (as described in Chapter 3).

The number of **ambient noise** p.e. that are added to each FADC bin is Poisson distributed about a mean that has been determined for each mirror for each *HiRes-2* dataset. For the time period of data in this analysis, mirror averages of HG channel variances for each hour of data taking were available in databases at Nevis laboratories. The variances in the 100 ns FADC time slices are determined from snapshots and averaged over 256 digitizations. A conversion factor of 2.15 between the average variances and the number of ambient noise p.e. in a HG channel was derived by John Boyer and is used in this analysis. I have determined the average number of noise p.e. of each *HiRes-2* dataset for each mirror, with a Gaussian fit to its variances (converted

into p.e.). One value per mirror per dataset is currently used in the MC to describe the ambient noise component. The mean number of ambient noise p.e. per FADC time bin, averaged over all mirrors, was 4.9 with an RMS of 0.5 for DS1, 6.3 with an RMS of 1.0 for DS2 and 6.2 with an RMS of 0.6 for DS3.

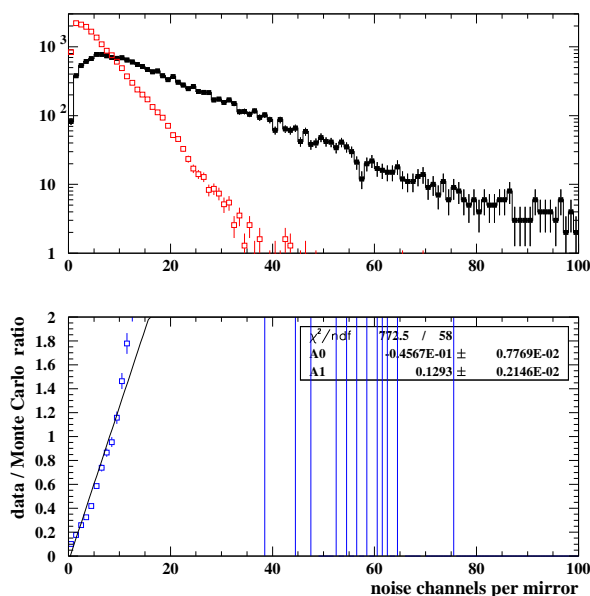


Figure 4.10: top: Distributions of number of noise channels in DS2 per mirror with only ambient noise in the MC. (open squares: MC , filled squares: data)
bottom: Ratio of data over MC with linear fit.

Figure 4.10 shows a data-MC comparison plot of the distribution of channels triggered by noise. The number of HG channels that have been rejected as noise in the reconstruction programs are histogrammed per mirror for data and MC events of DS2. Only ambient noise is included in the MC simulation. The simulated events do not accurately describe the large tail in the distribution, which comes from mirrors with more than the average number of noise hits seen in the data. I have added a second component of background noise — **high amplitude sky noise** (dubbed “extra hits”) — to achieve agreement between the noise hits distribution in data and MC. The data distribution shown in Figure 4.10 is a convolution of ambient noise and extra hits. In order to determine a realistic extra hits distribution for the MC, a Gaussian fit to the noise

distribution of each dataset was used initially to determine the number of extra hits for each mirror. In repeated MC simulations, the extra hits distribution was adjusted so that the final noise distribution was brought into better agreement with the data. Four parameters were used for tuning the extra hits distribution: the mean and width of the Gaussian, and the entries in the first two bins, i.e. the probability of observing 0 or 1 noise hits. Separate extra hits distributions were determined for mirrors with primary triggers, for mirrors read out due to the adjacent mirror trigger and for mirrors in the north-eastern quadrant of the detector, where scattered light from a nearby town (Ditto, UT) leads to increased background noise. The number of extra hits is taken from the tuned distribution, their amplitude, i.e. the number of p.e. per extra hit, is set to a fixed value (readout scan threshold plus one). Using Gaussian distributions of the number of p.e. did not improve the data-MC agreement.

The extra hits are added to random channels of each mirror and at random times. 150 FADC time slices have been added both before the first recorded p.e. arrival time in each mirror and after the last recorded time. Ambient sky noise is added over the whole range of FADC time slices, extra hits are only added after the first 50 and up to the last 50 FADC slices. Since signals are read out in 100 FADC slices, centered around a pulse, this ensures that all signals contain ambient noise fluctuations in each FADC slice. Extra hits are allowed to be added to channels that already contain a signal from the air shower. The distribution of noise hits in the MC, including both ambient noise and extra hits, is shown in Figure 4.11.

THE DISTRIBUTION OF EXTRA HITS IS THE ONLY PARAMETER IN THE MC SIMULATION THAT HAS BEEN TUNED TO MATCH THE DATA. ALL OTHER PARAMETERS WERE MEASURED OR DERIVED IN AN INDEPENDENT WAY.

The importance of a realistic description of background noise in the *HiRes-2* detector simulation becomes evident from Figures 4.12 and 4.13. Shown here are two more

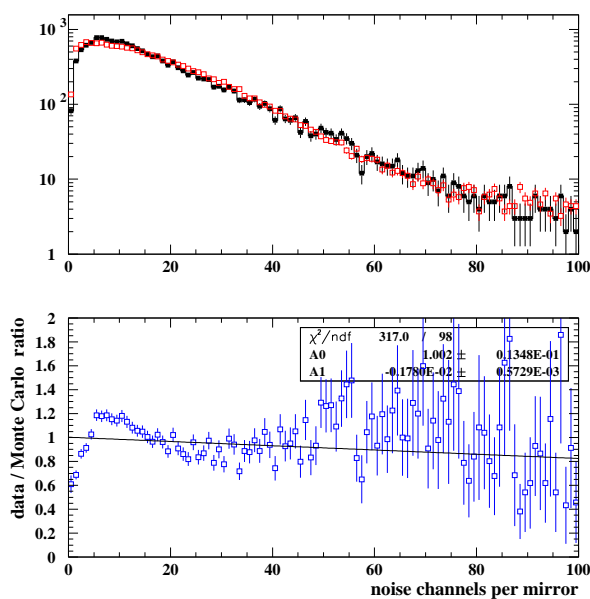


Figure 4.11: top: Distributions of number of noise channels in DS2 per mirror with ambient noise and extra hits in the MC. (open squares: MC , filled squares: data)
bottom: Ratio of data over MC with linear fit.

data-MC comparison plots: Both display the distribution of events over the shower-detector plane angle, the angle between the shower-detector plane and a vertical plane, which is also the angle of the shower track against a vertical line within the cluster box. Events with small track angles have tracks close to vertical, events with larger track angles have more inclined tracks. The deficit of close to vertical tracks in the MC distribution of Figure 4.12 is due to the lack of noise hits. The MC set displayed in this figure is the same as in Figure 4.10, i.e. it does not have any extra hits. Adding extra hits as in Figure 4.11 reduces the discrepancy between data and MC, as shown in Figure 4.13. The addition of extra hits is the only difference in the two MC sets. This effect is caused by an inefficiency in the *HiRes-2* primary trigger, which allows **noise assisted triggering**. The row and column pattern of the primary trigger causes it to be less sensitive to tracks that are nearly vertical than to inclined tracks. A vertical track from a shower with a weak light signal is seen only in one column and fails to trigger

coincidences in the column sums. Cracks between PMTs might further reduce the sensitivity to vertical tracks and worsen the bias towards more inclined tracks. However, as can be seen from the MC simulation, a channel triggered by background noise — ambient noise and extra hits — in the right location and at the right time, can help to lift the critical events above the trigger threshold.

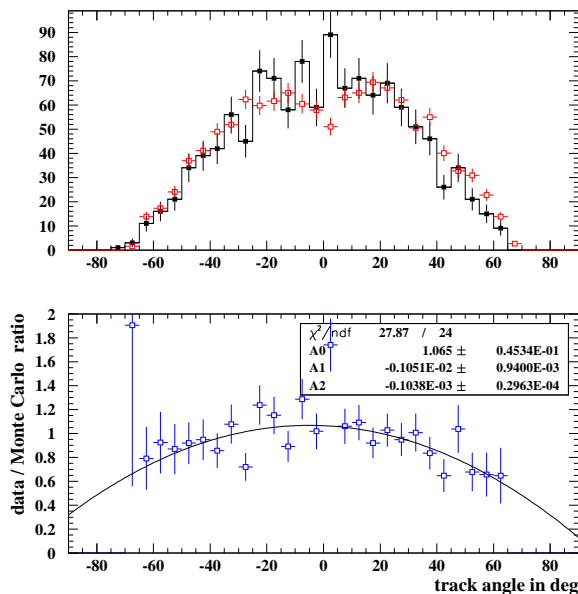


Figure 4.12: top: Distributions of track angles in DS2 with only ambient noise in the MC. (open squares: MC , filled squares: data)
bottom: Ratio of data over MC with quadratic fit.

The method described above for adding extra hits to the MC achieved satisfactory agreement with the data in the shower-detector plane angle distributions until the beginning of DS3. Comparing the numbers of noise channels per mirror for DS2 and DS3 in Figure 4.14, one can see that the average number of background noise hits was reduced apparently by almost 50%. The ambient noise measurements for DS2 and DS3 yield very similar averages, as reported above. Applying the same method for adding extra hits, as was used for DS1 and DS2, leads to an agreement in the noise hits distribution between data and MC (shown in Figure 4.15); the shower-detector plane angle distributions, however, still show a significant lack of close to vertical tracks in

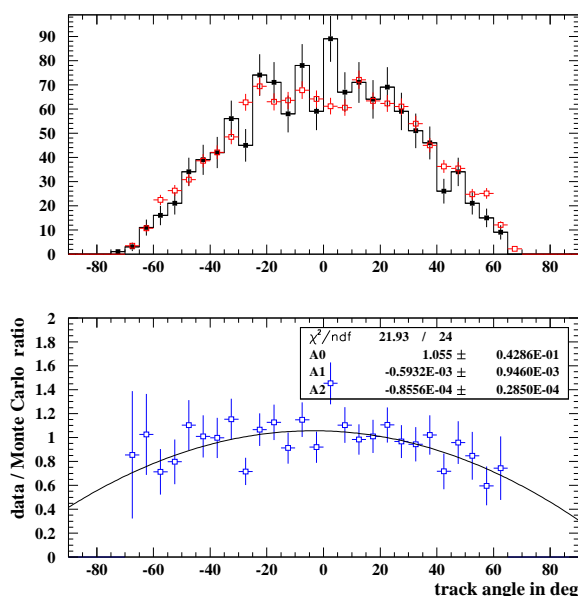


Figure 4.13: top: Distributions of track angles in DS2 with ambient noise and extra hits in the MC. (open squares: MC , filled squares: data)
bottom: Ratio of data over MC with quadratic fit.

the MC, as can be seen from Figure 4.16.

In order to get an agreement in the distribution of track angles between data and MC of the same quality as for the previous datasets, extra hits were added in a much higher multiplicity than suggested by the data. Figure 4.17 shows the data/MC comparison for noise channels that leads to the shower-detector plane angle distribution in Figure 4.18.

The reduction in the number of noise channels with the beginning of DS3 was unexpected because of the only minor changes in the trigger between DS2 and DS3. Apart from a slight change in the adjacent mirror trigger algorithm, the only difference lies in the **servoing of trigger DACs and pedestals** of HG and trigger channels. The servoing process was introduced to stabilize the trigger DACs and the pedestals against thermal drifts. The pedestals are servoed by a comparison of the mean of measured FADC distributions with a preset value (10.0 for HG and 20.0 for trigger channels) in each snapshot. The snapshot rate is just under 4.8 Hz; duration of a snapshot is 25.6 μ s.

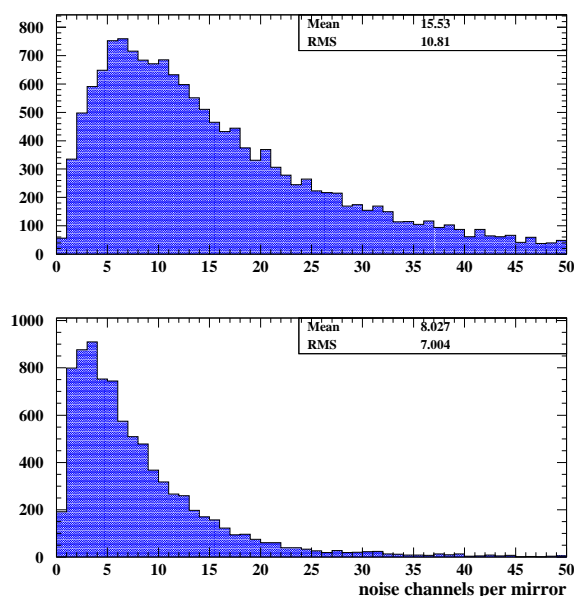


Figure 4.14: top: Number of noise channels per mirror in dataset 2.
bottom: Same distribution for dataset 3.

If the measured mean diverges from the preset value, the pedestal DAC is corrected by one count each snapshot, which changes the pedestal by about 1/16 FADC count, until agreement has been reached. If the measured reduction in noise hits is an artefact, it could be caused by the servoing of pedestals in the following way: Figure 4.19 shows a distribution of FADC counts in a HG channel, taken from a snapshot at a time after the servoing had been introduced. The distribution is cut off at 0, since only positive FADC counts are taken into account in the servoing process. A bright star shining into a phototube would widen the pulse and allow a situation like this, where a large part of the left tail is cut off. In this case, the servoing mechanism would read a mean of about 11, raise the pedestal by one count and move the pulse further to the left. A Gaussian fit, however, shows that the true mean of the pulse is at about 9 FADC counts. The servoing mechanism would lower the pedestal, driven by negative feedback, since an increasingly larger part of the pulse would be cut off at 0. This would push the pulse below the DSP scan threshold. In this way, a noise hit could disappear from

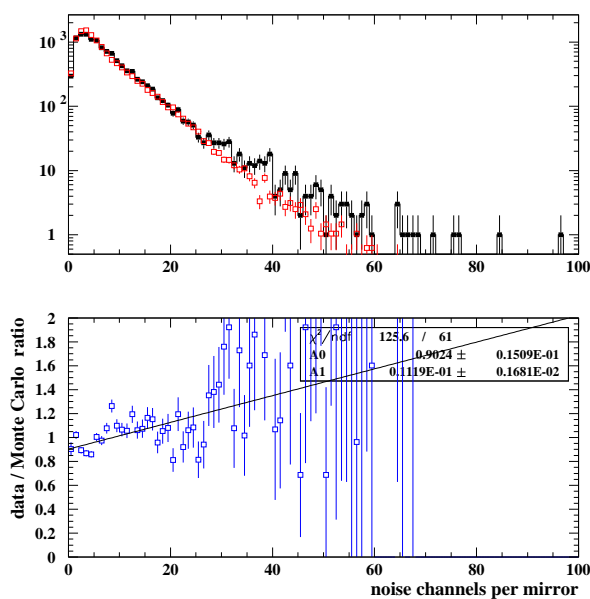


Figure 4.15: top: Distributions of number of noise channels in DS3 per mirror before our correction. (open squares: MC , filled squares: data)
 bottom: Ratio of data over MC with linear fit.

the data. By looking at snapshots alone, it was not possible to verify this mechanism (which was suggested by Gordon Thomson) in a quantitative way, because detailed information from snapshots is written out too infrequently.

Since an accurate description of the background noise for DS3 is impossible with the available data if the above hypothesis is correct, I have decided to avoid the problem of noise assisted triggering by introducing a cut on a certain class of vertical triggers for this dataset. The track angle distributions for data and MC of DS3 with the applied cut are shown in Figure 4.20. This cut will be discussed in more detail in Chapter 6.

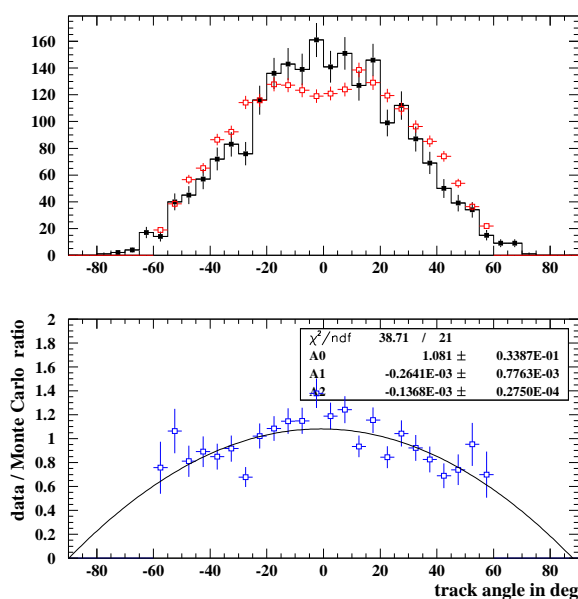


Figure 4.16: top: Distributions of track angles of DS3 with low noise in MC. (open squares: MC , filled squares: data) ; bottom: Ratio of data over MC with quadratic fit.

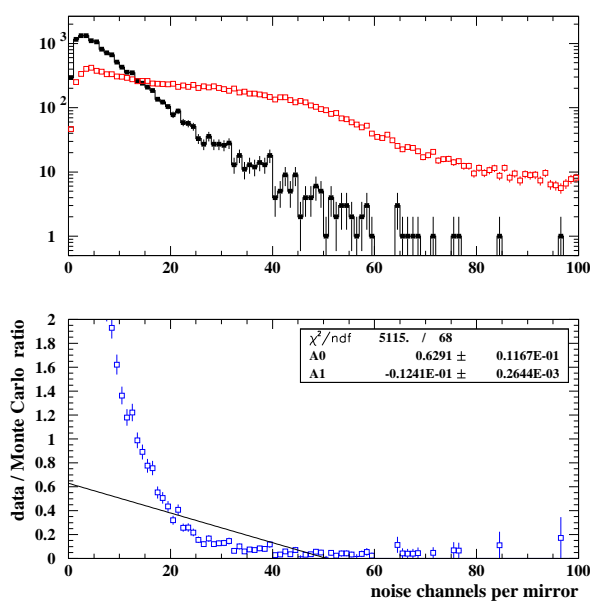


Figure 4.17: top: Distributions of number of noise channels per mirror after our correction. (open squares: MC , filled squares: data) ; bottom: Ratio of data over MC with linear fit.

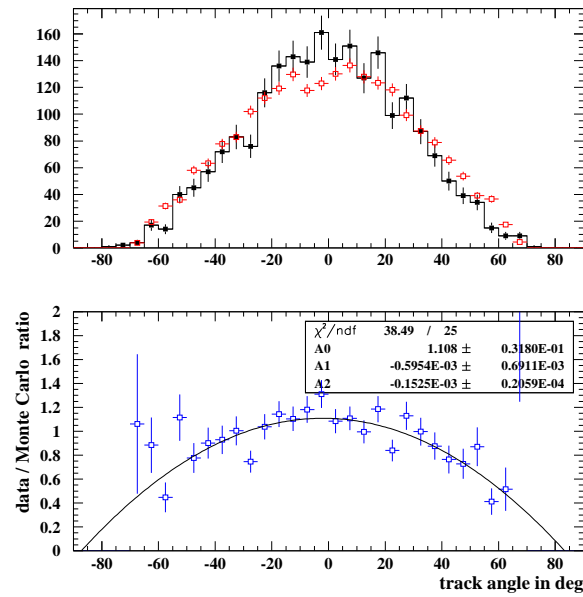


Figure 4.18: top: Distributions of track angles in DS3 with high noise in MC. (open squares: MC , filled squares: data) ; bottom: Ratio of data over MC with quadratic fit.

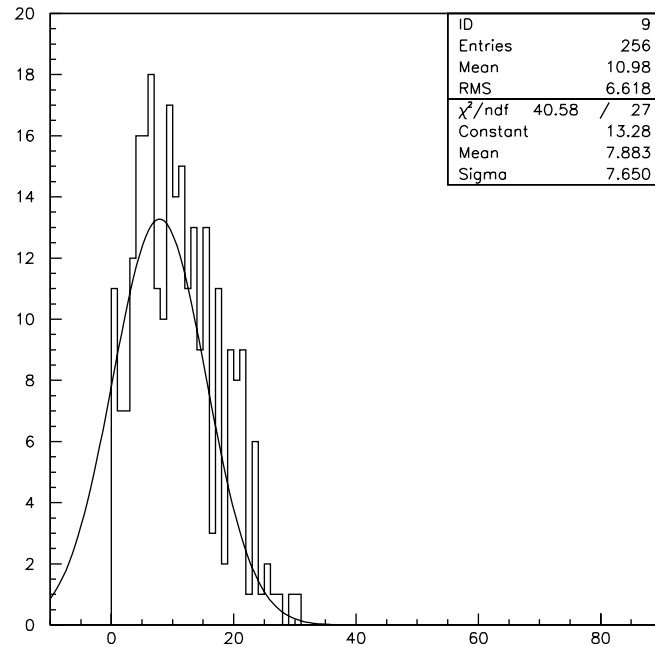


Figure 4.19: Distribution of FADC counts in a single HG channel from a DS3 snapshot. A Gaussian fit has been applied.

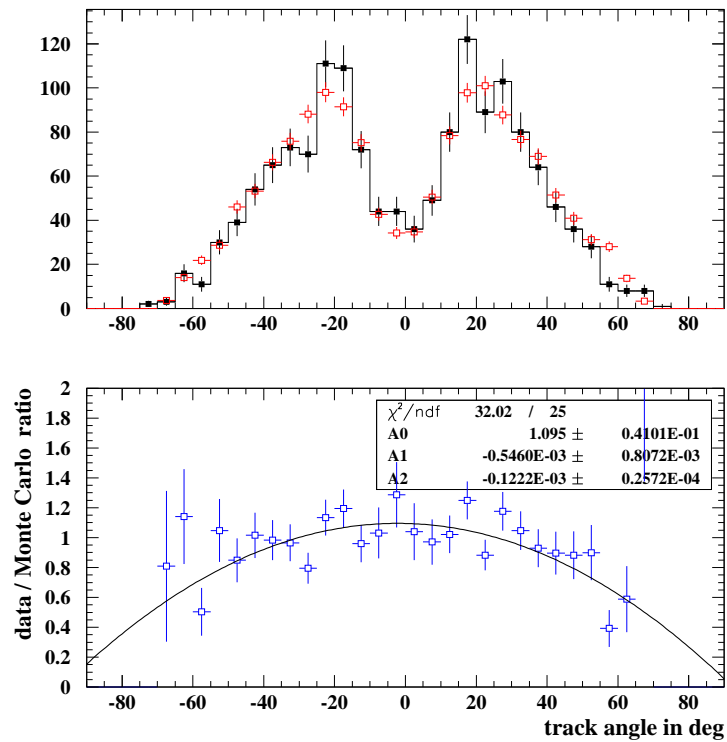


Figure 4.20: top: Distributions of track angles in DS3 after cut on vertical triggers. (open squares: MC , filled squares: data)

bottom: Ratio of data over MC with quadratic fit.

The ratio plot shown here agrees better with a linear fit than the one in Figure 4.18.

The $\chi^2/\text{d.o.f}$ changes from 3.6 to 2.1.

4.4.5 Atmospheric Analysis

Molecular and Aerosol Scattering

Attenuation of fluorescence light on its way from the air shower to the detector is mainly due to aerosol scattering and molecular scattering on the nitrogen and oxygen molecules of the atmosphere.

The **molecular component** can be described by Rayleigh scattering. Molecular scattering is relatively stable, with variations at the 5% level due to temperature and pressure changes with different seasons and weather systems [72]. Three different atmospheric profiles of the U.S. Standard Atmosphere have been included in the MC and the reconstruction routines to correctly simulate the seasonal changes in the atmospheric density. The attenuation of light from a point at height h_1 above surface to a point at height h_2 above surface is described in the MC by the following expression:

$$T_R = \exp \left[- \frac{X_S |(\exp(-h_2/h_R) - \exp(-h_1/h_R))|}{x_R \cos \theta} \cdot \left(\frac{400nm}{\lambda} \right)^4 \right] \quad (4.11)$$

T_R is the transmission factor due to Rayleigh scattering; X_S is the atmospheric depth (in g/cm^2) at the surface from which h_1 and h_2 are measured; θ is the zenith angle between the line connecting the two points and the vertical; h_R is the Rayleigh scale height (7.5 km); x_R is the Rayleigh attenuation length ($2,969.6 \text{ g/cm}^2$); λ is the wavelength in nm. The scattering probability as a function of the scattering angle ϑ , i.e. the phase function, is proportional to $1 + \cos^2(\vartheta)$.

The description of the **aerosol component** is more difficult. The Rayleigh approximation cannot be used in cases where scattering particles are large compared to the wavelength. Exact solutions of the wave equation exist (e.g. Mie's solution for spheres [99]), but extensive numerical calculations are needed to account for enough terms. Aerosols have a wide variety of sizes. Aerosols over the continents and away from urban areas are dominated by dust (70% of volumetric concentration), water soluble aerosols (29%) and soot (1%) [100]. The average sizes of these different aerosol components are of the order of $0.01 \mu\text{m}$ (soot), $0.1 \mu\text{m}$ (water soluble aerosols) and 1

μm (dust grains). The aerosol density of the atmosphere can change over short time scales, and variations in aerosol scattering are much larger than in the molecular case. Attenuation due to aerosols is described by the following model in the MC and reconstruction routines:

$$T_A = \exp \left[-\frac{h_A |(\exp(-(h_2 - h_m)/h_A) - \exp(-(h_1 - h_m)/h_A))|}{x_A f(\lambda) \cos \theta} \right] \quad (4.12)$$

T_A is the transmission factor due to aerosol scattering; h_A and x_A are the aerosol scale height and horizontal attenuation length at ground level, respectively; h_m is the mixing layer thickness; $f(\lambda)$ describes the wavelength dependence of x_A , normalized to 334 nm. h_1 , h_2 and $\cos \theta$ are defined the same way as in the Rayleigh model. The aerosol phase function varies with the type of the aerosol, but is always strongly forward peaked. The model used in our programs was supplied by Jerry Elbert and is shown in Figure 4.21. It has been normalized so that its integral over the solid angle $2\pi \sin \vartheta d\vartheta$ is 1. An a^{-4} particle size distribution was assumed for this model.

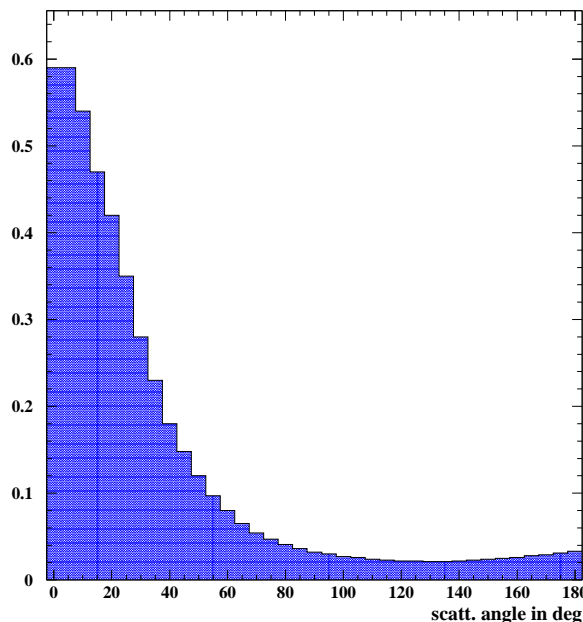


Figure 4.21: Aerosol phase function used in the MC and reconstruction code. The function has been normalized, so that its integral over solid angle equals 1.

The location of the two *HiRes* sites on top of two hills places the detectors above ground fog and low-lying dust. From laser data between fall 1999 and spring 2001, it was found that the bulk of the aerosol distribution is distributed in the lower 1.5 km of the atmosphere [72]. We have analyzed the scattered light signal from steerable lasers in order to determine the vertical aerosol optical depth (VAOD), horizontal aerosol attenuation length (HAL), and the aerosol phase function.

Measurement of Vertical Aerosol Optical Depth

The laser located at the *HiRes-2* site (dubbed “hr2sls”) was used in this analysis for atmospheric measurements. Over the period of data presented here, the polarization of this laser was found to have changed. Its initially circular polarization was seen to have acquired a variable elliptical component. In order to account for changes in the amount of laser light scattered into the *HiRes-1* detector due to this polarization shift, we divided the laser data into several **epochs of constant polarization**. We have determined these epochs by comparing the scattered light profiles from horizontal laser shots that passed the *HiRes-1* detector on its north and south side, i.e. north and south from the connecting line of sight between *HiRes-1* and *HiRes-2*. For a circularly polarized laser and for a uniform detector acceptance over all mirrors, one would expect the ratio of these profiles to be 1. The asymmetry in the polarization could be detected by a sine-wave like dependence of the north over south scattered light ratio versus scattering angle. We have fit sine functions to north over south ratios of all available horizontal laser data. With this method, we have been able to distinguish six different epochs of constant polarization within the time period of this analysis. Figure 4.22 shows the shift from “epoch 3” to “epoch 4” in the summer of 2000: The sine fit to the north over south ratio to laser data from “epoch 4” is shown in the top of the plot. The lower curve is a typical fit to data from “epoch 3”. Differences in the absolute normalizations and in the phases of the sine fits are clearly visible.

Next, we have determined one night with very small aerosol concentration per

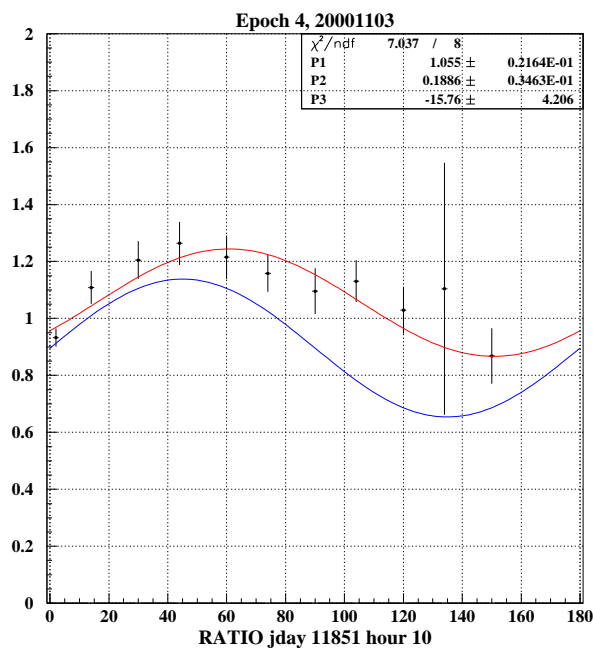


Figure 4.22: Sine fits to north over south ratios of horizontal laser shots used to determine epochs of constant laser polarization. Shown are data points from one hour of a night in “epoch 4”, i.e. ratios of scattered light from the shots north and south from *HiRes-1* versus scattering angle, with a sine fit. A typical sine fit to “epoch 3” data is shown for comparison below.

epoch. For these nights we assumed that light scattering was entirely due to Rayleigh scattering. We found these “Rayleigh nights” by comparing the amount of light from horizontal shots scattered into the forward region (small scattering angles) and into the backward region (large scattering angles). Ideally, one would expect a forward to backward ratio of close to one for pure Rayleigh scattering due to the symmetrical phase function, whereas Mie scattering is strongly forward peaked. This difference can be seen below in Figures 4.25 and 4.26. We have found nights with close to symmetrical scattering profiles in each epoch. These nights were used for **data normalization** of the measured VAODs within each epoch.

Vertical laser shots were used to derive an average VAOD for each hour of available data. If one assumes single scattering and horizontal uniformity of aerosol concentration, the total transmission through aerosols of light crossing the atmosphere at an

elevation angle δ towards the horizontal can be written as [72]:

$$T_A^{tot} = \exp(-\tau_A / \sin \delta) \quad (4.13)$$

Here the VAOD is denoted by τ_A . Since the laser is at a distance of 12.6 km from the detector and the detector unit that was used for this measurement (8 PMTs of mirror 7 of *HiRes-1*) has an elevation angle of about 15° , the light scattered into the detector from the vertical beam originates from far above the aerosol component of the atmosphere. In this case, the VAOD is independent of how aerosols are distributed vertically. Two transmission processes have to be taken into account in the measurement: first, the light from the laser beam crosses the aerosol component vertically from the ground upwards. Part of the light will then be scattered into the detector from above the aerosol layers. This is mainly due to Rayleigh scattering, since aerosol scattering is negligible at this altitude. The scattered light will cross the atmosphere again and reach the detector unit. The ratio of the number of photons that are observed from a single laser shot (N_{obs}) over the expected number assuming a purely molecular atmosphere (N_{mol}) is thus given by:

$$\frac{N_{obs}}{N_{mol}} = \exp \left[-\tau_A \cdot \left(\frac{1}{\sin \delta_1} + \frac{1}{\sin \delta_2} \right) \right] \quad (4.14)$$

δ_1 and δ_2 are the elevation angles of the laser beam (90°) and of the average viewing PMTs in the detector unit ($\sim 15^\circ$).

N_{obs} and N_{mol} are determined from the detected number of p.e. The observed p.e. are first normalized to the recorded laser power in the analysis program, which was written by William Hanlon. The number of p.e. recorded as hourly averages can be seen in Figure 4.23. We then normalized all measurements from each epoch to the N_{mol} photoelectrons given by the selected hour of the ‘‘Rayleigh night’’. With this method, we have measured the VAOD on an hourly basis and corrected for changes in laser polarization with data normalization. The results will be shown below.

For an estimate of the systematic uncertainty of the VAOD measurement using data normalization, two possible sources are quoted in [72]: an uncertainty due to

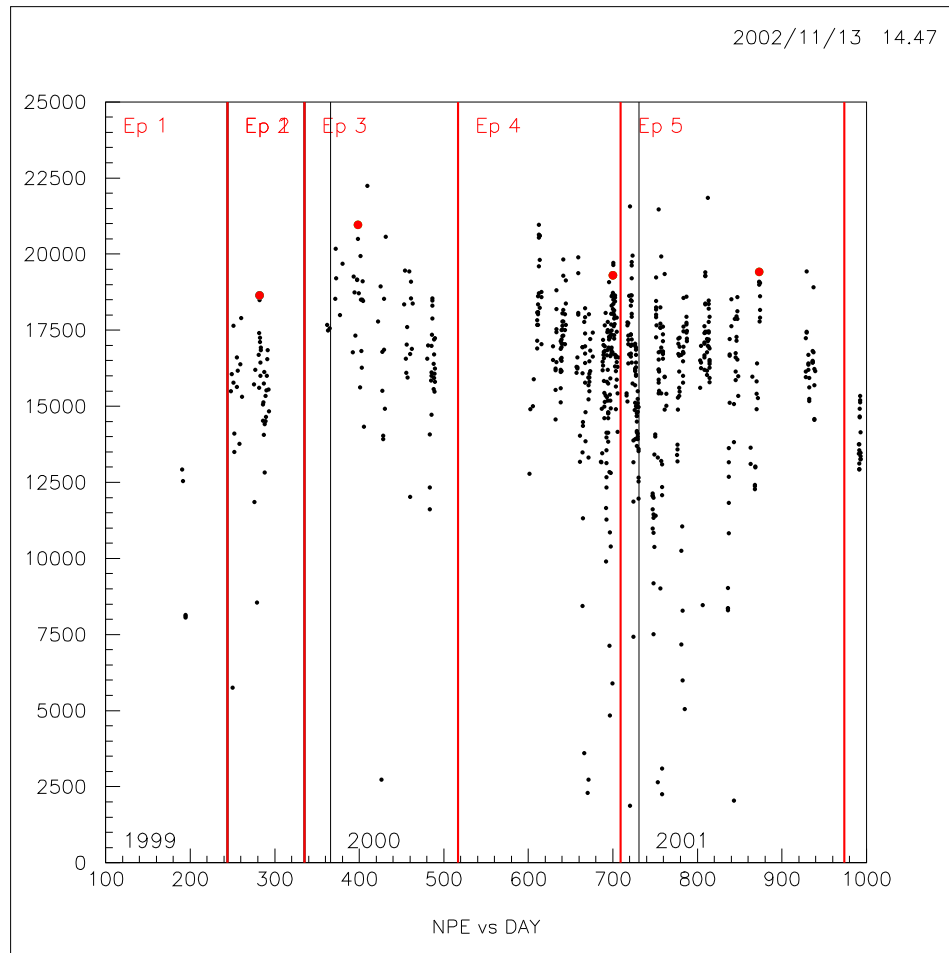


Figure 4.23: Each entry represents the average amount of scattered light, measured in photoelectrons, from observations of vertical laser shots as part of the VAOD measurement. The large dots mark selected hours of “Rayleigh nights” in each polarization epoch. The two thin vertical lines separate the three *HiRes-2* datasets; the thicker lines separate the epochs.

fluctuations in the PMT gains of 5% and an uncertainty in the VAOD of the chosen “Rayleigh nights” of 0.01. A $\pm 5\%$ change in N_{obs} would lead to a change in the measured VAOD of ± 0.01 , according to Equation 4.14. The total uncertainty would thus amount to ± 0.014 . Fluctuations in the uncertainty of the measured laser energies are small and have not been included here. The assumption of a 5% fluctuation in the PMT gains is a very conservative estimate.

Measurement of Aerosol Attenuation Length and Phase Function.

I have analyzed available data from horizontal laser shots (azimuthal angle: 2° north from the *HiRes-1* - *HiRes-2* connecting line of sight, elevation angle: between 0.55° and 0.65°) in order to determine the HAL and the aerosol phase function. Using slight modifications to programs written by Richard Gray, I have fit a model with four parameters to the measured hourly averages of scattered light profiles. The fitting routine simulates the scattering of light from a laser track into the *HiRes-1* detector, using the recorded laser geometry and energy. Attenuation of light in the beam and scattering out of the beam and into the detector due to Rayleigh and Mie processes are simulated, taking into account seasonal changes for Rayleigh scattering. A value of 0.95 was assumed for the aerosol single scattering albedo. The fraction of observed photons over emitted photons (N_{obs}/N_0), taking into account both Rayleigh and Mie scattering, is given by:

$$N_{obs}/N_0 = \exp(-d/\lambda) \quad (4.15)$$

Here d is the distance the photons have traveled through the atmosphere and λ is the combined interaction length, which equals $[\frac{1}{\lambda_{Mie}} + \frac{1}{\lambda_{Rayleigh}}]^{-1}$. The χ^2 between the simulated and the measured light profile is minimized by adjusting the parameters of the model. The fraction of light scattered by the Rayleigh process is kept constant.

The first fit parameter is a fudge factor in the laser power. I allowed the laser power assumed in the program to fluctuate by $\pm 15\%$ around the recorded value, in order to account for uncertainties in the recorded laser energy, and variations in the detector calibration and laser polarization. The HAL is the second parameter that is varied to adjust the simulated profile to the data. The attenuation length is allowed to vary between 1 and 500 km. A parameterization of the aerosol phase function contributes two more independent parameters to the fit. I describe the phase function in the following form:

$$\exp(-B\vartheta) + C \cdot \exp(+B\vartheta) \quad (4.16)$$

Its normalization is given by the amount of scattered light determined in the simulation. I have found that using only a single parameter B in both exponentials does not affect the quality of the fits. Before the fit, the phase function parameters are set to initial values that have been suggested by Longtin [101] ($B = 2.141$, $C = 0.0001$) for an average description of the desert atmosphere.

The above parameterization of the aerosol phase function has been tested against numerical calculations based on Mie theory [100]. I have found that the form of the phase function in Equation 4.16 fits the calculated profiles for dust, water soluble aerosols and soot (all assuming asymmetric particles) very well for ϑ between 30° and 150° , which is the range of scattering angles observed with the horizontal laser shots in this analysis. From these fits, I have determined loose lower and upper limits for the B parameter ($1.8 < B < 4.0$). Introducing these limits has improved the fits by avoiding unrealistic shapes of the aerosol phase function. The fits to the numerically calculated phase functions also revealed a problem in the forward scattering region. In the case of dust and water soluble aerosols, the fits that described the phase function well between 30° and 150° underestimated the amount of scattered light for the smallest scattering angles. Figure 4.24 shows the calculated phase function with arbitrary normalization, multiplied by $\sin \vartheta$ to indicate the relative amount of scattered light per solid angle. A fit to the phase function for scattering angles in the above mentioned range has been extended down to 0° and up to 180° , and also multiplied by $\sin \vartheta$. A difference of roughly 23% can be seen between the calculated amount of scattered light and the amount given by the fit, due to the discrepancy in the forward scattering region. The difference is about 21% for water soluble aerosols. I have added a correction to the normalization of the phase function in the fitting routine to account for this deficit, which has improved the quality of the fits.

Examples of two fits to horizontal laser data are shown in Figures 4.25 and 4.26 for a very clear night and a night with high aerosol contribution, respectively. The best fit values for the HAL were 192 km for the clear and 15 km for the “dirty” night.

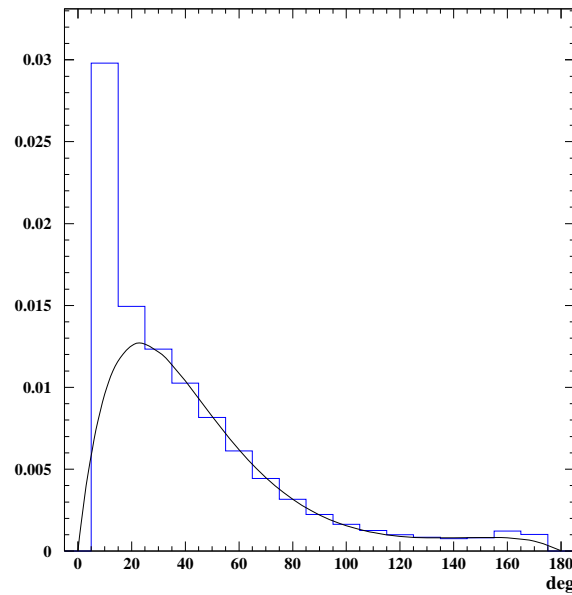


Figure 4.24: The histogram shows the numerically calculated phase function for dust aerosol scattering, multiplied by $\sin \vartheta$. A fit has been applied to the distribution for $30^\circ < \vartheta < 150^\circ$, extended to 0° and 180° , and multiplied by $\sin \vartheta$. A deficit in the normalization of the fit function of about 23% can be seen in the forward scattering region.

I have compared the absolute amount of detected light with the results of the HAL from the fitting routine. Since the phase function is relatively constant at scattering angles around 100° , the average number of detected photons between 100° and 110° were chosen as a measure of the total detected amount of light. A clear correlation with the attenuation lengths can be seen in Figure 4.27. This correlation is now used to determine the initial value of the HAL at the beginning of the fitting routines.

In order to estimate the systematic uncertainty of the HAL measurements, I have varied the limits on the laser fudge factor, the limits on the parameters in the phase function, and the correction factor of the phase function normalization. The HAL values from the fits remained stable to within roughly $\pm 10\%$. For nights with very little aerosol, the uncertainty in the HAL value is larger, but it affects the reconstructed energies much less.

Atmospheric Database

The hourly measurements of VAOD and HAL have been combined into a single atmospheric database. I have matched the hours of the VAOD and HAL databases for each included night and applied a cut on the χ^2 of the fits to the horizontal laser shots. VAOD values were set to 0.001, if they were smaller than this threshold. VAOD values larger than 0.2 were not included. HAL was set to 150 km where it exceeded that number. For HAL values this large, the light attenuation cannot be clearly distinguished from pure Rayleigh scattering.

Since the MC and reconstruction programs use the HAL and aerosol scale height for a description of the aerosol component, as noted above in Equation 4.12, a pseudo scale height h_p was calculated from the measured HAL (denoted by x_A) and VAOD using the relation:

$$h_p = \tau_A \cdot x_A \quad (4.17)$$

One finds this relation by setting h_2 in Equation 4.12 to 0 and by letting h_1 go to infinity, i.e. a height far above the aerosol layers of the atmosphere. A comparison with Equation 4.13 leads then to the above relation. In our description of the aerosol component, we assume the mixing layer thickness to be equal 0, which has proven to best fit our measurements.

The $1/\text{HAL}$ and VAOD distributions for selected clear nights that went into the *HiRes-2* analysis are shown in Figures 4.28, 4.29 and 4.30, divided into DS1, DS2 and DS3. In the database generated with this atmospheric analysis, HAL and VAOD values are available for 29 out of the 45 nights of DS1, 35 out of the 44 nights of DS2, and 18 out of the 33 nights of DS3. In the remaining nights, where measurements of both parameters were not available or were removed by cuts in the analysis, averages for each dataset were used for the systematics studies that will be presented in Chapter 8.

The combined results for all three datasets are shown in Figure 4.31 for all selected clear nights and in figure 4.32 for all nights included in the atmospheric database.

The averages for the three datasets found in this analysis represent a slightly clearer atmosphere than the values used in the *HiRes-1* and *HiRes-2* analyses ($\langle \text{HAL} \rangle = 25$ km and $\langle \text{VAOD} \rangle = 0.04$) [72], which were provided by Lawrence Wiencke and Mike Roberts, who carried out all the atmospheric measurements. This difference is due to the data normalization method applied here, which was not used in the original analysis. The averages determined in this atmospheric analysis ($\langle \text{HAL} \rangle = 27$ km and $\langle \text{VAOD} \rangle = 0.035$) are nevertheless well within the quoted uncertainties on the average used in the analysis.

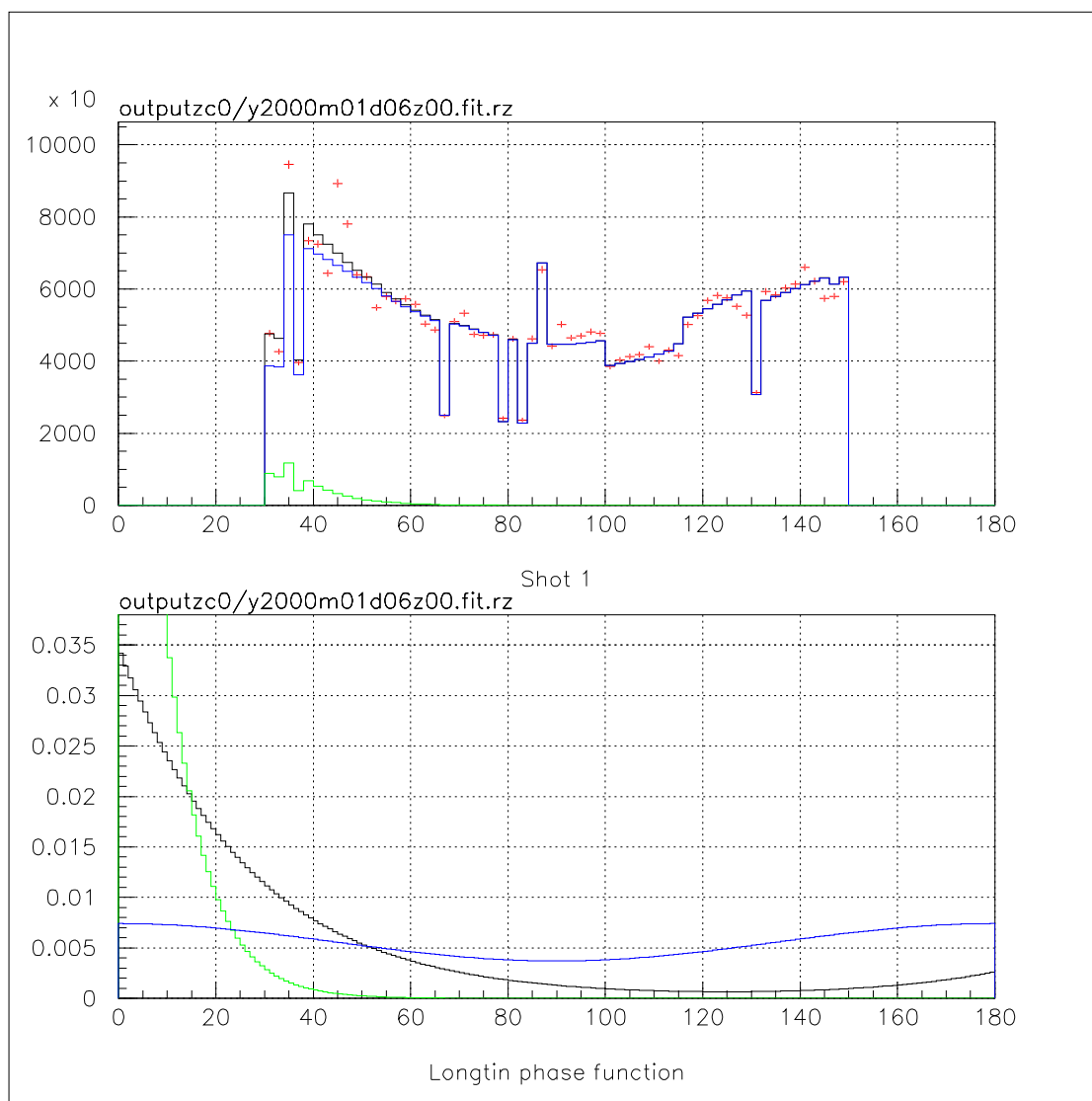


Figure 4.25: Horizontal laser profile in a night with small aerosol concentration. top panel: Scattered light from a horizontal shot, averaged over one hour (data points), versus scattering angle. The topmost histogram on the left edge shows the total simulated light profile, the other two represent the aerosol component (lowest histogram) and the Rayleigh component. bottom panel: Phase functions for Rayleigh scattering (symmetrical), fitted phase function for aerosol scattering (topmost on the left edge) and Longtin's phase function for comparison.

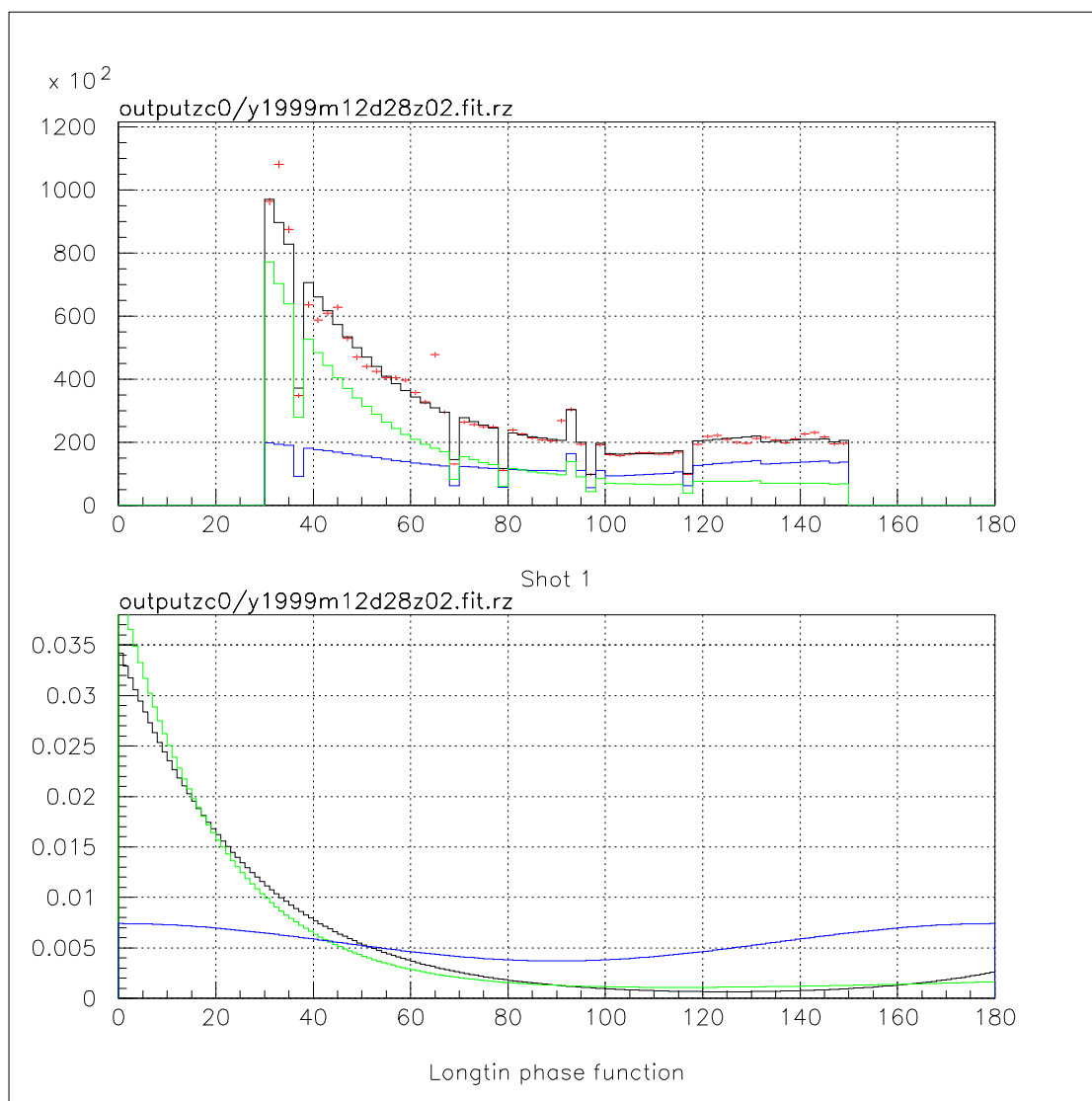


Figure 4.26: Horizontal laser profile in a night with large aerosol concentration. top panel: Scattered light from a horizontal shot, averaged over one hour (data points), versus scattering angle. The topmost histogram shows the total simulated light profile, the other two represent the aerosol component (large forward peak) and the Rayleigh component (close to symmetrical). bottom panel: Phase functions for Rayleigh scattering (symmetrical), fitted phase function for aerosol scattering (topmost on the left edge) and Longtin's phase function for comparison.

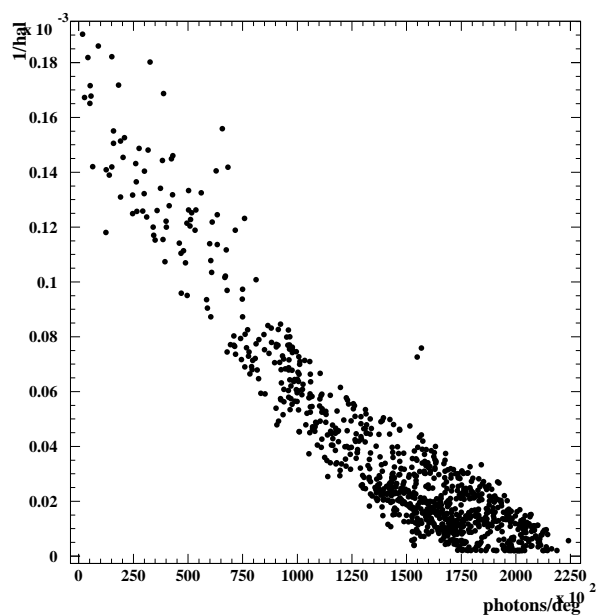


Figure 4.27: Correlation between the inverse aerosol attenuation length from the fitting routine and the amount of recorded light, i.e. the average number of detected photons per degree between 100° and 110° . Each entry is the average of one hour of laser shots.

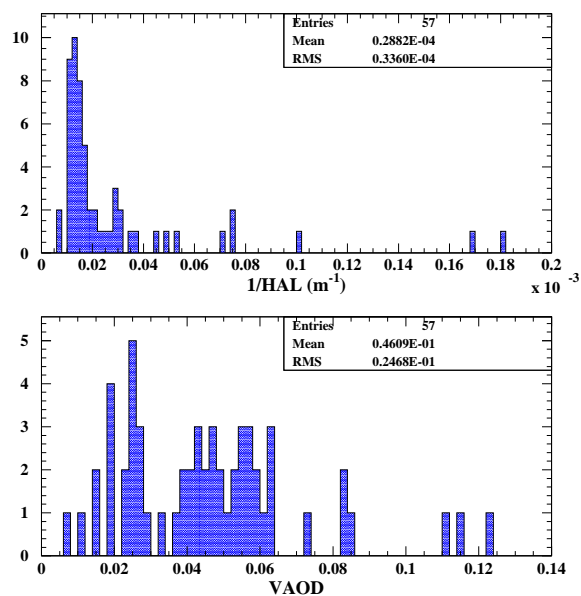


Figure 4.28: Hourly VAOD and inverse HAL measurements for DS1 nights (12/'99 - 05/'00).

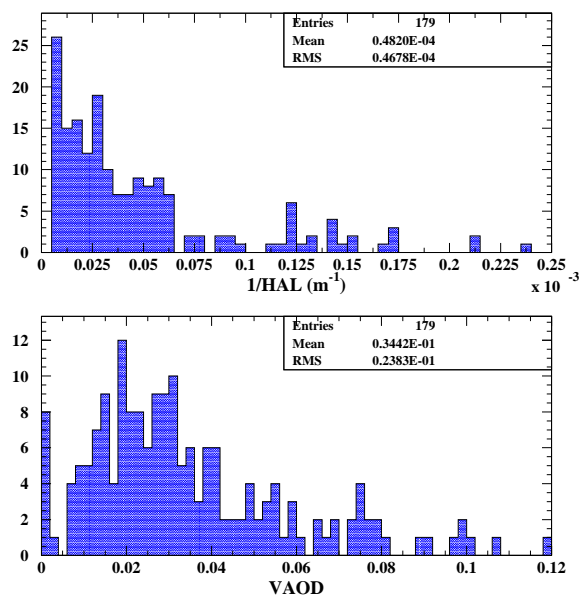


Figure 4.29: Hourly VAOD and inverse HAL measurements for DS2 nights (09/'00 - 03/'01).

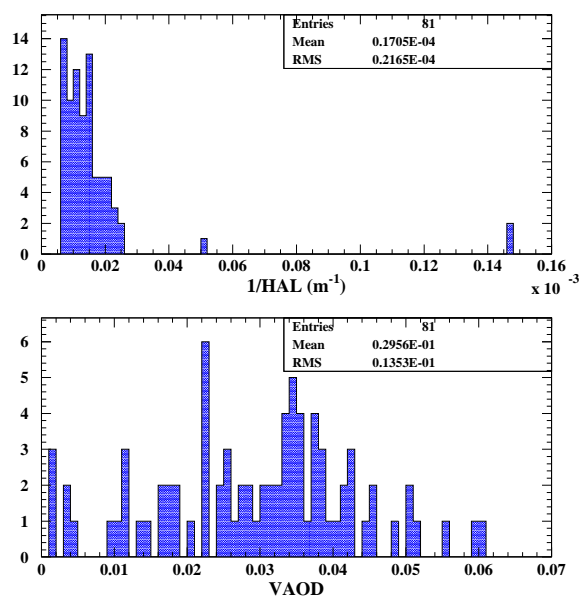


Figure 4.30: Hourly VAOD and inverse HAL measurements for DS3 nights (03/'01 - 09/'01).

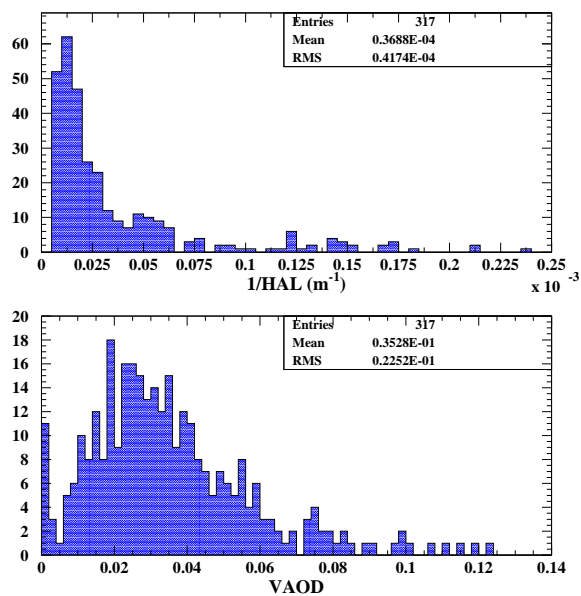


Figure 4.31: Hourly VAOD and inverse HAL measurements for all three datasets (12/'99 - 09/'01).

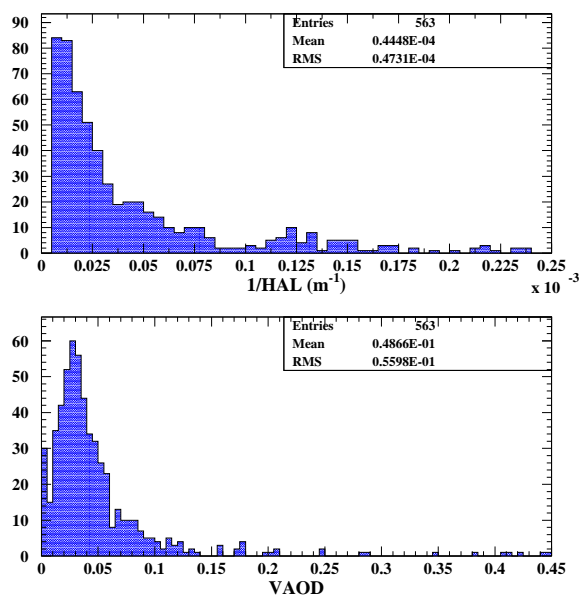


Figure 4.32: Hourly VAOD and inverse HAL measurements for all nights included in the atmospheric database.

Chapter 5

Event Reconstruction & Analysis

5.1 Reconstruction of the Shower Geometry

The analysis of a cosmic ray event — simulated or real — begins with the reconstruction of the air shower geometry. An illustration of the geometry of the EAS with respect to the detector can be seen in Figure 5.1. The shower-detector plane is determined by a fit to the track of illuminated PMTs. The geometry of the shower axis within this plane, i.e. the ψ -angle and distance R_p between shower axis and detector, can be derived from the timing information recorded together with the light signal from the shower. The reconstruction programs used in the *HiRes-2* analysis were written by Douglas Bergman.

A program called “rufpln” determines the shower geometry. It reads the *frawl* banks and *frgl* banks of each event and writes the reconstructed events into four different streams: downward going events, i.e. cosmic ray showers; upward going events, which are usually laser tracks and flashers; close to horizontal tracks, mostly from lasers; noise events, which were not reconstructible. The first step in the geometry reconstruction is the search for a cluster of triggered PMTs, which are in close proximity to each other. This cluster serves as a seed, to which more PMTs are added if they are nearby in space and time. A shower-detector plane is then fit to the track of PMTs marked as “good” in this pattern recognition procedure. The normal vector on the shower-detector plane is varied using *MINUIT* [102] so that the distances of “good” PMTs perpendicular to the plane, weighted by the number of p.e., are minimized. PMTs that are too far away from the fit plane are removed, and the fit can be

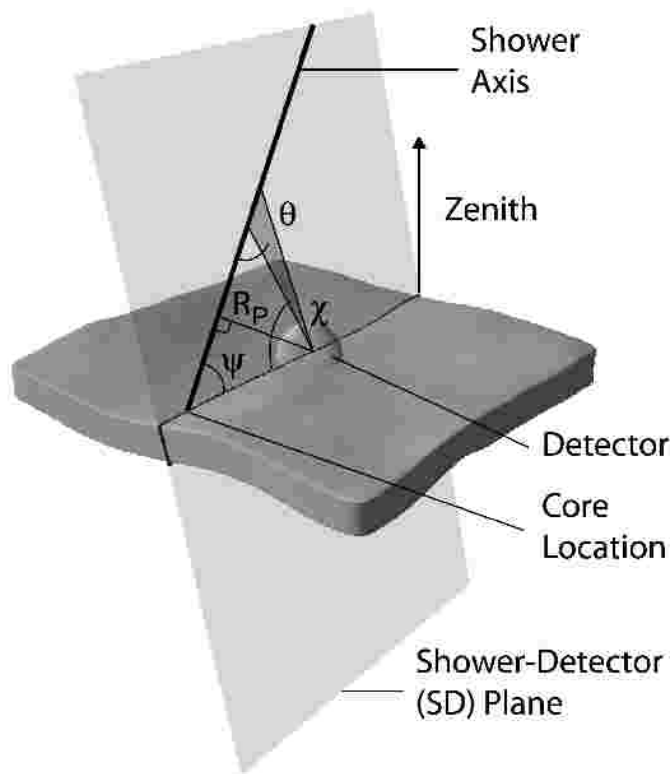


Figure 5.1: Geometry of the shower-detector plane.

repeated. A linear fit is applied to the pulse times of PMTs versus their angles along the track, within 5° of each “good” PMT. PMTs that are too far off in time are removed and the plane is re-fitted in an iterative procedure.

An example of a plane fit is shown in Figure 5.2. The PMT triggered by a shower observed in mirrors 16 and 15 of ring 2 and mirrors 21 and 20 of ring 1 can be seen as colored pixels with a line fit through the track. The change in colors represents the change in trigger times. The black pixels are recorded p.e. that have been identified as background noise. This event was observed on November 2nd, 2000. It was reconstructed at an energy of 1.18×10^{18} eV, at a distance R_p of 8,789.5 m and under a ψ -angle of 97.6° .

The results of the fit to the shower-detector plane are stored in the *rufpln* DST bank, summarized below in Table 5.1.

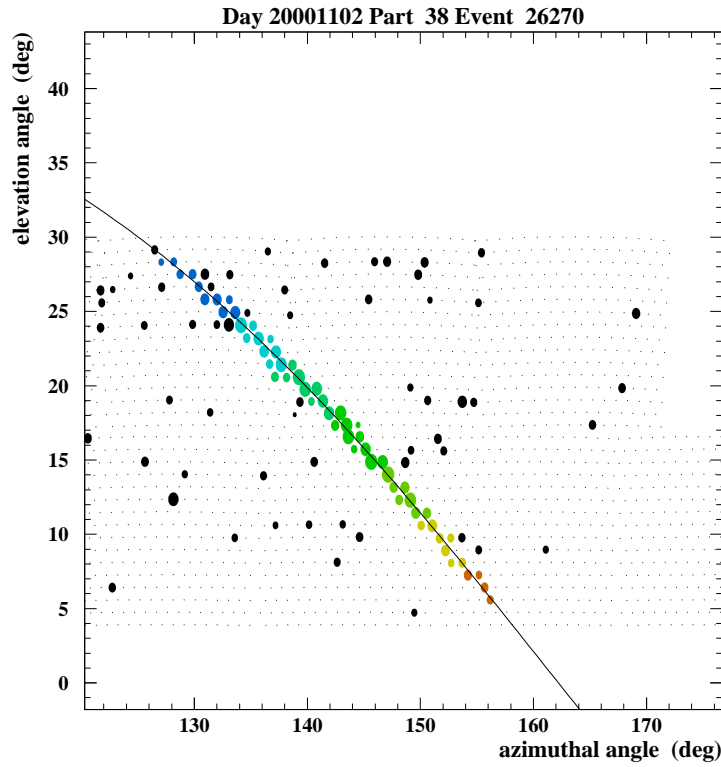


Figure 5.2: Fit to the track of an event. Colored pixels are “good” PMTs at different trigger times, fit to a line. Small dots give the locations of all PMTs. Black pixels are background noise triggers. The size of the pixels is proportional to the number of recorded p.e.

Next, a global fit of the PMTs’ pulse times versus their angles along the track is applied. In a first approximation, a linear fit is applied, followed by a “pseudo-tangent” fit with the ψ -angle set to 90° . PMTs that are too far off from the fits are removed. Finally, a three parameter tangent fit is applied to determine the full geometry of the air shower. The fit equation can be derived from Figure 5.1: The time difference between the arrival time t_i of the light signal from the shaded angle θ_i at the detector and the time t_0 it takes the shower to evolve to the point of closest approach (the intersection with the vector of length R_p), is given by:

$$t_i - t_0 = \frac{R_p}{c \cdot \sin \theta_i} - \frac{R_p}{c \cdot \tan \theta_i} \quad (5.1)$$

header:
date and time of the event number of mirrors number of triggered HG channels number of “good” HG channels normal vector to shower-detector plane error matrix to normal vector angular extent of track time extent of track
for each triggered HG channel:
mirror index PMT index number of p.e. flag for “good” / noise tubes flag for saturated tubes altitude and azimuth of the PMT alt. and azim. wrt. fit plane slope of local time versus angle fit

Table 5.1: Main entries in the *rufpln* bank.

This holds in the limit where the shower develops almost with the speed of light, denoted by c . With $(1 - \cos \alpha) / \sin \alpha = \tan(\alpha/2)$, it follows:

$$t_i = t_0 + \frac{R_p}{c} \tan\left(\frac{\pi - \psi - \chi_i}{2}\right) \quad (5.2)$$

This relation between the time of the light signal from a shower segment t_i and the viewing angle χ_i of that segment is used in the three parameter tangent fit. The χ^2 of this fit is minimized in an iterative procedure, in which PMTs can be added or removed and the initial plane can be re-fit. The best values for the three fit parameters, R_p , ψ and t_0 , are written out into the *ruffit* bank, summarized in Table 5.2.

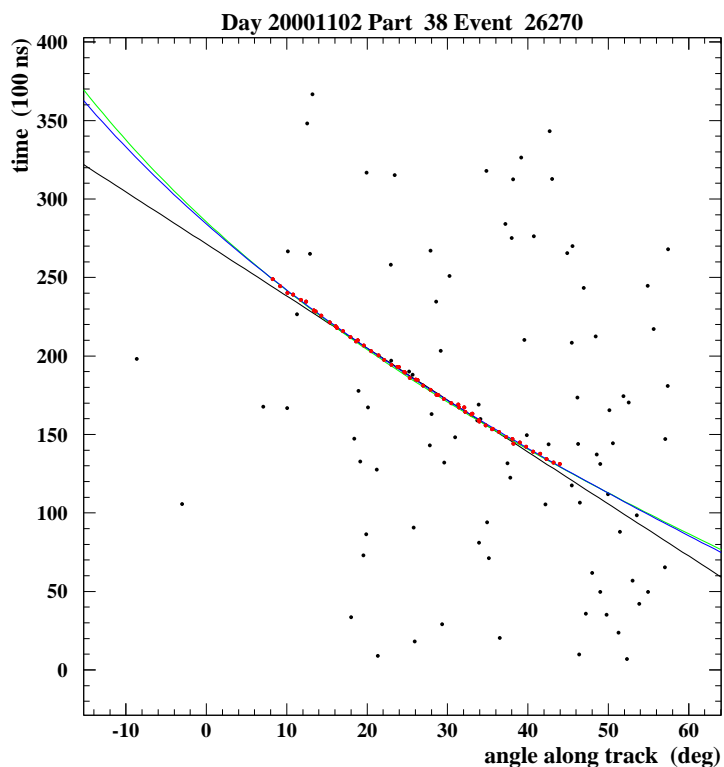


Figure 5.3: Time versus angle fit of an event. The linear fit (straight line) and tangent fit (curved line) to the “good” tubes (colored pixels along the lines) is shown. Black pixels are noise hits.

header:
linear fit slope and intercept errors and χ^2 of linear fit
pseudo tangent fit R_p and t_0 errors and χ^2 of pseudo tangent fit
tangent fit R_p , ψ and t_0 errors and χ^2 of tangent fit
for each triggered HG channel:
residual and χ^2 wrt linear fit
residual and χ^2 wrt linear fit
residual and χ^2 wrt linear fit

Table 5.2: Main entries in the *rufitf* bank.

5.2 Reconstruction of Shower Profile and Energy

The shower profile reconstruction is achieved with a program called “ruspgf”, which uses the “rufpln” output files as input. The charged particle profile of the shower is reconstructed using the now known shower geometry. The total calorimetric energy is then determined from a Gaisser-Hillas fit to the profile.

“ruspgf” starts with a scan over ψ -angles in 1° intervals. For each ψ -angle, it determines R_p and t_0 from a linear fit to the pulse times of the “good” tubes in the *rufpln* bank. The χ^2 of each fit is stored. The R_p , t_0 and ψ values for the best χ^2 are written out into the *ruspgf* bank, described below. This more careful fitting method yields better results for the reconstructed shower geometry than the time fit in “rufpln”.

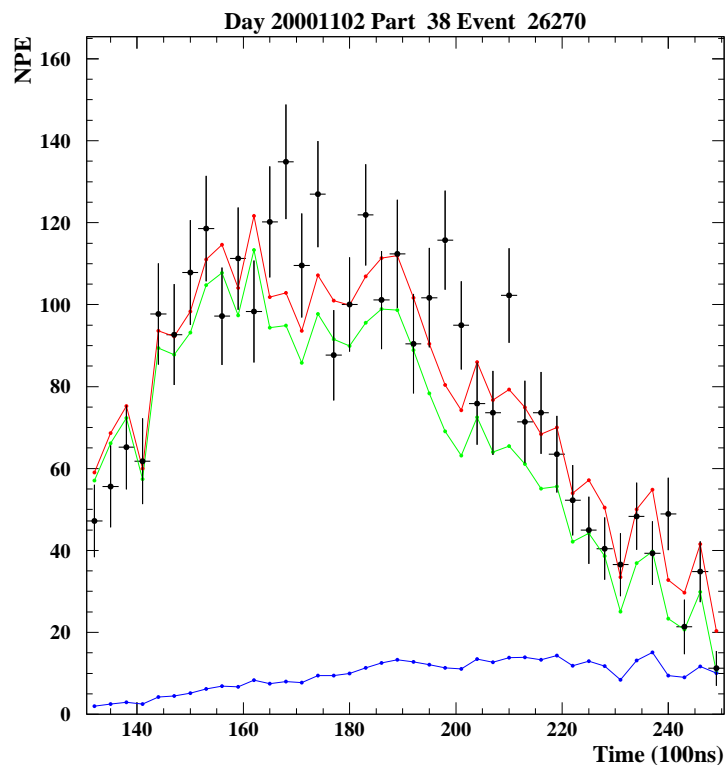


Figure 5.4: Reconstructed photoelectron distribution of an event. The recorded number of p.e. is shown (data points), together with the total reconstructed p.e. distribution (upper curve), the distribution of fluorescence p.e. (middle curve) and the Čerenkov contribution (lower curve).

Next, the program determines the shower profile for the geometry given by each ψ -angle in a second scan. The recorded p.e. in “good” tubes are binned in time bins, propagated back through the atmosphere to the location of the shower and converted into an electron distribution along the shower. With a given shower profile, the amount of Čerenkov light that is generated along the shower can be calculated numerically. In an iterative procedure, Čerenkov light is then subtracted from the recorded p.e. signal. The routines that handle generation and propagation of fluorescence and Čerenkov light have all been adopted from the MC package and are used to model the MC process in reverse — from the recorded signal to the shower. A PMT acceptance is calculated with the ray tracing routines from the MC. The same atmospheric database can be used in the MC and in the event reconstruction. In this analysis, the average values measured for HAL and VAOD were applied. The final distributions of reconstructed p.e., separated into p.e. from Čerenkov light and fluorescence light, are shown in Figure 5.4 for the event from November 2nd.

With the given shower geometry, the time bins can be converted into bins of atmospheric slant depth. For each assumed ψ -angle of the shower axis, a Gaisser-Hillas function of the form described in Equation 4.6 is then fit to the reconstructed profile of electrons. In these fits, the X_0 and λ parameters are set to fixed values, -60. and 70., respectively. The χ^2 for each profile fit is stored, together with the results for N_{max} and X_{max} . The best fit to the event from November 2nd is shown in Figure 5.5.

Finally, the stored χ^2 values from both the time fit and the profile fit are searched for a combined minimum χ^2 to determine the best ψ -value. The calorimetric energy of the shower is calculated from an integral over the Gaisser-Hillas fit to the profile at the best ψ , multiplied by the ionization loss rate. A mean ionization loss rate per particle of 2.19 MeV/(g/cm²), determined from *CORSIKA* simulations by Song et al. [95], has been assumed in this analysis. The main output of “ruspgf” is shown below in Table 5.3.

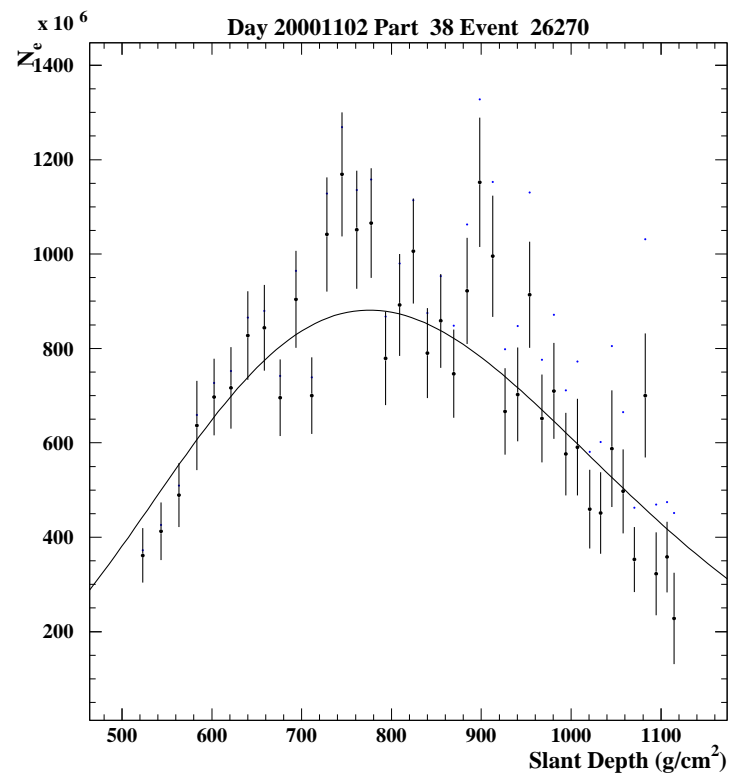


Figure 5.5: Gaisser-Hillas fit to the particle profile of an event. The points without error bars show the reconstructed profile before Čerenkov light subtraction.

header:
number of time bins
number of FADC slices per time bin
best values for R_p , ψ and t_0
errors on R_p , ψ and t_0
Gaisser-Hillas fit parameters N_{max} and X_{max}
errors on N_{max} and X_{max}
time fit χ^2
Gaisser-Hillas fit χ^2
calorimetric energy
error in calorimetric energy
for each time slice:
total number of p.e.
number of fluorescence p.e.
number of Čerenkov p.e.
atmospheric depth in (g/cm ²)
number of electrons
G.-H. fit residuals and χ^2 of time slice

Table 5.3: Main entries in the *ruspgf* bank.

5.3 Calibration Correction

Problems with the PMT calibration of the *HiRes-2* detector, caused by limited access to Dugway Proving Ground, made it necessary to introduce a correction into this analysis. The calibration correction was derived from a direct comparison of reconstructed energies of events seen by both detectors simultaneously.

In the “tandem” reconstruction, simulation and reconstruction programs from the *HiRes-1* and *HiRes-2* mono analyses are used in combination to analyze stereo events. The geometry of the shower axis is determined from the intersection of the two reconstructed shower-detector planes. This is illustrated in Figure 5.6.

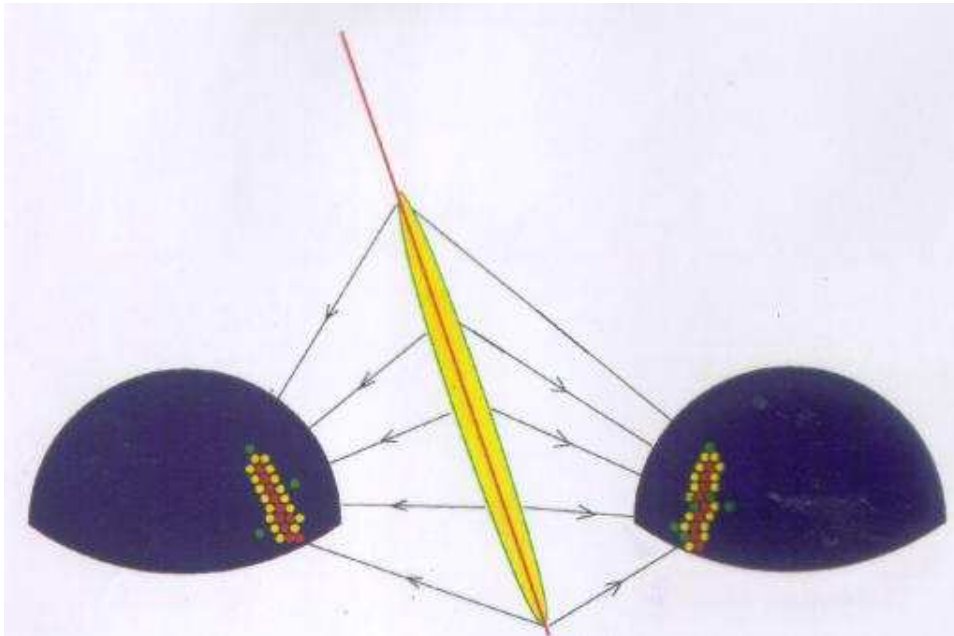


Figure 5.6: Illustration of stereoscopic event detection. The two shower-detector planes (indicated by arrows), intersect in the location of the shower axis.

After the geometry reconstruction, the energies of the stereo events are reconstructed separately from the signals seen in the two detectors. The ratios of the two energy estimates for stereo events are shown in Figure 5.7. Energy ratios have been determined for each *HiRes-2* dataset separately. The *HiRes-2* energy estimates of stereo events are systematically lower than the *HiRes-1* estimates. The shift in the mean of

Gaussian fits to the ratios is -22% for DS1, -11% for DS2 and -5% for DS3.

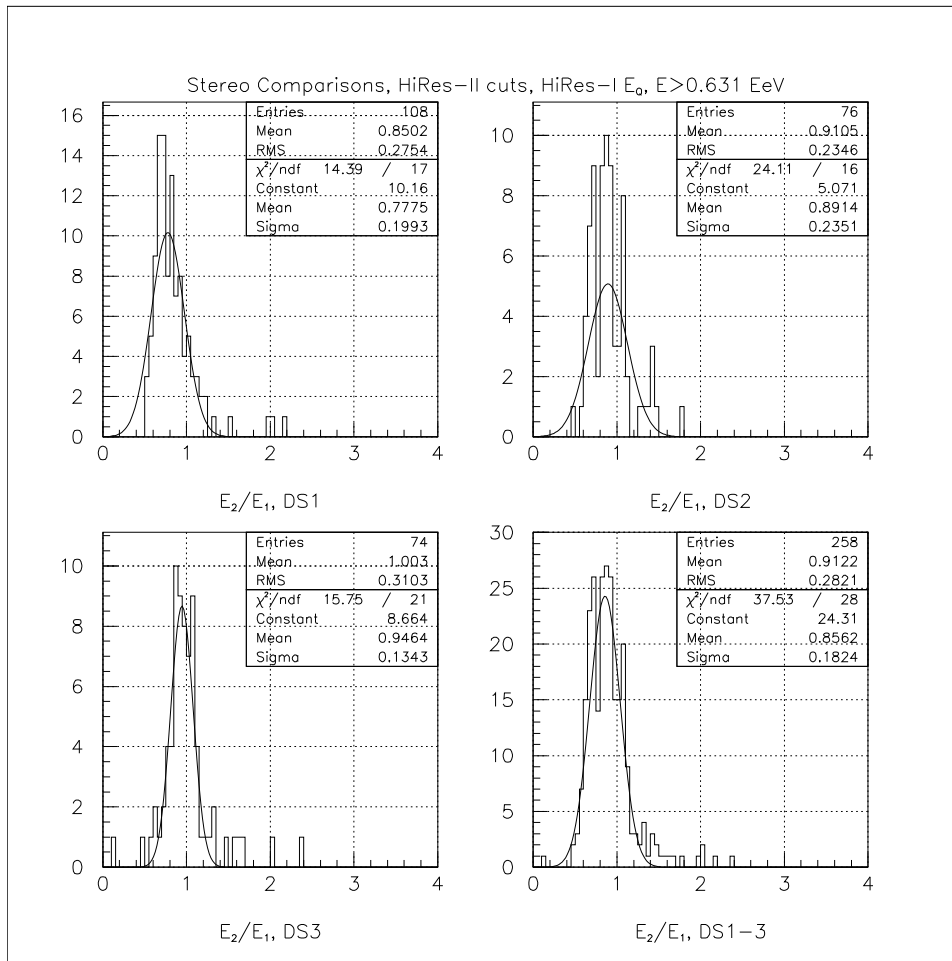


Figure 5.7: Ratio of HiRes-2 over HiRes-1 energy estimates for stereo events.

The measured differences have been used in “ruspgf” to correct the conversion from FADC counts to p.e. so that the reconstructed energies agree with the *HiRes-1* calibration. (For DS1 I have used a correction of only 21%, based on an earlier, rougher estimate.)

I have added an inverse correction to the conversion between p.e. and FADC counts in the MC routines to simulate the offset seen in the calibration of the *HiRes-2* data. Since the simulated noise p.e. are taken from the data, noise in the MC had to be excluded from this inverse correction. Both data and MC events are reconstructed with the same corrected “ruspgf” program. The boost of the number of p.e. per FADC count

in the reconstruction program increases the energies of data events to match the *HiRes-1* energy scale, while the MC energies are unchanged due to the inverse correction in the simulation programs.

5.4 Analysis Programs

The reconstructed MC and data events are analyzed with a program called “dsthist”, which is using *HBOOK* [103] routines to write out entries from the various DST banks into histograms. Parameters describing the event geometry, energy, profile, etc. are histogrammed at different cut levels (see next chapter). In this way, statistical distributions of event parameters as well as characteristics of single events can be studied in detail. A set of comparisons between data histograms and MC histograms will be shown in Chapter 7.

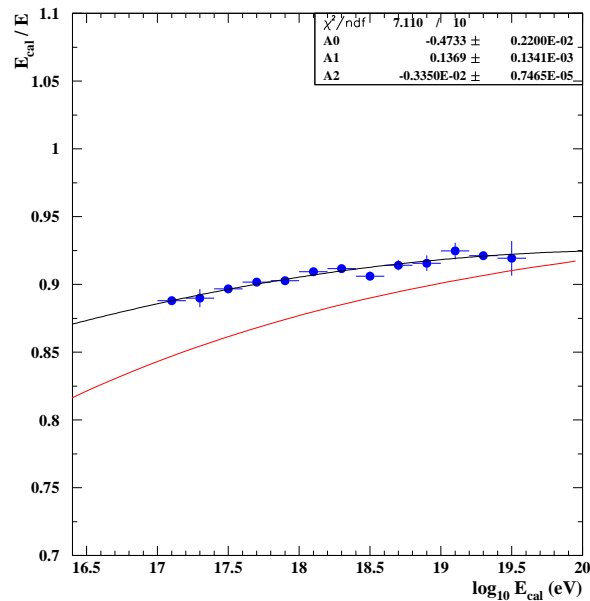


Figure 5.8: Correction for “missing energy”. The ratio of calorimetric energy over total energy versus the calorimetric energy is shown for MC events accepted in the detector response simulation. The quadratic fit to the points is used as “missing energy” correction. The line below the points is the result from Song et al. [95] for an average composition.

I have added a correction for “missing energy” to the reconstructed calorimetric energy from “ruspgf” in the analysis program in order to determine the total energy of the primary cosmic rays. The “missing energy” has been calculated from a set of MC events: For each event that was accepted in the detector response simulation, I wrote out its true (input) energy and its scaled Gaisser-Hillas parameters, which already include a correction for the *CORSIKA* energy cut-off. The calorimetric energy of the event was determined from the Gaisser-Hillas parameterization and compared to its true energy. The result is shown in Figure 5.8.

A quadratic fit to the ratio of calorimetric over true energies is used in the analysis programs to correct for the “missing energy”. The correction determined with this method is a few percent larger than the result by Song et al. [95], who calculated a correction for a mixed composition with 50% iron and 50% proton showers. Since the method presented here takes the acceptance of the detector and the actual, measured composition into account, the estimated correction is closer to the correction for pure proton showers.

After the same “missing energy” correction has been applied to both data and MC events, histograms with the total energy distributions can be generated, which are used in the calculation of the energy spectrum. For the acceptance calculation, histograms with the energy distribution of all generated MC events are taken from the MC output stream. Final results of these calculations will be presented in Chapter 8.

Chapter 6

Data Cuts & Resolution

6.1 Cuts & Data Statistics

Several cuts have been applied to the recorded data to improve the quality of the final data selection that is used for the spectrum calculation. Cuts have been chosen with regard to improvements in the resolution of the event geometries and energies. I have used MC simulations for resolution estimates. All cuts described here have been applied to data and MC events simultaneously, except for the cut on laser shots and the weather cut, since neither laser tracks nor weather conditions are simulated in the MC.

Before the process of event reconstruction, I applied a **weather cut** to all *HiRes-2* data, based on information recorded in the nightly log by the *HiRes-1* operators. This information consists mainly of a weather code, which is reported once per hour and indicates low-lying cloud coverage in all four directions, overhead cloud coverage, and haze. Additionally to the code, comments by the operators in the log concerning the weather were used in deciding whether a night should be included in the final datasets or not. Only nights that were indicated as mostly cloudless passed this cut. Other than in the *HiRes-1* analysis, which was carried out by Benjamin Stokes, nights were only included as a whole in this analysis, not divided into data parts. Out of the 246 nights between December 1st, 1999, and September 30th, 2001, on which the *HiRes-2* detector was operated (excluding test-runs), 122 nights passed the weather cut and were included in the three datasets. The analysis of atmospheric data for the selected nights, presented in Chapter 4, showed that the atmosphere was indeed very clear during the “good” nights.

All events caused by vertical flashers and most events caused by lasers are taken out of the data stream in “rufpln”. The remaining laser events are cut out in the analysis program “dsthist”, based on their characteristic time stamp. (Lasers are always fired at the same fraction of a second.) A set of minimal cuts is applied in the two reconstruction programs in order to exclude events that are not fully reconstructible. Since cuts on data always present a compromise between requirements on quality and statistics, three consecutive levels of cuts have been implemented in the analysis program to allow a great variety of data-MC comparisons.

The **first cut level** requires a minimum number of recorded p.e. per degree of track and a minimum number of “good” tubes to exclude events with very weak signals. A cut is applied on the “pseudo-distance”, which is a distance estimate based on the inverse angular speed of the shower, as it crosses the field of view. The angular shower speed is determined from the linear time fit in “rufpln”. A requirement of minimum pseudo-distance and of minimum track length is used to exclude blasts of direct Čerenkov light and to increase the quality of the geometry reconstruction. The resolution in the ψ -angle is improved with a first cut on the recorded error in the reconstructed ψ . Upper limits for the zenith angle and shower-detector plane angle of an event exclude events with pathological reconstructed geometries.

A **cut on trigger sums** has been added only for events in DS3 (and in the matching MC set) in order to avoid problems with noise assisted triggers in the absence of solid background noise measurements. This cut requires at least one mirror per event with more than two three-fold coincidences in the vertical trigger sums. Nearly vertical tracks with weak signals are effectively excluded, which has led to a reduction in the number of finally selected events by 26%.

At the **second cut level**, events are excluded based on the $\chi^2/\text{d.o.f.}$ of the three parameter time tangent fit and the Gaisser-Hillas fit to the shower profile. A loose cut on the average fraction of Čerenkov light in the event, determined iteratively in “ruspgf”, extracts remaining “Čerenkov blasts”. These fits have proven to result in a

better energy resolution in MC studies.

1st level of cuts		
CUT APPLIED TO:	LOWER LIMIT:	UPPER LIMIT:
weather conditions reported in log	/	/
laser shots	/	/
trigger sums in DS3	3 vert. coinc.	/
pseudo-distance	1.5 km	/
length of track (all events)	7.0°	/
length of track (events with only ring-2 mirrors)	10.0°	/
number of “good” tubes	6	/
number of p.e. per degree of track	25.	/
shower-detector plane angle	/	80.
zenith angle	/	80.
error in ψ -angle	/	36°
2nd level of cuts		
CUT APPLIED TO:	LOWER LIMIT:	UPPER LIMIT:
χ^2 /d.o.f of the time tangent fit	/	10.
χ^2 /d.o.f of the profile fit	0.1	10.
average Čerenkov light fraction	/	70%
3rd level of cuts		
CUT APPLIED TO:	LOWER LIMIT:	UPPER LIMIT:
X_{max} (bracketing cut)	/	/
slant depth of 1st recorded bin	150 g/cm ²	1200 g/cm ²
extent of recorded profile in slant depth	150 g/cm ²	/
ψ -angle	/	130°
error in ψ -angle	/	30°

Table 6.1: Cuts on reconstructed events in the analysis program.

The **third cut level** defines the selection of events for the spectrum calculation. A cut on the ψ -angle itself and a tightened cut on its recorded error are used to improve the ψ resolution. A “bracketing cut” is usually applied to further improve energy resolution of the event. It requires the reconstructed X_{max} to lie within the recorded shower profile; events in which only the rising or falling part of the profile is seen are discarded. In this analysis I have relaxed the bracketing cut, based on MC studies by Gareth Hughes, to include cases where the reconstructed X_{max} is within 50 g/cm² of the lower

or upper edge of the recorded profile. A requirement of a minimum extent of the shower profile and limits on the slant depth of the upper and lower edge of the profile exclude pathological profile reconstructions. The different cuts at all levels are summarized in Table 6.1.

After the first cut level, the three datasets contained 6,262 reconstructed events. The second level of cuts reduced this number to 4,997 events. Mainly due to the bracketing cut, the number of events was further reduced to a final set of 2,666 events, which were used in the calculation of the spectrum. The total live-time of the *HiRes-2* detector for the “good” nights in all three datasets was 531 hours.

6.2 Monte Carlo Resolution Studies

The plots shown in Figures 6.1, 6.2 and 6.3 have been generated from MC events at the three cut levels described above. Simulated events included in the plots of this and the following chapter have five times the statistics of the three *HiRes-2* datasets and were generated under the exact data taking conditions of DS1, DS2 and DS3. An estimate of the energy resolution is given here by the ratio of reconstructed over true event energies. Non-Gaussian tails are visible in all three figures, but are reduced considerably at the highest cut level (Figure 6.1). The Gaussian fit to the resolution after all cuts has a width of $\sigma = 18\%$ in the ratio of reconstructed over true energy. The energy resolution is centered on a ratio of 1.00. Figure 6.4 shows the dependence of the energy resolution on the true energies. A systematic shift in the mean of the resolution from -2.8% for energies below 10^{18} eV to 9.3% for energies above 10^{19} eV can be seen. The improvement in the width of the shown distributions with energy is due to the fact that EAS at higher energies have clearer signals.

The resolution in the depth of the shower maximum X_{max} is shown in Figure 6.5.

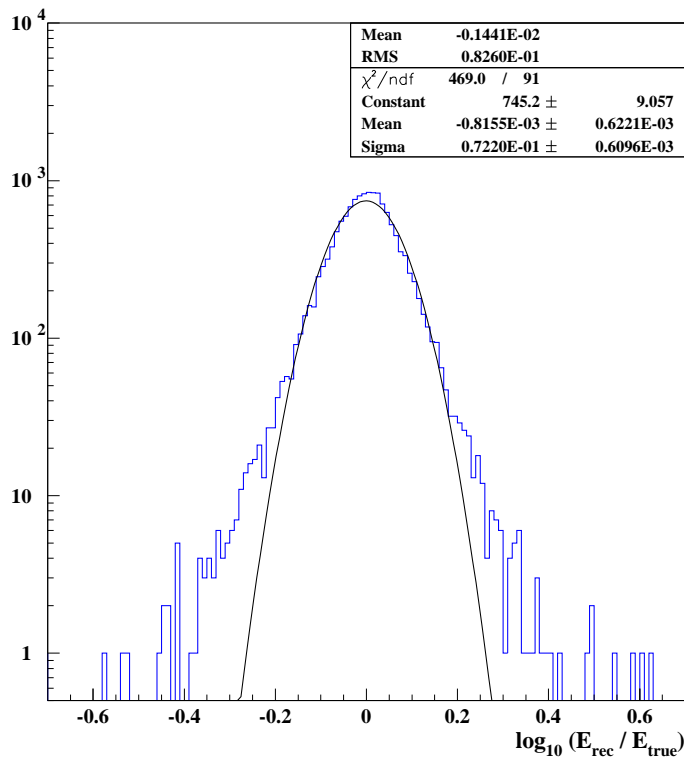


Figure 6.1: Energy resolution at the third cut level. Shown is the decadic logarithm of the ratio of reconstructed over true (input) energy for MC events. A Gaussian fit has been applied.

The reconstructed X_{max} values are shifted systematically by -49 g/cm^2 . This systematic error could be resolved in a recent update of the *HiRes-2* reconstruction programs [104]. An unbiased X_{max} resolution is of great importance for composition studies. The influence of this bias on the calculation of the energy spectrum, however, is not significant.

Figures 6.6 and 6.7 show estimates of the resolution in R_p and ψ , using the same set of MC events at the highest cut level. The resolution in the distance of the shower axis, R_p , is 7.6%. A small offset of 1% can be seen in the mean of the Gaussian. A Gaussian fit to the center region of the ψ resolution plot has a width of $\sigma \simeq 6^\circ$. The mean of the Gaussian has a small offset of 1.5°

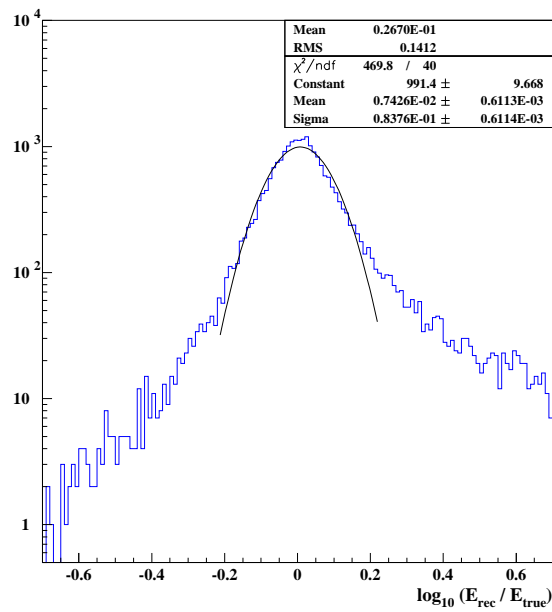


Figure 6.2: Energy resolution at the second cut level. Shown is the decadic logarithm of the ratio of reconstructed over true (input) energy for MC events. A Gaussian fit has been applied to the center region.

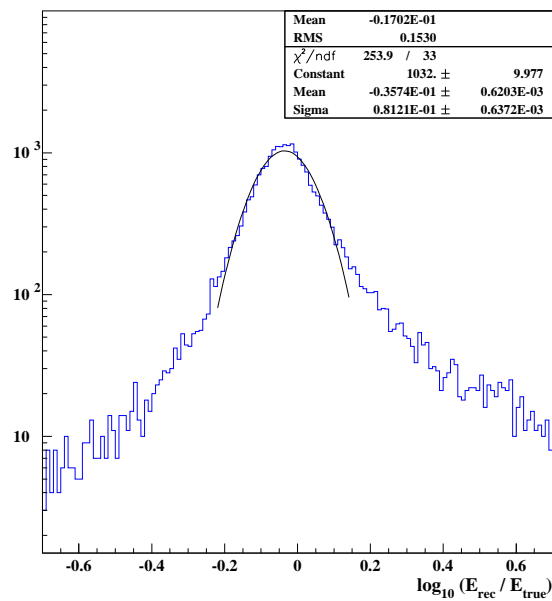


Figure 6.3: Energy resolution at the first cut level. Shown is the decadic logarithm of the ratio of reconstructed over true (input) energy for MC events. A Gaussian fit has been applied to the center region.

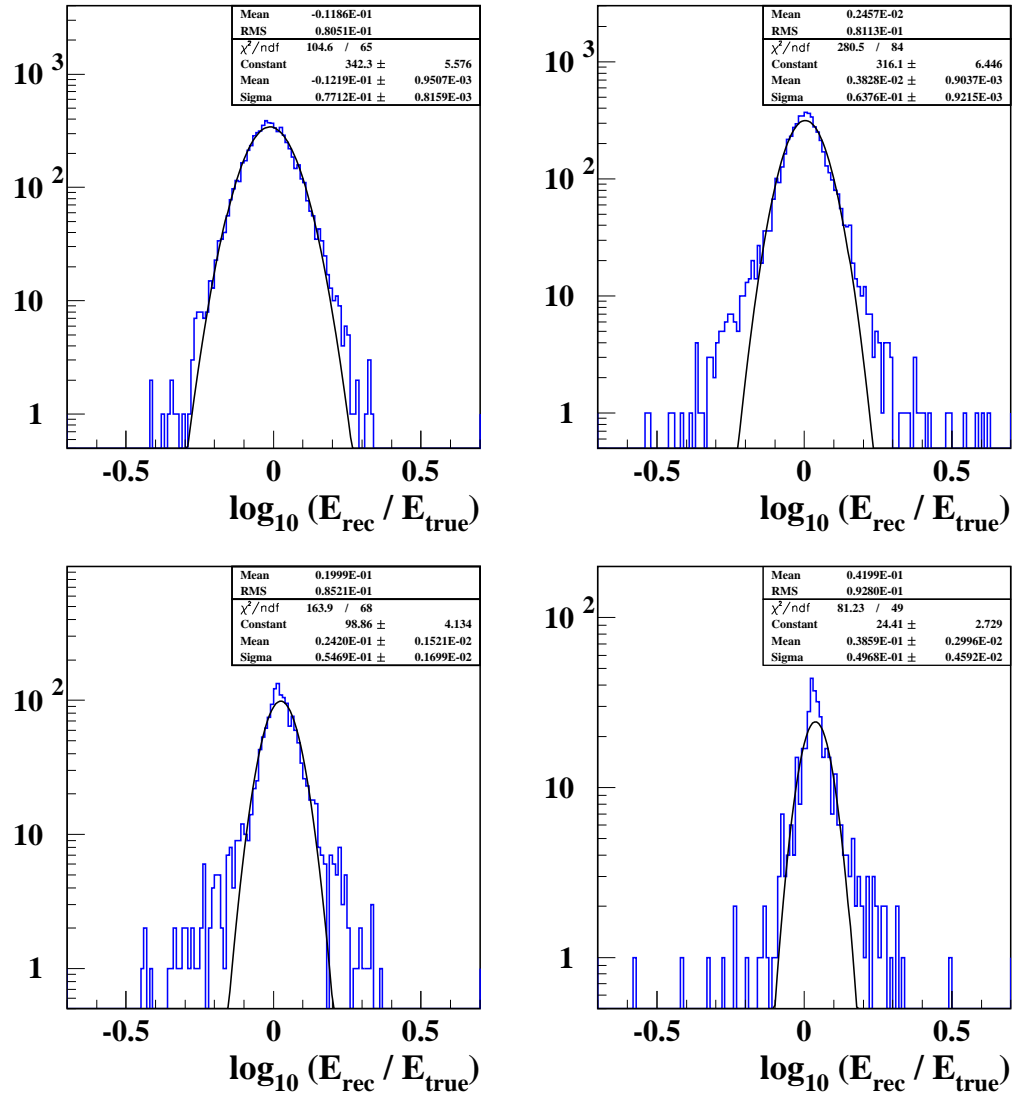


Figure 6.4: Energy resolution for different energy ranges. Shown is the decadic logarithm of the ratio of reconstructed over true (input) energy for MC events. The upper panel shows resolution plots for events with energies below 10^{18} eV (left), and between 10^{18} eV and $10^{18.5}$ eV (right). The lower panel shows plots for events with energies between $10^{18.5}$ eV and 10^{19} eV (left), and above 10^{19} eV (right). Gaussian fits have been applied to all distributions.

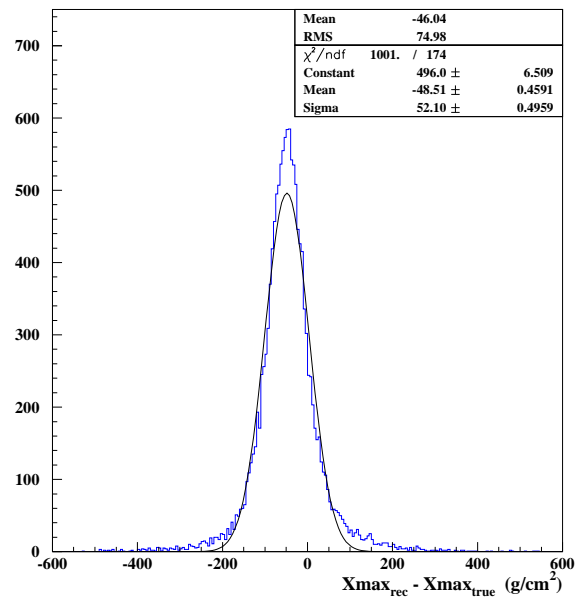


Figure 6.5: Resolution in X_{max} . Shown is the difference between the reconstructed and true X_{max} (in g/cm^2) for MC events. A Gaussian fit has been applied to the center region.

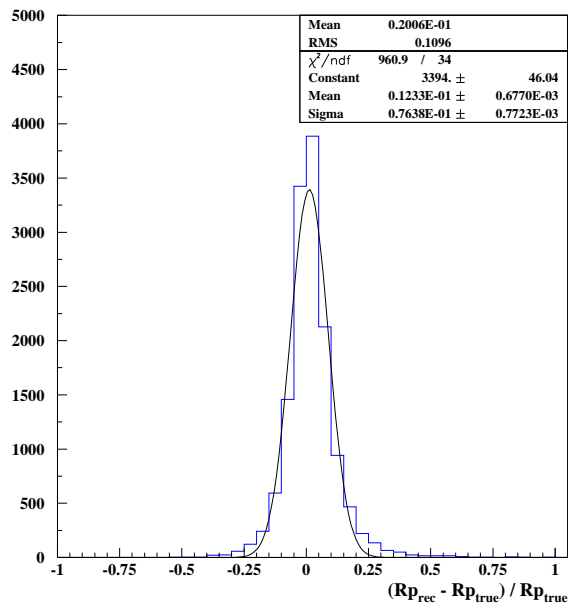


Figure 6.6: Resolution in R_p . Shown is the difference between the reconstructed and true R_p as a fraction of the true R_p for MC events. A Gaussian fit has been applied.

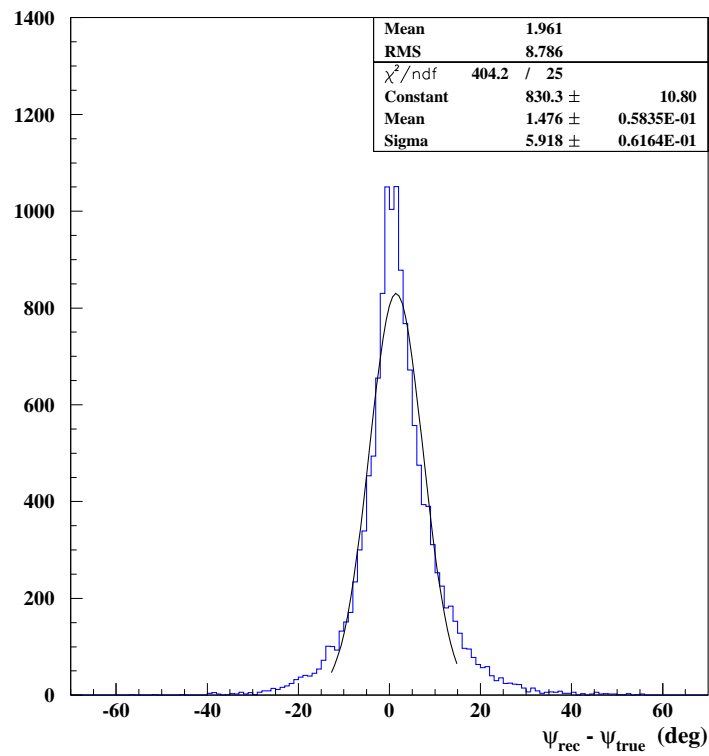


Figure 6.7: Resolution in the ψ -angle. Shown is the difference between reconstructed and true ψ -angle (in degrees) for MC events. A Gaussian fit has been applied to the center region.

Chapter 7

Comparisons between data and Monte Carlo

We use an extensive set of comparison plots between data and simulated events to test all the details of the MC programs. I have generated histograms for a multitude of parameters describing the geometry and profile of the reconstructed showers, the detector response, and the quality of the fits used in the reconstruction routines. A sample of these comparison plots is presented in this chapter. The MC events included in the following plots have about five times the statistics of the data events.

7.1 Comparisons of Geometric Parameters

The first four figures show geometric parameters of reconstructed air showers: the distance of the shower axis from the detector R_p (Figure 7.1), the ψ -angle distribution (Figure 7.2) before cuts on ψ , the zenith angle distribution (Figure 7.3), and the pseudo-distance (Figure 7.4). Agreement in the first two comparison plots is very good. A problem is visible in the zenith angle distributions: The simulated events show a deficit at small zenith angles. The source of this problem lies partially in a remaining discrepancy in the track angle distributions, but could not be fully resolved. The pseudo-distance comparison shows good agreement.

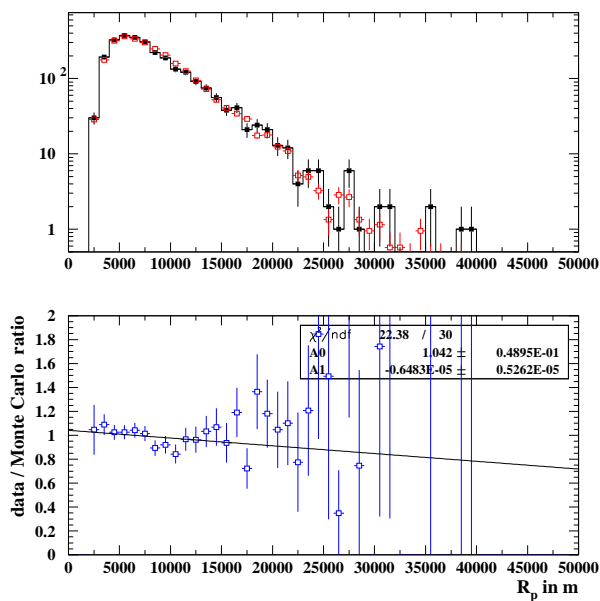


Figure 7.1: top: R_p distributions in meters, after final cuts.
 (open squares: MC , filled squares: data)
 bottom: Ratio of data over MC with linear fit.

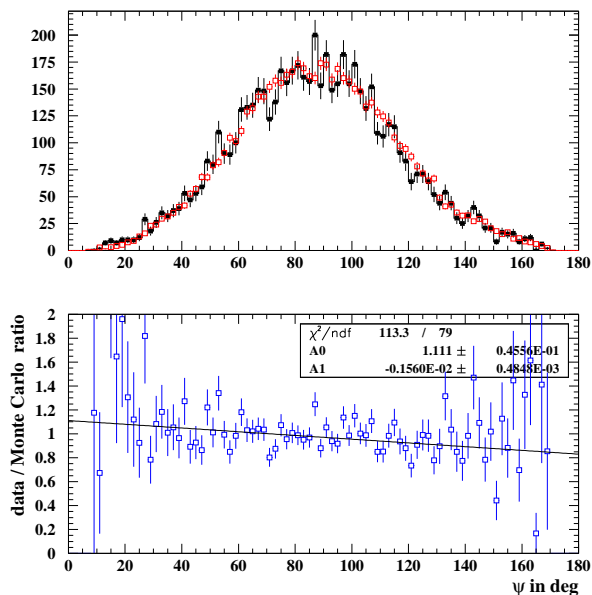


Figure 7.2: top: ψ -angle distributions in degrees, at lowest cut level.
 (open squares: MC , filled squares: data)
 bottom: Ratio of data over MC with linear fit.

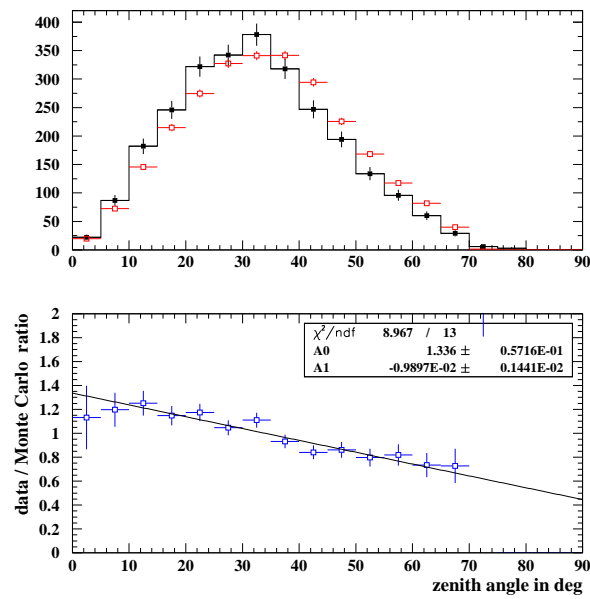


Figure 7.3: top: Zenith angle distributions in degrees, after final cuts.
 (open squares: MC , filled squares: data)
 bottom: Ratio of data over MC with linear fit.

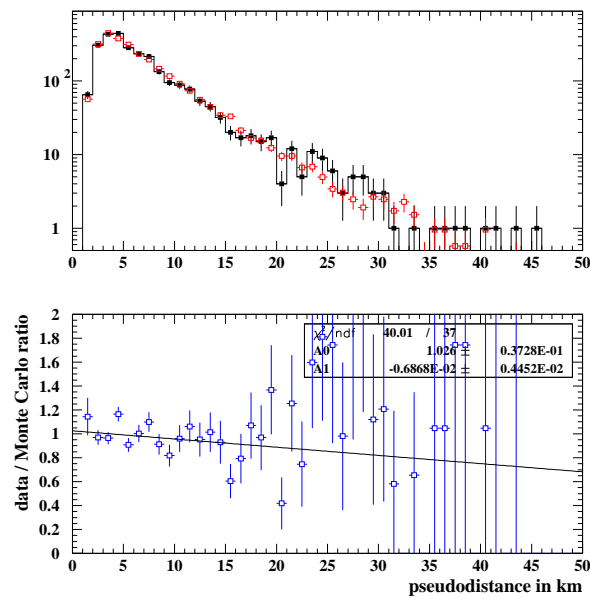


Figure 7.4: top: Pseudo-distance in km, after final cuts.
 (open squares: MC , filled squares: data)
 bottom: Ratio of data over MC with linear fit.

7.2 Comparisons of Shower Characteristics

Characteristics of the signal from air showers are shown in the following plots. Figure 7.5 is a comparison of the amount of simulated p.e. per track length with the p.e. recorded in the data, and thus a direct test of the amount of simulated versus observed light from air showers. We have found that this distribution is very sensitive to the accurate description of the trigger. Figure 7.6 compares the average contributions of Čerenkov light to the total signal, which is calculated in the reconstruction programs for data and MC events. The X_{max} distribution of events, before the bracketing cut, is presented in Figure 7.7. The final energy distributions that are used in the spectrum calculation are shown in Figure 7.8.

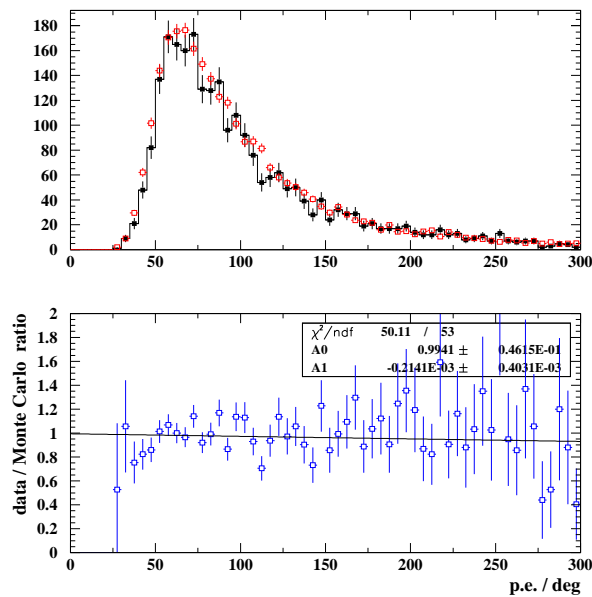


Figure 7.5: top: Distributions of p.e. per degree of track, after final cuts.
 (open squares: MC , filled squares: data)
 bottom: Ratio of data over MC with linear fit.

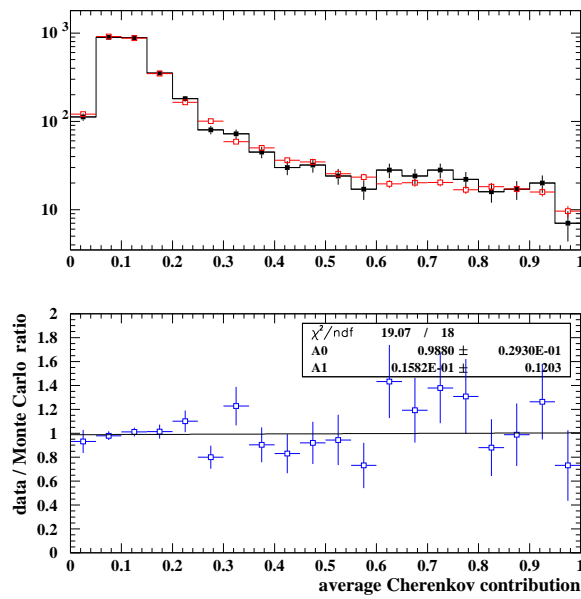


Figure 7.6: top: Average Čerenkov contribution, after second cut level and bracketing cut. (open squares: MC , filled squares: data)
bottom: Ratio of data over MC with linear fit.

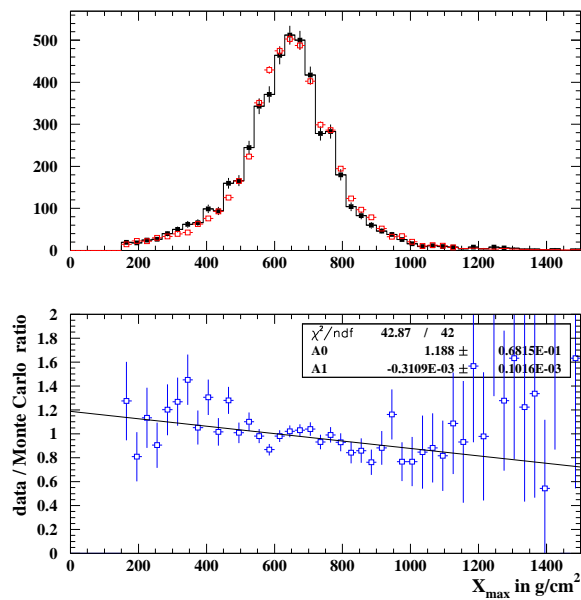


Figure 7.7: top: X_{max} distributions in g/cm^2 , after second cut level.
(open squares: MC , filled squares: data)
bottom: Ratio of data over MC with linear fit.

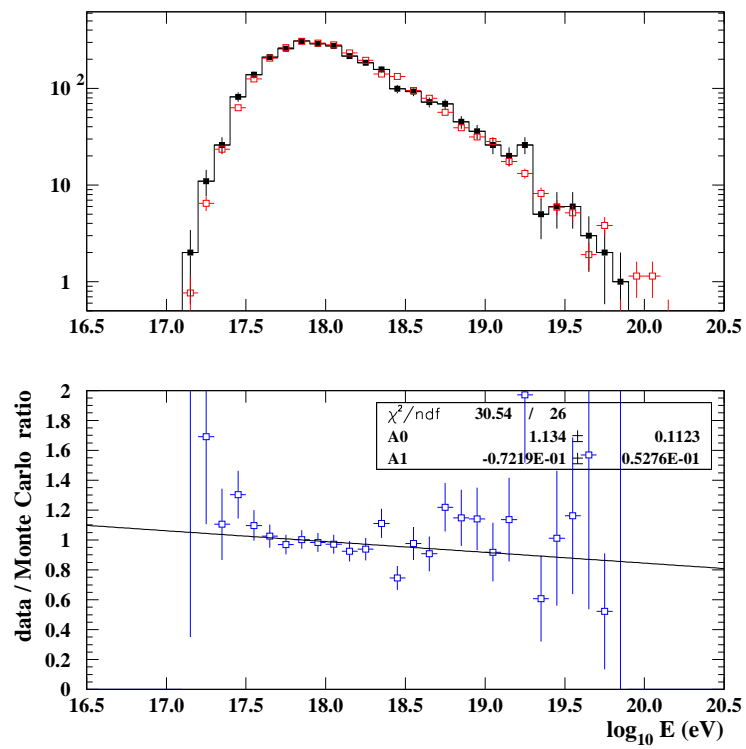


Figure 7.8: top: Energy distribution, after final cuts.
 (open squares: MC , filled squares: data)
 bottom: Ratio of data over MC with linear fit.

7.3 Comparisons of Trigger Characteristics

The comparison plots shown in the following illustrate the detector response to simulated and real events. Figure 7.9 shows the number of “good” tubes, i.e. PMTs that have been included in the track by the reconstruction routines. The length of recorded tracks is shown in Figure 7.10, where a strong peak around 27° is caused by nearly vertical tracks from showers seen in both rings. A smaller peak at about 13° was visible in DS1 for events that triggered only one ring, but the introduction of the adjacent mirror trigger has depleted this smaller peak in the combination of the three datasets. The number of read out mirrors per event can be seen in Figure 7.11. The two peaks at 6 and 2 are characteristic for data periods with and without the adjacent mirror trigger, respectively. Figure 7.12 shows the distribution of tracks over mirrors. For each event, one entry has been added to each mirror that contained at least one “good” tube. The patterns in these distributions are caused by “dead” mirrors, differences in trigger DACs, and the different trigger rates in mirrors of ring 1 and ring 2.

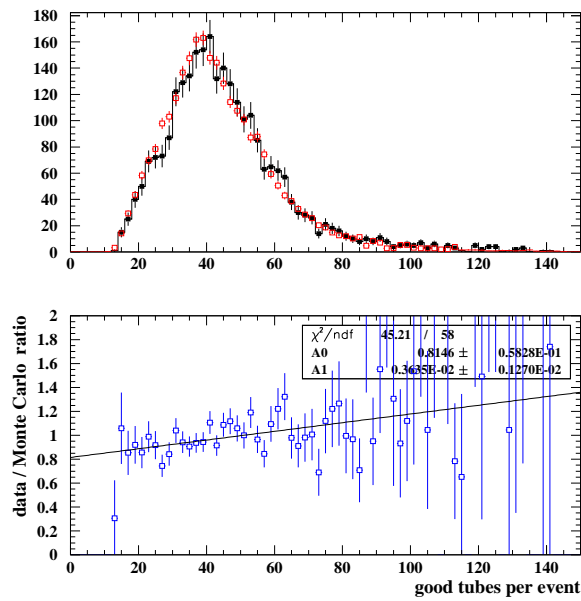


Figure 7.9: top: Distributions of “good” tubes per event, after final cuts.
 (open squares: MC , filled squares: data)
 bottom: Ratio of data over MC with linear fit.

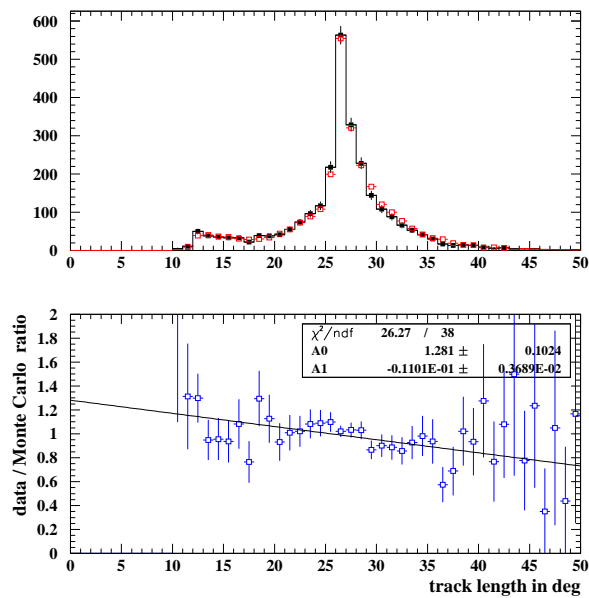


Figure 7.10: top: Track length distributions in degrees, after final cuts.
 (open squares: MC , filled squares: data)
 bottom: Ratio of data over MC with linear fit.

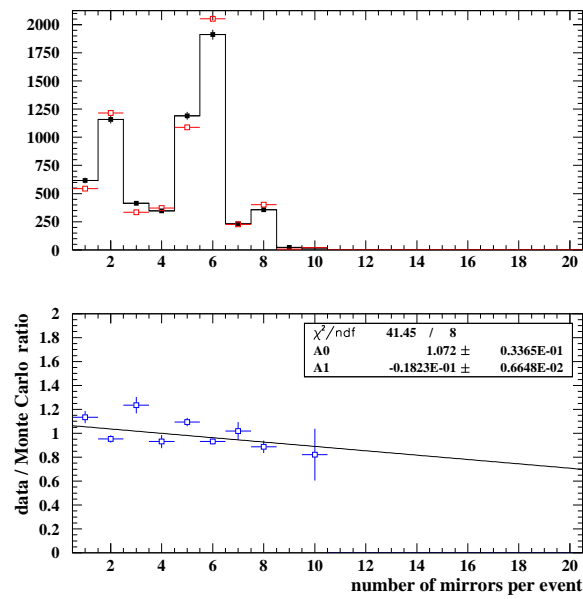


Figure 7.11: top: Number of read out mirrors per event, at lowest cut level.
(open squares: MC , filled squares: data)
bottom: Ratio of data over MC with linear fit.

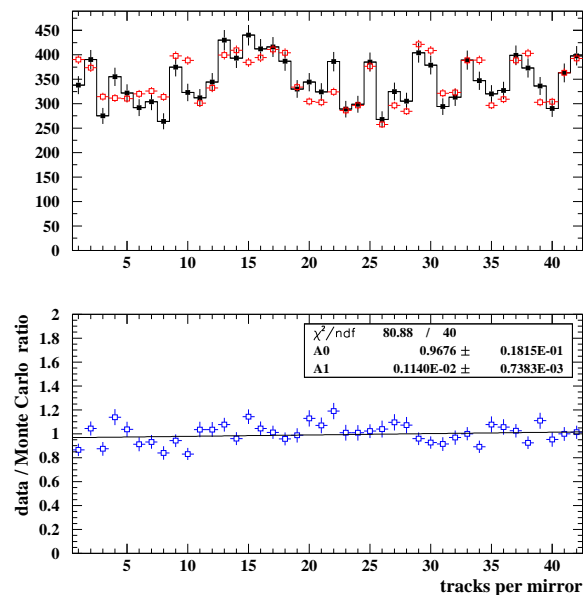


Figure 7.12: top: Distribution of reconstructed tracks over mirror indices, at lowest cut level. (open squares: MC , filled squares: data)
bottom: Ratio of data over MC with linear fit.

7.4 Comparisons of fit χ^2

Two χ^2 distributions are shown below: the χ^2 /d.o.f. of the linear time fit (Figure 7.13) and the χ^2 /d.o.f. of the time tangent fit (Figure 7.14). Adding the correct amount of background noise (ambient noise and extra hits) was important for an agreement in these comparisons.

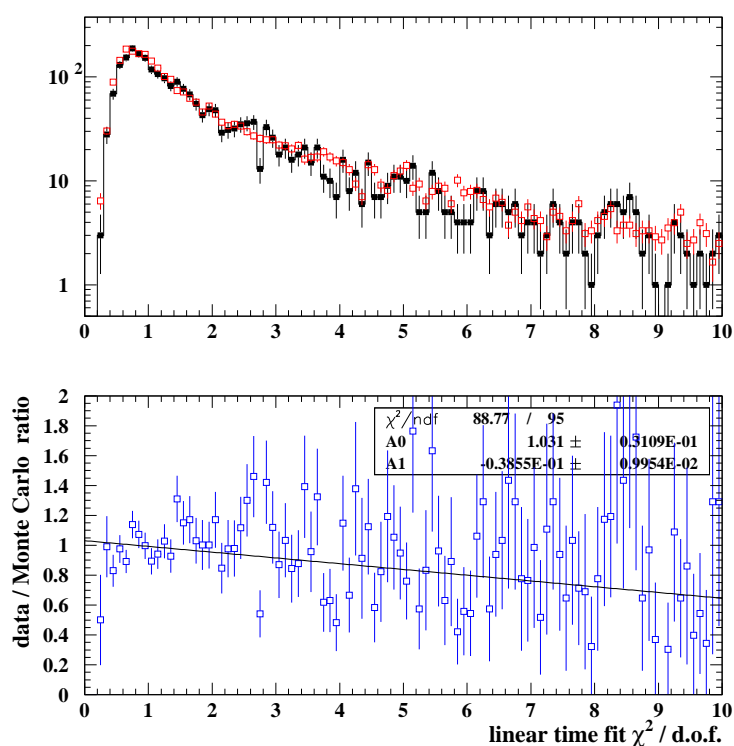


Figure 7.13: top: χ^2 /d.o.f. of linear time fit, after final cuts.
 (open squares: MC , filled squares: data)
 bottom: Ratio of data over MC with linear fit.

7.5 Conclusion

The data-MC comparisons presented here show an overall very good agreement between data and simulated events. Especially the agreement in p.e. per degree of track is important for the correct energy reconstruction. Our simulation programs describe

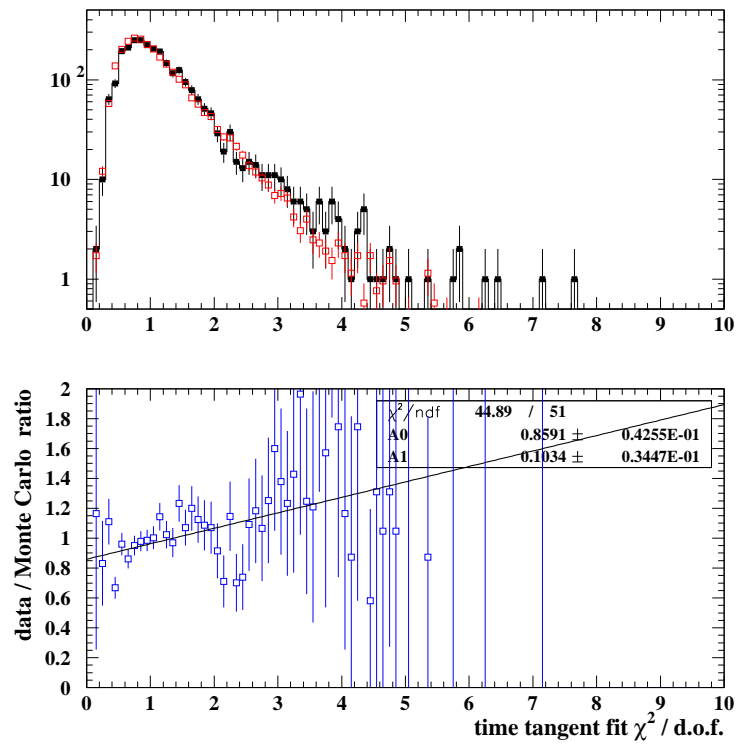


Figure 7.14: top: $\chi^2/\text{d.o.f.}$ of time tangent fit, after final cuts.
 (open squares: MC , filled squares: data)
 bottom: Ratio of data over MC with linear fit.

accurately the detector response for the data under analysis. After this crucial test of the MC programs, the simulated acceptance can be used in the calculation of the cosmic ray spectrum.

Chapter 8

HiRes-2 Energy Spectrum & Systematics

8.1 HiRes-2 Aperture

With the estimate of the detector acceptance given by MC simulations, the calculation of the cosmic ray energy spectrum from reconstructed data is now straightforward. The selected events are divided into energy bins of width ΔE (0.1 in log (E/eV)) and the differential flux in each energy bin is calculated according to the following equation:

$$J(E_i) = N(E_i) \cdot \frac{1}{\Delta E} \cdot \frac{1}{\frac{\nu_i^{MC}}{\mu_i^{MC}} \cdot A\Omega \cdot t} \quad (8.1)$$

Here $\frac{\nu_i^{MC}}{\mu_i^{MC}}$ is the acceptance for the energy bin centered on energy E_i . The geometric aperture $A\Omega$, for which the acceptance was estimated, is calculated with the limits set in the MC simulation on R_p (0.01 km to 35.00 km), the zenith angle θ (0° to 70°) and azimuth angle ϕ (0° to 360°). The geometric aperture is given by:

$$\begin{aligned} A\Omega &= \int_0^{2\pi} \int_{\theta_{min}}^{\theta_{max}} \int_{R_{p_{min}}}^{R_{p_{max}}} 2\pi r \sin \theta \, dr d\theta d\phi \\ &= 2\pi^2 (R_{p_{max}}^2 - R_{p_{min}}^2) (\cos \theta_{min} - \cos \theta_{max}) \end{aligned} \quad (8.2)$$

With the limits given above, this results in: $A\Omega \simeq 15,910.30 \text{ km}^2\text{sr}$. The total live-time of the detector t for the selected nights was 1,911,326 s. The three datasets cover live-times of ~ 194 hours (DS1), ~ 176 hours (DS2) and ~ 161 hours (DS3).

The simulated acceptances for the three datasets can be seen in Figure 8.1. With the changes in the trigger, i.e. the lowering of DSP scan thresholds and the raising of trigger DACs, the acceptance increased. This explains the systematically lower points of the curve for DS1 at energies below $\sim 10^{18.5}$ eV. The acceptance curve for DS3 is

somewhat lower than the one for DS2 because of the cut on the trigger sums in DS3. At the highest energies ($> 10^{20}$ eV), the MC event sample used in this analysis loses its statistical power, even though MC sets with higher statistics have been included for all three datasets for energies above $10^{18.8}$ eV.

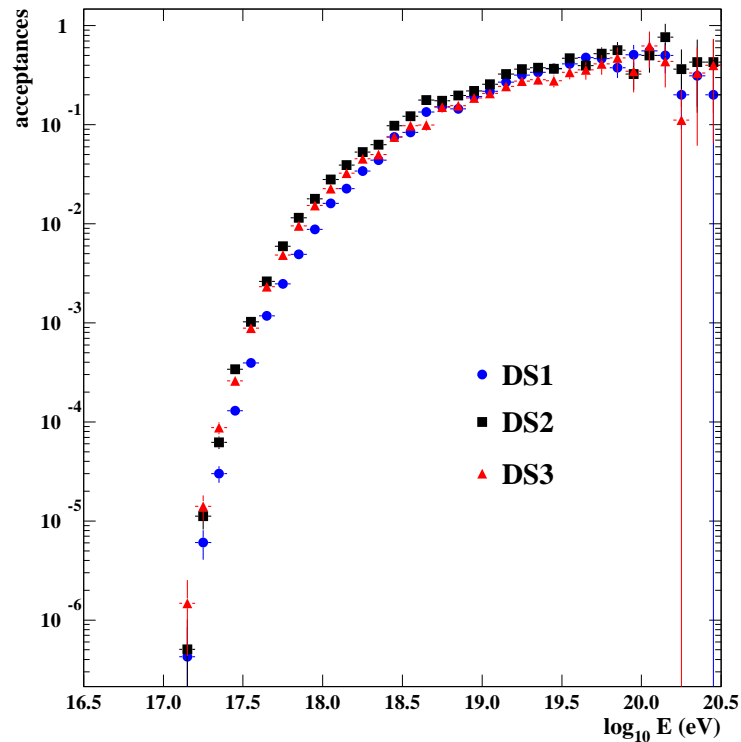


Figure 8.1: Acceptances of DS1, DS2 and DS3 versus the decadic logarithm of the reconstructed energy.

The instant aperture of the *HiRes-2* detector, averaged over the three datasets taking into account the different live-times, is shown in Figure 8.2. The instant aperture, i.e. the product of geometric aperture and acceptance, is close to 10^4 km²sr at the highest energies.

Figure 8.3 shows a histogram of the total exposure, i.e. the sum of instant apertures of the three datasets multiplied by the corresponding detector live-times. The simulated

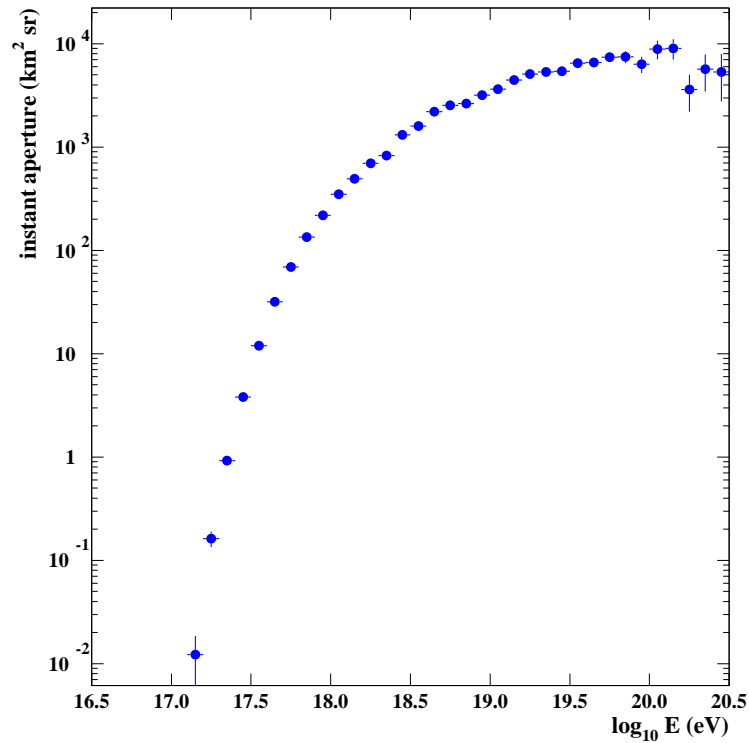


Figure 8.2: Instant aperture, averaged over the three datasets taking into account the different live-times. The instant aperture (in km^2sr) is plotted against the decadic logarithm of the reconstructed energy.

exposure points have been fit to a sum of three functions of the form:

$$\exp [a \cdot (1 - \exp [b(x - c)])]$$

The fit parameters a , b and c have been determined for each of the three terms by fits over a decade in energy, i.e. from 10^{17} eV to 10^{18} eV to 10^{19} eV to 10^{20} eV. In order to smooth out statistical fluctuations in the simulated exposure, I have used this fit for the exposure estimate in the spectrum calculation. The “smoothed” exposure can be seen in Figure 8.4. The errors on the points, derived from the covariance matrix of the fit, are all smaller than the markers in the plot.

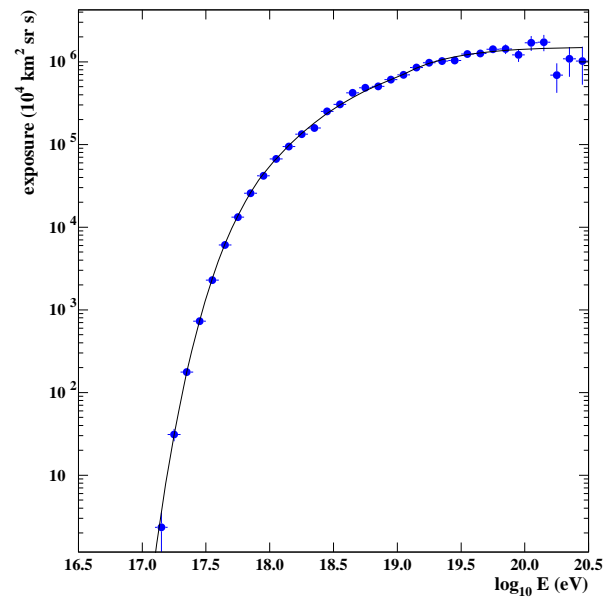


Figure 8.3: Exposure with fit function.

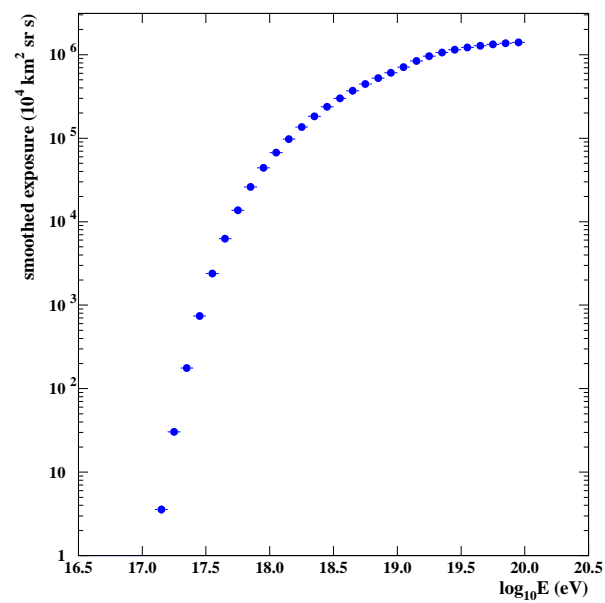


Figure 8.4: Smoothed exposure used for the spectrum calculation.

8.2 Energy Spectrum

The *HiRes-2* energy spectrum is shown in Figure 8.5 in a JE^3 plot. The statistical errors included in the plot are calculated from the event statistics in each bin and from the small statistical errors in the smoothed exposure. Above an energy of $10^{18.8}$ eV, the bin-width is doubled to smooth out fluctuations due to the decline in event statistics at the highest energies. A discussion of the spectral features and comparison with other measurements will follow in the next chapter. Table 8.1 lists the measured flux J , JE^3 , the statistical errors on J and JE^3 , and the number of events for each energy bin. The bin centered at $10^{17.15}$ eV has not been included in the spectrum plot due to lack of statistics in the data, which is caused by the low acceptance of the *HiRes-2* detector at the low energy end.

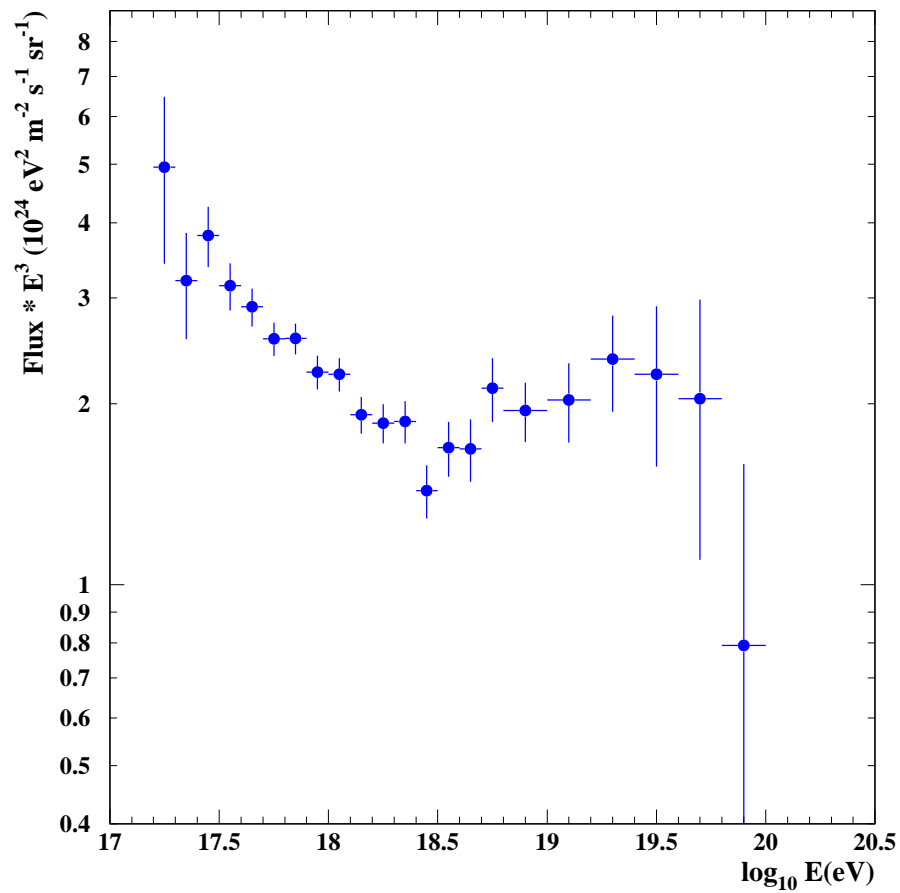


Figure 8.5: The UHECR energy spectrum measured by *HiRes-2*. The flux, multiplied by the cube of the energy in each bin, is plotted against the decadic logarithm of the energy.

$\log(E)$	J	δJ	JE^3	$\delta(JE^3)$	events
17.15	0.172E-02	0.123E-02	0.485E+01	0.348E+01	2
17.25	0.879E-03	0.272E-03	0.494E+01	0.153E+01	11
17.35	0.285E-03	0.572E-04	0.320E+01	0.642E+00	26
17.45	0.170E-03	0.196E-04	0.381E+01	0.438E+00	82
17.55	0.703E-04	0.630E-05	0.314E+01	0.281E+00	138
17.65	0.325E-04	0.235E-05	0.290E+01	0.209E+00	210
17.75	0.144E-04	0.921E-06	0.256E+01	0.164E+00	257
17.85	0.723E-05	0.427E-06	0.257E+01	0.151E+00	309
17.95	0.319E-05	0.206E-06	0.226E+01	0.146E+00	290
18.05	0.158E-05	0.102E-06	0.224E+01	0.144E+00	275
18.15	0.680E-06	0.475E-07	0.192E+01	0.134E+00	216
18.25	0.330E-06	0.247E-07	0.186E+01	0.139E+00	184
18.35	0.166E-06	0.134E-07	0.187E+01	0.151E+00	157
18.45	0.640E-07	0.649E-08	0.143E+01	0.145E+00	99
18.55	0.378E-07	0.396E-08	0.169E+01	0.177E+00	93
18.65	0.189E-07	0.225E-08	0.168E+01	0.200E+00	72
18.75	0.119E-07	0.145E-08	0.212E+01	0.258E+00	69
18.85	0.524E-08	0.788E-09	0.186E+01	0.279E+00	45
18.95	0.287E-08	0.483E-09	0.203E+01	0.342E+00	36
19.05	0.142E-08	0.284E-09	0.200E+01	0.401E+00	26
19.15	0.730E-09	0.164E-09	0.206E+01	0.463E+00	20
19.25	0.661E-09	0.130E-09	0.372E+01	0.733E+00	26
19.35	0.912E-10	0.409E-10	0.102E+01	0.459E+00	5
19.45	0.803E-10	0.330E-10	0.180E+01	0.739E+00	6
19.55	0.599E-10	0.248E-10	0.268E+01	0.111E+01	6
19.65	0.227E-10	0.132E-10	0.202E+01	0.118E+01	3
19.75	0.116E-10	0.825E-11	0.206E+01	0.147E+01	2
19.85	0.446E-11	0.449E-11	0.158E+01	0.159E+01	1

Table 8.1: *HiRes-2* measurement of flux and number of events per energy bin. Entries (from left to right column): decadic logarithm of the energy (in eV) at the middle of the bin, differential flux J (in $10^{-24} \text{ eV}^{-1} \text{ m}^{-2} \text{ s}^{-1} \text{ sr}^{-1}$), statistical error in J (same units), JE^3 (in $10^{24} \text{ eV}^2 \text{ m}^{-2} \text{ s}^{-1} \text{ sr}^{-1}$), statistical error in JE^3 (same units), number of observed events. Statistical errors are calculated from the event numbers and the small errors in the exposure.

8.3 Systematic Uncertainties

The largest systematic uncertainties in the HiRes monocular spectra have been reported in [3]: uncertainties in the absolute phototube calibration ($\pm 10\%$), the fluorescence yield ($\pm 10\%$) and the “missing energy” correction ($\pm 5\%$). Not taking into account atmospheric effects, the uncertainty in the energy scale is $\pm 15\%$, which results in a systematic uncertainty in the flux J of $\pm 27\%$.

The effect on the *HiRes-2* energy scale of a variation of the average VAOD value by ± 1 RMS value, from 0.04 to 0.06 and 0.02, is not larger than 6%. This results in a total uncertainty in the *HiRes-2* energy scale of 16%. The effect of the same VAOD variation on the aperture leads to an average atmospheric uncertainty in the flux J of $\pm 15\%$. Thus, the total uncertainty in the flux is $\pm 31\%$.

The estimate of the atmospheric uncertainty in our measurements will be reviewed below with use of the atmospheric database. Another possible source of uncertainty, which has not been included in the above summary, is the assumption of the input composition, i.e. the ratio of proton and iron showers, in the simulation of the detector acceptance.

8.3.1 Uncertainties in the Input Composition

As described in Chapter 4, the fraction of showers initiated by light and heavy (i.e. proton and iron) cosmic rays in the MC is determined from composition measurements by the *HiRes/MIA* and *HiRes* stereo experiments. The difference in the simulated acceptance between a MC set with only iron events and a set with only proton events can be seen in Figure 8.6: Shown here are the exposures that result for the two MC sets. At the low energy end of the spectrum, the acceptance for iron cosmic rays is lower because iron showers develop higher up in the atmosphere and are more likely to be outside of the *HiRes-2* elevation coverage than proton showers. This leads to larger differences between the two exposures at lower energies. For energies above $\sim 10^{18}$

eV, where the HiRes stereo composition measurement is used, no difference was seen in the acceptances for iron and proton showers.

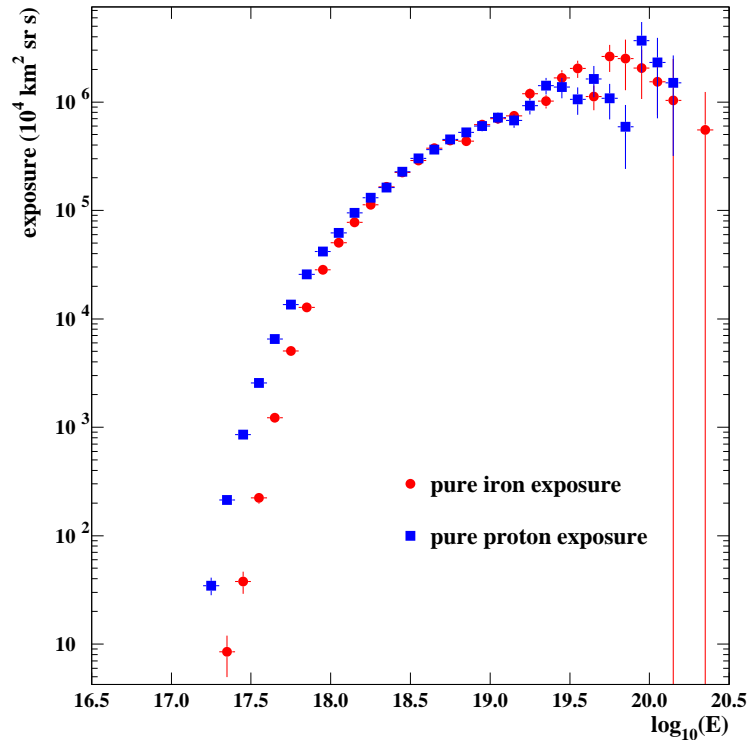


Figure 8.6: Exposures for pure iron and pure proton MC sets.

With the help of the results for the pure iron and pure proton exposures, I have calculated the effect of a change in the initially assumed proton fraction on the simulated exposure. The proton fraction f_p is here defined as the ratio of generated proton showers over the sum of generated proton and iron showers in the MC: $f_p = \mu_p / (\mu_p + \mu_{fe})$. The acceptance for a MC set with a proton fraction f_p is given by:

$$a_{mix} = \frac{\nu_p + \nu_{fe}}{\mu_p + \mu_{fe}} = \frac{\nu_p(1 + \nu_{fe}/\nu_p)}{\mu_p/f_p} = a_p f_p (1 + R(\frac{1}{f_p} - 1)) = a_p (R + f_p(1 - R)) \quad (8.3)$$

Here ν_p and ν_{fe} are the accepted, i.e. triggered and well reconstructed, proton and iron events, respectively. a_{mix} and a_p are the acceptances for a MC set with proton fraction f_p and 1, respectively. R is given here by the ratio of the acceptance for pure iron

and the acceptance for pure proton MC sets $\left(\frac{\nu_{fe} \cdot \mu_p}{\mu_{fe} \cdot \nu_p}\right)$. This ratio can be determined directly from the two curves shown in Figure 8.6. With R known, Equation 8.3 yields the acceptance a_{mix} for a given proton fraction f_p as a fraction of the acceptance for pure proton showers a_p in each energy bin. Thus, the effect of a change in the proton fraction on the resulting acceptance and exposure can be determined.

The uncertainties in the *HiRes/MIA* measurement ([4], [61]) that translate into the *HiRes-2* spectrum calculation add up to $\sim 5\%$. Their sources are the detector calibration ($< 5\%$ uncertainty in energy), the aerosol component of the atmosphere ($< 10\%$ uncertainty in energy) and the statistical uncertainty of a fit to the *HiRes/MIA* data ($\sim 3\%$) [104]. A 10% uncertainty in the fluorescence yield is common to both *HiRes* and *HiRes/MIA*, and is therefore not included. The difference in the predictions of pure iron and pure proton maximum shower depths (X_{max}) between different hadronic interaction models of about 25 g/cm^2 is not taken into account either, since we are not concerned about the fraction of real proton and iron showers here, but only about the fraction of showers with a certain X_{max} . The uncertainties in the final spectrum from a $\pm 5\%$ variation in the proton fraction are shown in Figure 8.7 as thick error bars.

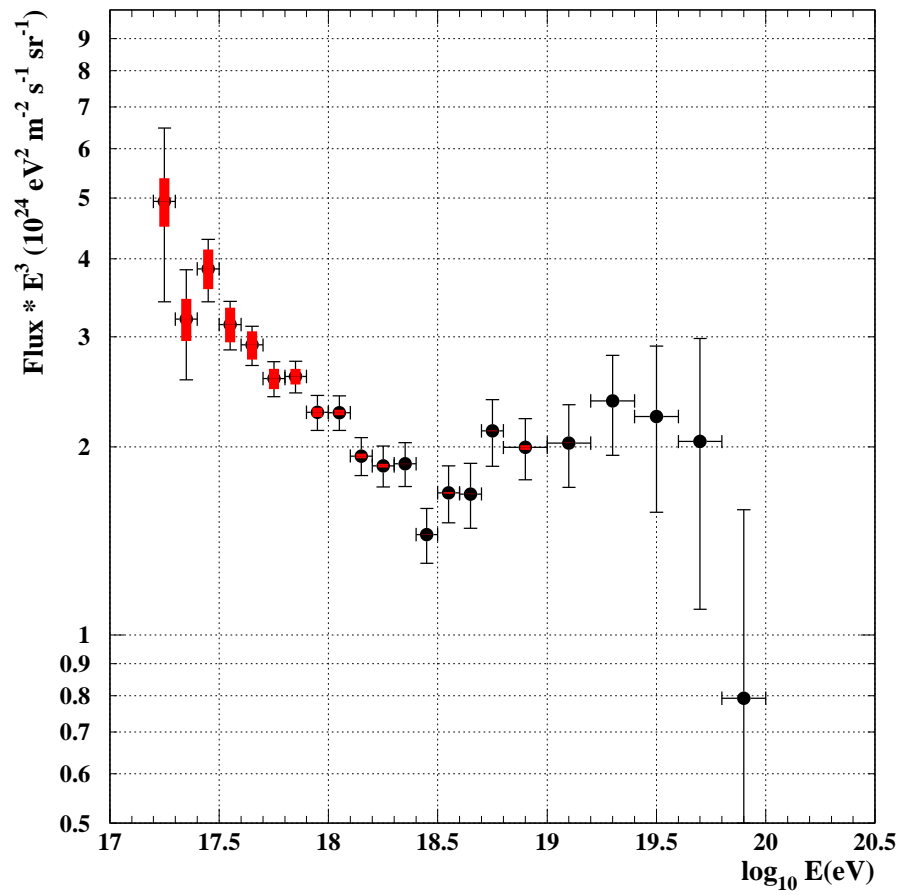


Figure 8.7: *HiRes-2* energy spectrum with systematic uncertainties (thick error bars) corresponding to a $\pm 5\%$ change in the proton fraction of the MC.

8.3.2 Atmospheric Uncertainties

In order to study the effect of variations in the aerosol component of the atmosphere on the **reconstructed energies**, I have analyzed the data of all three datasets using the atmospheric database described in Chapter 4. The energy distribution from this analysis can be seen in Figure 8.8 in comparison with the result of using an average atmosphere for each dataset, determined from the same atmospheric database. The average atmospheric values for the dataset were also used when no data were available in the database for a certain night. As can be seen from this plot, the two distributions do not show a significant difference: The slope of the linear fit is only 1% per decade in energy. This is consistent with the above statement that the effect of atmospheric variations on the *HiRes-2* energy scale are small.

Variations in the reconstructed energies can also be analyzed on an event-by-event basis. Since all data events were reconstructed with the atmospheric database and also with average atmospheric values, the ratio of the energy estimates can be calculated for each event (provided it passed the “bracketing cut” in both cases). The resulting distribution of those ratios is shown in Figure 8.9. The variation in reconstructed energies is centered around 0.99 and has a width of 7% (RMS). More than 88% of all event energies vary by less than 10%, and there are no large tails in the distribution.

The effect of atmospheric variations on the **energy resolution** can be studied with simulated events. I have generated a MC set with about four times data statistics, using the atmospheric database. The MC events have been reconstructed in two different ways: first with the average atmospheric values for each dataset period, and then with the database for nights when atmospheric data were available. A comparison of the resolution estimates is shown in Figure 8.10. Reconstructing the MC events with the average atmospheric values of each dataset instead of using the atmospheric database widens the resolution by 0.9%.

Finally, I have analyzed the effect of using the atmospheric database rather than

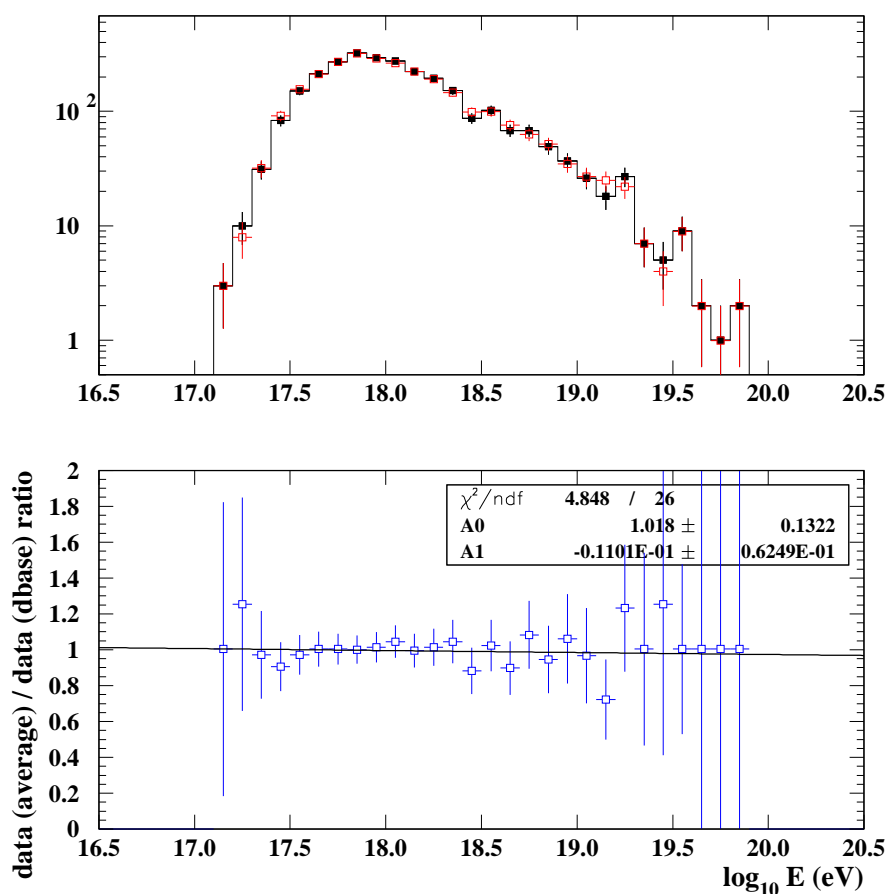


Figure 8.8: top: Energy distributions of all *HiRes-2* data. (open squares: data reconstructed with atmospheric database , filled squares: data reconstructed with average atmosphere)

bottom: Ratio of data distribution with average atmosphere over data distribution with atmospheric database. A linear fit has been applied to the ratio.

The strong correlations between the two distributions cause *HBOOK*, the histogramming program we use, to overestimate the error bars in the ratio plot.

the measured average on the **energy spectrum**: I have calculated an acceptance from a MC set that was generated and reconstructed with the database. The *HiRes-2* data of all three datasets were also reconstructed with use of the atmospheric database. In this way, the hourly measurements of atmospheric variations were included in every step of the analysis. The energy spectrum that resulted from this analysis is compared to the spectrum using the measured averages of VAOD (0.04) and HAL (25 km) in

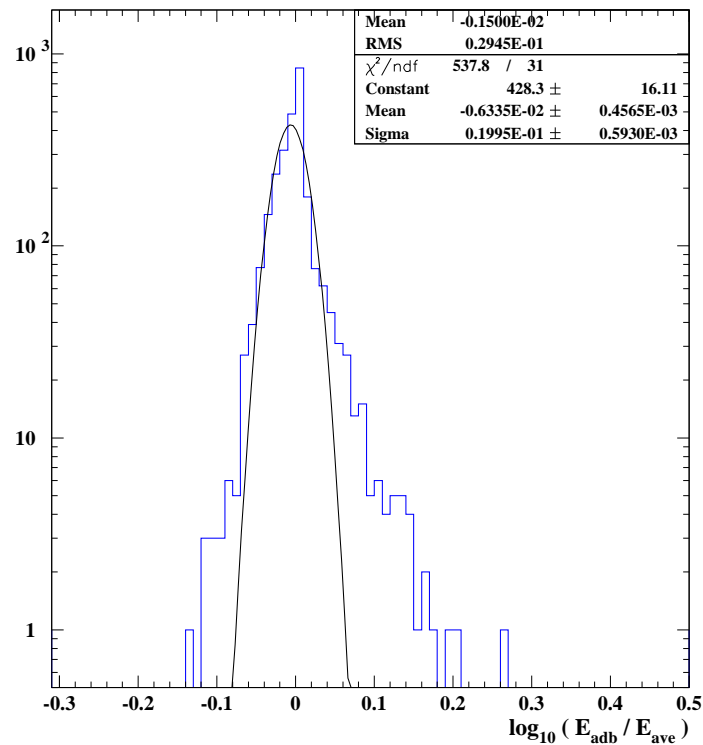


Figure 8.9: Difference in reconstructed energies due to atmospheric variations. The energy of each data event has been reconstructed in two ways: using the atmospheric database and using an average atmosphere. Shown is the decadic logarithm of the ratio of the two energy estimates for each event. (numerator: with database, denominator: average atmosphere) The width of the distribution of the energy ratios is: 7% (RMS) and 5% (σ of the Gaussian fit).

Figure 8.11. The ratio plot of the two spectra shows that the result for JE^3 does not vary by more than $\pm 15\%$ at any energy, except for the first and the last two bins, where statistics are low. The error bars shown in this plot have been scaled down by a factor of 2.5 to yield reasonable errors in the fit parameters despite the strong correlations between the two energy spectra, which led to an overestimation of the error bars in the *HBOOK* program.

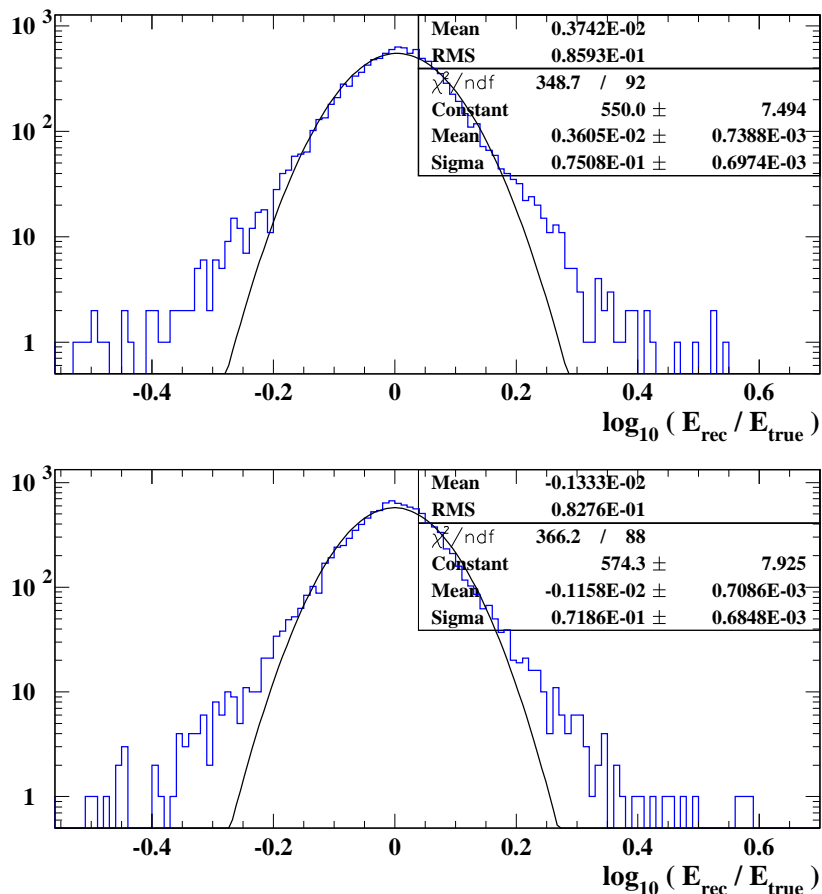


Figure 8.10: Shown is the energy resolution as the decadic logarithm of the ratio of reconstructed over true (input) energy. top: Energy resolution of a MC set generated with the atmospheric database and reconstructed with an average atmosphere. The width of the ratio of reconstructed over true energy is: 21.9% (RMS) and 18.9% (σ of the Gaussian fit).

bottom: Energy resolution of the same MC set, but reconstructed with the atmospheric database. The width of the distribution of the energy ratios is: 21.0% (RMS) and 18.0% (σ of the Gaussian fit).

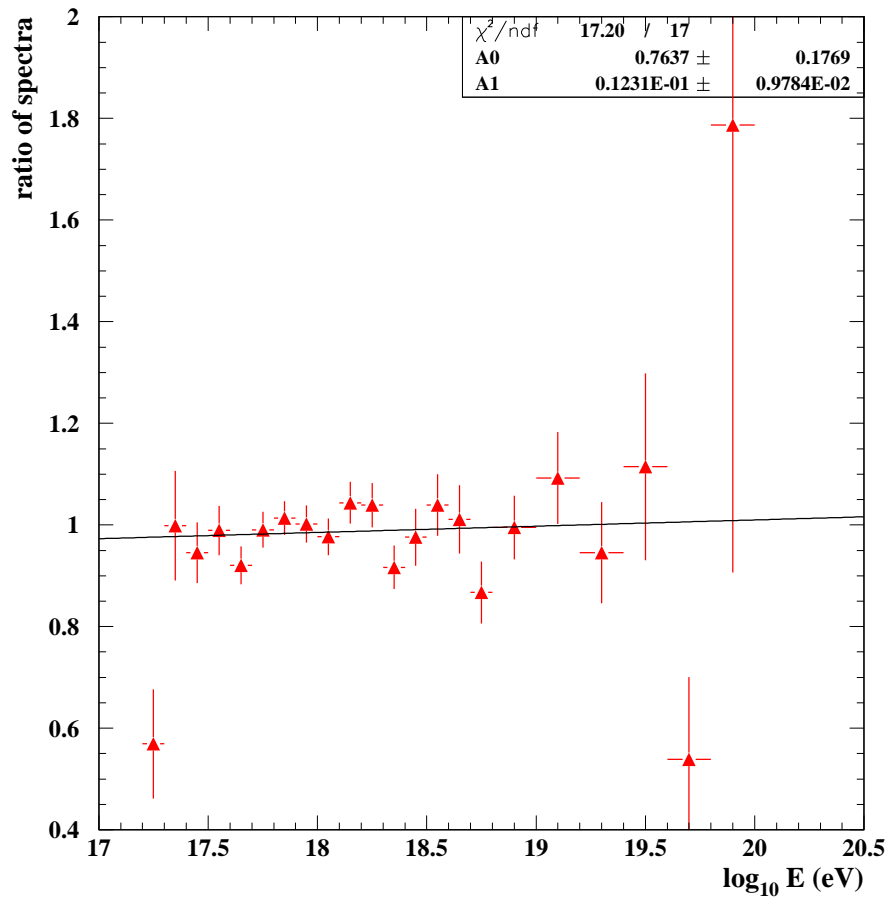


Figure 8.11: Ratio of energy spectra analyzed with and without atmospheric database. The spectrum in the numerator has been calculated using the atmospheric database in the generation of MC events and in the reconstruction of both data and simulated events. In the denominator is the spectrum calculated using the nominal average to describe the atmosphere. A linear fit has been applied to the ratio excluding the first non-empty bin and the last two non-empty bins. The error bars were overestimated by *HBOOK* and have been scaled down by a factor of 2.5 .

Chapter 9

Conclusions

The “ankle” is observed in the *HiRes-2* measurement of the UHECR spectrum at an energy of about $10^{18.5}$ eV. This is consistent with the previous measurement by the *Fly’s Eye* experiment [24]. We have applied fits of the form $p_1 \cdot 10^{(3.-p_2) \cdot (\log(E)-18.)}$ to the JE^3 plot of the *HiRes-2* spectrum to measure the power index of the cosmic ray flux for energies below and above the “ankle”. The binned maximum likelihood method [105] was used for the fits presented here.

The fit below the “ankle” is shown in Figure 9.1. As end-point of this fit, I have adopted the energy measured by *Fly’s Eye* for the “ankle” ($10^{18.5}$ eV). The start-point was chosen to be $10^{17.5}$ eV. The power index from this fit (p_2) is given by 3.320 ± 0.038 . This is within errors of the *Fly’s Eye* result (3.27 ± 0.02). The normalization p_1 at 10^{18} eV in the usual JE^3 units (10^{24} eV²m⁻²s⁻¹sr⁻¹) is 2.241 ± 0.045 . The $\chi^2/\text{d.o.f.}$ is $4.25/8$. Extending the start-point to lower energies does not change this result significantly, due to low event statistics in the first three non-zero bins. The “second knee” cannot be observed in the *HiRes-2* data analyzed here due to the low statistics. More recent data, which are currently under analysis, are expected to improve the statistical power at the low energy end of the spectrum significantly.

A similar fit to energies above the “ankle” can be seen in Figure 9.2. Here, the start-point of the fit was the $10^{18.5}$ eV bin and the end-point was determined by the threshold energy of the GZK effect ($10^{19.8}$ eV). The power index derived from this fit is 2.844 ± 0.078 , which is larger than the *Fly’s Eye* measurement of 2.71 ± 0.10 , but still within the quoted errors. The difference is most likely due to a different atmospheric

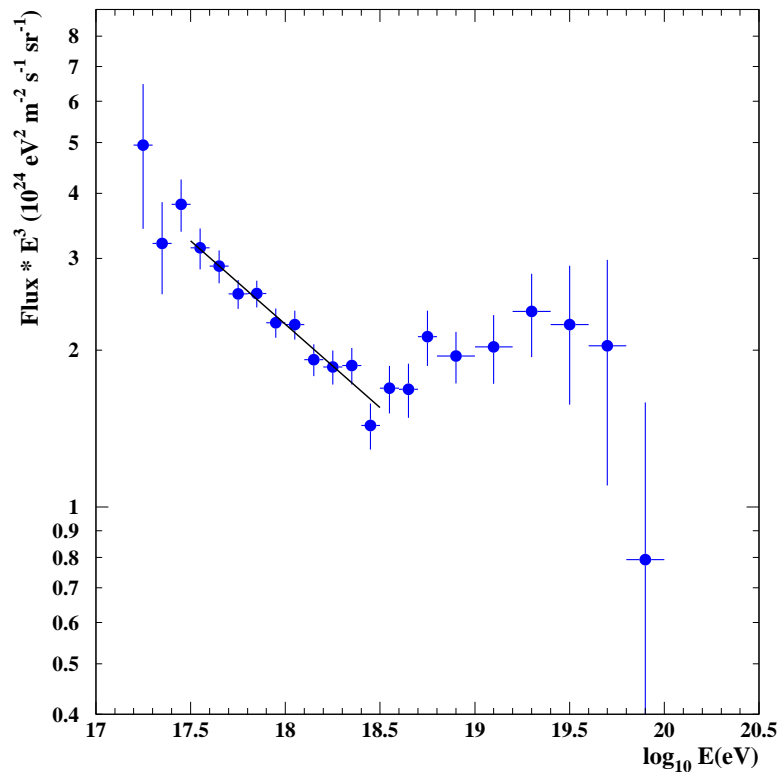


Figure 9.1: Fit to the *HiRes-2* spectrum below the “ankle”.

model used in the *Fly’s Eye* experiment. The slope in the *HiRes-2* fit agrees well with the *HiRes-1* monocular measurement. The $\chi^2/\text{d.o.f.}$ is 2.71/6, and the normalization at 10^{18} eV is 1.42 ± 0.22 .

Even with the low statistics at the high energy end, it is interesting to ask the question whether the *HiRes-2* spectrum is consistent with a continuation of the cosmic ray flux beyond the GZK threshold energy with the same spectral index that is seen above the “ankle”. As described in Chapter 1, such an unchanged continuation has been observed in the *AGASA* experiment at the highest energies. I have calculated the expected number of events for energies above $10^{19.8}$ eV, assuming a flux following the power law derived from the fit above the “ankle”, and using the *HiRes-2* exposure estimate. The *HiRes-2* exposure at the highest energies is very large and will allow detection of “super-GZK” events if they exist. The expected number of events above $10^{19.8}$ eV was

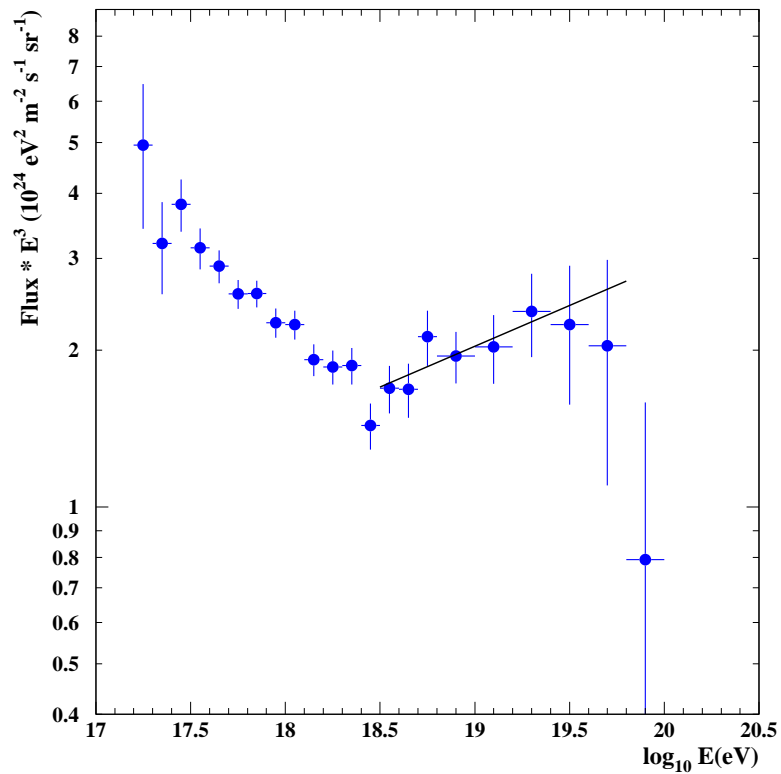


Figure 9.2: Fit to the *HiRes-2* spectrum above the “ankle”.

compared to the observed number of events in the *HiRes-2* data analyzed here. One would expect to observe 5.2 events above this energy, where only 1 event is detected. The Poisson probability for observation of 1 or 0 events with a mean of 5.2 events is 3.4%.

A more significant result can be obtained with the combination of statistics from the two *HiRes* monocular spectra, which are shown in Figure 9.3. The *HiRes-1* data included in this graph have been recorded between June of 1997 and February of 2003. The two monocular measurements of the energy spectrum are in close agreement. A similar fit for energies above the “ankle” to the combined monocular spectra results in an expected number of 28.0 events above $10^{19.8}$ eV given the HiRes aperture, where only 11 events were observed [106]. The Poisson probability for 11 or fewer events

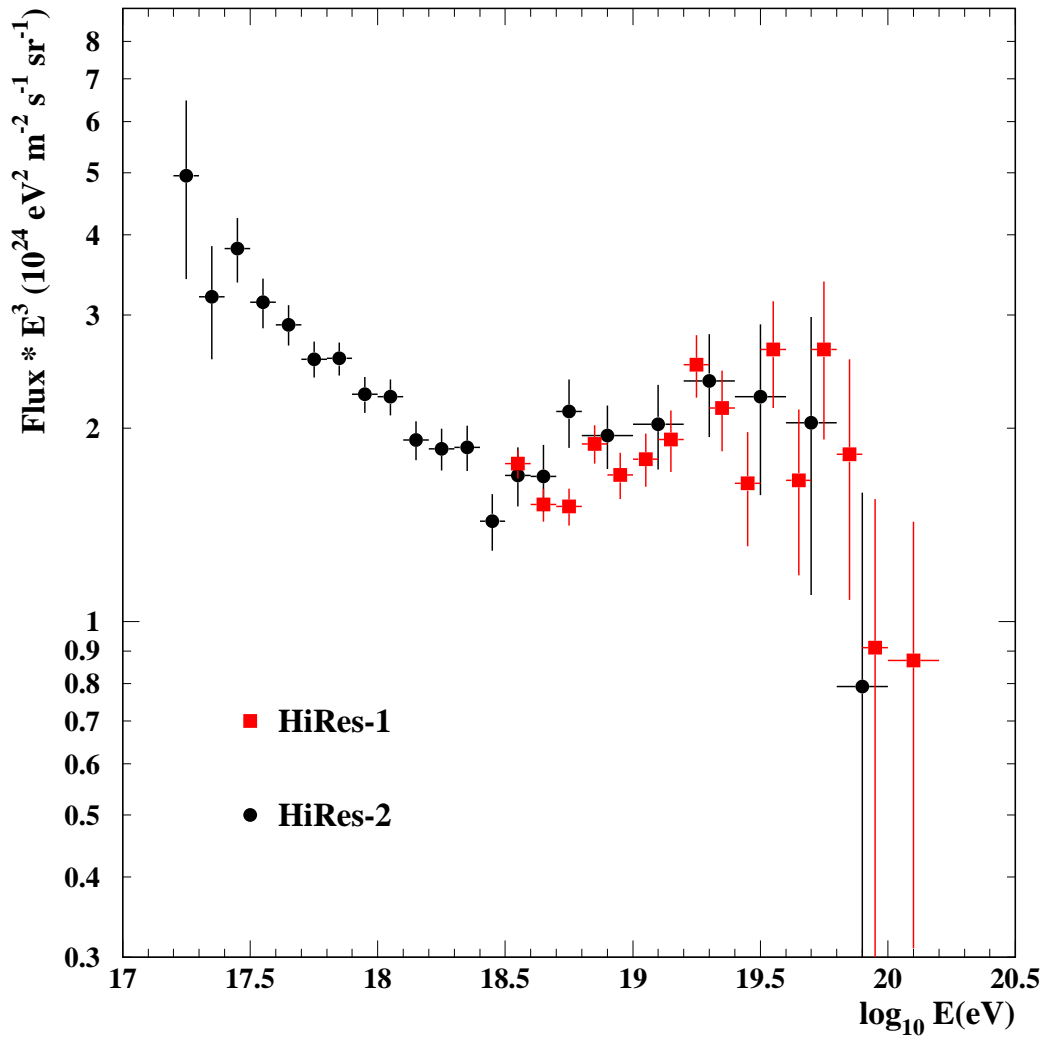


Figure 9.3: UHECR energy spectrum measured by *HiRes* in monocular mode.

with a mean of 28 is 2.4×10^{-4} . More sophisticated fits to the combined spectra, assuming a galactic and an extragalactic component of the cosmic ray flux, show that the *HiRes* spectra are consistent with the theoretically predicted GZK flux suppression [73] [3] [78] [107].

The preliminary *HiRes* stereo measurement of the UHECR spectrum can be seen in Figure 9.4 in comparison with the monocular spectra. The stereo analysis is still in progress, though, and the stereo spectrum shown here is not a final result.

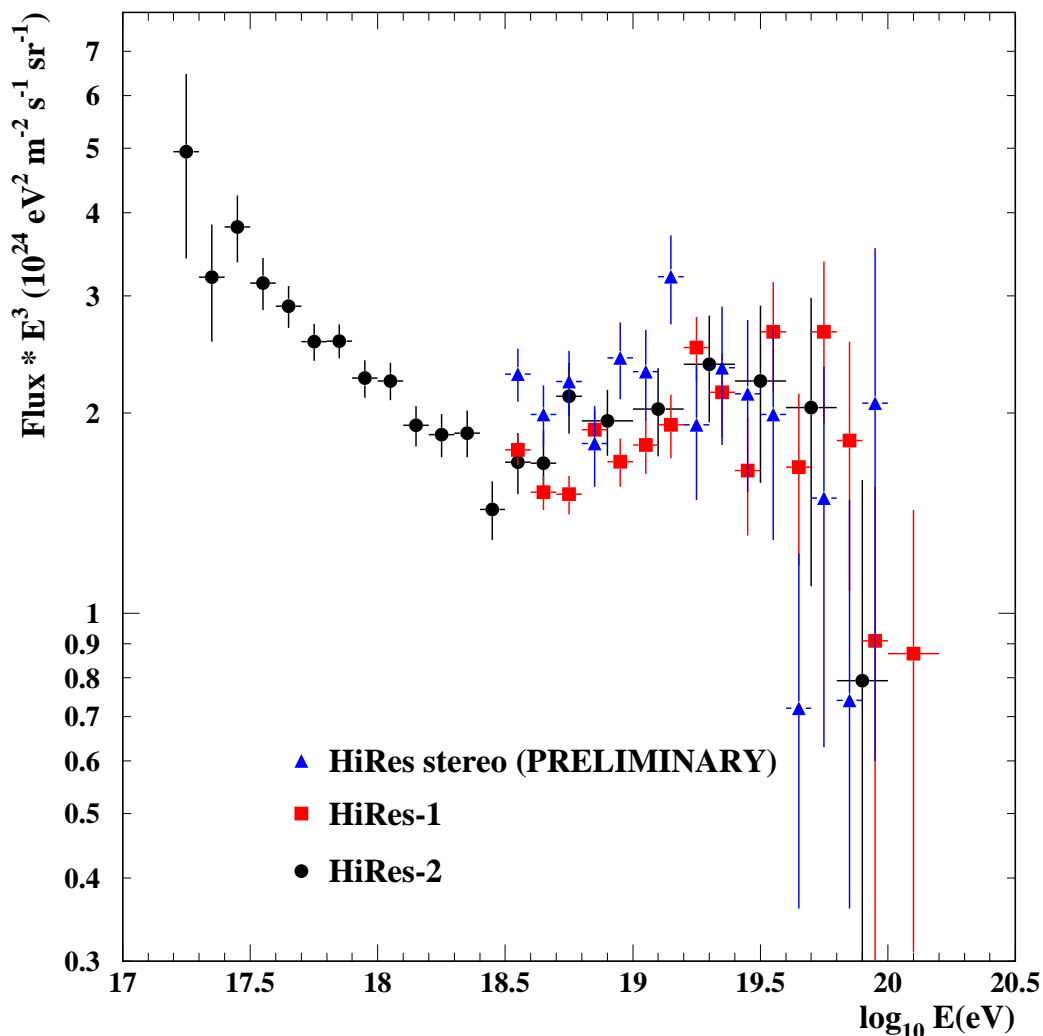


Figure 9.4: *HiRes* monocular and preliminary stereo measurements of the UHECR spectrum.

Figure 9.5 compares the spectrum of our predecessor experiment, *Fly's Eye*, with the *HiRes* monocular results. The agreement is very good, except for the different slope for energies above the “ankle”, as mentioned above. From this graph can also be seen that the *HiRes-2* spectrum is consistent with the “second knee” observed by *Fly's Eye*, although we cannot claim detection of this feature due to low statistics.

The spectrum measured by the *HiRes/MIA* experiment is roughly 30% lower than

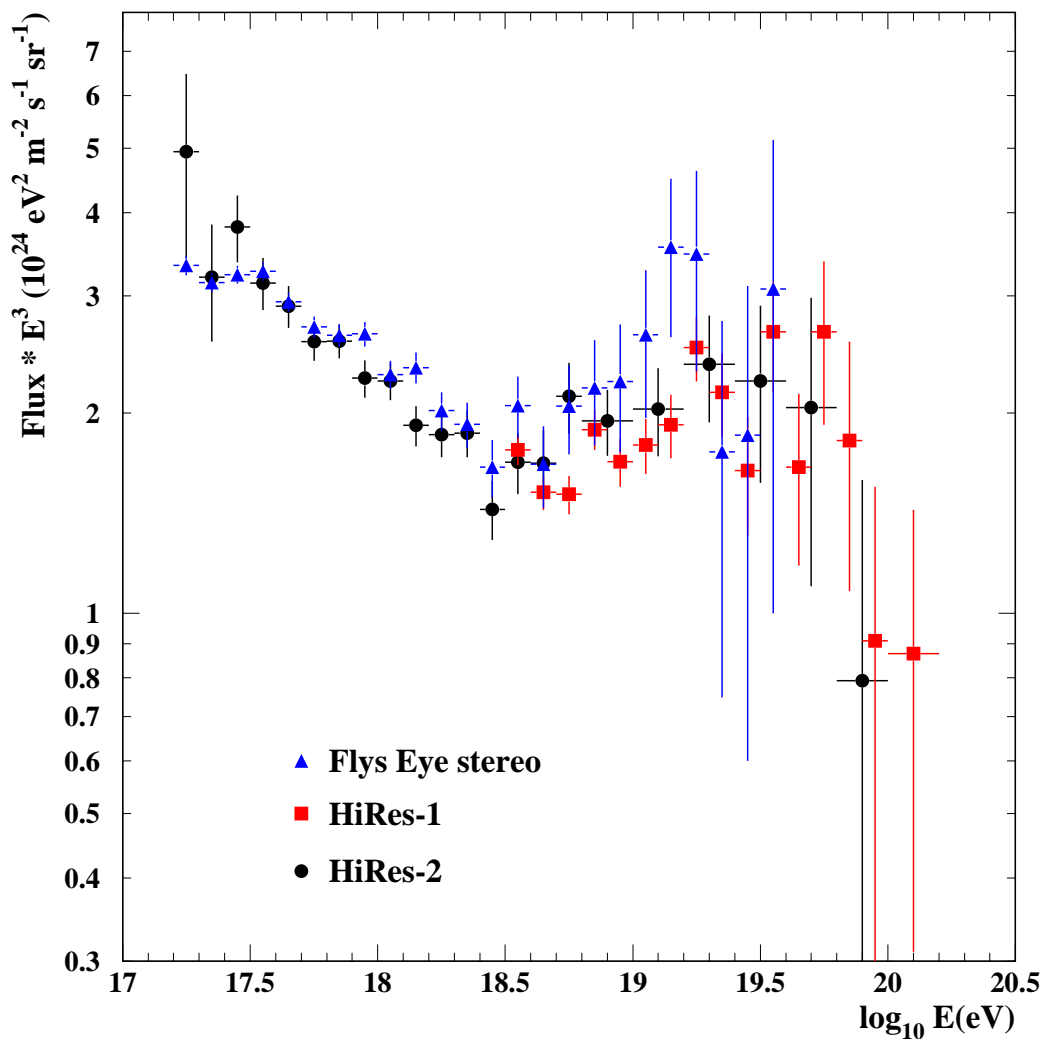


Figure 9.5: *HiRes* monocular and *Fly's Eye* stereo measurements of the UHECR spectrum.

the *HiRes-2* measurement, as can be seen in Figure 9.6. However, statistics in the first non-zero bins of the *HiRes-2* spectrum are low and the same is true for *HiRes-MIA* at higher energies.

In the comparison of the *Yakutsk* measurement with the *HiRes* monocular spectra in Figure 9.7, the difference in the absolute normalization of the two experiments becomes apparent: The *Yakutsk* “trigger 500” points are roughly a factor of 2.5 higher than the

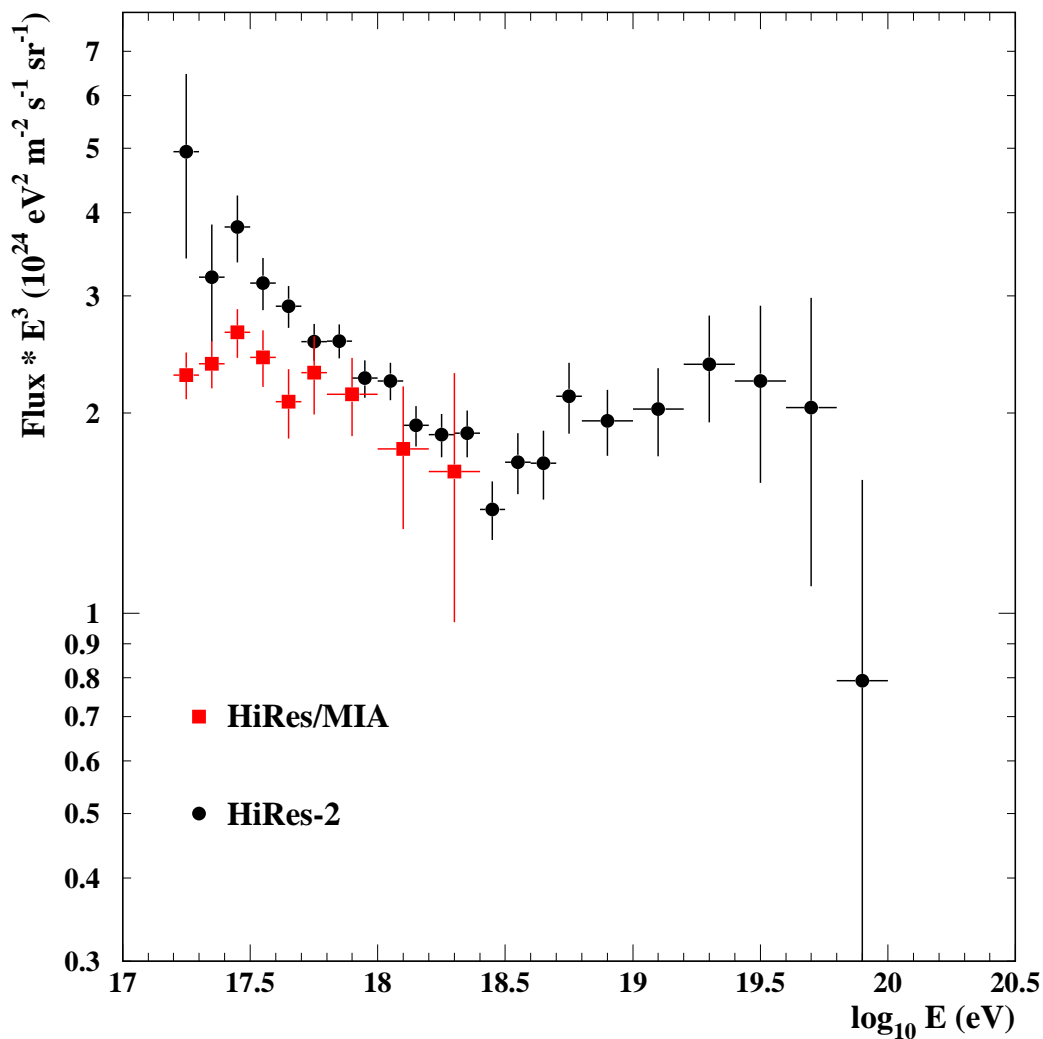


Figure 9.6: *HiRes* monocular and *HiRes/MIA* measurements of the UHECR spectrum.

HiRes points. The feature of the “ankle” in the *Yakutsk* spectrum appears at an energy roughly a factor of 4.5 higher than in the *HiRes* measurement.

The *Haverah Park* measurement of the UHECR spectrum, assuming a bi-modal composition of 34% protons and 66% iron nuclei, is compared to the *HiRes* spectra in Figure 9.8. The discrepancies between these measurements are within statistical errors for the points of the *Haverah Park* measurement that are included in the spectrum published in [7]. However, the re-calculated flux of the four highest energy events in

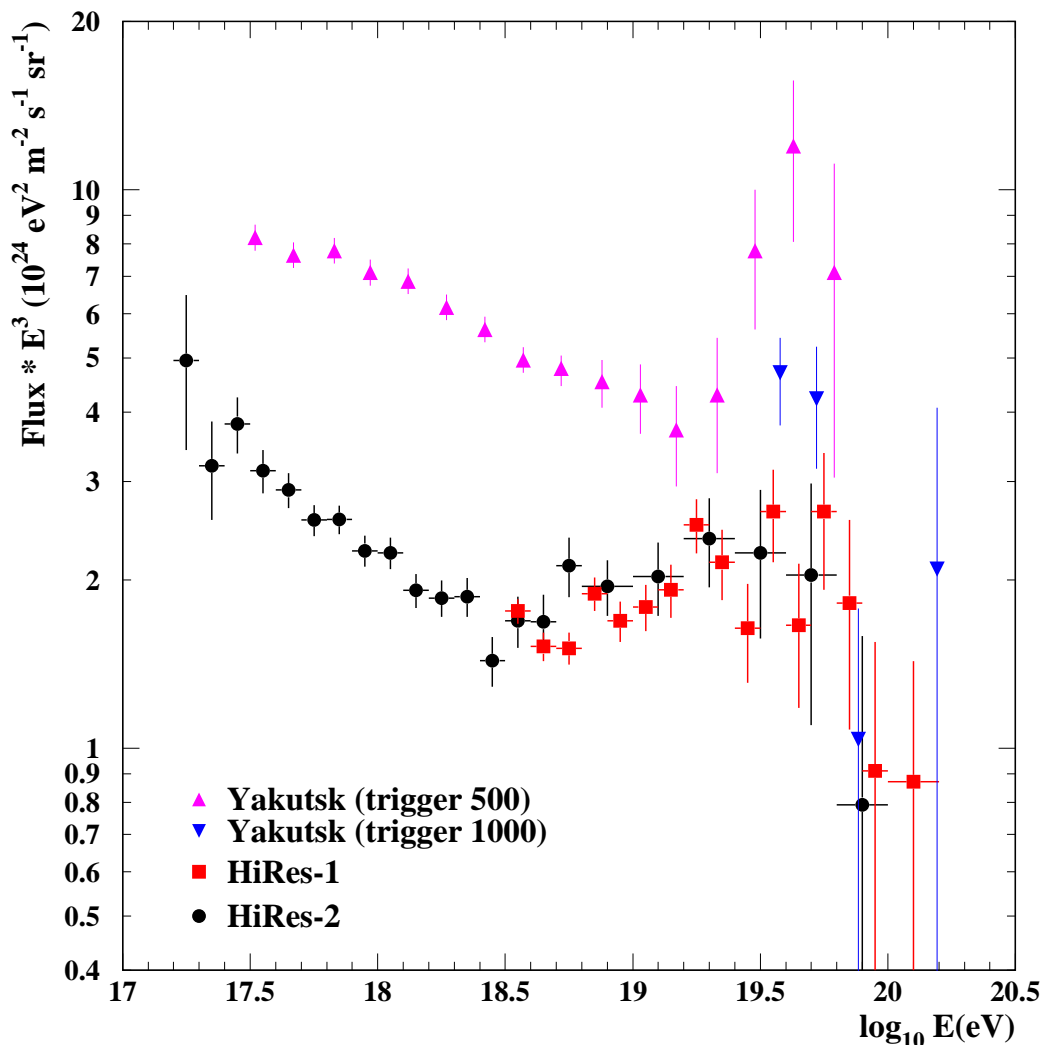


Figure 9.7: *HiRes* monocular and *Yakutsk* measurements of the UHECR spectrum. The data points of the *Yakutsk* spectrum have been taken from [40].

the *Haverah Park* data, which has been included here, is about a factor of 3 higher than the *HiRes* spectrum at the corresponding energy.

In the last figure (Fig. 9.9), the *AGASA* measurement of the spectrum can be seen in comparison to the *HiRes* spectra. *AGASA* is the only experiment that observes a continuation of the cosmic ray spectrum to energies above 10^{20} eV without a GZK flux suppression, which is in contradiction to the *HiRes* measurements. The difference

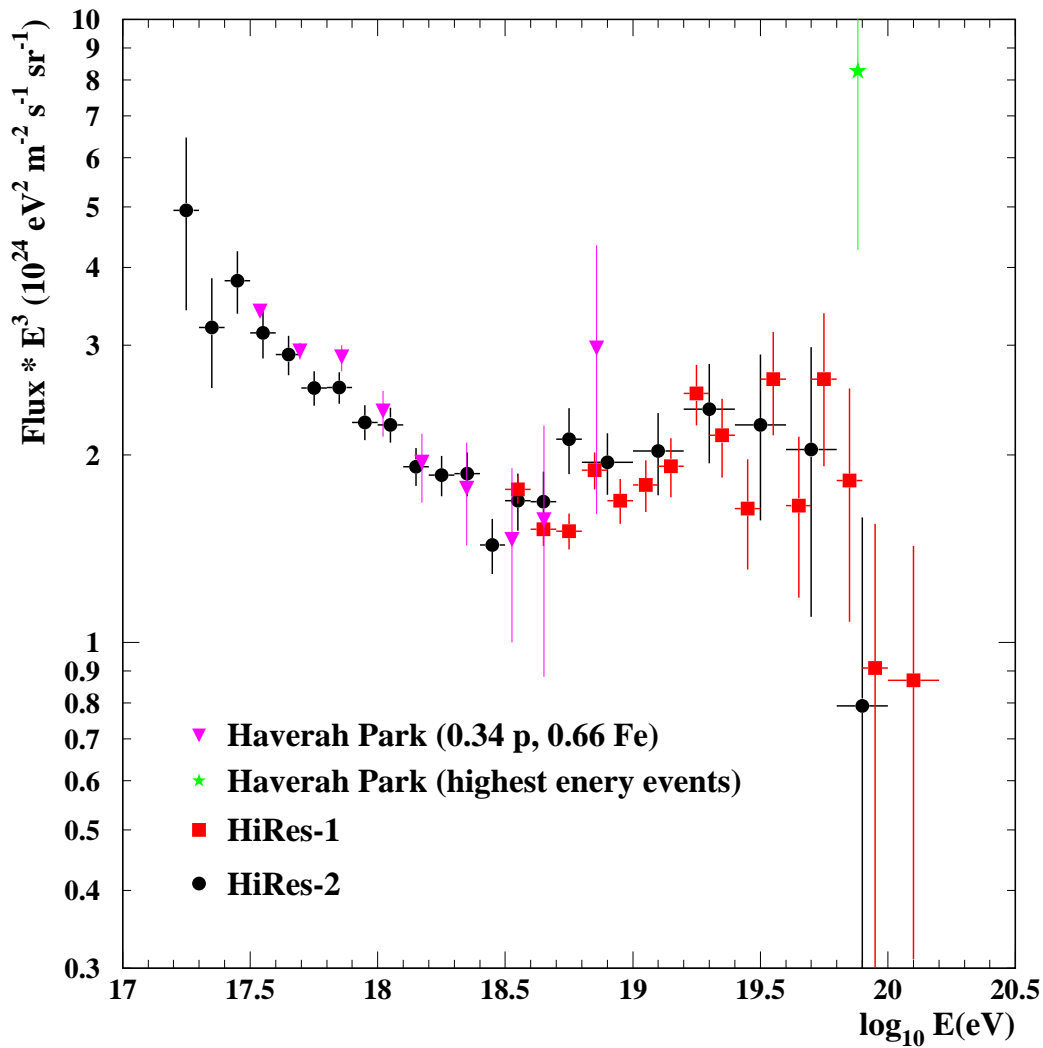


Figure 9.8: *HiRes* monocular and *Haverah Park* measurements of the UHECR spectrum. The *Haverah Park* spectrum and the highest energy point have been taken from [7]. This spectrum is based on a composition of 34% protons and 66% iron, in accordance with the measurement by the *Haverah Park* group.

in the absolute normalization of JE^3 corresponds to a 30% shift in energy, if it is due only to a difference in energy estimates. Such a shift would also reduce the discrepancy between the energies of the “ankle” seen by the two experiments.

In conclusion, we have measured the UHECR spectrum with the *HiRes-2* detector, which complements the *HiRes-1* measurement and is in good agreement with the *Fly’s*

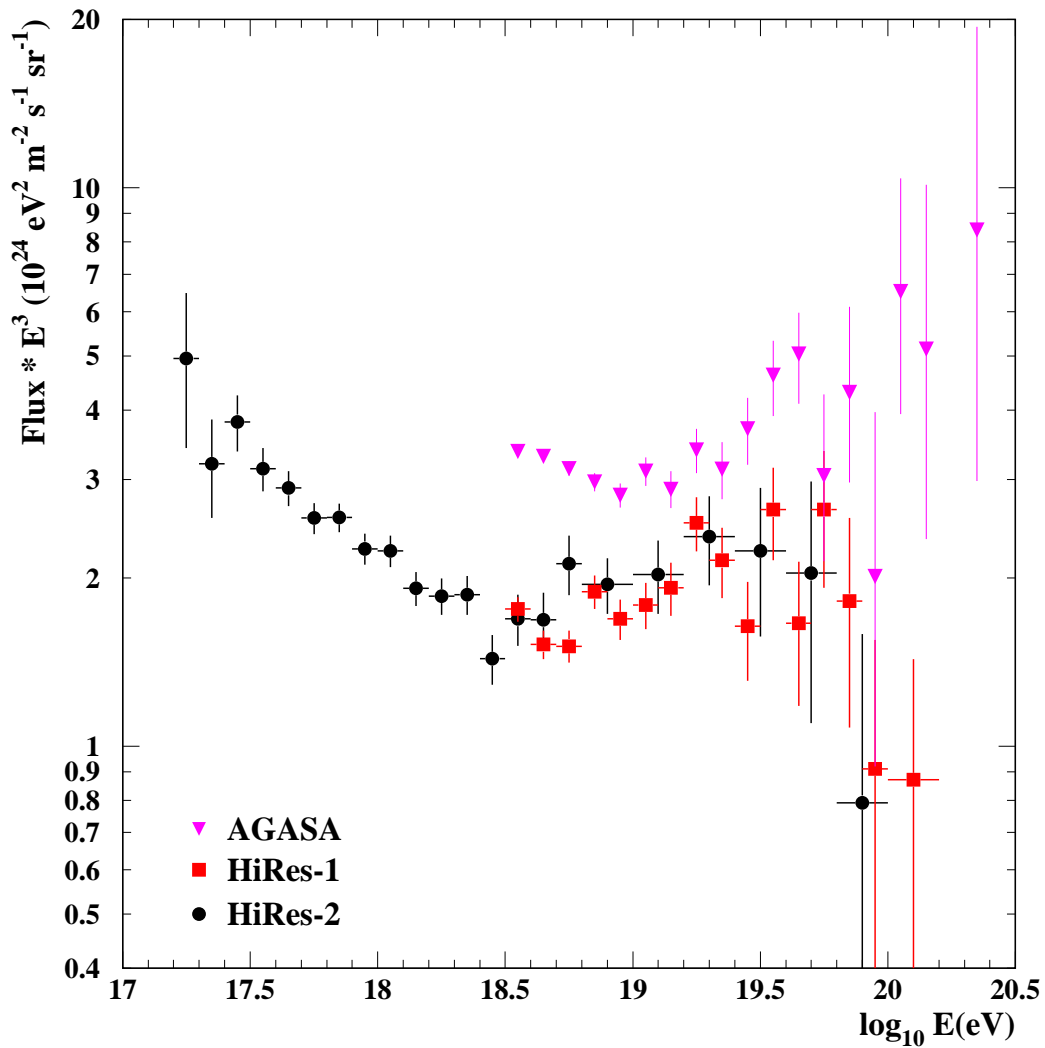


Figure 9.9: *HiRes* monocular and *AGASA* measurements of the UHECR spectrum. The *AGASA* measurement has been taken from [42].

Eye stereo spectrum. We have used a detailed MC simulation of the detector response to air showers generated with *CORSIKA* and *QGSJet* to estimate the acceptance of the *HiRes-2* detector. The shower library, trigger database, input spectrum and composition, background noise, and trigger algorithm I have added to the MC have made the simulation more realistic. Comparisons of different parameters between real and simulated events show an overall very good agreement. After applying a set of quality cuts,

a correction for “missing energy”, and a correction of the *HiRes-2* energy scale using the *HiRes-1* calibration, I have calculated the energy spectrum using the simulated detector acceptance. A study of the systematic uncertainty in the spectrum due to the uncertainty in the input composition has been presented. I have also studied the effect on the spectrum of using an atmospheric database instead of a measurement of the average aerosol content of the atmosphere. Results from those two studies show very small effects on the spectrum. We observe the feature of the “ankle” in the *HiRes-2* spectrum at an energy of about $10^{18.5}$ eV. The *HiRes-2* UHECR spectrum is consistent with the “second knee”, which was observed by the *Fly’s Eye* experiment, and the GZK flux suppression. However, we cannot claim evidence for these features from this analysis due to the low statistics in the analyzed *HiRes-2* data at the low and high energy end of the spectrum presented here.

Appendix A

List of Acronyms

AC	alternate current
CCD	charge coupled device (camera)
CMBR	cosmic microwave background radiation
DAC	digital to analog converter
DS1	dataset 1 (of HiRes-2 data from 12/99 to 05/00)
DS2	dataset 2 (of HiRes-2 data from 09/00 to 03/01)
DS3	dataset 3 (of HiRes-2 data from 03/01 to 09/01)
DSP	digital signal processor
DST	data storage “tape” (format)
EAS	extensive air shower
FADC	“flash” analog to digital converter
FRII	Fanaroff-Riley class II (radio galaxies and quasars)
GRB	gamma-ray burst
GZK	Greisen-Zatsepin-Kuz’min (cosmic ray flux suppression)
HAL	horizontal attenuation length (in aerosol)
HBOOK	FORTRAN based data analysis software
HG	high gain (channel)
HPD	hybrid photo-diode
LG	low gain (channel)
MC	Monte Carlo simulation
NIST	National Institute of Standards and Technology
p.e.	photoelectron
PLD	programmable logic device
PMT	photomultiplier tube
PPG	programmable pulse generator
QDC	charge to digital converter
RXF	“roving” xenon flash lamp
UHECR	ultra-high energy cosmic ray
VAOD	vertical aerosol optical depth
VME	Versa Module Europa bus system (computer protocol)
VNC	virtual network connection
YAG	yttrium-aluminum-garnet (laser)

References

- [1] *Auger Design Report*, 1997, <http://www.auger.org/admin/DesignReport>.
- [2] W. Heitler and L. Janossy, *Proc. Phys. Soc. (London) Sect. A* **62**, 669 (1949).
- [3] R. U. Abbasi *et al.*, *Phys. Rev. Lett.* **92**, (2004), arXiv: astro-ph/0208243.
- [4] T. Abu-Zayyad *et al.*, *Astrophys.J.* **557**, 686 (2001), arXiv: astro-ph/0010652.
- [5] G. W. Clark *et al.*, *Phys. Rev.* **122**, 637 (1961).
- [6] J. Linsley, *Proceedings of the 19th International Cosmic Ray Conference* **9**, 475 (1985).
- [7] M. Ave *et al.*, *Astropart. Phys.* **19**, 47 (2003), arXiv: astro-ph/0112253.
- [8] M. Ave *et al.*, *Astropart. Phys.* **19**, 61 (2003), arXiv: astro-ph/0203150.
- [9] L. Anchordoqui and H. Goldberg, *Phys. Lett. B* **583**, 213 (2004), arXiv: hep-ph/0310054.
- [10] A. A. Ivaonv, S. P. Knurenko, and I. Y. Sleptsov, *Nucl. Phys. Proc. Suppl.* **122**, 226 (2003), arXiv: astro-ph/0305053.
- [11] M. Teshima *et al.*, *Nucl. Inst. Meth.* **A247**, 399 (1997).
- [12] A. Borione *et al.*, *APJ* **493**, 175 (1998).
- [13] http://www.icrr.u-tokyo.ac.jp/em/tibet_exp/paper/paper.html.
- [14] S. P. Swordy and D. B. Kieda, *Astropart. Phys.* **13**, (2000), arXiv: astro-ph/9909381.
- [15] M. Cassidy *et al.*, *Proceedings of the 25th International Cosmic Ray Conference* (1997), arXiv: astro-ph/970738.
- [16] A. N. Bunner, Ph.D. thesis, Cornell University, 1967.
- [17] G. Davidson and R. O'Neil, *J. Chem. Phys.* **41**, 3946 (1964).
- [18] F. Kakimoto *et al.*, *Nucl. Inst. Meth. A* **372**, 527 (1996).
- [19] B. Dawson, Technical report, University of Adelaide (unpublished).
- [20] A. N. Bunner, K. Greisen, and P. Landecker, *Can. J. of Phys.* **46**, 266 (1967).

- [21] T. Hara *et al.*, Acta Physica Academiae Hungaricae Suppl. 3 **29**, 361 (1970).
- [22] H. E. Bergeson *et al.*, Phys. Rev. Lett. **39**, 847 (1977).
- [23] R. M. Baltrusaitis *et al.*, Nucl. Instrum Methods Phys. Res. A **240**, 410 (1985).
- [24] D. J. Bird *et al.*, Phys. Rev. Lett. **71**, 3401 (1993).
- [25] K. Bernloehr *et al.*, Astropart. Phys. **20**, 111 (2003), arXiv: astro-ph-0308246 & 7.
- [26] N. Goetting, Proceedings of the HEP2003 Europhysics Conference (2003), arXiv: astro-ph/0310308.
- [27] R. A. Ong, International Symposium: The Universe Viewed in Gamma Rays (2002), arXiv: astro-ph/0302610.
- [28] J. Flix, Proceedings of the "Satellites and tidal streams" conference (2003), arXiv: astro-ph/0311207.
- [29] <http://www-ik.fzk.de/KASCADE>.
- [30] O. Ravel *et al.*, 8th Pisa Meeting on Advanced Detectors (2003), arXiv: astro-ph/0306255.
- [31] T. Huege and H. Falcke, Proceedings of the 6th European VLBI Network Symposium (2002), arXiv: astro-ph/0207647.
- [32] T. K. Gaisser, *Cosmic Rays and Particle Physics* (Cambridge University Press, first edition, 1990).
- [33] P. Sokolsky, *Introduction to Ultrahigh Energy Cosmic Ray Physics* (Addison-Wesley Publishing Company, Inc., first edition, 1989).
- [34] M. Ostrowski, Astropart. Phys. **18**, 229 (2002), arXiv: astro-ph/0101053.
- [35] A. M. Hillas, A.R.A.&A. **22**, 425 (1984).
- [36] K. Greisen, Phys. Rev. Lett. **16**, 748 (1966).
- [37] G. T. Zatsepin and V. A. Kuz'min, JETP Lett. **4**, 78 (1966).
- [38] V. Berezhinsky, Physics of Atomic Nuclei **66**, 423 (2003), arXiv: astro-ph/0107306.
- [39] *Physical Review D*, No. 1-I in *Third Series*, edited by E. J. Weinberg and D. L. Nordstrom (The American Physical Society, Ridge, NY, USA, 2002), p. 60.
- [40] A. V. Glushkov *et al.*, Proceedings of the 28th International Cosmic Ray Conference 389 (2003).

- [41] D. J. Bird *et al.*, *Astrophys.J.* **441**, 144 (1995), arXiv: astro-ph/9410067.
- [42] M. Takeda *et al.*, *Astropart. Phys.* **19**, 447 (2003), arXiv: astro-ph/0209422.
- [43] J. R. Hörandel, *Astropart. Phys.* **19**, 193 (2003), arXiv: astro-ph/0210453.
- [44] N. Hayashida *et al.*, *Astropart. Phys.* **10**, 303 (1999), arXiv: astro-ph/9807045.
- [45] N. Hayashida *et al.*, Proceedings of the 26th International Cosmic Ray Conference (1999), arXiv: astro-ph/9906056.
- [46] D. J. Bird *et al.*, *Astrophys.J.* **511**, 739 (1999).
- [47] J. A. Bellido, Ph.D. thesis, University of Adelaide, 2002.
- [48] G. L. Cassidy *et al.*, *Phys. Rev. Lett.* **62**, 383 (1989).
- [49] M. Teshima *et al.*, *Phys. Rev. Lett.* **64**, 1628 (1990).
- [50] M. A. Lawrence, D. C. Prosser, and A. A. Watson, *Phys. Rev. Lett.* **63**, 1121 (1989).
- [51] A. A. Watson, *Nucl. Phys. B. (Proc. Suppl.)* **22**, 116 (1991).
- [52] M. Takeda *et al.*, *Astrophys.J.* **522**, 225 (1999).
- [53] T. Stanev *et al.*, *Phys. Rev. Lett.* **75**, 3056 (1995).
- [54] N. Hayashida *et al.*, Appendix to *ApJ* 522(1999)225 (2000), arXiv: astro-ph/0008102.
- [55] D. S. Gorbunov *et al.*, *Astrophys.J.* **L93**, 577 (2002), arXiv: astro-ph/0204360.
- [56] <http://www.auger.org>.
- [57] <http://www.euso-mission.org>.
- [58] <http://owl.gsfc.nasa.gov>.
- [59] M. Fukushima, *J. Phys. Soc. Jpn. Suppl. B* **70**, 204 (2001).
- [60] T. Abu-Zayyad *et al.*, *Nucl. Instrum Methods Phys. Res. A* **450**, 253 (2000).
- [61] T. Abu-Zayyad *et al.*, *Phys. Rev. Lett.* **84**, 4276 (2000).
- [62] K. Reil, Ph.D. thesis, University of Utah, 2002.
- [63] C. R. Wilkinson, Ph.D. thesis, University of Adelaide, 1998.
- [64] J. N. Matthews and S. B. Thomas, Proceedings of the 28th International Cosmic Ray Conference (2003).
- [65] J. H. V. Girard *et al.*, *Nucl.Inst.Meth.A* **460**, (2001).

- [66] D. Bergman, Proceedings of the 27th International Cosmic Ray Conference 639 (2001).
- [67] P. A. Sadowski *et al.*, *Astropart. Phys.* **18**, 237 (2002).
- [68] R.W.Clay *et al.*, Proceedings of the 27th International Cosmic Ray Conference 649 (2001).
- [69] L. R. Wiencke *et al.*, *Nucl. Inst. and Meth.* **A428**, 593 (1999).
- [70] M. D. Roberts, Proceedings of the 27th International Cosmic Ray Conference 627 (2001).
- [71] M. D. Roberts, Proceedings of the 27th International Cosmic Ray Conference 631 (2001).
- [72] L. R. Wiencke *et al.*, (in preparation).
- [73] R. U. Abbasi *et al.*, submitted to *Astroparticle Physics* , arXiv: astro-ph/0208301.
- [74] J. N. Bahcall and E. Waxman, *Phys. Lett. B* **556**, 1 (2003), arXiv: hep-ph/0206217.
- [75] D. D. Marco, P. Blasi, and A. V. Olinto, *Astropart. Phys.* **20**, 53 (2003), arXiv: astro-ph/0301497.
- [76] D. R. Bergman, (in preparation) .
- [77] G. C. Archbold, Ph.D. thesis, University of Utah, 2002.
- [78] D. R. Bergman, Proceedings of the Cosmic Ray International Seminar CRIS 04 (2004).
- [79] R. U. Abassi *et al.*, *Astropart. Phys.* **21**, 111 (2004), arXiv: astro-ph/0309457.
- [80] R. U. Abassi *et al.*, *Astrophys.J.* **L73**, 610 (2004).
- [81] R. U. Abassi *et al.*, accepted for publ. in *Astropart. Phys.* (2004), arXiv: astro-ph/0404366.
- [82] C. B. Finley and S. Westerhoff, *Astropart. Phys.* **21**, 359 (2004), arXiv: astro-ph/0309159.
- [83] J. H. Boyer *et al.*, *Nucl. Instrum Methods Phys. Res. A* **482**, 457 (2002).
- [84] J. H. Boyer *et al.*, Proceedings of the 26th International Cosmic Ray Conference **5**, 441 (1999).
- [85] G. Cowan, *Statistical Data Analysis* (Oxford Science Publications, first edition, 1998).

- [86] D. Heck, J. Knapp, J. N. Capdevielle, G. Schatz, and T. Thouw, Report FZKA 6019, Forschungszentrum Karlsruhe (1998), http://www-ik3.fzk.de/~heck/corsika/physics_description/corsika_phys.html.
- [87] <http://nssdc.gsfc.nasa.gov/space/model/models/igrf.html>.
- [88] W. R. Nelson, H. Hirayama, and D. W. O. Rogers, SLAC Report **265**, (1985).
- [89] H. Fesefeldt, Report PITHA-85/02, RWTH Aachen (1985).
- [90] N. N. Kalmykov, S. S. Ostapchenko, and A. I. Pavlov, Nucl. Phys. B (Proc. Suppl.) **52B**, 17 (1997).
- [91] L. A. Anchordoqui *et al.*, Physical Review D **59**, (1999).
- [92] R. J. Glauber and G. Matthiae, Nucl. Phys. **B21**, 135 (1970).
- [93] R. Engel, T. K. Gaisser, and T. Stanev, Proceedings of the 27th International Cosmic Ray Conference 431 (2001).
- [94] T. K. Gaisser and A. M. Hillas, Proceedings of the 15th International Cosmic Ray Conference **8**, 353 (1977).
- [95] C. Song *et al.*, Astropart. Phys. **14**, 7 (2000), arXiv: astro-ph/9910195.
- [96] K. Kamata and J. Nishimura, Prog. Theoretical Phys. Suppl. **6**, (1958).
- [97] F. Arqueros *et al.*, Astron. Astrophys. **359**, (2000), arXiv:astro-ph/9908202.
- [98] *John Boyer, private communication.*
- [99] G. Mie, Ann. Phys. **25**, 377 (1908).
- [100] A. Kokhanovsky, *Optics of Light Scattering Media* (John Wiley & Sons, first edition, 1999).
- [101] D. R. Longtin, Air Force Geophysics Laboratory, AFL-TR-88-0112 (1998).
- [102] <http://wwwasdoc.web.cern.ch/wwwasdoc/minuit/minmain.html>.
- [103] http://wwwasdoc.web.cern.ch/wwwasdoc/hbook_html3/hboomain.html.
- [104] *Douglas Bergman, private communication.*
- [105] *Physical Review D*, No. 1-I in *Third Series*, edited by E. J. Weinberg and D. L. Nordstrom (The American Physical Society, Ridge, NY, USA, 2002), p. 230.
- [106] R. U. Abbasi *et al.*, (in preparation).
- [107] D. R. Bergman, (in preparation) .

Vita

Andreas Zech

Education

10/2004	Ph.D. degree at Rutgers University, USA.
09/2000 - 10/2004	Research in cosmic ray physics (<i>High Resolution Fly's Eye Experiment</i>) in the Rutgers Ph.D. program.
09/1999 - 09/2000	Research in cosmic ray physics (<i>High Resolution Fly's Eye Experiment</i>) in the Rutgers M.S. program.
09/1998 - 09/1999	Graduate studies in physics at the Universität Würzburg (Germany).
09/1998	Vordiplom (equivalent to B.S. degree) at the Universität Würzburg.
09/1996 - 09/1998	Undergraduate studies in physics at the Universität Würzburg.
09/1995 - 09/1996	Alternative civilian service in Aschaffenburg (Germany).
06/1995	Abitur (baccalaureate degree) at the Kronberg Gymnasium Aschaffenburg.

Publications

Measurement of the Flux of Ultrahigh Energy Cosmic Rays from Monocular Observations by the High Resolution Fly's Eye Experiment, HiRes Collaboration, Phys. Rev. Lett. 92 , 151101 (2004)

Search for Global Dipole Enhancements in the HiRes-I Monocular Data above $10^{18.5}$ eV, HiRes Collaboration , Astroparticle Physics 21 (2004) pp. 111-123

Study of Small-Scale Anisotropy of Ultrahigh Energy Cosmic Rays Observed in Stereo by HiRes, HiRes Collaboration, *Astrophys. Journal* L73 (2004) 610

Testing the HiRes Detector Simulation against UHECR Data., A. Zech, *Proceedings of the 28th Int. Cosmic Ray Conf.* (2003) p. 567 ff.

Geometry and Optics Calibration of Air Fluorescence Detectors using Star Light, HiRes Collaboration, *Astroparticle Physics* 18 (2002) 237

Comparison of CORSIKA-generated Showers with HiRes Data, A. Zech, *Proceedings of the 27th Int. Cosmic Ray Conf.* (2001) p. 494 ff.